SINTERING AND THERMAL BEHAVIOR OF URANIUM DIOXIDE IN BERYLLIUM OXIDE MATRIX

A Thesis

by

CHAD BENJAMIN GARCIA

Submitted to the Office of Graduate and Professional Studies of
Texas A&M University
in partial fulfillment of the requirements for the degree of

MASTER OF SCIENCE

Chair of Committee,	Sean M. McDeavitt
Committee Members,	Jean C. Ragusa
	Miladin Radovic
Head of Department,	Yassin A. Hassan

May 2014

Major Subject: Nuclear Engineering

ABSTRACT

The primary fuel used in light water nuclear reactors (LWRs) is uranium dioxide (UO_2), which has a low thermal conductivity that causes a large thermal gradient across the fuel pin during operation. One proposed method to improve the thermal conductivity of the fuel is to insert a thermally conductive additive such as beryllium oxide (BeO) or other ceramic materials into the fuel structure. This study is focused on a particular fuel design developed at Purdue University wherein large UO_2 microspheres are dispersed within a continuous BeO matrix. The BeO has a relatively high thermal conductivity for an oxide material and the interconnected matrix is intended to enable higher heat removal from the fuel. Therefore it is of interests to characterize the effective thermal conductivity of this UO_2-BeO fuel concept and consider variations of this property with BeO composition of 2.5, 5, 7.5, and 10 volume % BeO.

As part of this study, the basic pellet manufacturing procedures were improved over previous work to create samples suitable for characterization that did not crack or have a large volume of porosity. The pellet pressing and sintering methods were reproduced and then modified; densification measurements were performed to track the pellet status prior to, during, and after sintering using geometric measurements, immersion mass-based measurements, and LVDT dilatometery. The pellet samples were prepared using ball milled UO_2 powder that was compacted with high pressure (680MPa). The compacted pellets were crushed then self-milled to create green

spherical granules. These granules were mixed with jet-milled BeO powder, and the mixture was pressed and sintered.

The pellet processing parameters were modified from literature values to achieve pellet with less than 8% porosity and minimal cracking. The optimal parameters determined for this study include: 1) pre-compaction pressure of 680 MPa, 2) pellet final compaction pressure of 200 MPa, 3) sintering temperature of 1600°C, 4) sintering time from 4 to 6hr, and 5) sintering atmosphere of flowing Ar-5%H_2. The thermal conductivity was measured by Light Flash Analysis (LFA) at temperatures from 25 to 250°C. From this study it was found that the thermal conductivity of the baseline UO_2 was improved approximately 10% for each 1 volume percent BeO over the measured temperature range.

DEDICATION

This thesis is for their push for me to be my best. For their support and all they have allowed me to learn. This is for their help and kind words in times of struggling. This is for the years I was honored to have their guidance. This is for the little lessons like counting my toes. This is for the big lesson like using your mind over using your fist. This is to my parents, Charles and Ramona, for their love, care, and constant prayer.

ACKNOWLEDGEMENTS

I would like to thank my advisor Dr.McDeavitt, for his continued guidance and patience throughout my research. I would also like to thank the rest of my committee, Dr. Ragusa and Dr. Radovic for their support and advice. I would also like to thank IBC and Texas A&M for funding and facilitating this research.

All the help from the FCML group was much appreciated. Those who helped directly on the project, Brandon Blamer, Karyn Stern, Daniel Custead, Matthew, Alifya Faizullah, and Ryan Brito, were much appreciated. Thanks also go to Dr. Dela Perez-Nunez for all her help and for finding usable powder for this research. Thanks to both Carissa Helmreich and Brian Barnhart for teaching how to use the LFA, and Dr. Sandeep Irukuvarghula and Dr. Ahn Sangjoon for teaching me about the MRF and DSC. I would also like to thank Grant Helmreich for his help with the microprobe on the weekends. Special thanks to Dr. Luis Ortega, Dr. Adam Parkison, Marie Arrieta for listening and their input.

I would also like to thank the help received from the EMPE , BETA, and the Electron Microprobe Laboratories at Texas A&M, specifically Dr. Ray Guillemette for his time and advise. The advice in powder compaction from Liangfa Hu was also much appreciated. I would also like to thank Mark Norman for his input on the electrical design of the LVDT setup.

Finally I would like to thank my family for all their much needed support and aid. A special thanks to my wife for being there for me, even when I had long nights and weeks in alone.

NOMENCLATURE

BeO	Beryllium Oxide/Beryllia
UO_2	Uranium Doixide
$UO_{2+\eta}$	Hyperstoichiometric UO_2
$UO_{2-\eta}$	Hypostoichiometric UO_2
η	Difference from Stoichiometry
U_3O_8	Uranium
LVDT	Linear Variable Differential Transformer
LWR	Light Water Reactor
EBOR	Experimental Beryllium Oxide Reactor
LFA	Laser Flash Analysis
ETC	Effective Thermal Conductivity
C_p	Heat Capacity
ARE	Aircraft Reactor Experiment
MGCR	Maritime Gas-Cooled Reactor
ACRR	Annular Core Research Reactor
ρ	Density
k	Thermal Conductivity
k_L	Lattice Thermal Conductivity
k_{AM}	Ambipolor Thermal Conductivity
k_0	Thermal conductivity without pores

k_p	Thermal conductivity with pores
k_{eff}	Effective Thermal Conductivity
T_m	Melting Temperature
α	Thermal Diffusivity
q''	Heat Rate per Unit Length
f(r,e)	Flux Depression Factor
CIM	Conductivity Integral to Melt
T	Temperature
p	Porosity
V_i	Volume Fraction of i Phase
n	Shape Factor
ψ	Shape Factor
GG	Green Granules
SB	Slug Bisque
FEM	Finite Element Model
SSA	Specific Surface Area
APS	Average Particle Size
O:M	Oxygen to Metal Raito
WDS	Wavelength Dispersive X-Ray Spectrometry
MRF	Materials Research Furnace
m_d	Dry Mass
m_w	Wet Mass

m_i	Imersed mass
DAQ	Data Acquisition Device
RTD	Resistance temperature Detector
ε	Strain
BSE	Backscater Electron Microscopy
CATH	Cathodoluminescence Microscopy
SE	Secondar Electron Microscopy
PM	Photomultiplier Tube
Al_2O_3	Aluminum Oxide/Alumina
EDS	Energy-dispersive X-ray Spectroscopy

TABLE OF CONTENTS

Page

LIST OF FIGURES

Page

LIST OF TABLES

Page

1. INTRODUCTION

Nuclear fuel for commercial Light Water Reactors (LWRs) is predominantly manufactured using enriched uranium oxide (UO_2). The selection of UO_2 was due, in part, to the high melting point of UO_2, high irradiation stability, and its relative inertness in the LWR system [1]. One of this materials' main limitations is its low thermal conductivity. This low conductivity causes large thermal gradients within the fuel and high centerline temperatures during reactor operation, both of which limit the fuel performance and safety. One approach that is being evaluated to improve the thermal conductivity of the fuel is with the addition of beryllium oxide (BeO), which is one of the most thermal conductive oxides [2]. Other additives have been and are currently being evaluated around the world, including thorium oxide [3], silicon carbide (SiC) , diamond , and even carbon nanotubes [4]. However, the development project reported here is focused on improving the fabrication methodology for UO_2-BeO pellets and characterizing the thermal conductivity of the ceramic composite.

The ceramic BeO has been used in several reactor fuel pellet designs ranging from gas cooled reactors to molten salt reactors and even in medical isotope production reactors [5, 6]. Because of BeO's favorable neutronic properties it was evaluated for use as a reflector and moderator material; the low atomic mass of Be is good for neutron moderation, it enables a neutron production reaction (n,2n), and it has a relatively low neutron capture cross section (0.01b) [7, 8]. In the 60's, one of the first uses for this type of fuel was the 10 MW_{th} Experimental Beryllium Oxide Reactor which was designed to

determine how different BeO-UO_2 fuel designs would hold up under irradiation [9-11]. This fuel type's thermal conductivity prior to irradiation was studied against composition and manufacturing methods in order to predict the improvement to the fuel's temperature profile within a reactor. The tests did show that the UO_2-BeO fuel withstood irradiation damage better with course dispersed UO_2 particles compared to fine UO_2 particles. It also showed that less 0.1% of produced fission gas was released when using fine dispersed UO_2 particles [9-11].

The current development of UO_2-BeO composite fuel was conducted at Purdue under the supervision of Dr. Solomon. This fuel type was altered from differed from other incarnations in that the dispersed UO_2 microspheres would be larger from 50 to 500µm, as well as small UO_2 particles within the BeO matrix as shown if Figure 1 [4, 12].

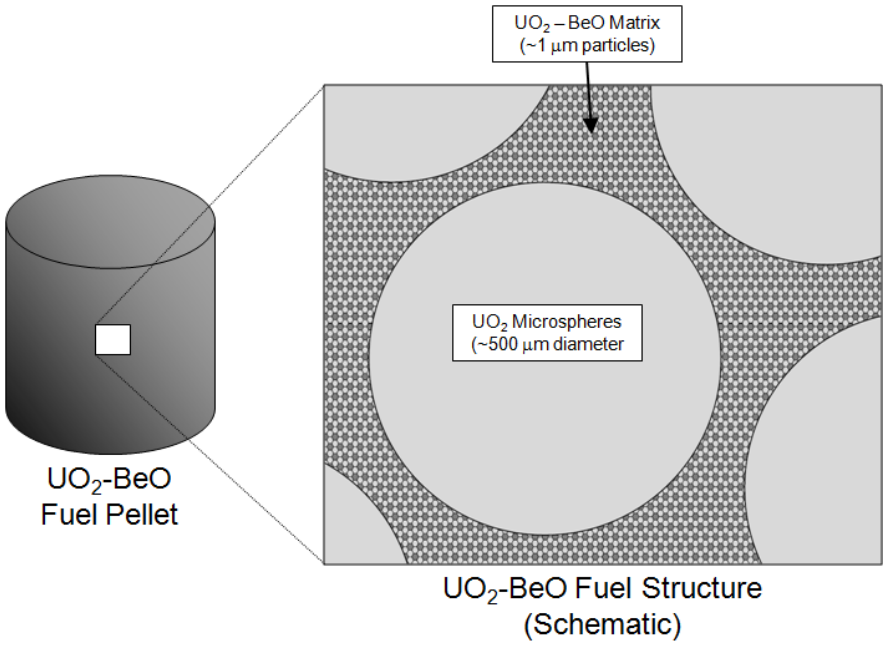

Figure 1. UO_2-BeO Fuel Design

Two different methods were developed to produce this fuel type, the first was labeled slug bisque (SB) and the second was the green granules (GG) method. Both methods first compact the UO_2 to 680MPa, and the compact is then ground to produce granules of the desired size. These granules are then milled to a round shape. The green granules method mixes these granules with the BeO which is then compacted to 260MPa and sintered at 1700°C. The SB method would first pre-sinter the milled granules prior to introducing the BeO, final compacting, and sintering. Solomon et al was able to produce samples with less than 3% porosity and showed approximately a 50% increase in thermal conductivity with UO_2-10v%BeO. The resulting microstructure of the UO_2-BeO can be seen in Figure 2 [4, 12, 13].

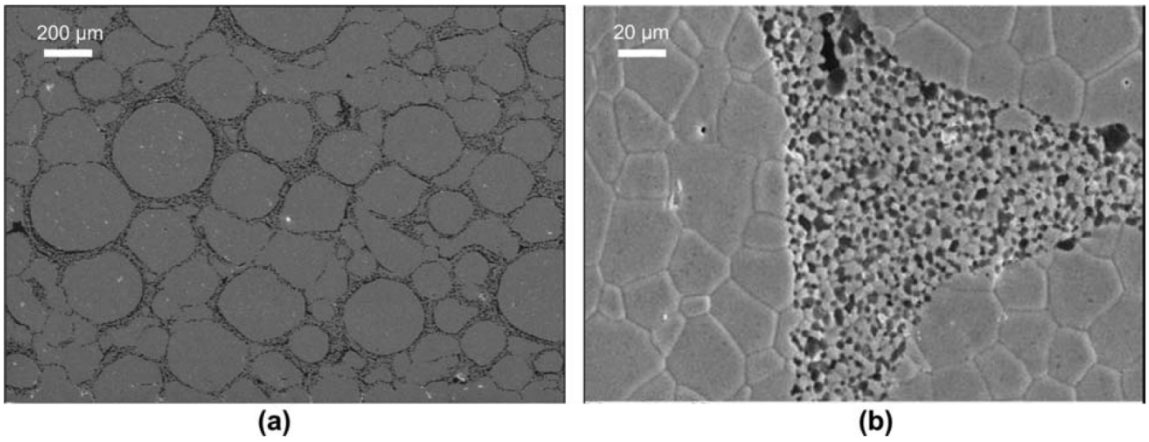

Figure 2. UO_2-10v%BeO Microstructure [12, 13]

The goal of this work was then to reproduce and attempt to improve upon Solomon's GG method for producing UO_2-BeO for low concentrations of BeO. Other goals for this study also include characterizing this fuel's sintering as well as its thermal conductivity. This was done by milling UO_2 and BeO to fine powders. The UO_2 was

then pre-compacted to 680MPa, which was then broken up into granules using a mortar and pestle and sieved to between 50 and 500μm. These granules were then self-milled and in a jar with a helical copper wire to improve the powder's tumbling. The powder was then mixed with the BeO at volume fractions of 2.5, 5, 7.5, and 10%BeO. The final compaction was varied from 200MPa to 275MPa in order to see its effects on sintering. The final compact was then sintered at 1600°C for 8hr in Ar-5%H_2 while measuring the height change of the pellets in situ to sintering, to determine when the peak sintering rate was and how long to sinter the pellets for. The pellets dimensions were then measured prior to and after sintering to determine how the shrinkage of the pellet and if it is isotropic. The final densities of the pellets were measured using immersion techniques. The structure and volume fraction of the UO_2-BeO was also determined with BSE and Cathodoluminescence. Finally the thermal conductivity was found for the samples of the different BeO volume fractions from 25 to 250°C, by measuring the thermal diffusivity using light flash analysis (LFA) then calculating the conductivity. This had to be optimized in order to find the minimum LFA sample thickness.

This study was able to produce samples with densities greater than 92% of theoretical density and show that with lower final compaction pressures between 200 and 225MPa the densities greatly improved. It was also seen that there is a peek sintering rate for these samples between 1450 and 1550°C. The thermal conductivity data showed that there is a 10% improvement for each 1 volume percent BeO over the measured temperature range compared to baseline UO_2.

This body of work will look at the thermal conductivities effect on fuel performance, the history of UO_2-BeO in reactors, thermal conductivity of UO_2 and BeO, and their respective fabrication steps in Chapter 2. Chapter 3 will discuss the procedures and materials used in the study. Chapter 4 will present the results, while Chapter 5 will discuss their meaning and implications.

2. BACKGROUND

This chapter contains a review of the effect thermal conductivity has on the fuel performance of oxide nuclear fuel. It also covers fuel designs that are meant to improve the thermal conductivity of oxide fuels with emphases on the addition of BeO. This chapter also looks at the history of BeO in nuclear reactors and reactor designs, as well as the thermal properties of UO_2 and BeO and there fabrication methods.

2.1 Impact of Thermal Conductivity on Oxide Fuel Performance

Uranium dioxide is the most common fuel material used in nuclear energy systems due, in part, to its chemical and mechanical stability and high melting temperature (~2800°C). On the other hand the low thermal conductivity of UO_2makes it a good thermal insulator which is not a desirable property for this application. Thermal conductivity is an important property for any nuclear fuel as it limits the power density for the system and effectively creates very large temperature gradients as thermal energy is generated within the fuel. The fuel temperature in a nominal nuclear system will range from about 300°C at the pellet surface up to 1000°C to 2000°C (depending on the system) at the fuel centerline. This large gradient enables various performance-limiting phenomena such as fission gas swelling and gas release and significant grain restructuring [14, 15]. The gradient also creates large thermal stresses across the pellet which can cause cracking and plastic deformation in the cooler and hotter regions respectively [14-17].

One of the notable effects from the steep temperature gradient is the restructuring of the fuel. The fuel tends to have three distinct regions after restructuring, as seen in Figure 3. In region 1, the hottest region, the fuel densifies and the grains grow and become columnar. The columnar grains are formed from the trails of the radial pore migration, and generally require temperatures above 1900°C, depending on burnup. This columnar restructuring is also the primary mechanism for fission gas release, releasing approximately 80 to 100% of fission gasses [18, 19]. In the equiaxed region the temperature is too low to allow pore migration but is high enough to cause grains to grow. The microstructure of the UO_2 in the as-fabricated region does not change much during irradiation due to the temperature being too low to cause grain growth or pore migration [15, 16, 18-20].

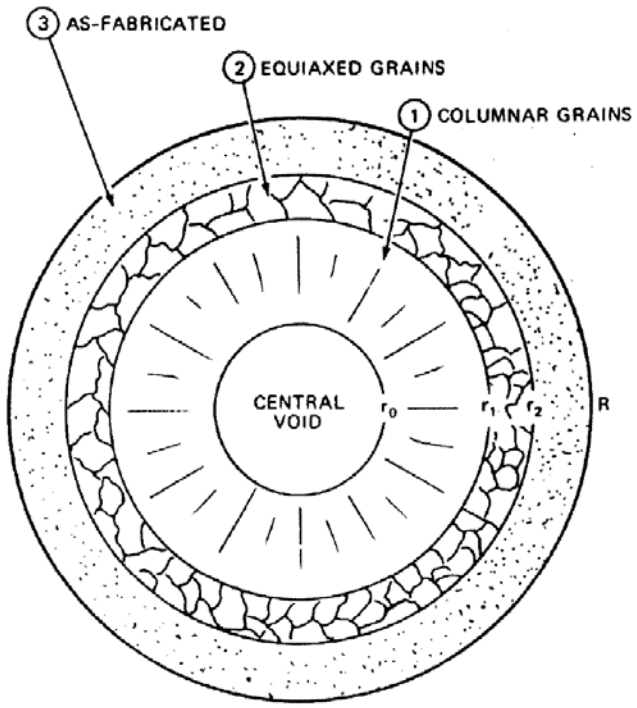

Figure 3. Fuel Restructuring [14]

2.2 Challenges of UO_2-BeO and Other High Thermal Conductivity Fuels

While the proposed UO_2-BeO fuel material does have higher thermal conductivity, there are other parameters and phenomena to consider before it is possible to develop it as new nuclear fuel option. From the perspective of reactor phsics and economics, the displacement of fissile uranium atoms by the BeO and the resultant increased enrichment required for operation it an engineering tradeoff that must be considered. That point is beyond the scope of this study, but it is a very important issue.

One of the main challenges would be from the eutectic interaction between UO_2 and BeO near 2100°C which is much lower than the melting temperature of UO_2 at 2800°C. This eutectic may be brought on by the phase transition of BeO at around the same temperature. There is also the inhalation hazard that comes with working with BeO. With the addition of BeO there will be less fissile material in the same volume of UO_2, which already has a low uranium density. Finally there is still a necessity to see how the fuel will hold up and how the conductivity will change to high burn-ups [4, 21-23].

There are other fuel designs that would improve the thermal conductivity of UO_2 or are alternates to UO_2. One design enhances the fuels conductivity with the addition of silicon carbide (SiC). SiC has a high thermal conductivity ($4.9 Wcm^{-1}K^{-1}$ at 300K) and high melting temperature (2973°C) much like BeO, but reacts with UO_2 at 1370°C and the mixture melts around 1700°C. The UO_2-SiC designs also vary (Figure 4) such as

continuous phase, dispersed powder (a), and discontinuous fibers (b), both of which have nearly the same improvements to the fuel as each other [4, 13, 24-31].

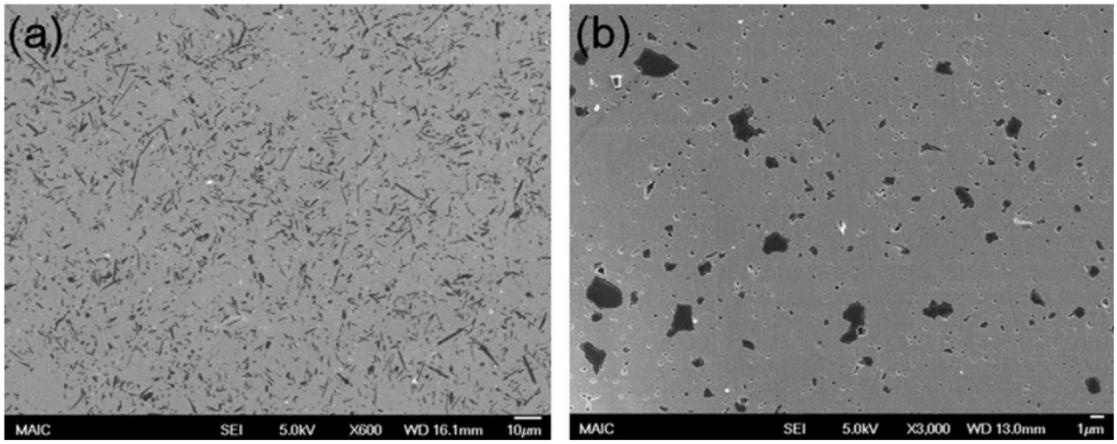

Figure 4. UO_2-10v%SiC [31]

There are other fuel designs that try various additives to UO_2 in order to improve the fuels conductivity and/or performance. These are usually chosen for their thermal, chemical, and nuclear properties. Some of these additives that have been studied are TiO_2 and SnO_2 [32].

2.3 History of UO_2-BeO Fuel

Beryllium oxide has been in reactor designs since the 1940s; most of early concepts were gas-cooled reactors [33]. BeO had many properties both nuclear and thermal that are attractive to nuclear reactor designs. Beryllium is a good moderator due to the low atomic mass of Be which enables significant neutron energy loss in a single scattering collision. It also has a low neutron cross section on the order of 0.01b at

thermal neutron energies [8]. In addition, Be has favorable neutron production interactions such as (n,2n) and (α,n), which are helpful in creating a slight reactivity increase in the reactor system [34]. Thermally, BeO has one of the highest thermal conductivities of any oxide on the same order as metallic aluminum [35]. BeO has other favorable properties such as low chemical reactivity at high temperatures [5, 8, 36, 37].

One of the first designs for a pebble-bed helium cooled reactor, was designed by Farrington Daniels [5]. The reactor was going to utilize BeO as a moderator and reflector. The fuel was planned to be extruded UO_2 dispersed in either graphite or BeO, and ThO_2 was going to be used for breeding. The design had several major issues mostly the high operating temperature, with an outlet coolant temperature of 760°C. This high temperature as well as the effects of irradiation during operation left the strong requirements of the materials, and at the time there was a insufficient knowledge on how the BeO would behave in that environment. After the project was discontinued some research on BeO in reactors was continued [5].

In the 1950's the United States began working on the Aircraft Reactor Experiment (ARE), which was looking at nuclear propulsion for aircrafts [5, 38]. Again, BeO was selected to be the moderator and reflector. The ARE was to be fueled with a molten salt liquid fuel, NaF-ZrF-UF_4, and the BeO was cooled with a sodium-potassium liquid (NaK). The BeO had good stability in hot dry-air and also exhibited vary little to no reaction with the sodium coolant. It was also noted that the primary corrosion mechanism was mechanical erosion of the BeO surface [5, 38-41].

In 1958, there was interest in developing a reactor for marine applications, so the Maritime Gas-Cooled Reactor (MGCR) was designed [5, 37, 42]. By this time there was more experimental data developed for BeO use in a reactor, which led to BeO being considered as a moderator again. The BeO was found to have more favorable properties over graphite, such as having twice the volumetric heat capacity of graphite, and showed adequate resistance to irradiation damage [42]. During the life of the MGCR program the cost of manufacturing BeO had also dropped. The MGCR was designed to be fueled with compacts of 22v% UO_2 in a BeO matrix. This fuel design showed significantly lower fuel temperatures which resulted in lower fission gas release. The UO_2-BeO showed good dimensional stability during irradiation [5, 37, 42].

In the 1960's the MGCR program designed a land based reactor to test its fuel and moderator designs, called the Experimental Beryllium Oxide Reactor (EBOR) [5]. The tests conducted at EBOR did not reveal any significant swelling and the release of fission gasses was relatively low (0.6 to 2.7%). These pellets had a fuel centerline temperature of approximately 1600°C and were 80wt% UO_2. There did appear to be severe damage to the UO_2 at the UO_2-BeO interface and close to the surface of the pellet. It was also observed that at high fission densities very fine grains in the BeO and UO_2 were formed giving the appearance of an amorphous structure. The neutron irradiation damage to the BeO was reduced at elevated temperatures [1, 5, 9-11, 33].

In another system design in the early 1960's, UO_2-BeO fuel was then to be used in the Aerojet-General Nucleonics Army Gas-Cooled Reactor, the ML-1 [5, 11, 43]. The fuel type was continued to be tested at EBOR for the ML-1. The ML-1 was

designed to be a mobile reactor that could supply power to remote locations. The reactor was going to use a closed loop Brayton cycle and would have been water moderated [1, 5, 10, 43].

Around the same time the Pluto ramjet reactor was being developed. The ramjet used extruded UO_2-BeO was to heat up the air flowing through it and its reactor was able to produce around 500MW of heat [43, 44].

Since 1978, Sandia National Laboratory has been operating the Annular Core Research Reactor (ACRR) and it has been using UO_2-BeO fuel since it was created [6, 45]. The fuel has the composition of 78.5wt%BeO, with an enrichment of 35%. The UO_2-BeO fuel is planned to be replaced with low enriched TRIGA UZrH fuel. ACRR is used for the production of medical radioisotopes [6, 45].

2.4 UO_2 and BeO Thermal Properties

2.4.1 Thermal Conductivity of UO_2

As previously discussed UO_2 has a low thermal conductivity ($6.0 Wm^{-1}K^{-1}$ at 200°C) which affects its performance as a reactor fuel. As such, the thermal conductivity for UO_2 has been constant area of study [15, 46]. This was commonly done by measuring the specific heat and thermal diffusivity of UO_2 which was used to calculate the conductivity with the well-known relationship eq.(1),

$$k=\alpha\rho c_p \quad \textbf{(1)}$$

where α is the thermal diffusivity, ρ is the material density, and c_p is the specific heat capacity [15, 47]. A diagram of heat capacity of UO_2 is shown in Figure 5 [48]. It is

interesting to note the step at approximately 2340°C is due to Bredeg transition and can be seen both experimentally and by molecular dynamics models. This transition is common in other materials with the fluorite crystal structure and occurs around 0.8 of the materials melting temperature (T_m) [14, 20, 47, 49-51].

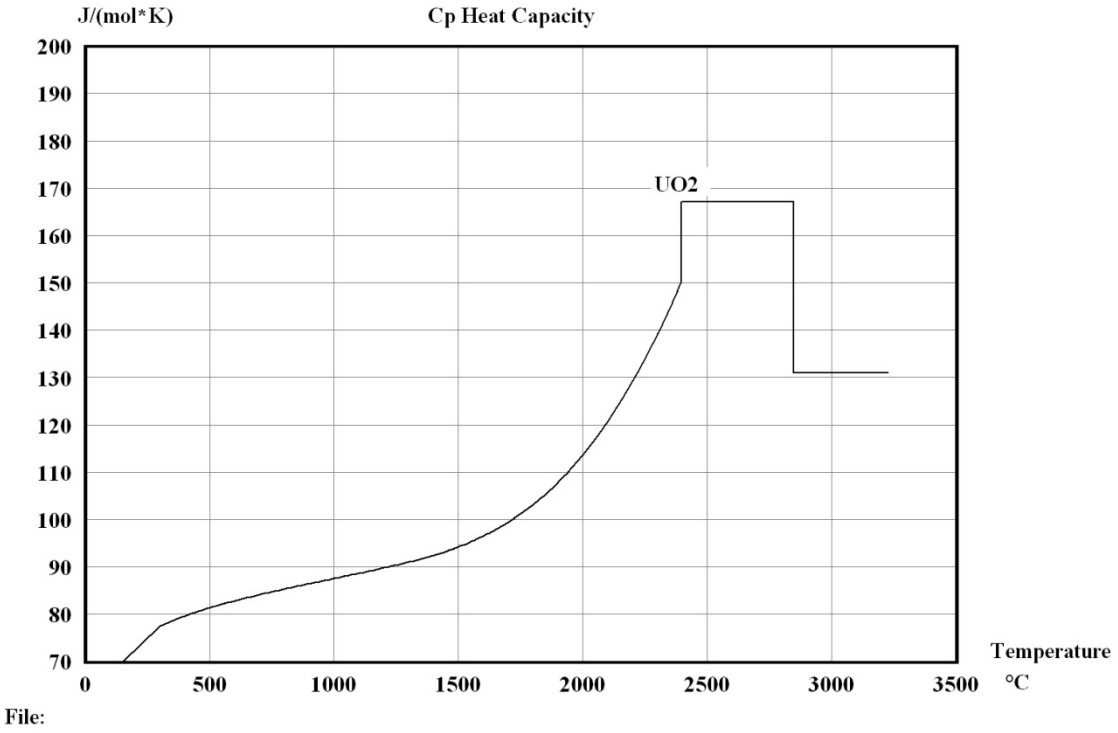

Figure 5. Sketch of the Heat Capacity of UO_2 [48]

From the many thermal conductivity measurements it was then important to fit the data to a curve. This has been done in several ways from simple curve fitting to incorporating the different contributing thermal conductivity phenomena, such as contributions from the small polarons and lattice, into models. Ronchi et al. found from previous data that the polarons gave the ambipolar contribution, k_{AM}, shown in eq.(2),

where t=T/1000K. The lattice contribution, k_L, was also found using k_{Am} and linear fitting k^{-1}, eq.(3) [46, 47, 49, 52, 53].

$$k_{AM}=\frac{6600e^{-16.35/t}}{t^{\frac{5}{2}}}\ Wm^{-1}K^{-1} \quad \textbf{(2)}$$

$$k_L=\frac{100}{6.548+23.533t}\ Wm^{-1}K^{-1} \quad \textbf{(3)}$$

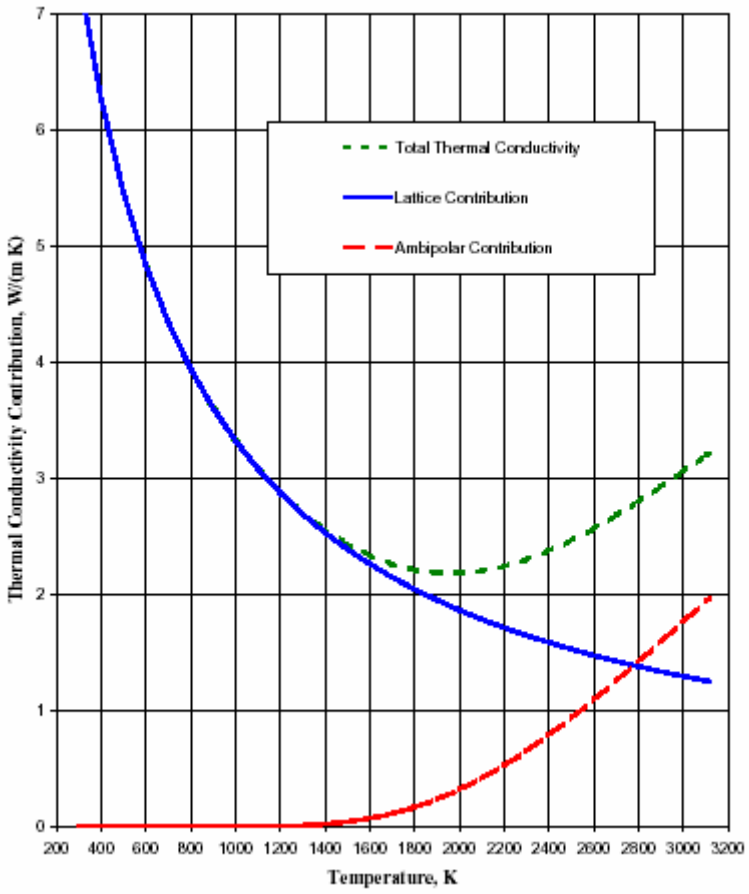

Figure 6. Thermal Conductivity and Its Lattice and Ambipolar Contributions [47]

When the theoretical thermal conductivity (sum of eqs (2) and (3)) is compared to experimental conductivity measurements, the theory was low at temperatures below

265°C [46]. To improve the fit the lattice contribution was then added to the model by using a quadratic fit to k-1 instead of a linear fit by Fink et al. [46]. This gave the thermal conductivity expression in eq.(4).

$$k = \frac{100}{7.5408 + 17.692t + 3.1642t^2} + \frac{6400e^{-16.35/t}}{t^{\frac{5}{2}}}\ Wm^{-1}K^{-1} \quad \textbf{(4)}$$

This fit gave a standard deviation of 6.2% compared to 7.9% from Ronchi et al's fit. Both these fits are done for UO_2 that is 95% dense. The two curves compared to measured UO_2 data can be seen in Figure 7 [46, 47, 49].

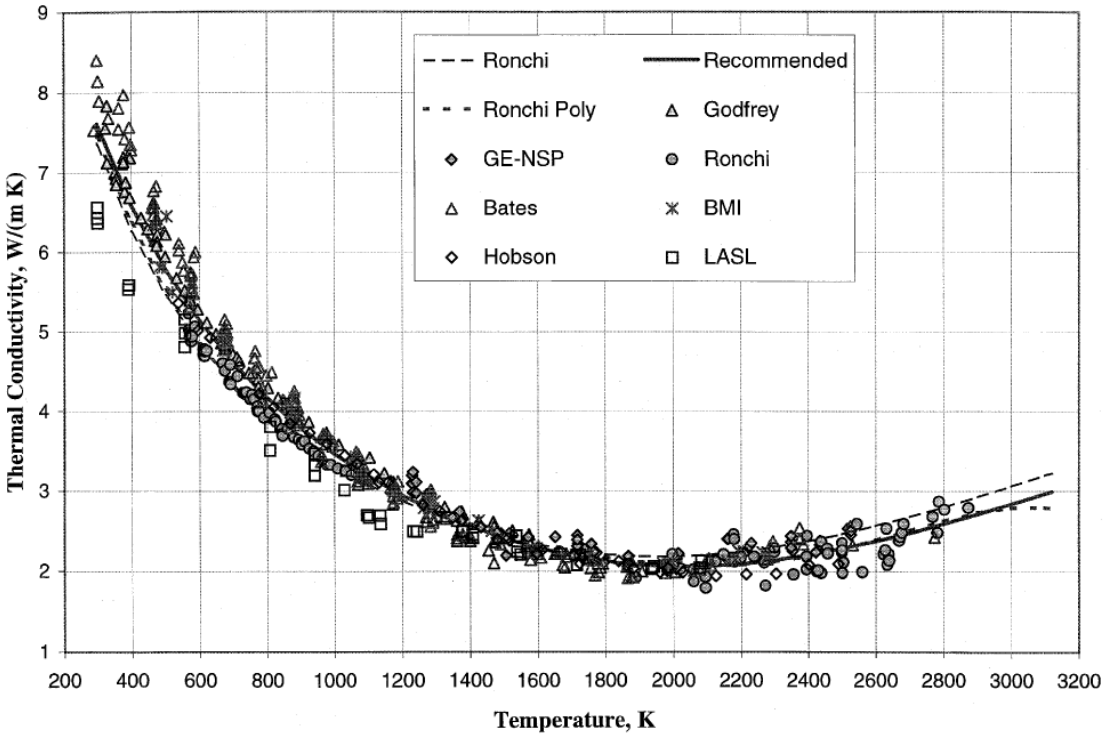

Figure 7. UO_2 Thermal Conductivity [46]

Another method to evaluate the thermal conductivity of UO_2 was solving for the in-reactor conductivity integral to melt (CIM) eq.(5),

$$CIM = \int_{500}^{T_m} kdT = q''f(r,e) \quad \textbf{(5)}$$

where q" is the heat rate per unit length and f(r,e) is the flux depression factor related to diameter and enrichment [14]. The right hand of the equation can be measured using a calorimeter and the fuel enrichment and diameter. Now with the known CIM of 63Wcm^{-1} and the shape of the conductivity versus temperature, the conductivity curve was found to be eq.(6).

$$k = \frac{38.24}{402.4 + T} + 6.1256 \times 10^{-13} T \; Wm^{-1}K^{-1} \quad \textbf{(6)}$$

The CIM from Rochi et al and Fink et al were 6.08 and 6.09Wcm^{-1}. There are limitations to CIM method however. These come from errors in the evaluating pellets surface temperature from the cladding and gas gap [46, 47, 49, 54, 55].

The bulk thermal conductivity is strongly affected on the porosity of the pellet and the pellet porosity if affected by the fabrication procedures as well as internal fission gas generation during operation [20, 56]. For example, it is common practice to manufacture fresh UO_2 fuel pellets with 5 volume percent porosity. During operation, the coalescence of fission gas bubbles causes the fuel pellets to swell with as much as 20

to 25 volume bubble-induced porosity [15]. For most materials, the conductivity of a fully dense pellet is commonly expressed with eq.(7),

$$k_0 = \frac{k_p}{1-p} \quad \textbf{(7)}$$

where k_0 is the conductivity at full density, k_p is the conductivity of the porous sample, and p is the porosity of the sample. However, this expression does not hold for UO_2, which requires an empirical correction factor, α as seen in eq.(8) [14, 20, 47, 54, 56-59].

$$k_0 = \frac{k_p}{1-\alpha p} \quad \textbf{(8)}$$

Early studies showed that α for UO_2 was approximately 2.6, but with further research α has a dependency on temperature. This led to the following expression for α.

$$\alpha = 2.6 - 0.5t \quad \textbf{(9)}$$

Stoichiometry also plays a role in the thermal conductivity of UO_2. For oxygen-rich hyperstoichiometric UO_2, designated as $UO_{2+\eta}$, the thermal conductivity is significantly lower than stoichiometric UO_2. This effect is greater at lower temperatures and less dramatic at elevated temperatures. The conductivity for hyperstoichiometric UO_2 where η is between 0 and 0.02 can be estimated using eq.(10) for temperatures below 1800K and eq.(11) for temperatures above 1800K,

$$k_{+\eta} = \frac{1}{0.035 + 3.47\eta - 7.26\eta^2 + 2.25\times10^{-4}T + (83.0 + 537\eta + 7610\eta^2)\times10^{-12}T^3} \quad \textbf{(10)}$$

$$k_{+\eta} = \frac{1}{0.035 + 3.47\eta\phi - 7.26\eta^2\phi + 2.25 \times 10^{-4}T + (83.0 + 537\eta\phi + 7610\eta^2\phi) \times 10^{-12}T^3} \quad \textbf{(11)}$$

where ϕ is (3120-T)/1347. Oxygen poor, or hypostoichiometric, UO_2 is designated as $UO_{2-\eta}$ and it tends to exhibit larger values than UO_2. For η equal to 0 to 0.05 the thermal conductivity is estimated by multiplying the conductivity of UO_2 by $(1+\eta)$ as represented by eq.(12) [20, 59-63].

$$k_{-\eta} = k_{UO2} * (1 + \eta) \quad \textbf{(12)}$$

The thermal conductivity decreases over the operational lifetime of the fuel [56, 63]. This decrease is shown can be seen in Figure 8. One cause of this is the fission fragments that are produced. The fission fragments can go into solid solution or precipitates in the fuel, they can also form gas bubbles, depending of the fission fragment. Solid fragments affect the conductivity of the fuel by changing the lattice contributions to k. Since many of the precipitates are metallic they have a higher conductivity than UO_2, thus improving the conductivity. Conversely, the fragments that dissolve in the fuel lower the conductivity, primarily because of the mass differences between the atoms. The gas bubble and pores will also negatively affect the fuels conductivity due to the low conductivity of gasses.

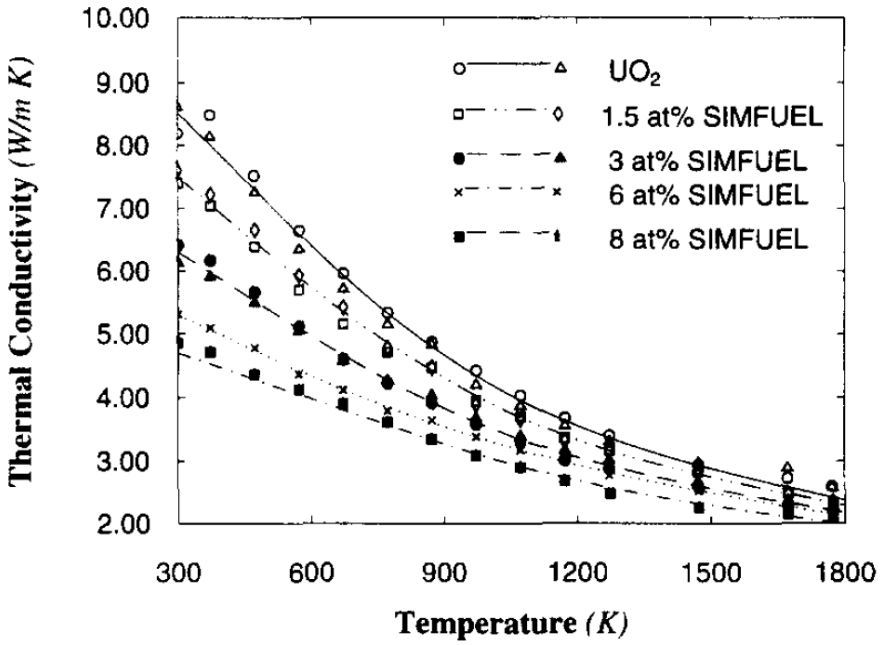

Figure 8. Change in UO_2 Conductivity at Different Burnups from Simulations [63]

The conductivity of the UO_2 is also affected by radiation damage as well as changing stoichiometry. As mentioned earlier the non-stoichiometric UO_2 would further decrease the thermal conductivity of the fuel. Radiation damage also will result in lower thermal conductivity due the increased amount of defects. The radiation damage effect happens quickly (within minutes) and at temperatures below 1000K and causes a maximum of 25% in the fuels thermal conductivity. After about $10^{23} n/m^2$ though, radiation damages effect doesn't decrease the fuels conductivity any further [63, 64].

2.4.2 Thermal Conductivity of BeO

The thermal conductivity of beryllium oxide 3.7 $Wcm^{-1}K^{-1}$ at 25°C, which is high compared to other oxide ceramics. At room temperature, the conductivity of BeO is comparable to aluminum metal and is even higher than beryllium metal [65]. This high thermal conductivity can be attributed to the BeO's low average atomic mass and its high Debye temperature of 1280 K [2]. The BeO compound is also nearly isotopically pure due Be^{9} is the only natural occurring Be isotope and oxygen is 99.8% O^{16}. The phonons mean free path in BeO is approximately 1.1mm (very long) between 2 and 10K and appears to be limited to boundary scattering [2, 35, 65-68].

The thermal conductivity of BeO decreases at low temperatures under the influence of neutron irradiation, as shown in Figure 9 [69]. After neutron irradiation the thermal conductivity at 80°C was close to unirradiated BeO at 1400°C. It was also observed that with higher neutron doses, BeO's conductivity dependence on temperature weakened. The drop in conductivity from the neutron damage is completely recovered though at temperatures above 1200°C [69].

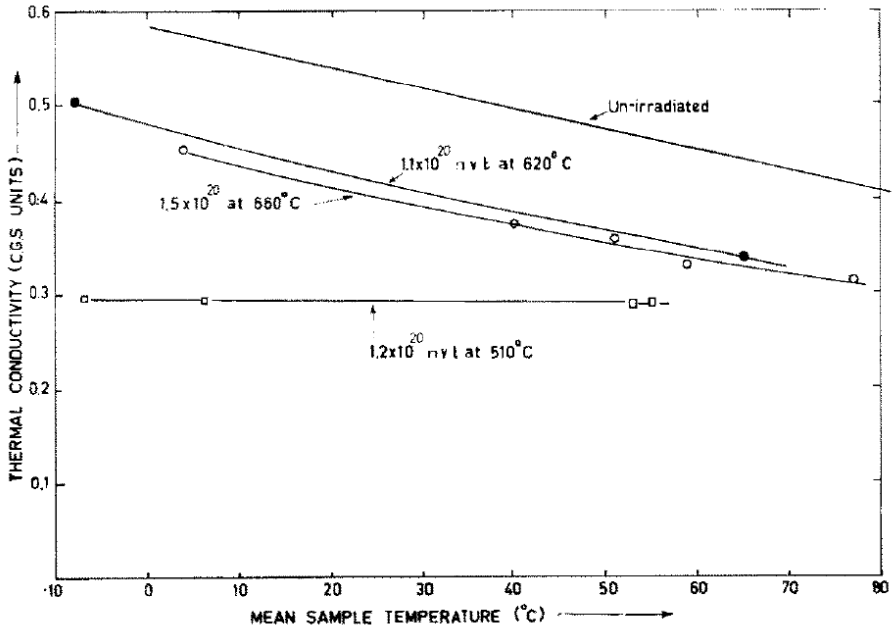

Figure 9. Thermal Conductivity of Irradiated BeO [69]

2.4.3 Thermal Conductivity of Binary Heterogeneous Composites

When considering the thermal conductivity of composites it is important consider the heterogeneity of the material. Composites are heterogeneous and can have many types of microstructural forms, but the relevant morphology of interest to this study is a discontinuous phase (UO_2) dispersed within a continuous phase (BeO). The effective conductivity, k_{eff}, derived by Maxwell [70] and Fricke [71] for this type of heterogeneous material has a general expression shown in eq.(13),

$$k_{eff} = \frac{k_1 V_1 \left(dT/dx\right)_1 + k_2 V_2 \left(dT/dx\right)_2}{V_1 \left(dT/dx\right)_1 + V_2 \left(dT/dx\right)_2} \quad \textbf{(13)}$$

where k_1 and V_1 are the conductivity and volume fraction for the continuous component respectively and k_2 and V_2 are for the discontinuous phase [72]. Maxwell and Fricke determined the average gradient ratio in the two phases, eq.(14),

$$\frac{\left(dT/dx\right)_2}{\left(dT/dx\right)_1} = \frac{nk_1}{k_2 + (n-1)k_1} \tag{14}$$

which may then be inserted into eq.(13) to yield the conductivity for binary composite eq.(15).

$$k_{eff} = k_1\left[\frac{k_2 + (n-1)k_1 - (n-1)V_2(k_1 - k_2)}{k_2 + (n-1)k_1 + V_2(k_1 - k_2)}\right] \tag{15}$$

This model is considered reasonably valid for volume fractions below 30% and for spheres [72-75]. The shape factor for the discontinuous phase, n, is typically 2 for spherical shapes, and is challenging to derive for shapes other than ellipsoidal. This shape factor also tends to be more of a function of the two conductivities as well as the oblateness of the particles. When particles are not spherical it has been shown that n=3 gives good agreement to empirical data [72, 73, 75].

Another model derived for the effective thermal conductivity of a two phase system is one based off Hadley's model, as given in eq.(16) and (17).

$$\nabla\langle T\rangle = V_1\langle\nabla T_1\rangle^1 + (1 - V_1)\langle\nabla T_2\rangle^2 \tag{16}$$

$$\frac{k_{eff}}{k_1}\nabla\langle T\rangle = V_1\langle\nabla T_1\rangle^1 + \frac{k_2}{k_1}(1 - V_1)\langle\nabla T_2\rangle^2 \tag{17}$$

Given the assumption that the average temperature gradients, $\langle\nabla T_i\rangle^i$, in parallel directions are equivalent and inversely proportional to ratio of their respective conductivities in the perpendicular direction, the effective conductivity is found to be the

following equation, where ψ is another shape factor that is 1 for spheres and less than 1 for other shapes [75, 76].

$$k_{eff} = \frac{k_1(1-V_1)F + k_2[1-(1-V_1)F]}{1-(1-V_1)(1-F)+\frac{k_2}{k_1}(1-V_1)(1-F)} \quad \textbf{(18)}$$

$$F = e^{-\psi\left(\frac{k_1}{k_2}\right)^{\frac{1}{3}}} \quad \textbf{(19)}$$

Numerical models are also used to determine the thermal conductivity of heterogenous materials. These models can be done using finite element analysis methods to do heat transfer calculations. This method can take into account the shape of the dispersed phase as well as pores and cracks that are observed from images of the microstructure. These methods do a good job estimating the effective thermal conductivity; even 2D analysis gives reasonable results [77, 78].

2.4.4 UO_2-BeO

The UO_2-BeO composite fuel form under development here follows a number of studies on the impact of BeO as an additive with different compositions and different microstructural configurations. Ishimoto, et al [58] characterized the behavior multiple UO_2-BeO morphologies created using various fabrication methods. Figure 10 shows examples where BeO is formed as (A) a continuous matrix BeO, (B) dispersed precipitates of BeO, and (C) lamellar eutectic phases [79, 80].

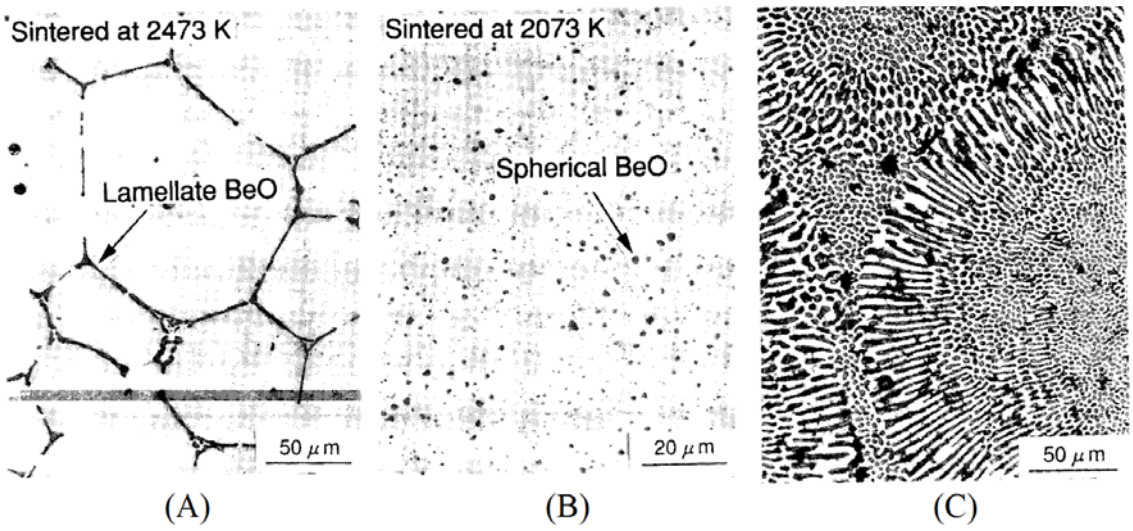

Figure 10. Various UO_2-BeO Structures [79]

Solomon, et al. [12] created the processing pathway and fuel morphology being promulgated in this document after the Ishimoto data. As noted in Chapter 1 (Figure 1), this composite design comprises UO_2 microspheres surrounded by a matrix of BeO or finely mixed UO_2-BeO phases that form a conductive network throughout the fuel.

In the Ishimoto structures, each structural variation exhibited some improvement to thermal conductivity over UO_2, with the continuous BeO matrix (Figure 10A) showing a greater increase from UO_2 than dispersed or lammelar BeO (Figure 10 B or 9C). The improvements to the effective conductivity where seen to be more predominant at lower temperatures. The study also showed that the volume fraction of BeO has greater impact in the continuous matrix BeO conductivity than the dispersed BeO [79].

Further insight from Ishimoto, *et al.* indicates that the continuous BeO has a strong dependence on shape factors with F equaling 0.333 and 0.015 for dispersed and continuous BeO respectively. The following expression was also found for the effective thermal conductivity of the UO_2-BeO for BeO less than 4.2 vol.% and for temperatures between 300 and 1900K, which as a 10% error[79].

$$1 - \mathrm{V_{BeO}} = \left(\frac{k_{UO_2}}{k_{UO_2-BeO}}\right)^m \left[\frac{k_{BeO} - k_{UO_2-BeO}}{k_{BeO} - k_{UO_2}}\right]\left[\frac{k_{UO_2-BeO} + nk_{BeO}}{k_{UO_2} + nk_{BeO}}\right]^q, \quad m = \frac{3F(1-2F)}{2-3F}, \quad n = \frac{2-3F}{1+3F}, \quad \mathrm{q} = -\frac{2(1-3\mathrm{F})^2}{(2-3\mathrm{F})(1+3\mathrm{F})} \tag{20}$$

It was also shown that diffusivity measurements were independent of sample thickness for various temperatures for samples with a continuous BeO matrix [79].

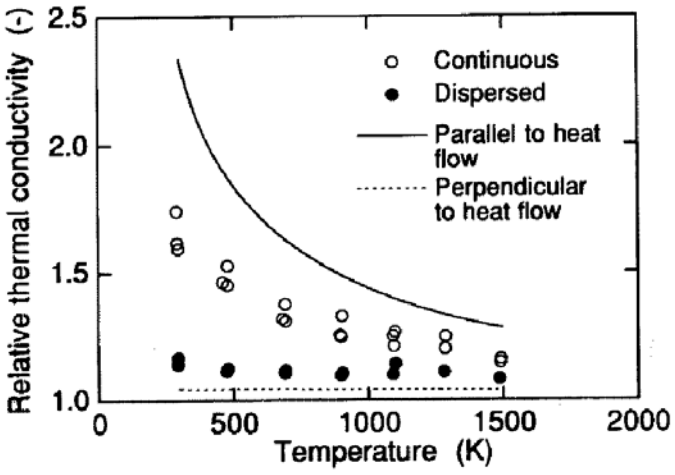

Figure 11. Thermal Conductivity UO_2-BeO for Dispersed and Continuous BeO [79]

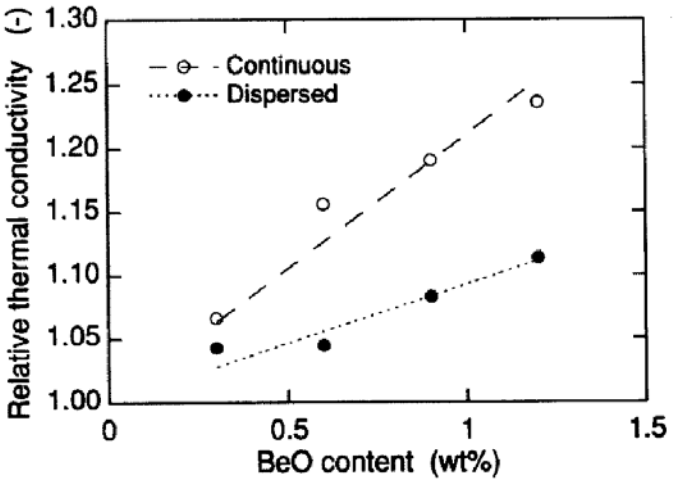

Figure 12. Thermal Conductivity at 1000K for Various BeO Content [79]

When Solomon, et al. [12] initiated the development of the current concept (Fig. 1), they considered two parallel processing strategies to generate the UO_2-BeO form with a continuous BeO matrix. The two methods were compared to determine if they gave comparable thermal results. The first was designated the slug bisque (SB) method which a UO_2-BeO pellet is made from ground sintered UO_2 (~95% theoretical density) and fine BeO powder. The second method was designated the green granules (GG) method where the UO_2-BeO pellets were made from large unsintered agglomerates of spherical UO_2 granules mixed with fine BeO powder; variations included leaving remnants of fine UO_2 powder in the mix.

Revankar, *et al*. [26] developed a finite element model to compare the thermal conductivity arising from these two fabrications. The two methods gave similar conductivities, Figure 13. The model initially under estimated the SB method and overestimated the GG method, but it was corrected by reducing the thermal conductivity

of BeO by 30% which then better fit the data. This implies that the interface resistance between BeO and UO_2 is not negligible [12, 13, 26, 81].

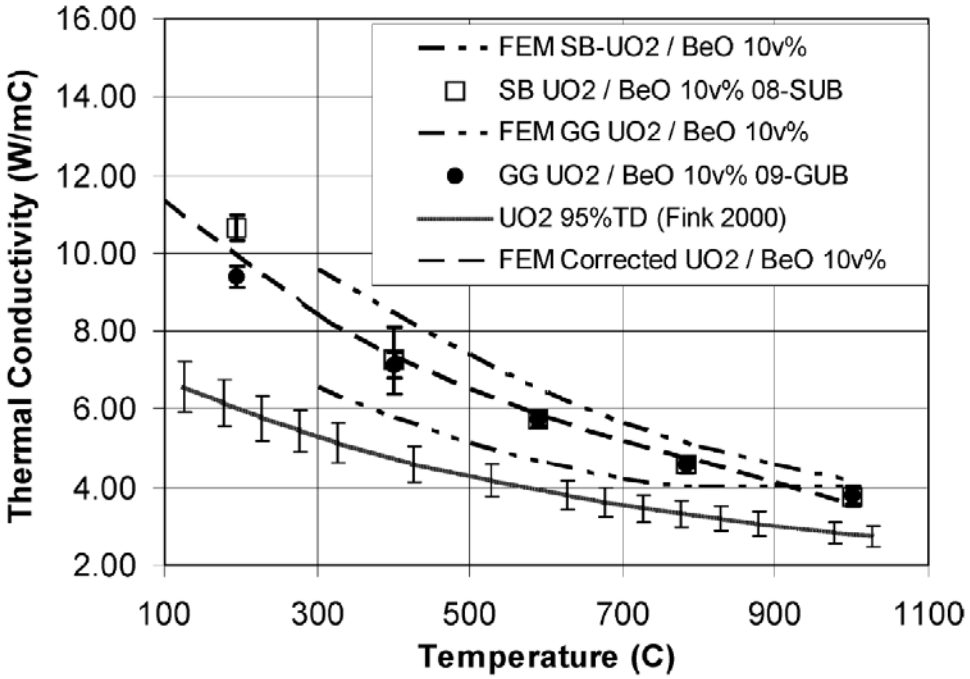

Figure 13. Thermal Conductivity of SB and GG UO_2-BeO [26]

3. EXPERIMENTAL METHODS AND PROCEDURES

This Chapter describes the methods used in this study. The powder handling methods will first be discussed with emphasis on the milling of the powders. The next two sections (3.2 and 3.3) section will then look at the characterizing of the powders and microstructure of the sintered pellets with microscopy methods. Section 3.4 describes the experimental setup used to measure geometric changes in pellets during sintering, and Section 3.5 discusses the fabrication process of the UO_2-BeO pellets. Section 3.6 explains the methods used to measure geometric changes in the green and sintered pellets as well as their densities. The final section 3.7 provides the methods used to analyze the thermal diffusivity and conductivity of the UO_2-BeO composite.

3.1 Powder Processing

The as-received UO_2 (International Bio-Analytical Industries Inc., less than 300μm) and BeO powders were larger than the desired nominal size of less than 10μm, so they were milled using two different techniques. The first method of milling involved ball milling in a gentle rolling mill, which was only used on the UO_2. Both the UO_2 and BeO powders were milled using a jet mill.

Ball milling was accomplished using a 0.3 liter Model 774 Roalox Alumina-Fortified Grinding Jars. The UO_2 powder was inserted into the jar along with spherical yittra stabilized zirconia grinding media of varying sizes (14 15mm balls, 50 10mm balls, 300 5mm balls, and 175 2mm balls) tumbled using a rotary jar mill (U.S.

Stoneware CV-80461). The larger grinding media was used to speed up the milling process while the finer media was used to produce finer powder. The grinding media was placed in the jar first to fill approximately half of the jar. The jar was then filled with approximately 200gm of UO_2 powder until the grinding media was no longer visible. The filled jar was closed and placed on the jar mill and the powder was milled for 24hrs with the jar rotating at 72rpm. After milling, the grinding media was separated from the powder using a large mesh sieve. All of the powder handling s performed in a fume hood while wearing a full-face respirator. The respirator was more necessary for the BeO activities but it was used in this step since it was available.

The second milling method was accomplished using a jet mill (Model 00-Jet-O-Mizer, Fluid Energy), Figure 14, which was expected to mill the powders to less than 10μm. The jet mill was setup inside a glove box with a HEPA filter due to safety concerns related to BeO handling (see Section 2.2). The jet mill was connected to an argon tank and the pusher and grinding pressures were set to 0.55MPa (80 psig) and 0.69MPa (100 psig), respectively.

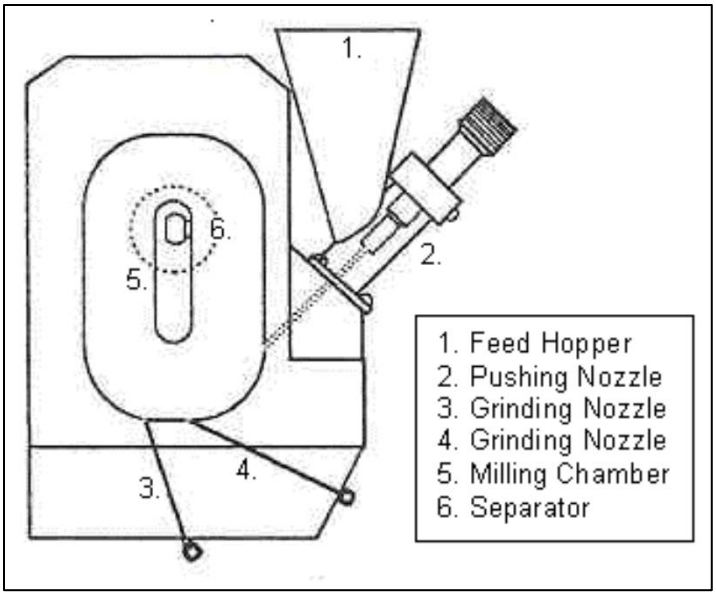

Figure 14. Jet Mill Schematics [82]

The powder to be milled was placed on a vibratory feeder, which fed the large-sized powder into the mill hopper at a continuous rate. The shaker setting was varied slightly during operation to help control the feed rate. When the powder was low the shaker was refilled. The milling continued till all the desired powder was milled. The inlet to the collector containers was then closed and gas was back-filled into the container in order to release the powder from the system filter. The powder is then collected from the jet mill collection vessel.

3.2 Powder Characterization

3.2.1 Particle Size Analysis

The powder sizes were determined via image analysis with the use of a HIROX KH-1300 digital microscope and its lens MX-5040 SX; because of the hazardous nature

of the powders in use, more precise analytical services were not open to this project. A small quantity of the powder to be analyzed was placed in a sealable vial, which was then filled 85% of the way with mineral oil. The vial and sample were then soincated for 2hrs in order to disperse the powder. The powder, not fully dispersed, was then shaken to disperse the powder throughout the mineral oil. The powder was then sampled from the vial with pipet. A drop of the powder/mineral oil was then placed on a slide which was then covered.

The powder sample was then taken to the optical microscope were it was observed at 700X and multiple images were taken. The images were then manipulated to see be particle clearly in black and white, by varying the contrast and brightness, thresholding, and eroding the noise. This step varied from image to image. The resulting image was then analyzed to count the particles as well as measure there effective diameter. The diameter was the averaged to obtain the average particle size.

3.2.3 Powder Stoichiometry

The uranium oxide powder was examined using the electron microprobe in order to determine its oxygen to metal ratio. The powder samples were prepared by placing a small amount of powder on a well-polished, hardened steel rod. Another hardened steel rod was then placed on top of the holder and first rod. The contact perimeter of the two rod was then taped in order to keep them together and minimize any loss of powder. The powder was then pressed between these two rods with a load of at least 3.6tonne. The tape is then removed and the top rod is removed. The paper backing atop the adhesive end of the sample mount was then removed. The sample mount was pressed to

the rod and powder by hand and centering the powder in the adhesive. The mount was then removed and the loose powder is knocked off.

The prepared powder sample is then taken to the microprobe Cameca SX50 and analyzed using Wavelength Dispersive X-Ray Spectrometry (WDS). Two to five analysis points where taken for each sample to get an average composition. Each point was chosen based on how flat and smooth the analysis area was around the analysis spot, Figure 15. The measurements were compared against a UO_2 standard.

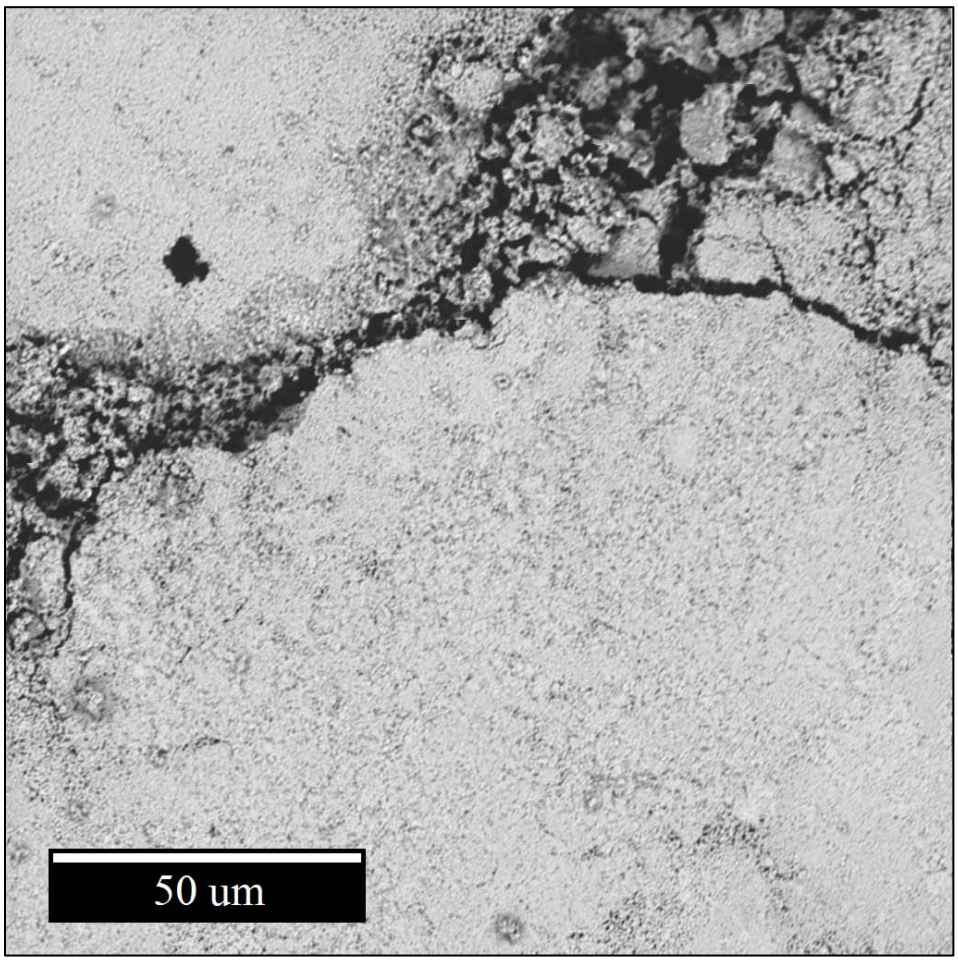

Figure 15. Sample Area of Compacted UO_2 Powder for WDS Analysis

3.3 Microstructure Analysis of Sintered Samples

The structure of the samples were analyzed in order to observe if the beryllium oxide formed a continuous matrix around the uranium oxide and to validate that the samples had the desired volume fraction designated during the fabrication steps. The structures of the samples were analyzed using the Electron Microprobe Cameca SX50 at the Electron Microprobe Laboratory in the Geoscience department at Texas A&M University.

The samples were prepared for analysis by sectioning a thin sample from a sintered pellet using the same section procedure as done with LFA samples (Section 3.6). The thin section (0.5 to 1.0 mm thick) was mounted in epoxy and polished. Due to the fine BeO features being easily pulled out from the sample during grinding, the mounted sample was polished slowly and started with 600 grit SiC grinding media. Once the sample had been flattened and there no more sectioning scratches were visible, the sample was polished using the 800 and 1200 grit media. The sample was then polished using 6, 3, and then 1 micron diamond suspension atop a nylon polishing cloth. The polished sample was cleaned between each polishing step with ethanol and lens clean wipes.

The polished sample was taken to the microprobe to observe the UO_2 and the BeO phases using X-ray maps, Back Scatter Electron microscopy (BSE), and cathodoluminescence (CATH). Due to the difference in atomic mass between uranium and beryllium it was difficult to differentiate between BeO and a crock of pore. In order

to get a better distinction between UO_2 and BeO CATH was used since BeO is cathodoluminescent and UO_2 is not. For the BSE and CATH images were done at the same points using a grind of 5X5 or 7X7 using a 10nA electron beam. These images were taken at 200X magnification. The images were analyzed using ImageJ 1.47v by thresholding the image and despecling and then measuring the area fraction for each image. Several other images were taken of the samples at various magnifications with BSE, CATH, and secondary electron (SE).

3.4 Dilatometry

A M-5X12 Materials Research Furnace (MRF) was equipped with a customized vertical dilatometer to measure the geometric changes of pressed pellets with varying temperature during sintering. This was accomplished by attaching a Linear Variable Differential Transformer (LVDT) on top of the MRF exterior shell with a closed-end stainless steel tube open to the system internal volume. The LVDT measurement housing is supported on the exterior of the tube and held in place using two stainless steel collars. The LVDT's position along the tube can be adjusted to an optimum position to accommodate various samples heights, Figure 16.

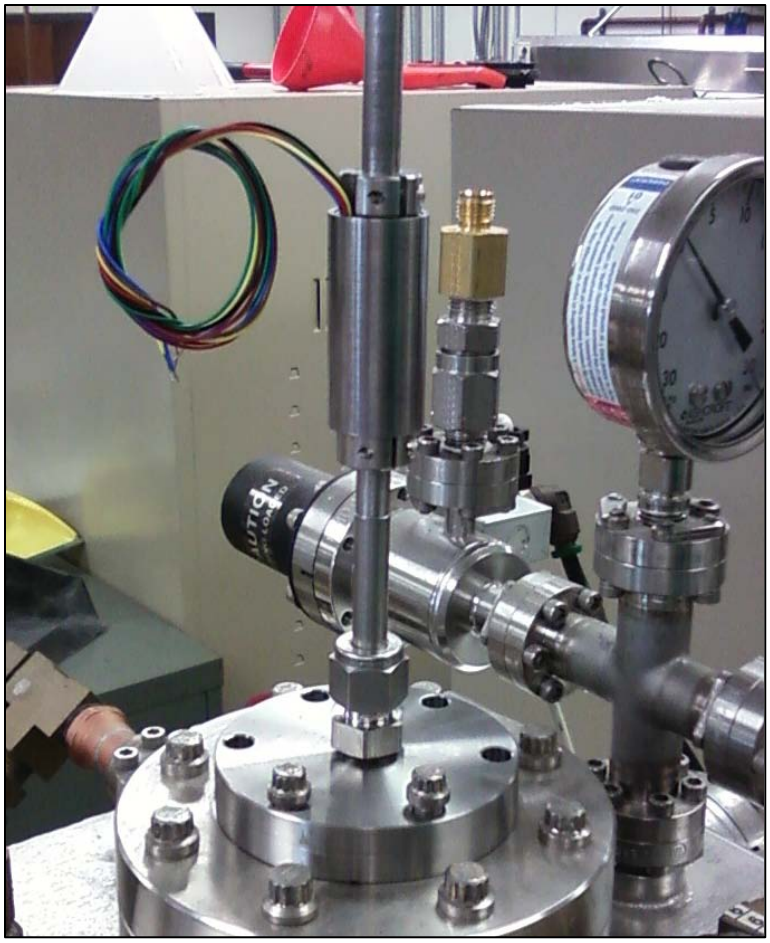

Figure 16. LVDT Configuration on the MRF

The magnetic core is positioned inside the stainless steel tube resting on the top end of a long push-rod that extends into the furnace and is able to freely move vertically. The push rod is a 99.8% dense alumina rod that is rests on a tungsten plate that sits on the sample, Figure 17.

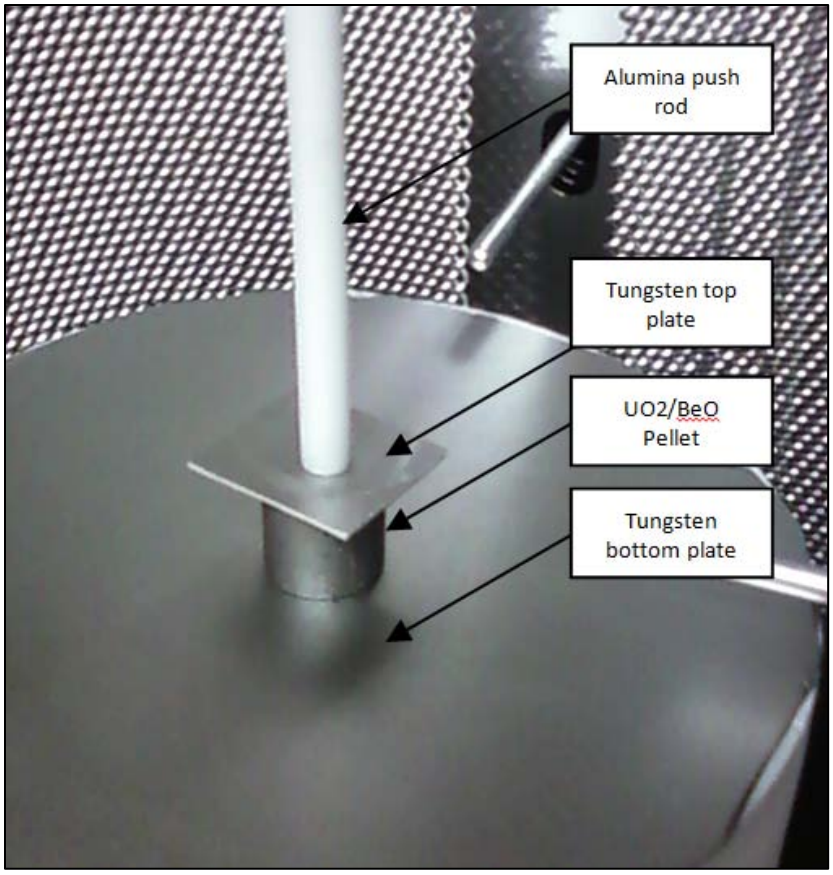

Figure 17. LVDT Sample Setup

The LVDT sensor is wired to a Macro Sensors EAZY-CAL MMX Series push-button LVDT signal conditioner, which is also wired to a National Instruments' Data Acquisition Device (DAQ) NI USB-6008. Two type C thermocouples are inserted into the furnace level with the sample that are also monitored using a separate DAQ board (National Instruments NI 9211). Both DAQ systems are monitored simultaneously using National Instruments LabVIEW 2010 version 10.0f2 (32-bit).

The LabView program was programmed to use the LVDT and thermocouple signals to enable the observation of sample height and temperature changes in real time.

This is done by inputting the initial height, diameter, mass, and target BeO volume fraction into the software. The program then estimates the initial density (g/cm^3) and relative density (%TD) as initial parameters that are monitored during the test. The program also calculates statistics for the signals which is used to determine the initial LVDT signal. As the LVDT signal from the initial core position changes, the linear slope of the height change, strain, and density. The thermocouple signal is converted to a temperature within the LabView software by determining the signal to temperature correlation from data tables provided by Omega for type C thermocouples. The cold junction temperature was determined from the DAQ's internal resistance temperature detector (RTD).

Before use, the LVDT and signal conditioner are calibrated. Using gage blocks of varying heights, the range for the LVDT is set. The rage is set to ±3.81mm which allows enough expansion of the furnace and sample up to 1600°C. The linear slope of the magnetic core position to the output signal voltage was found to be 0.7595 ±0.0076mm/V. The gage blocks were used to check this slope prior to running the furnace.

Once the system is calibrated, the expansion of the furnace and LVDT assemble were measured without the presence of a sintering pellet. This is accomplished by operating the furnace with the assembly in place without a sample while taking measurements using a single crystal sapphire with the axis oriented in the <<c>> axis with known thermal expansion behavior. Once the furnace is at thermal equilibrium at room temperature, an initial voltage is measured. The standard then undergoes the same

temperature profile as the samples to be sintered. Once the data is collected the LVDT signal is converted to change in height by multiplying the difference between LVDT signal and the initial voltage by the slope calculated from the calibration. The thermal expansion from the standard is then calculated and subtracted from the resulting height change. A curve is then fit to this height change versus temperature and will then be subtracted from the samples change in height as a function of temperature.

Samples are set up the same as the sapphire standard and run under the same temperature profile. The change in height of the sample is then found from by multiplying the difference between LVDT signal and the initial voltage by the slope calculated from the calibration. The height change of the sample is corrected by subtracting the background signal (from sapphire) from the height change. The strain/shrinkage of the sample is found by dividing the corrected sample height change by the samples initial height. The density during sinter can now be found using the following equation.

$$\rho = \frac{\rho_0}{(\epsilon_H + 1)^3} \quad \textbf{(21)}$$

3.5 Powder Compaction and Sintering

The UO_2-BeO pellets were fabricated using methods similar to those reported for the Green Granules option in previous studies (Section 2.4.5) [13] with variations established during this project to achieve improved final pellets; the current, as-modified, process flow diagram can be seen in Figure 18. The fabrication process is divided into three steps: (1) powder granulation, (2) final compaction, and (3) sintering.

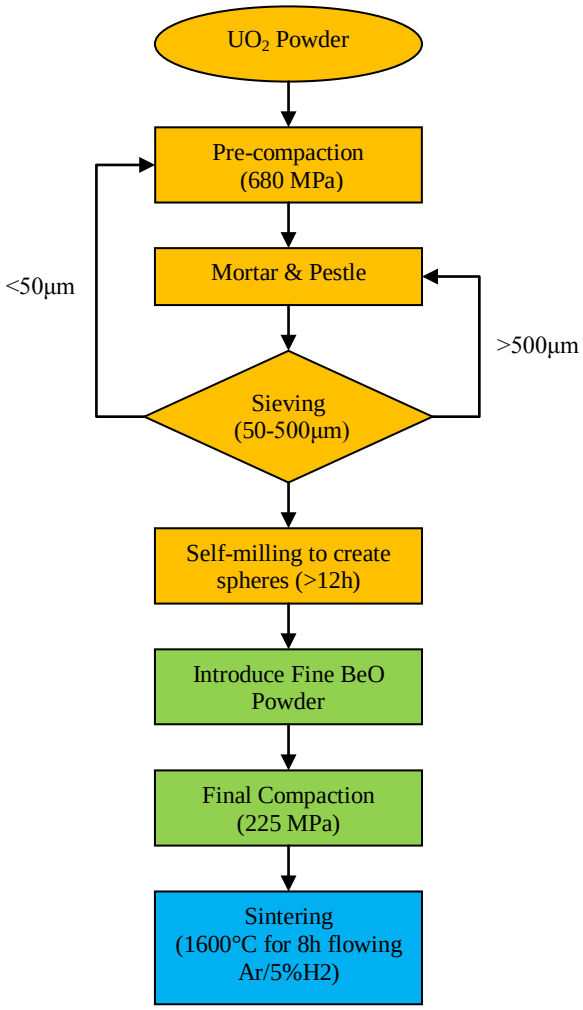

Figure 18. UO_2-BeO Pellet Fabrication Flow Chart (Orange) Granulation, (Green) Final Compaction, (Blue) Sintering

The granulation procedure comprises the pre-compaction steps through the self-milling step in the flow diagram. This begins with the milled UO_2 powder being pressed in a 13mm split sleeve die lubricated with a thin film of LPS-2 Heavy-Duty Lubricant from Leadership Performance Sustainability Laboratories to a load of 9.07tonne or a pressure of 680MPa using the Atlas 40T automatic hydraulic press from Specac. The

load was held for 5 minutes before extracting the pellet from the die. Two pressed compacts are simultaneously ground into a course granulated powder agglomerates using an alumina mortar and pestle. The powder is then separated into three sizes by sieving using 35 and 270 mesh (500 and 53μm respectively) sizes for at least 30 min using a shaker (Dual Manufacturing Co. Inc. model D-4326). The powder larger than the 500μm sieve was recovered for later grinding. The powder smaller than 50μm was combined with the milled UO_2 powder and recycled through the granulation steps. The granules with particle sizes between 50 and 500 μm (i.e., the powder recovered in the central sieve tray) were then self-milled for 12hr in a small glass jar with a helical copper wire inside to promote tumbling, as seen in Figure 19. This self-milling step smoothes the edges of the rough particles, creates larger agglomerates, and knocks off loose powder from the larger agglomerates; Figure 20 shows an example of powder before and after this self-milling step. These spherical "green granules" are used in the final compaction step.

Figure 19. Glass Jar with Copper Wire for Self-Milling the UO_2 Agglomerates

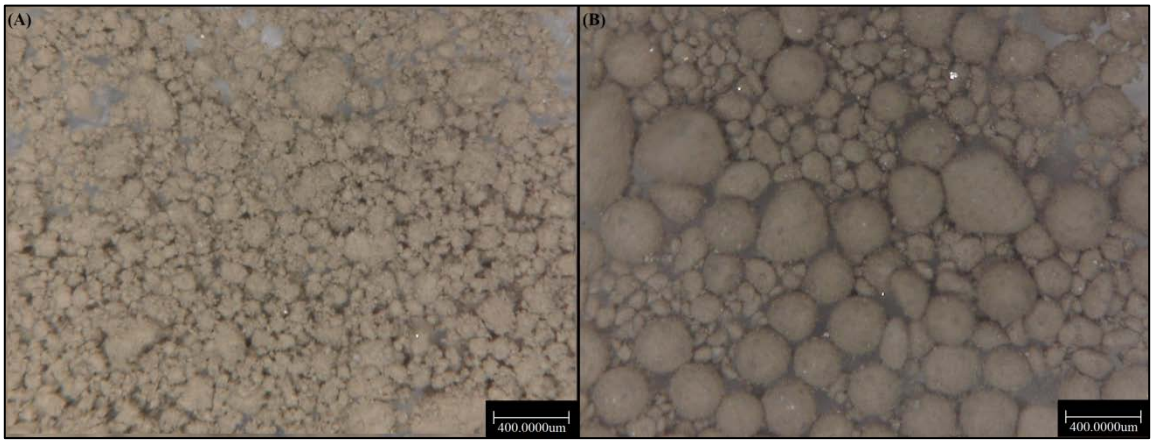

Figure 20. UO_2 Agglomerates (A) Before Self-Milling and (B) After Self-Milling

The final compaction step is where a final UO_2-BeO compact is made. The first step is to verify that the electronic balance is still accurately calibrated. Then the volume

fraction of BeO to be used is selected and the green volume of the compact is assumed to have a diameter, height and relative density of 15mm, 7.5mm, and 60% respectively. Then mass for both UO_2 and BeO components of the pellet are then calculated using simple geometric and density combination estimates. Table 1 shows the outcome of this estimate and these values were used as a guide for preparing the correct powder mixtures.

Table 1. Calculated Mass of UO_2 & BeO Powder for Each Pellet Composition

BeO v%	*Mass UO_2*	*Mass BeO*	*Density*	*BeO m%*
0.0	4.3618	0.0000	10.97	0.00
2.5	4.2527	0.0300	10.77	0.70
5.0	4.1437	0.0600	10.57	1.43
7.5	4.0346	0.0901	10.37	2.18
10.0	3.9256	0.1201	10.18	2.97
100.0	0.0000	1.2008	3.02	100.00

The mass of the UO_2 and BeO powders were measured carefully to be within 0.0002g of the requisite calculated values that were predetermined for the intended volume fraction. The BeO powder is then poured into the UO_2 container and the total mass verified before pressing. The container is then wrapped in electrical tap and placed within a larger glass jar and the powders are then mixed for 45 to 60min on the rolling mill. After mixing, a zinc stearate binder is added (7±0.5mg) to the powders followed by one final mixing step for 5min. A 15mm diameter die is cleaned and coated with a thin film of LPS-2 lubricant in preparation for pellet pressing. The powder is then fed into the die and compacted with a load from 3.6 to 5.0tonne, or 200MPa to 275MPa and the load is maintained for 5min and then slowly released. The pressed compact is then

extracted from the die and the height, diameter, and mass are then measured (see section 3.5).

The pressed pellets were transferred to the furnace were they were sintered. The pellets are placed on a platform level with two type C thermocouples that record the temperature near the pellet within the furnace during sintering. If the pellet dimensional changes are going to be measured with the LVDT, the pellet is placed within the LVDT assembly described in section 3.3. The furnace chamber is then sealed and evacuated with a roughing vacuum pump and backfilled with Argon- 5%Hydrogen at least three times. On the final evacuation a turbo pump is used to achieve a vacuum on the order of ~0.5 mTorr. On the last backfill the MRF is filled to a pressure of 14kPa (gage) this is the working pressure to be maintained for the duration of sintering. The gas inlet flow rate is controlled by a rotameter with a size 3 tube and a 316 SS float, which has a flow rate of approximately 1380cc/min at 150mm for argon gas. The exhaust valve and rotameter are then adjusted to maintain a constant flow rate of approximately 1100cc/min. The furnace chiller is turned on and the system is allowed time to reach equilibrium as observed using the LVDT and thermocouple signals.

The furnace is then programmed to ramp to 700°C at 5°C/min and hold for 30min to allow the binder to be burn off and enable the system to reach a new equilibrium. The temperature is them increased to 1600°C at 5°C/min and held for a soak time of 8h. The furnace is then cooled to room temperature at 9°C/min and the sintered pellet is taken out where it will be analyzed further.

Each sample is designated with a numbered label with the following format: XX-Y-ZZZ, where XX is the sintering set, Y is the sample number in the heat run, and ZZZ is the volume fraction of BeO present in the pellet. An example would be three pellets are sintered at together on the 5th heat run all of which are 5 vol% BeO, the second pellet of the set would be labeled 05-2-050.

3.6 Physical Measurements

The bulk densities of each sintered pellet was measured using two different methods. The first was accomplished by measuring the mass and geometric dimensions of the pellet. The second was accomplished via liquid immersion using Archimedes' principle to determine the volume. Due to pores, cracks, and chipping it is expected that the immersion method is more accurate in determining the bulk density and porosity of samples. The relative densities of the samples are then determined from the ratio between the bulk density and the theoretical density of the composition.

3.6.1 Geometric Measurements and Densities

The pellet geometries were measured before and after sintering in order to determine how the sample changed during sintering and to get a rough value for each density. For these measurements, a Mitutoyo Digimatic Caliper was used with a measurement uncertainty of ±(200+10L)µin where L is the nominal length in inches. Assuming each sample was a perfect cylinder, the height (H) and diameter (D) were

measured five to ten times in different locations for each sample and the average measurements were used to estimate the pellet volume.

In order to evaluate the geometric changes that the samples underwent during sintering, the change in height and diameter were normalized to the initial height and diameter respectively. These normalized values are analogous to strain and are thus referred to a sintering strain (ε). This sintering strain is then defined in eq.(22).

$$\varepsilon = \frac{H_f - H_i}{H_i} \quad \textbf{(22)}$$

The samples mass (m_d) was measured using a METTLER TOLEDO AB204-S balance. Before use, the balance was calibrated and checked for accuracy using an ANSI/ASTM Class 1 tolerance 200g calibration weight. The geometric densities (ρ_g) were then determined using the following equation.

$$\rho_g = \frac{m_d}{\pi H \frac{D^2}{4}} \quad \textbf{(23)}$$

3.6.2 Archimedes Density Measurement

The densities of the samples were also measured using Archimedes' principle. This is done by measuring the mass of the sample when it is dry (m_d), when it is wet (m_w), and when the sample is immersed (m_i). The dry mass is simply found by measuring the mass of the sample on the same balance used for the geometric densities. The wet mass is measured by wetting the samples in ethanol, wiping the wet sample on paper towels pre-soaked with ethanol, and quickly placing the container in an airtight container. The wet mass is then determined by the difference in mass between the

empty container and the container holding the sample. The immersed mass is then determined by setting up a hanging basket which is supported on the balance with the basket completely immersed in ethanol, Figure 21.

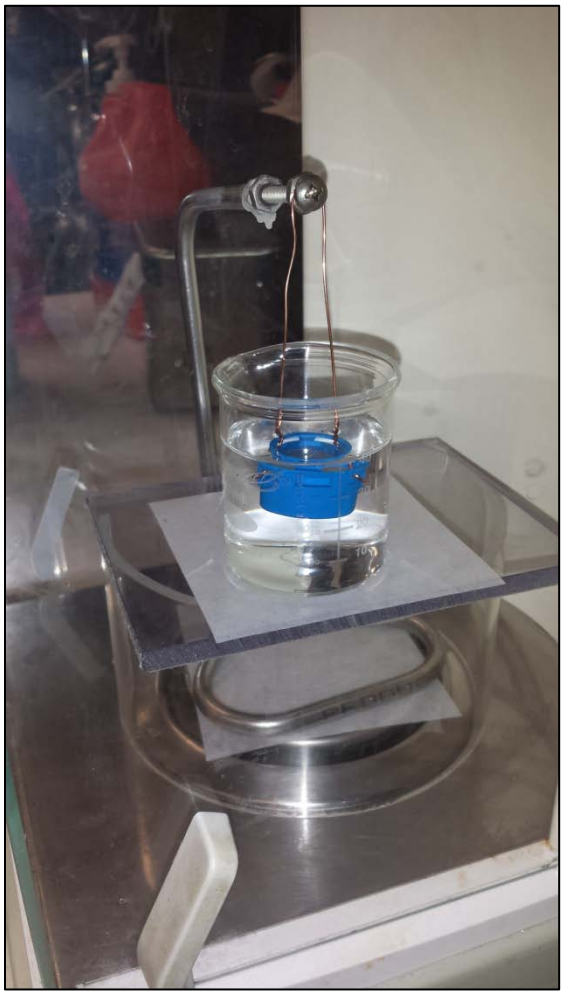

Figure 21. Immersed Sample Mass Measuring Setup

The pellet is then placed in the immersed basket. The mass is recorded before and after placing the sample in the basket. The bulk density and the apartment porosity (p) of the samples were then determined using the following equations respectively.

$$\rho_B = \frac{m_d}{m_w - m_i} \rho_{fl} \quad \textbf{(24)}$$

$$p = \frac{m_w - m_d}{m_w - m_i} \quad \textbf{(25)}$$

The density of the ethanol (ρ_{fl}) was found by measuring the mass of a known volume of ethanol using a graduated cylinder.

3.7 Thermal Analysis

The thermal conductivity for the composite UO_2-BeO material was estimated by measuring the thermal diffusivity of pellets with various compositions and thickness. The conductivity is calculated using the diffusivity and density of each sample, along with the specific heat calculated using a simple rule of mixing, due to the immiscibility between the two phases.

The thermal diffusivity was measured using the NETZSCH LFA 447 NanoFlash instrument over the temperature range from 25 to 250°C in increments of 25°C. The samples were prepared from selected sintered pellets. In order to enable fine parallel face sectioning, the pellets were mounted on the end of a machined aluminum rod with mounting wax MWH135 from South Bay Technology. The aluminum rod and pellets were simultaneously heated to 180°C, and then the top surface of the aluminum rod was lightly coated with mounting wax. The pellet was then placed atop the aluminum and gently pressed down while the aluminum and pellet cooled down to ensure the contacting surfaces were as flat against each other as possible.

The bonded pellet and rod were clamped into a Buehler Isomet Low Speed Saw (Buehler 11-1180) with the back of the aluminum flush against the back of the clamp to have each slice be as parallel as possible. The saw speed was set to a moderate speed (the “6” setting on the dial) with a cutting load of 25g. After the pellets were sectioned they were dismounted and ultrasonically cleaned using acetone and cleaned again using ethanol. The post-sectioning dimensions and density of each section were then measured using the methods discussed in section 3.5.

The prepared pellets were coated with a thin layer of dry graphite using an aerosol (Sprayon Dry Film Graphite Lubricant, LU 204). The graphite enabled the samples surfaces to act as a "black body," absorbing the entire thermal pulse, when analyzed in the LFA 447. The samples were coated in a fume hood and the aerosol is initially sprayed on one side of the samples by holding the spray nozzle approximately 30 cm (12 in) above the pellets. The graphite aerosol spray cone is passed over the samples two to four times. The graphite is then allowed to dry for three to five minutes and then the process is repeated three to five times to ensure an even coating of graphite. The pellets are flipped and coated again using the same steps.

The coated pellets were placed in the sample holders in the LFA 447. The LFA is filled with liquid nitrogen and the NETZCH LFA 447 NanoFlash and the system is initiated. The sample name, height, diameter, and density are input in to the software. The software is set up to take analyze the samples starting at 25 and at increasing temperatures up to 250°C in increments of 25°C and to take 10 measurements at each temperature. The pulse width was set to medium from the options, but on the occasions

where the signal to noise ratio was too high, the pulse width was increased to long. The system would also take one to five shots to optimize the measurement time and the signal gain for diffusivity analysis. The system was then operated automatically and the liquid nitrogen was refilled every two to three hours at a time that would not influence the signal in any way.

Once all the data were collected it was then analyzed using NETZSCH LFA Analysis software (Version 4.8.4) and the thermal diffusivity was then calculated from the data using the Cowen model within the software. The thermal conductivity was then estimated using the diffusivities, densities, and the estimated specific heats using the ratio method, eq.(26).

$$k_m = \rho c_p \alpha \quad \textbf{(26)}$$

4. RESULTS

This chapter provides a summary of the key results generated during this project. The first section (Section 4.1) provides an overview of all experiments and the general observations. Section 4.2 provides information on the powder characteristics such as stoichiometery and particle size distribution. Section 4.3 looks at the stoichiometery of the sintered pellet as well as any residual contamination after sintering. Section 4.4 shows how compaction pressure and beryllia concentration affect the shrinkage and densification of the UO_2-BeO composite. Section 4.5 shows results from measuring the shrinkage of the pellets during sintering. Section 4.6 illustrates the microstructure using various methods such as x-ray mapping, backscatter electron and cathodoluminescence. The final section shows the results of the thermal diffusivity of the UO_2-BeO composite.

4.1 Overview of Pellet Fabrication Outcomes

Table 2 presents an overview of the UO_2-BeO samples prepared during this study. Due to low densities and cracking in early the sample sets 01 and 02, different steps were taken to improve the quality of the final pellet, such as varying the compaction pressure and adding a binder. There were multiple pellets generated as parametric surveys were performed on compaction pressures (04-1-100, 04-2-100, 05-1-100, 05-2-100, and 05-3-100), BeO volume fraction (03-2-100, 05-2-100, 06-1-100, 06-4-025, 06-5-050, 06-6-075, 07-1-100, 08-1-075, 09-1-050, and 10-1-025), and alumina introduction (05-2-100, 06-1-100, 06-2-100, and 06-3-100).

Table 2. Sample

Sample ID	BeO Vol. Fraction (%)	M_{UO2} (g)	M_{BeO} (g)	Sintering Temp (°C)	Sintering Time (h)	Green Density (g/cm^3)	Density B (g/cm^3)
01-1-100	10.0	3.2649	0.0998	1580	4	6.087	9.161
01-2-100	10.0	3.2649	0.0996	1580	4	6.100	9.137
01-3-100	10.0	3.2651	0.0998	1580	4	6.152	8.703
02-1-000	0.0	3.7830	0	1600	5	6.436	10.445
02-2-100	10.0	3.4022	0.1042	1600	5	6.139	9.424
03-1-100	10.0	3.9257	0.1202	1600	5	---	9.424
03-2-100	10.0	3.9255	0.1200	1600	5	6.034	9.420
03-3-100	10.0	3.9255	0.1201	1600	5	---	8.428
03-4-999	100.0	0	1.0319	1600	5	---	8.428
04-1-100	10.0	3.9254	0.1202	1600	5	6.098	8.474
04-2-100	10.0	3.9255	0.1202	1600	5	6.066	10.196
04-3-100	10.0	1.6739	0.0512	1600	5	5.373	8.901
05-1-100	10.0	3.9256	0.1203	1600	5	6.036	9.162
05-2-100	10.0	3.9255	0.1201	1600	5	6.084	9.281
05-3-100	10.0	3.9257	0.1202	1600	5	6.021	9.166
06-1-100	10.0	3.9255	0.1203	1600	5	5.878	9.311
06-2-100	10.0	3.9255	0.1201	1600	5	6.104	9.307
06-3-100	10.0	3.9257	0.1199	1600	5	6.051	9.228
06-4-025	2.5	4.2526	0.0299	1600	5	6.330	10.074
06-5-050	5.0	4.1435	0.0598	1600	5	6.221	9.867
06-6-075	7.5	4.0346	0.0899	1600	5	6.158	9.644
07-1-100	10.0	3.9258	0.1203	1600	8	5.919	9.379
08-1-075	7.5	4.0348	0.0902	1600	8	6.133	9.613
09-1-050	5.0	4.1438	0.0602	1600	8	6.162	9.861
10-1-025	2.5	4.2528	0.0301	1600	8	6.209	9.911

During the powder processing of the UO_2 and BeO powders, it was observed that the UO_2 would stick to the surface of the milling jar and grinding media after hours of rolling. This made it difficult to collect all the ground powder since the compacted powder was also strongly agglomerated and not useful for pellet preparation. It has been

shown in prior milling studies the UO_2 should not be milled longer than 4hr at a time [83]. Therefore, the UO_2 milling time for this project was limited to 3hr after this observation was made.

It was observed that the jet mill also not effective for milling UO_2 powder in air under the conditions available to this project because the uranium oxide powder clung to the walls in the hopper and did not flow through the milling system properly. On the other hand, the BeO powder was easily milled, but it underwent a slight color change during the milling. The BeO went from sold white in appearance to varying degrees of grey.

4.2 Powder Characterization

4.2.1 Particle Size Analysis

Images were taken to estimate the particle size of the UO_2 and BeO powder. The UO_2 was initial less 300µm from the manufacturer. Once the UO_2 was milled, a quantity of the powder was dispersed in mineral oil to estimate the powder size, Figure 22. From this image the powder appears to approximately 10µm or smaller, thus showing that the ball milling was effective.

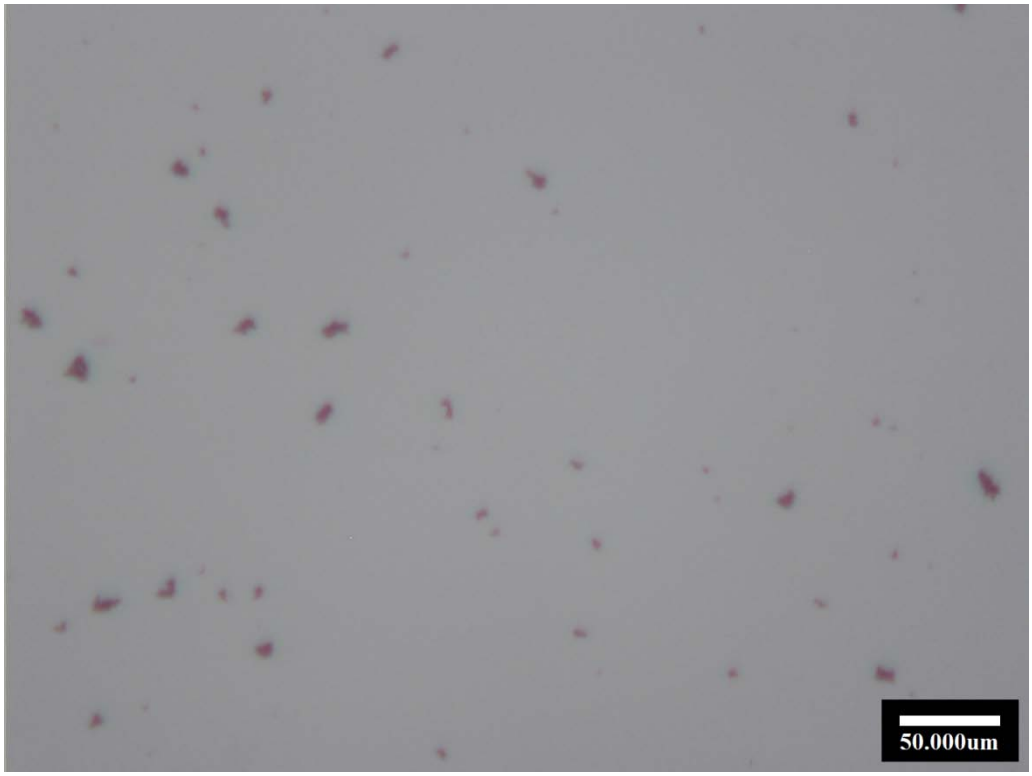

Figure 22. Optical Microscopy of Ball Milled UO_2 Dispersed in Mineral Oil

In Figure 23 shows the raw BeO powder which has large particle sizes. The powder also showed that there was fine powder within the raw BeO. To determine the distribution between the fine powder to large powder, the BeO was sieved through a 325 mesh which showed that approximately 20wt% of the powder was less than 45µm.

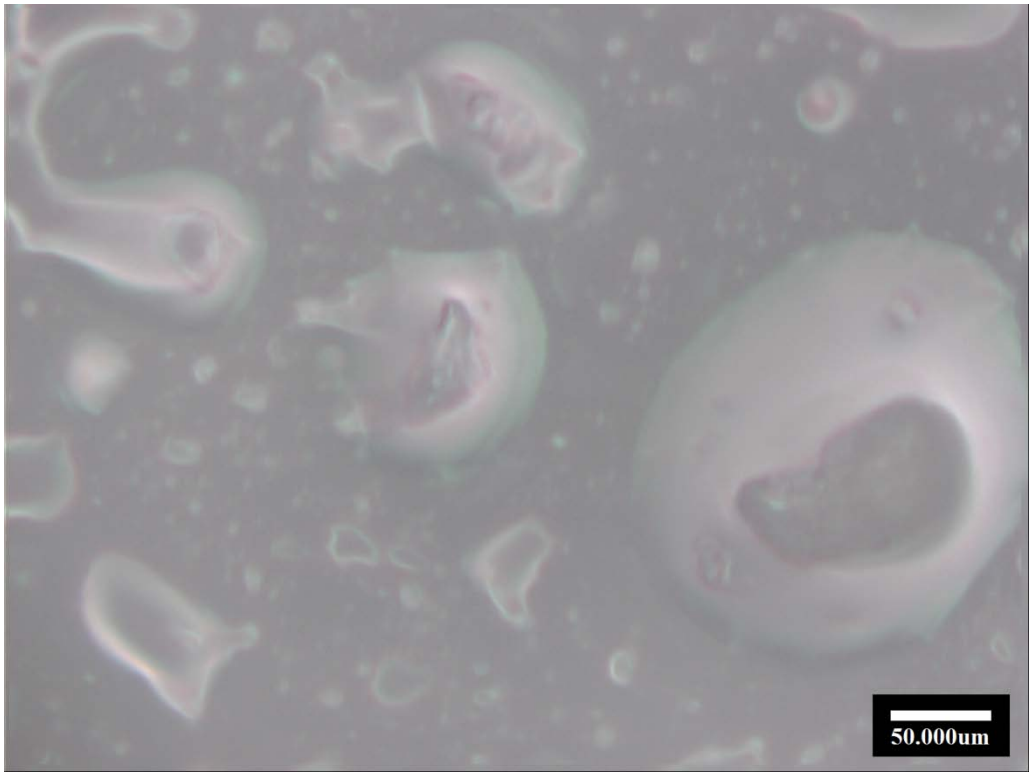

Figure 23. Un-milled BeO Powder Dispersed in Mineral Oil

The jet milled BeO powder was observed via the same methods as above, Figure 23. It was shown that the powder was milled below 10µm but gathered trace amounts of contamination (the white particles in Figure 24). This contamination could have been caused from the BeO particles abasing the jet mill's walls.

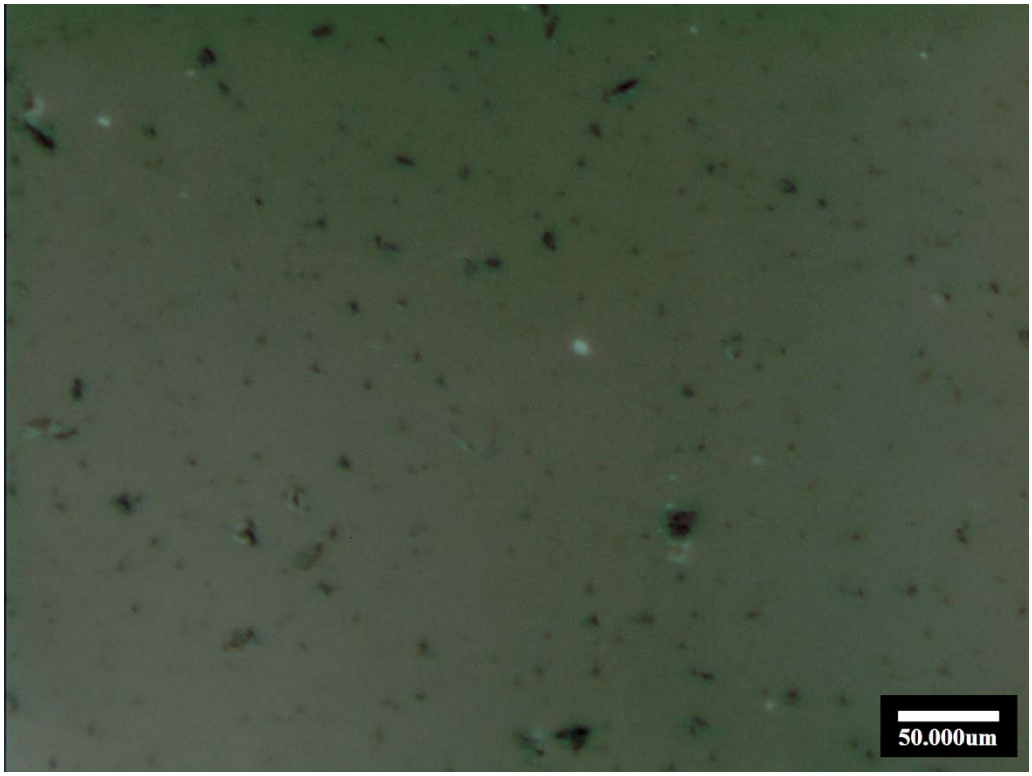

Figure 24. Inverted Optical Image of Milled BeO Dispersed in Mineral Oil.

4.2.2 Powder Stoichiometry

The UO_2 powder used in the study was analyzed by characterizing the composition the raw powder samples using electron microprobe analysis. Four probe counts were collected at each point of analysis and at least two points were evaluated per sample for three samples. The mean oxygen to metal ratio was found to be 2.289±0.198, which is higher than the ideal stoichiometric UO_2 but is typical of fine UO_2 powder due to its high surface reactivity [84].

Table 3. WDS of Second Raw Uranium Oxide Powder

	wt%		*at%*		
	O	*U*	*O*	*U*	*O/U*
UO_X 3	13.150	85.050	69.646	30.336	2.296
UO_X 4	13.217	84.803	69.794	30.196	2.311
UO_X 5	12.883	85.394	68.989	30.995	2.226

4.3 EDS and WDS Analysis of Sintered Samples

It was important to verify the stoichiometry of the UO_2 in the sintered pellets to ensure they were UO_2, especially since it was determined that the starting powder was approximately $UO_{2.3}$ (Section 4.2). As with the powder, this was done using WDS analysis on the UO_2 phase of the samples. Composition measurements were acquired at five mutually exclusive points were taken on two separate samples and three points on a UO_2 standard. The average oxygen-to-metal (O:M) ratio for the two sintered pellets were 1.998±0.005 and 1.991±0.009 ad the measured O:M ratio of the UO_2 standard was 2.020±0.004,

The samples were examined for contamination using energy dispersive spectroscopy (EDS); this was especially of concert to verify that the zinc stearate binder did not leave a residue in the pellets. Figure 25 and Figure 26 show the EDS results from the UO_2 phase where no contamination is evident; the carbon peaks are due to the carbon coating on the samples.

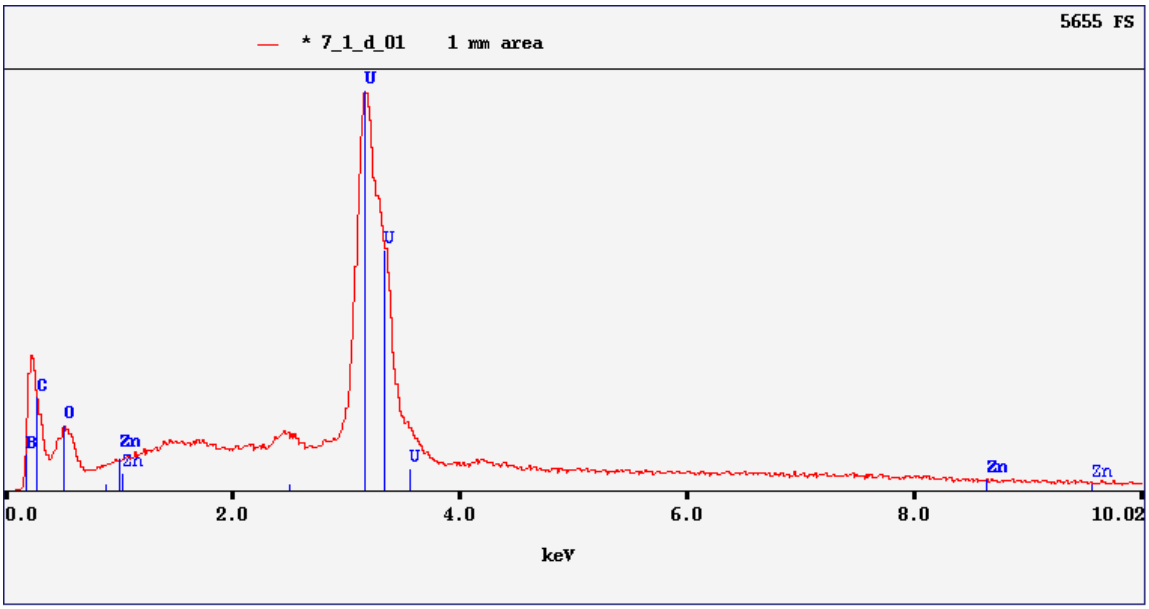

Figure 25. Energy Dispersive Spectroscopy of UO_2 Phase in Sample 07-1-100

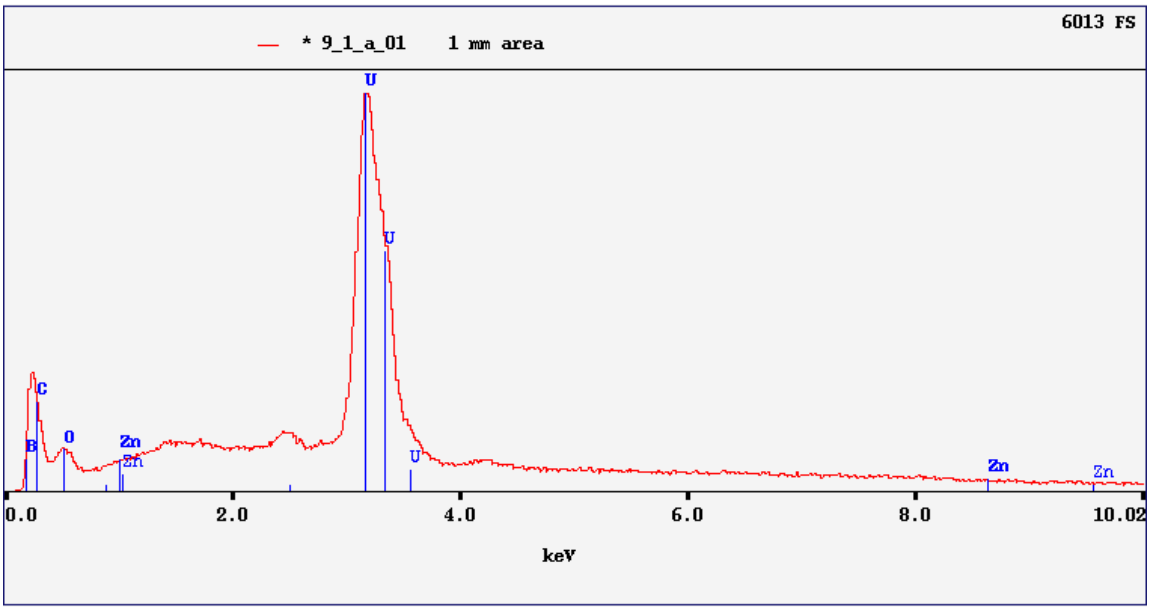

Figure 26. Energy Dispersive Spectroscopy of UO_2 Phase in Sample 09-1-050

An EDS spectrum was also acquired from the BeO phase (Figure 27) and no noticeable contamination was observed. it is therefore evident that the zinc stearate most likely left the sample during sintering as it is designed to do.

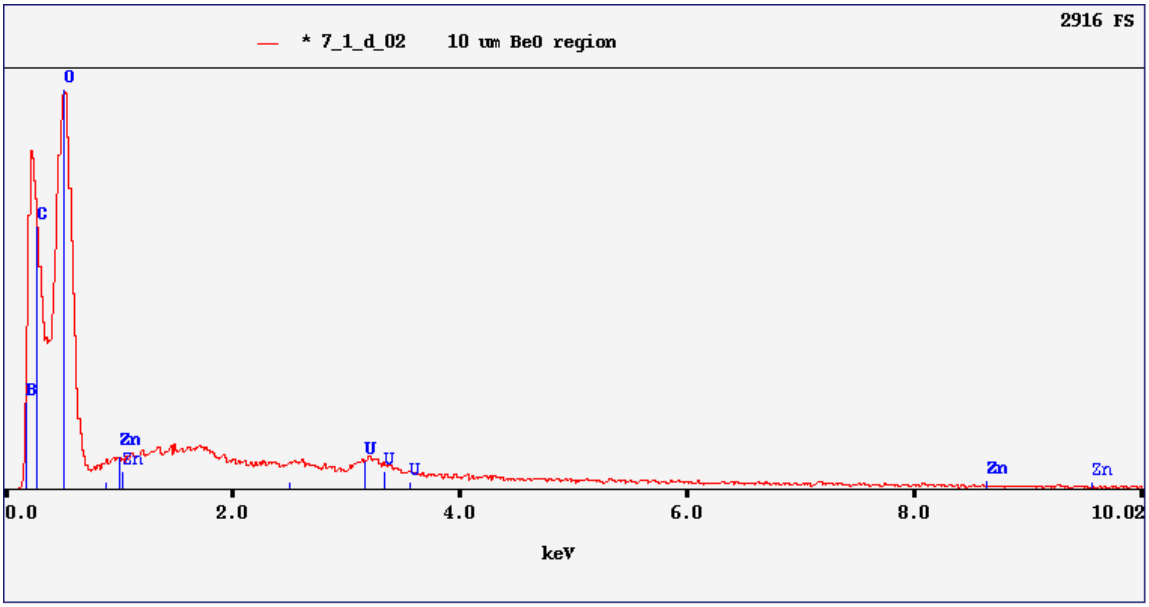

Figure 27. Energy Dispersive Spectroscopy of BeO Phase in Sample 07-1-100

4.4 Sintering Bulk Measurements and Surface Observation from UO_2-BeO Pellets

The sintering of UO_2-BeO was monitored by measuring the dimensional and density changes the sample pellets underwent during sintering. This was done by measuring the height and diameter of each pellet. The final density was measured for the sample pellets using Archimedes' method. Furthermore samples height changes were measured in situ during sintering.

The dimensions, height and diameter, of the UO_2-BeO pellets were measured using calipers both before and after sintering. The dimensional changes for each pellet were then calculated and normalized to the initial measurement prior to sintering. This geometric density was measured and are reported in Table 4 along with the pellet pre-compaction and final compaction pressures. Table 5 presents bulk density and porosity for each of the same pellets as determined using Archimedes' method (Section 3.5).

Table 4. Percent Changes & Ratio of Diameter to Height Percent Change in UO_2-BeO Pellets

Sample	*Pre-Compaction (MPa)*	*Final Compompaction (MPa)*	*Height Change (%)*	*Diameter Change (%)*	*Diameter/ Height*	*Volume Change (%)*
01-1-100	603	268	-13.2	-10.2	1.285	-32.3
01-2-100	603	268	-13.2	-10.3	1.283	-32.4
01-3-100	603	268	-12.3	-4.5	2.714	-26.6
02-1-000	670	268	-14.7	-13.3	1.110	-36.9
02-2-100	670	268	-13.2	-11.5	1.150	-33.4
03-2-100	670	201	-14.0	-12.5	1.116	-35.1
04-1-100	670	277	-13.2	-10.3	1.279	-32.4
04-2-100*	670	277	-13.2	-10.3	1.282	-32.3
04-3-100	670	277	-13.1	-10.0	1.317	-32.0
05-1-100*	670	252	-13.8	-11.6	1.184	-34.3
05-2-100*	670	227	-13.7	-12.0	1.141	-34.5
05-3-100*	670	201	-13.7	-12.2	1.127	-34.6
06-1-100	670	227	-14.0	-12.8	1.090	-35.5
06-2-100*	670	227	-13.9	-11.5	1.213	-34.3
06-3-100*	670	227	-13.7	-12.4	1.102	-34.7
06-4-025*	670	227	-15.2	-14.1	1.084	-38.3
06-5-050*	670	227	-14.6	-13.3	1.095	-36.8
06-6-075*	670	227	-14.2	-13.1	1.083	-36.1
07-1-100**	670	227	-14.2	-12.8	1.109	-35.7
08-1-075**	670	227	-14.6	-13.2	1.102	-36.6
09-1-050**	670	201	-15.1	-14.0	1.082	-38.0
10-1-025**	670	201	-15.3	-13.6	1.125	-38.0

*Al_2O_3 Contamination, **Zinc Stearate Binder

Table 5. Geometric and Immersion Densities and Porosity of UO_2-BeO Pellets

Sample	*Geometric Density (g/cm^3)*	*Open Porosity (%)*	*Total Porosity (%)*	*Relative Density*
01-1-100	9.161	4.9	10.0	90.0
01-2-100	9.137	6.5	10.2	89.8
01-3-100	8.703	7.9	14.5	85.5
02-1-000	10.445	-5.5	4.8	95.2
02-2-100	9.424	2.5	7.4	92.6
03-2-100	9.420	3.0	7.4	92.6
03-3-100	8.428	15.3	17.2	82.8
04-1-100	8.474	3.5	16.7	83.3
04-3-100	8.901	9.1	12.5	87.5
05-1-100	9.162	4.0	9.3	90.7
05-2-100	9.281	3.1	8.4	91.6
05-3-100	9.166	4.4	9.6	90.4
06-1-100	9.311	4.1	8.5	91.5
06-2-100	9.307	3.4	7.7	92.3
06-3-100	9.228	4.0	8.1	91.9
06-4-025	10.074	2.1	6.2	93.9
06-5-050	9.867	1.5	6.2	93.8
06-6-075	9.644	2.0	6.7	93.3
07-1-100	9.379	3.2	7.8	92.2
08-1-075	9.613	2.7	7.3	92.7
09-1-050	9.861	1.9	6.7	93.3
10-1-025	9.911	2.0	8.0	92.0

Various subsets of the data in Table 4 and Table 5 may be presented separately to elaborate on the impact of particular processing variables. The first variable to be examined is the final compaction pressure for samples with 10v%BeO. The samples 04-1-100, 04-2-100, 05-1-100, 05-2-100, and 05-3-100 (recall that the -100 identifier indicates 10.0 vol. % BeO) were pressed with the respective pressures of 277, 277, 252, 227, and 201MPa, respectively. These pressures were selected based on literature values for compacting UO_2 (268MPa) [20, 84] and BeO (300MPa) [85] pellets individually.

Figure 28 shows this impact of the final compaction pressure on the pellets densification, with lower pressures yielding higher densities. Sample 04-2-100 was not used for its volumetric shrinkage due to large crack that occurred to the sample prior to sintering, so 04-1-100 was used due to its similar processing. One of the observable features in the pellets pressed at 277MPa was severe macroscopic cracking in the sintered pellet, as shown in Figure 29. Cracking of this type was not evident at lower pressures. Based on this sequence of tests, subsequent pellets were pressed at 227MPa unless otherwise specified.

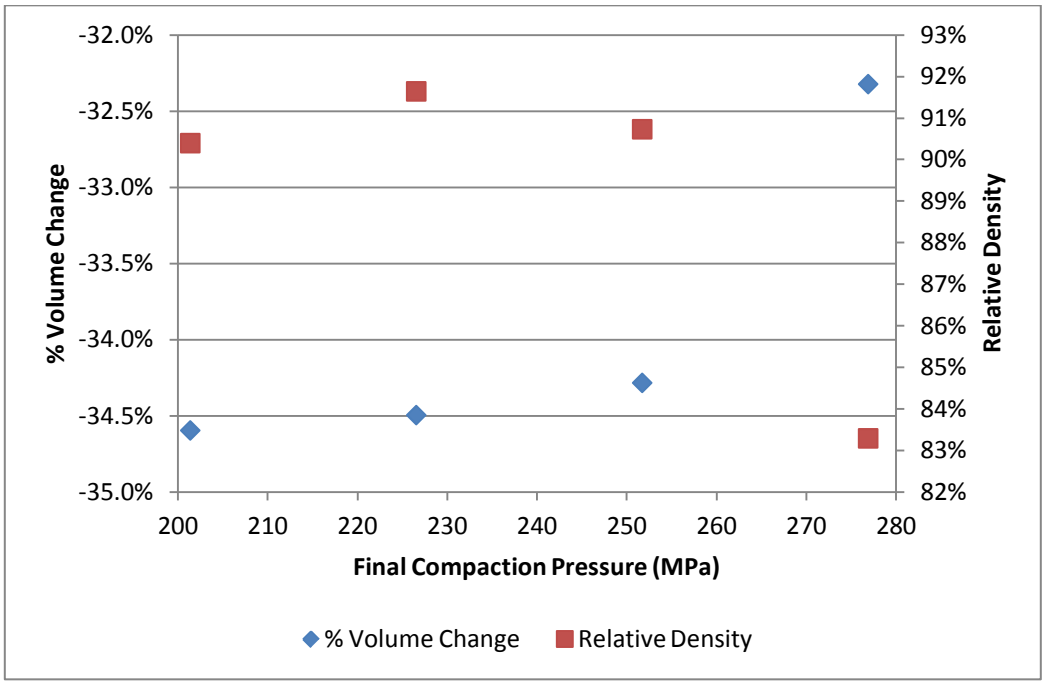

Figure 28. Effect of Final Compaction Pressure on Densification.

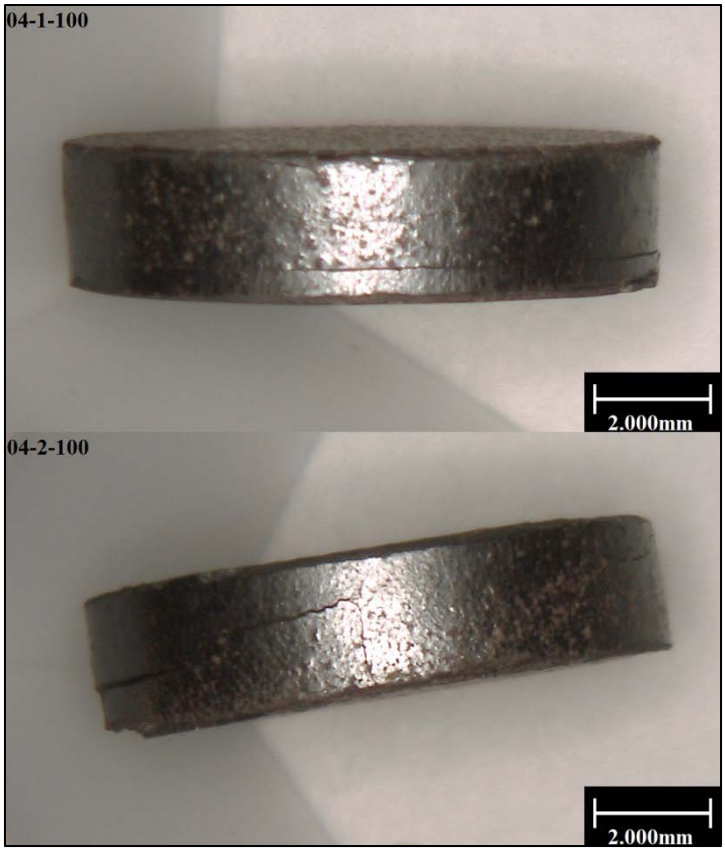

Figure 29. Circumferential Cracks in Samples 04-1-100 and 04-2-100 that Arise Due to High Compaction Pressures

A second notable, but of minimal importance, subset of the data elucidates the effect of an alumina contamination on the sintering of the UO_2-BeO pellets. The alumina was included in these samples as a binder option and a sintering aid according to the volume fractions in Table 6. Only four samples were used due to their similar processing such as final compaction pressures. The alumina did indeed exhibit an improving effect on the final pellet density, as shown in Figure 30. This minor alumina additive was rejected as not useful for the final pellet production procedure.

Table 6. Estimated Volume Fractions of the UO_2-BeO-Al_2O_3 Components

Sample	*v%Al_2O_3*	*v%BeO*	*v%UO_2*
06-1-100	0.0	10.0	90.0%
05-2-100	0.8	9.9	89.3
06-2-100	1.4	9.9	88.7
06-3-100	2.2	9.8	88.1

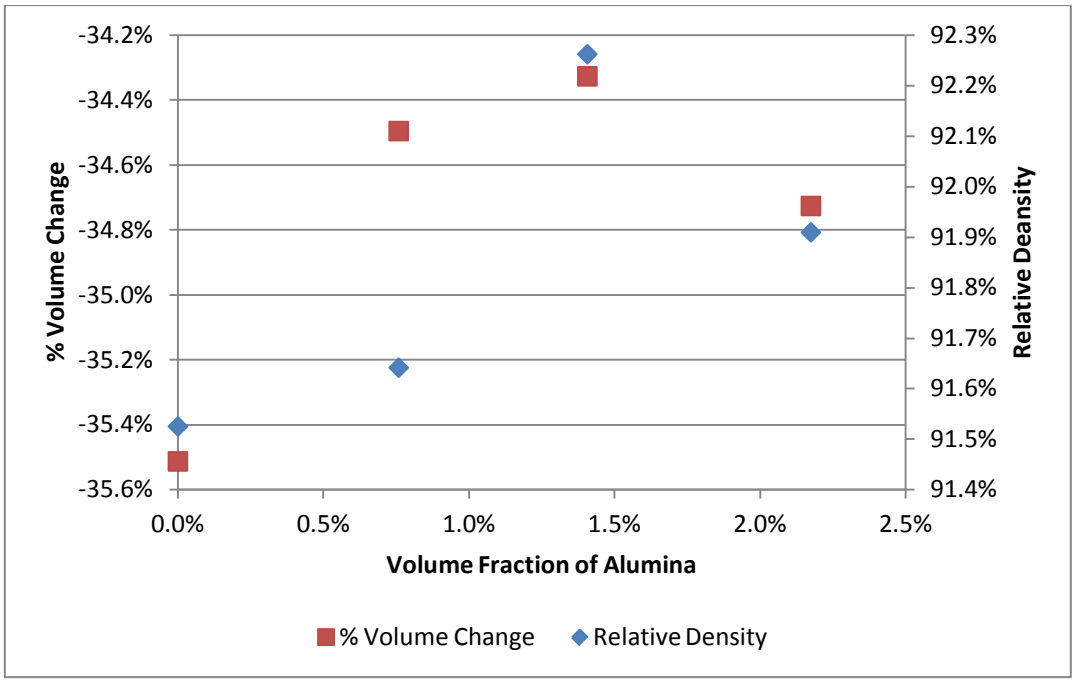

Figure 30. Alumina Contamination Effect on Densification

The final parametric collection of data is from the group of pellets fabricated with different volume fractions of BeO ranging from 2.5 vol.% BeO to 10v% BeO. This was done in order to observe if the BeO matrix would maintain continuity at lower

concentrations. These tests are divided into two sets, one using 0.5v% zinc stearate, and the other with less than 1.0v% alumina. Two additional data points are included that comprise low compaction pressure (less than 226MPa) pellets that contain neither binder nor alumina. Figure 31 shows that at lower BeO volume fractions the alumina additive yields higher densities than with a binder, and at 5.0v%BeO there appears to be a peak density. The higher values for the pellets without binder or alumina were for a pellet compacted at 201MPa while the lower point was compacted at 226MPa.

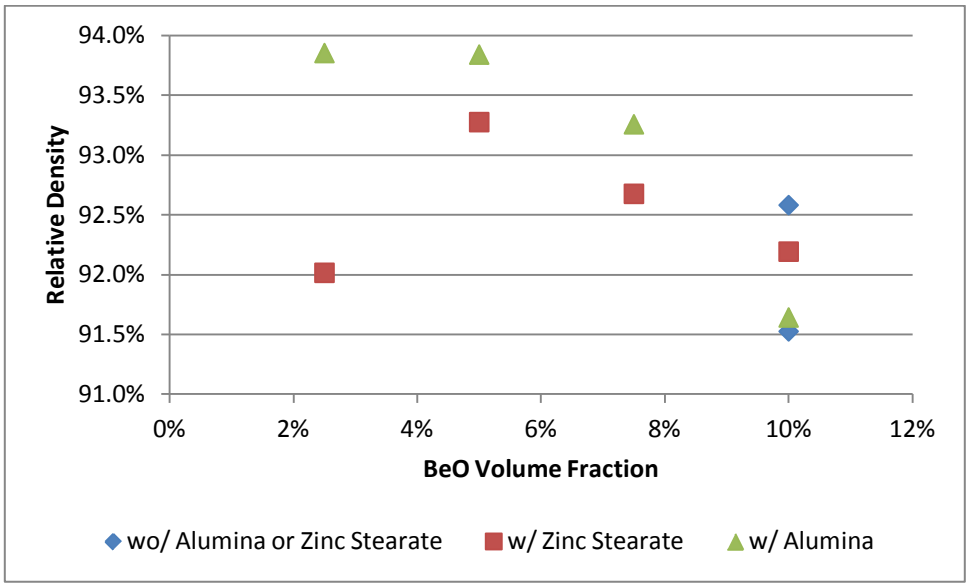

Figure 31. Relative Densities for Various BeO Volume Fractions

The shrinkage data from these pellets reveals that the binder improved the volumetric changes more than the alumina above 2.5v%BeO, Figure 32, and that the pellet with 5 vol.% BeO exhibits the maximum shrinkage for this set.

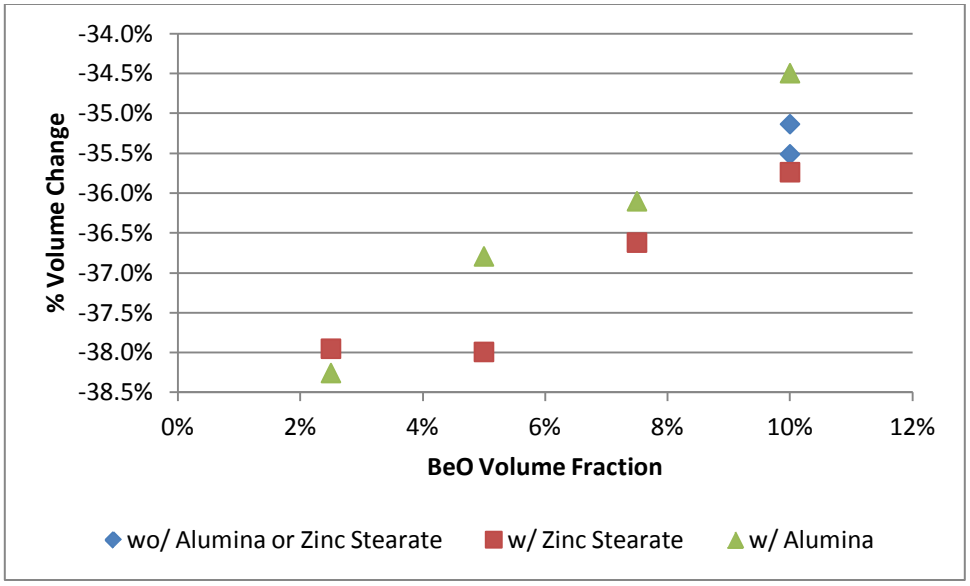

Figure 32. Pellet Shrinkage for Various BeO Volume Fractions

4.5 Vertical Shrinkage Data via LVDT Dilatometry

The vertical dilatometry data sets collected using the system described in Section 3.3 are described in the following sections. Calibration measurements made using a sapphire standard are presented in Section 4.5.1 and the actual shrinkage data for UO_2-BeO pellets are presented in Section 4.5.2.

4.5.1 LVDT Dilatometry Standard Measurements and Limitations

The LVDT calibration was verified repeatedly as the experiments progressed to verify that the instrumentation precision did not drift over time. The transducer was calibrated with a precision micrometer with the stainless steel tube and magnet configuration used in the tests and the data consistently yielded a calibration slope of

0.0299 ±0.0003in/V. This conversion was used to determine the height change, ΔH,of a sample. The system background signal was measured using a 100% dense sapphire crystal as a standard insert in place of a densifying pellet. The expansion of the sapphire was subtracted from the background and the change in height was fitted piecewise to its corresponding temperature in degrees Celsius. The mean absolute error from this curve fitting for the entire temperature range and for temperatures above 700°C was found to be 5.72×10^{-4}mm and 5.85×10^{-4}mm respectively.

The LVDT system was evaluated to determine sources of error that could affect the sintering results. The primary source of error observed was from the temperature variation of the water cooling in the outer shell of the MRF process chamber. The water temperature would regularly vary during a sintering run as the external water recirculation chiller would turn on and off causing the furnace to contract and expand with the changing water temperatures. This error created a periodic ripple in the LVDT signal that started when the MRF chiller's compressor turned on but had a time delay that varied with temperature. The amplitude of the ripple was approximately 0.02 V at room temperature which corresponds to approximately 6.00×10^{-4}mm. Another noticeable error in the signal arose as an effect from the internal gas pressure of the MRF process chamber. The gas pressure had the dual impact of causing the MRF chamber to contract or expand if changed and altering the convection currents of the cover gas in the chamber. These errors were observed during the evacuation and backfilling the furnace, as presented in Figure 33.

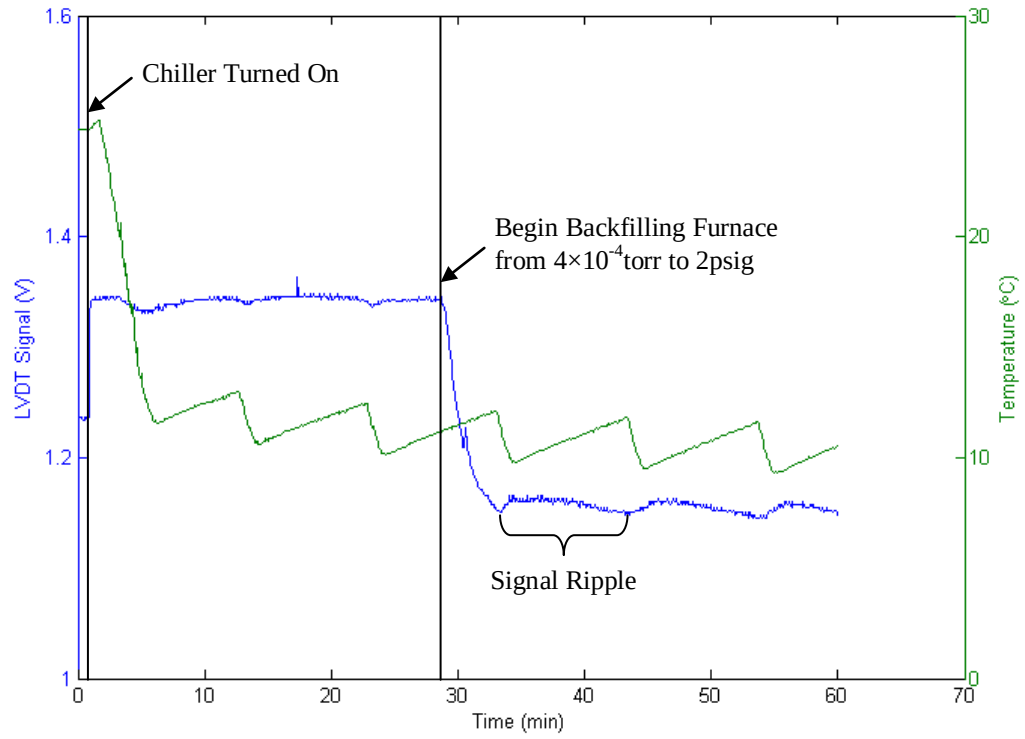

Figure 33. LVDT Error From Chiller and Internal Pressure During Backfill

The LVDT system was also used to examine the behavior of a molybdenum sample; the system noise errors noted above was too large (an order of magnitude grater than expected thermal expansion value) to determine the thermal expansion, as can be seen in Figure 34 where the water temperature was measured inside the walls of the furnace. Again, this data fluctuation was primarily attributed to the temperature of the MRF's surface. The delay in the LVDT signal seeing the effect of the furnace coolant can also be seen in this plot. In general, the noise of the system is too significant for fine measurements of thermal expansion, but it is not too severe for sintering measurements, as shown in the next section.

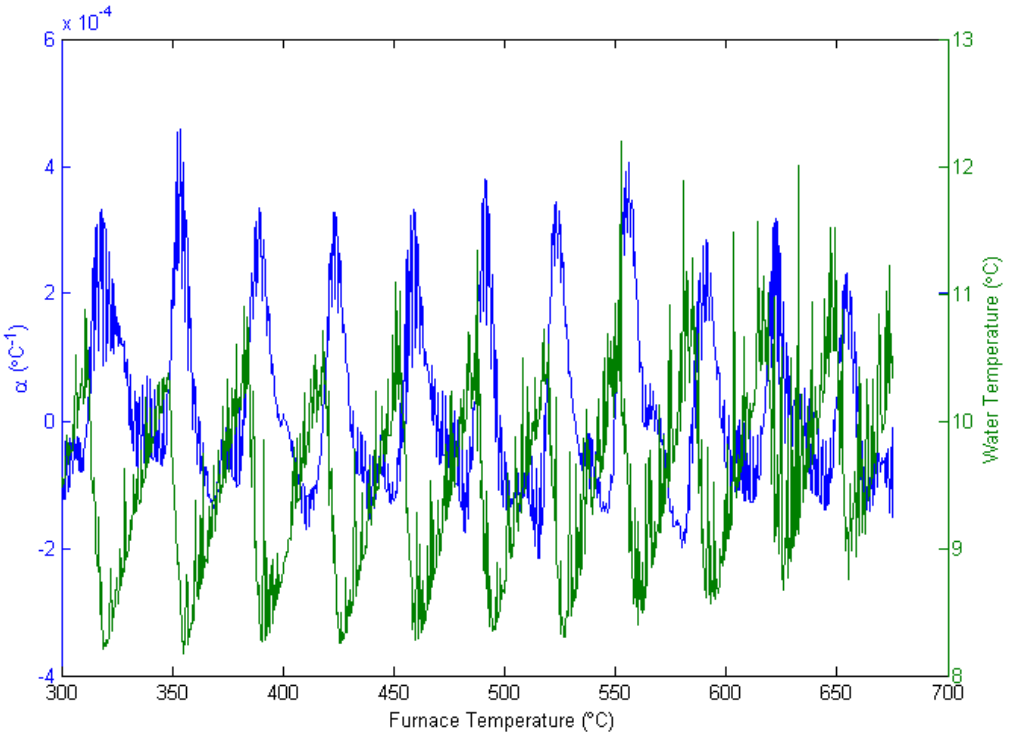

Figure 34. Thermal Expansion Measurement for Mo from 300 to 675°C

4.5.2 Sintering Curves for UO_2-BeO Pellets

The LVDT setup was used to quantify the sintering behavior of UO_2-BeO at low BeO volume fractions (2.5, 5, 7.5, and 10 vol. %). Each sample was sintered under the same conditions and temperature profile as the standard shown in Figure 35.

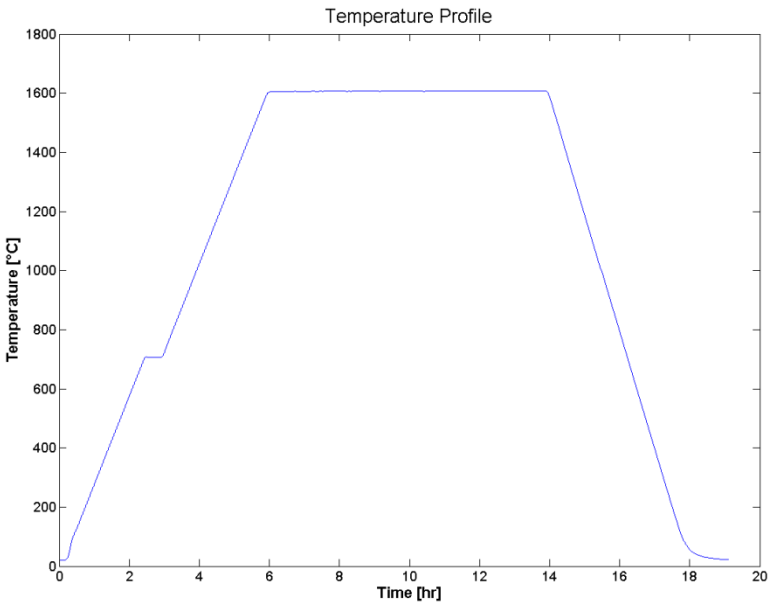

Figure 35. Furnace Temperature Profile Used to Sinter Samples

From the LVDT data and the background correction from the standard, the sintering strain rates were calculated and plotted against time (Figure 36).

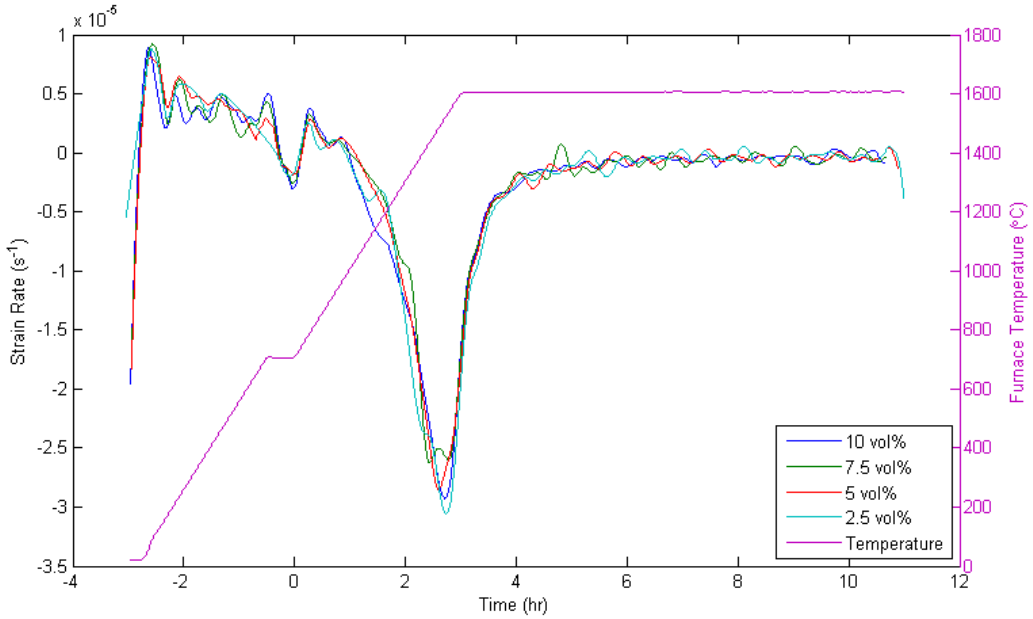

Figure 36. Sintering Strain Rate and Temperature Vs Time

The strain and strain rate were also plotted versus temperature as shown if Figure 37 and Figure 38 respectively. In these figures, it is evident that sintering begins between 800 and 1000°C. The peak negative strain rates were found by looking at the local minimum and can be seen in Table 7.

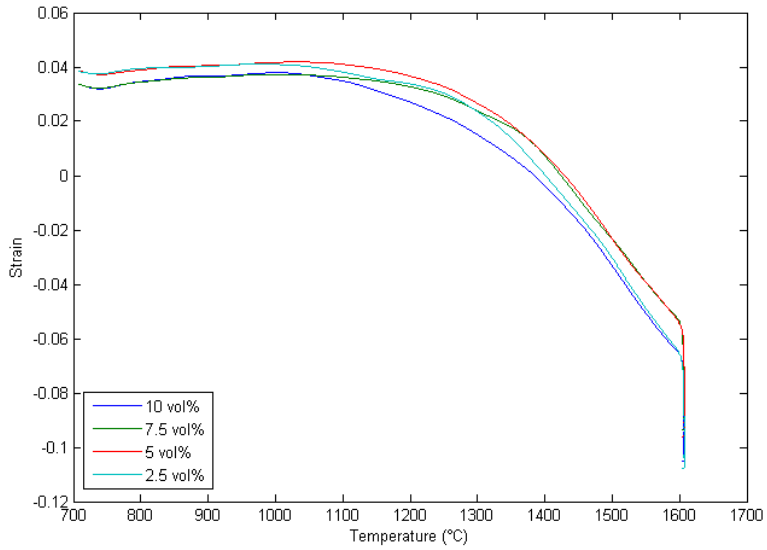

Figure 37. Sintering Strain Vs Temperature for UO_2-xBeO Pellets (x=2.5, 5.0, 7.5, 10)

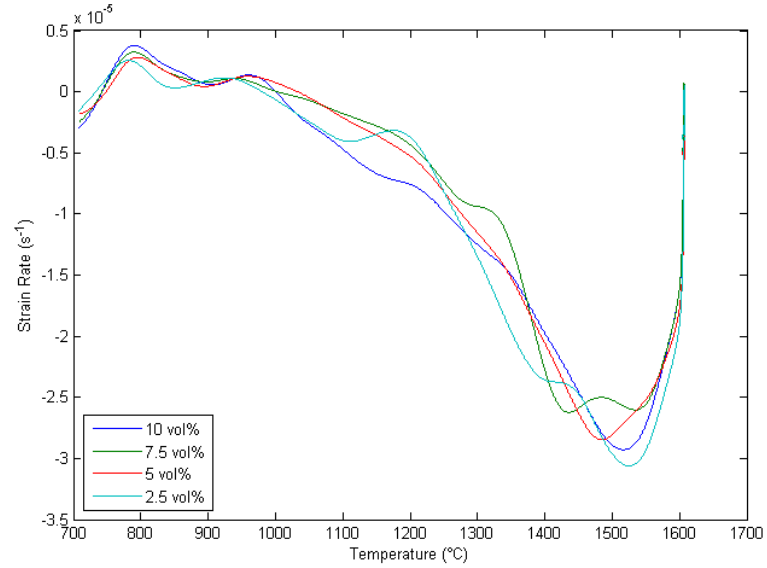

Figure 38. Sintering Strain Rate Vs Temperature for UO_2-xBeO Pellets (x=2.5, 5.0, 7.5, 10)

Table 7. Peak Strain Rates and Their Respective Temperatures

BeO Volume Fraction	*Peak Strain Rate* ($s^{-1} \times -10^{6}$)	*Temperature at Peak Rate* (°C)
10%	29.3	1518
7.5%	26.3	1436
5%	28.5	1486
2.5%	30.6	1525

From this data, the changes in relative density were calculated by using the final density of each pellet as the final density on the curve the densities on the other points with eq.(21) from Section 3.4. This equation uses the assumption that the pellets shrink isotropicaly though as seen in Section 4.4 the pellets don't shrink in a perfectly isotropic manner. Therefore, this estimation is not precise, but it does illustrate the dynamics of the pellet sintering process. These estimated densities were then plotted against temperature, Figure 39.

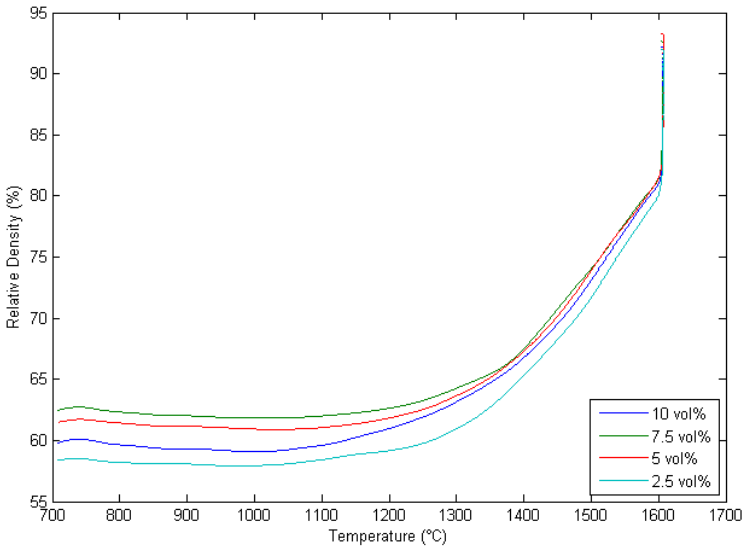

Figure 39. Relative Density Vs Furnace Temperature

Finally, the data may be represented as in Figure 32 to show how the pellets densify with time and temperature. Clearly sintering begins and has a maximum rate during the temperature ramp to the soak temperature but continues for several hours. The majority of the densification happens before the sintering temperature is achieved, but the long hold time is needed to achieve the higher densities desired for this process.

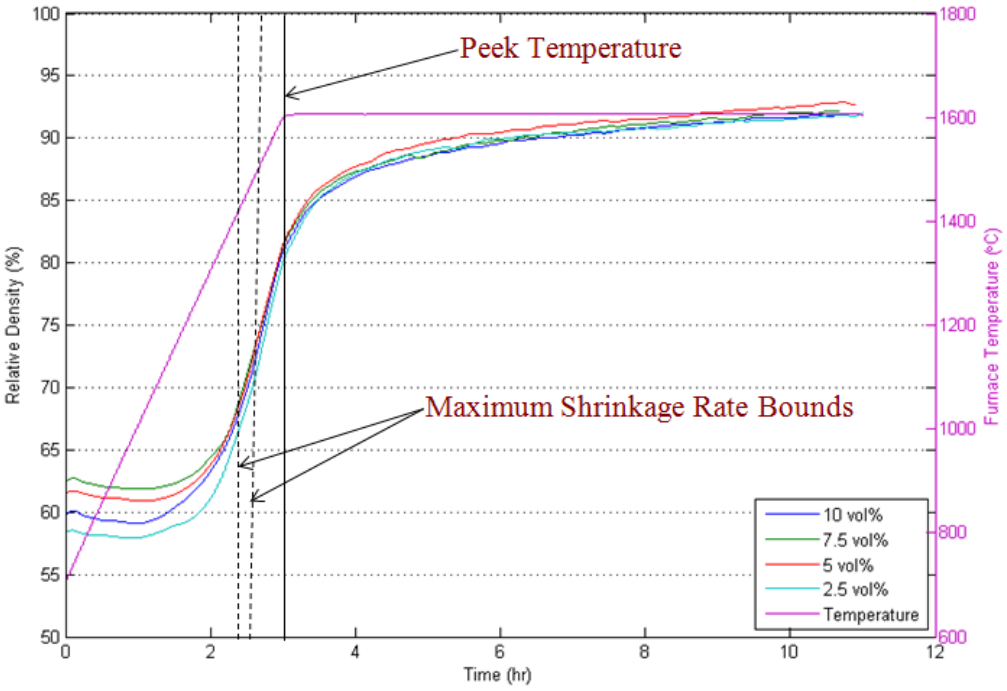

Figure 40. Pellets Densification and Temperature Profile Vs Time

4.6 Sintered Surface and Microstructure Analysis

4.6.1 Image Analysis

Image analysis was used to validate the volume fraction of BeO in the sintered pellets and to ensure the samples had the desired structure. The first step was to

determine the best method for viewing the BeO since the low atomic number of beryllium makes it challenging to observe in an electron microprobe. One method used was the creation of x-ray maps using the K-α peeks for Be in BeO and oxygen and M-α peeks for uranium. Figure 41 shows an example of a resulting x-ray map where it is evident that the backscattered electron (BSE) image gives a good representation for UO_2 as well does the uranium image. The BeO is most distinguishable when looking at oxygen, yet difficult to visualize with the beryllium K-α map, this is mostly due to the beryllium K-α's being shielded by the window protecting the detector. From the BSE image it was also difficult to determine the difference between a crack in the pellet and BeO phase.

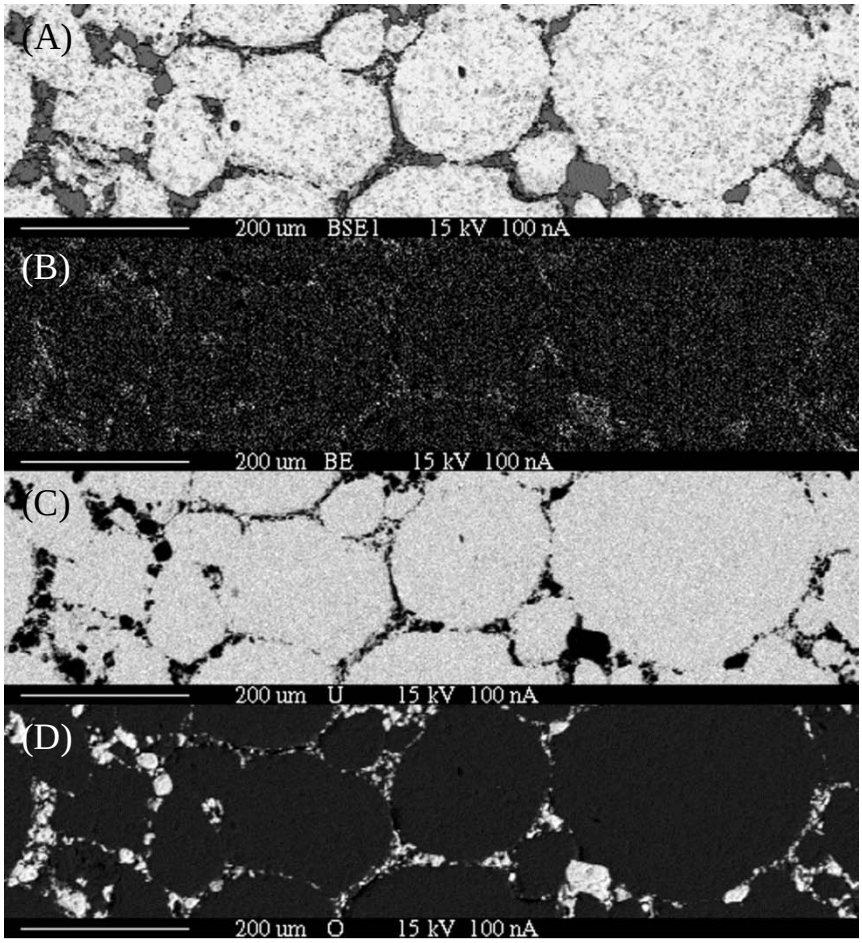

Figure 41. X-Ray Map of UO_2-10v%BeO (A) BSE, (B) Be, (C) U, (D) O

Even though an adequate impression of the morphology was available from the X-ray maps, cathodaluminescence (CATH) was determined to be far superior for imaging the BeO phases in the pellets. With this method, the BeO phase is clearly illuminated and the UO_2 is completely inactive, or black, in the image (Figure 42). This method has a couple advantages over the x-ray map. First, less time is required to acquire the image, enabling the collection of many more images in the same amount of

time. Another advantage is the sensor for the BSE and PM tube are oriented in the same direction so there is no displacement in the position of each image.

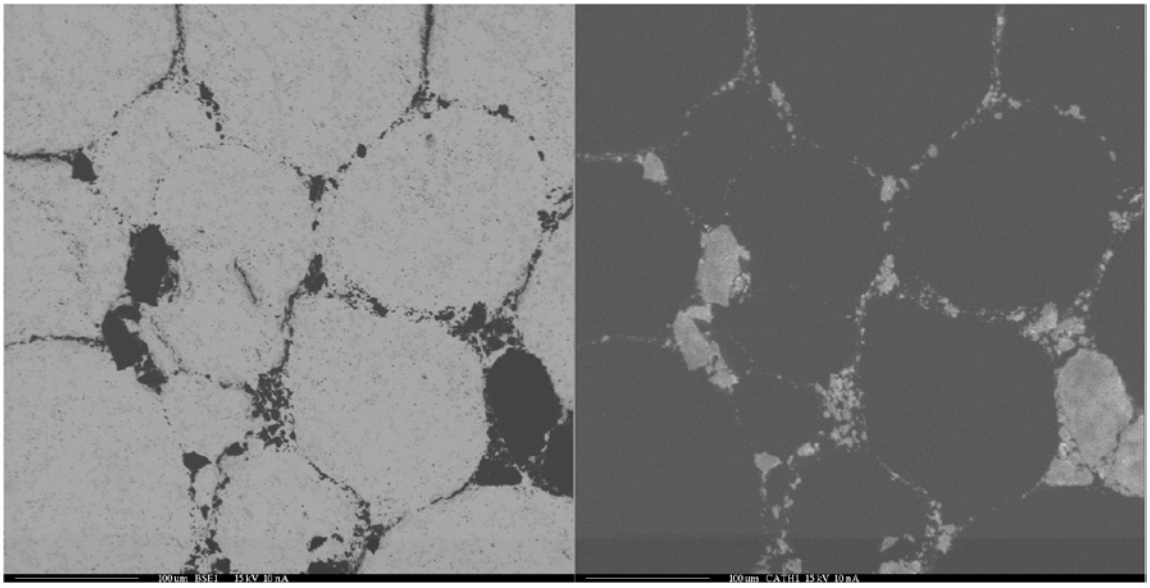

Figure 42. Comparing BSE (right) to CATH (left) Imaging of UO_2-10v%BeO

There were some limitations to using CATH to evaluate the volume fraction of BeO. The predominant limitation of CATH is that the corners of the edges are not as bright. So BeO can be in those areas when setting the imaging threshold, as can be seen in Figure 43. Another limitation arose when analyzing the samples with the Al_2O_3 contamination, since the Al_2O_3 created streaks in the image. This made resolving the BeO difficult for samples with Al_2O_3.

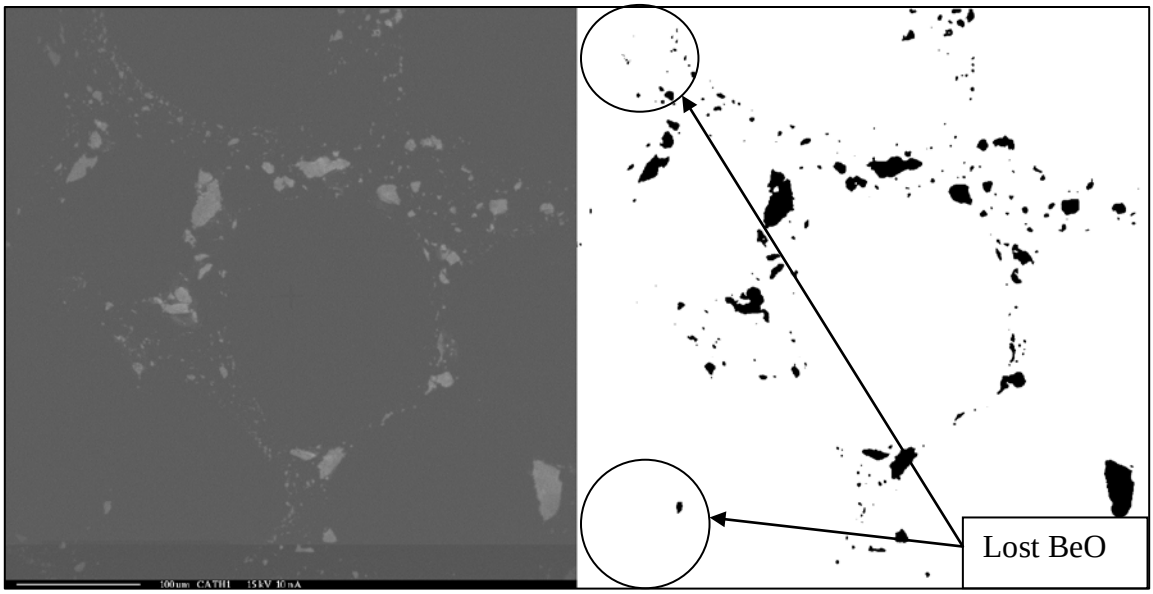

Figure 43. Lost BeO in Processed CATH Image for Image Analysis

It was important to evaluate how many images are required to get good statistical data for the volume fraction. This was done by looking at two samples with 10% volume fraction of BeO, and each with a minimum of 35 images. The area fraction for each image was measured and arranged in a random order with 1000 different permutations. The median was found as a function of number of sample points for each permutation. The derivative of this median with respect to the number of sample points was then, Figure 44. These plots show that the minimum number of samples to be used to solve for the volume fraction of BeO in the UO_2 is between 20 and 25. Figure 44 also demonstrates the high heterogeneity of the UO_2-BeO samples with the strong variations of BeO's volume fraction from area to area.

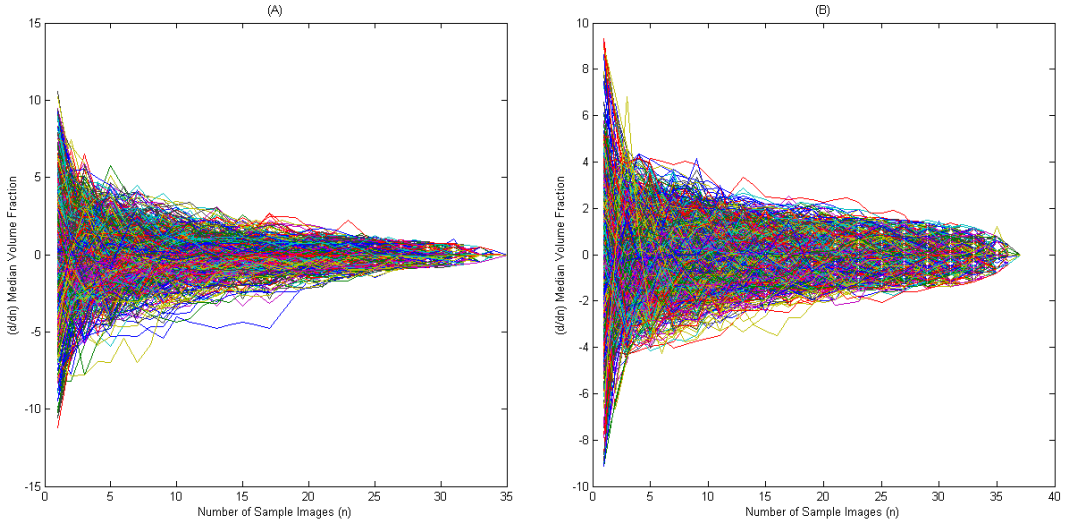

Figure 44. Change in the Median Volume with Respect to the Number of Data Points

The each permutation was then given a one-sample t-test as a function of number of samples. The p- values from the t-test were averaged at each sample number in order to see if the minimum of 20 points would be acceptable. From Figure 45 it is clear that 20 is more than enough for a good estimate of the volume fraction.

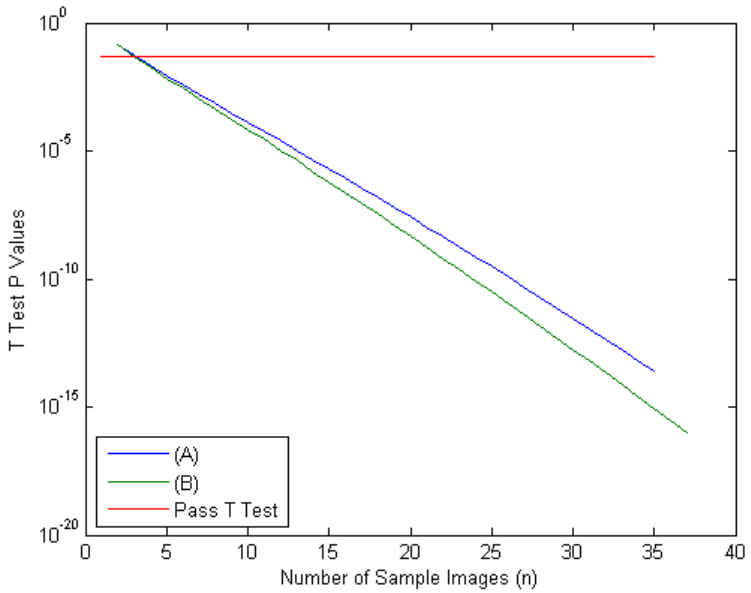

Figure 45. Average P-Values for Volume Fraction Measurment Againts the Number of Data Points

4.6.2 UO_2-BeO Interface and Porosity

Two to five high magnification images were taken near the UO_2-BeO interface in order to determine if the BeO filled the space and if there were any cracking near the interface for sample set 07, 08, 09, and 10. Figure 46 shows a secondary electron (SE) image of the interface at 1000X (left) and 3000X (right). It is evident the interface is not continuous at all points on the surface plane, and at other spots the interface appears torn apart. It is also apparent that there are more small pores in the UO_2 phase than the BeO phase. But while the BeO phase has fewer pores, the pores are larger than the ones observed in UO_2.

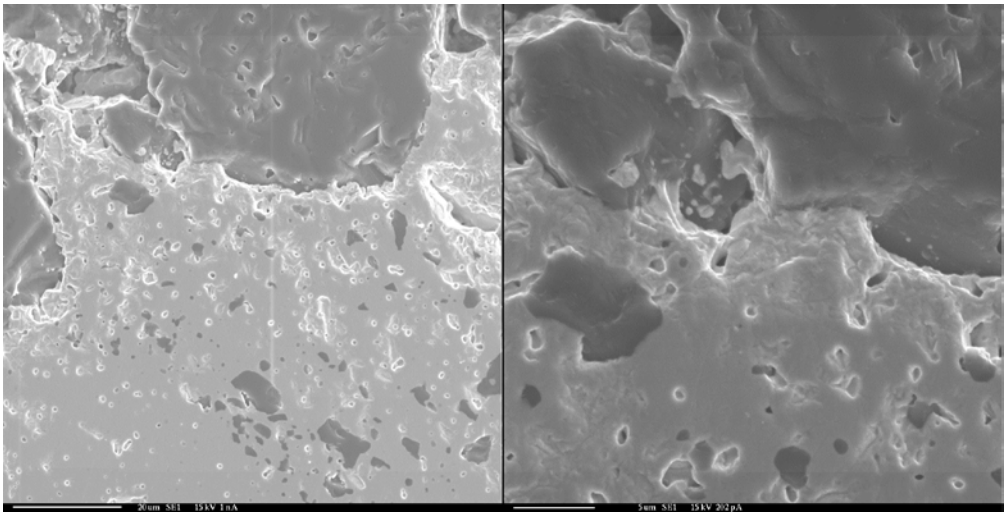

Figure 46. SE Image of UO_2-BeO Interface

The cracks at the UO_2-BeO interface do not appear to be exclusive to the UO_2-BeO interface. Similar cracks are also seen at the point of contact where two large UO_2 agglomerates have sintered together, Figure 47; The CATH image in Fig. 39b reveals the negligible presence of BeO in the crack.

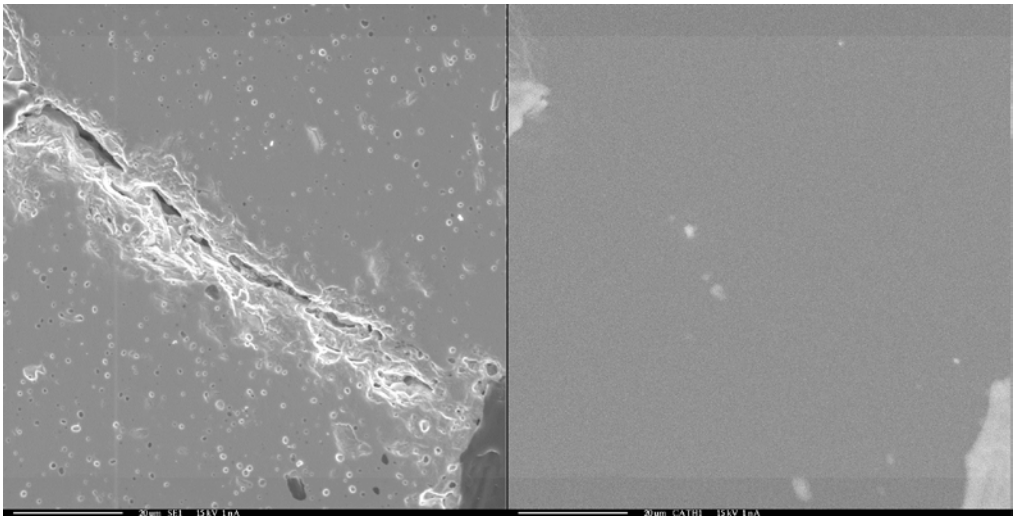

Figure 47. Crack within UO_2 Phase

These cracks at the UO_2-UO_2 interface may also be observed at lower magnification when combining the binary BSE and CATH images, as in Figure 48 (blue:UO_2, magenta:BeO). This image was taken of a 2.5v%BeO sample to minimize any influence from the BeO. This is not predominantly seen throughout the samples but is frequent enough to make a note of.

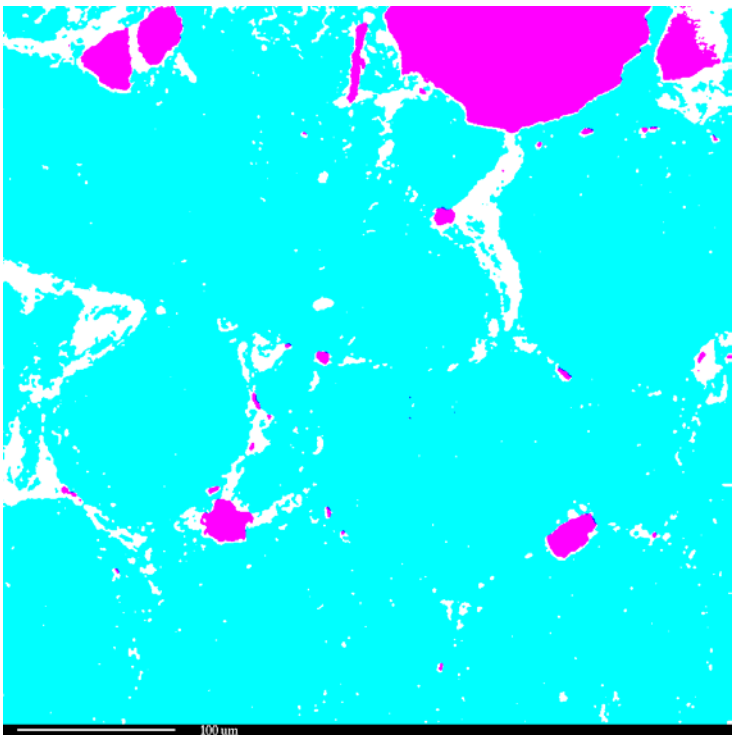

Figure 48. Cracks Not Near UO_2-BeO Interface

4.6.3 Pellets with Various BeO Particle Size

During the course of the initial experiments, four different forms of BeO powder were used for pellet preparation: (1) BeO less than 150µm, (2) raw BeO sieved with 325 mesh, and (3,4) two different sets of jet milled BeO powder. For all pellets discussed in this section, the BeO content was set at 10 vol. %. It was important to determine how

the different powder source materials impacted the microstructure of the UO_2-BeO samples. These structures were observed with both optical and electron microscopy.

The as received BeO powder produced low density pellets (85%TD). In optical microscope images, it is observed that the BeO is scattered and does not from a continuous matrix over the entire surface. Figure 49 shows the two extremes of the structure, where on the right image a BeO matrix is forming (near the center of the sample), on the right image the BeO is more dispersed. The BeO that is dispersed over the surface also appears large in size. An optical scan of the surface was taken were the structure and cracking throughout the sample can be seen, Figure 50.

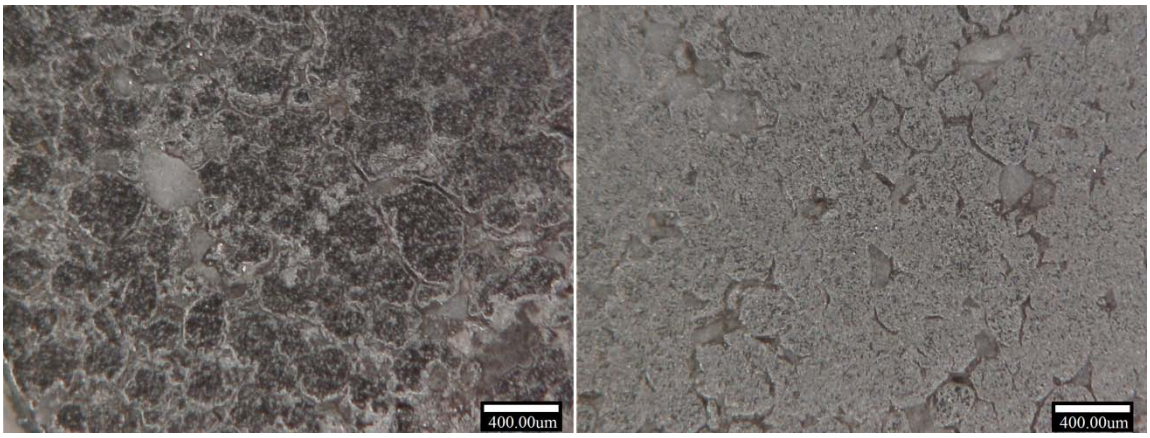

Figure 49. Optical Images of UO_2-10v%Raw BeO

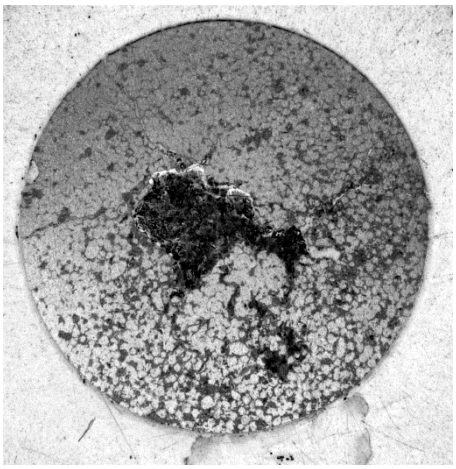

Figure 50. Optical Scan of Sectioned UO_2-10v% Raw BeO with Large Crack in the Center, 11.6mm Diameter

When this sample was examined using backscatter electron microscopy, the large heterogeneity observed optically was also observed, Figure 51.

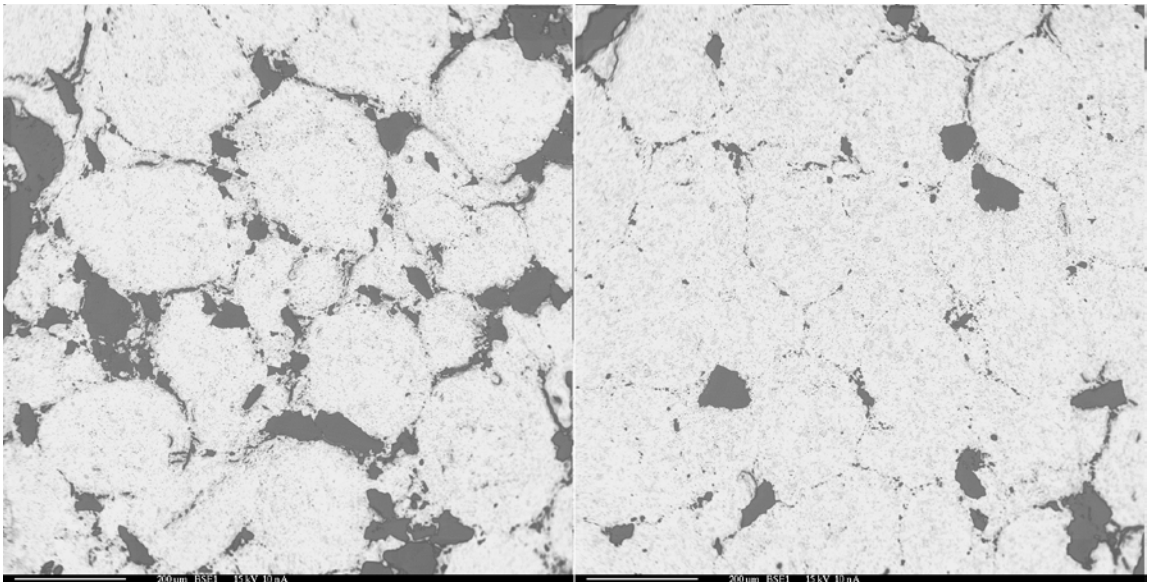

Figure 51. BSE of UO_2-10v%Raw BeO

The pellets prepared using jet-milled BeO powder were prepared with two sets of BeO powder milled at separate times. Both gave similar structures, as can be seen from their optical scans in Figure 52. They both exhibited a large internal crack which could have been cause from the use of the trapezoidal split sleeve die. The BSE images also showed a more desirable structure than the sample that used the raw BeO powder with a more apparent continuous matrix, Figure 53.

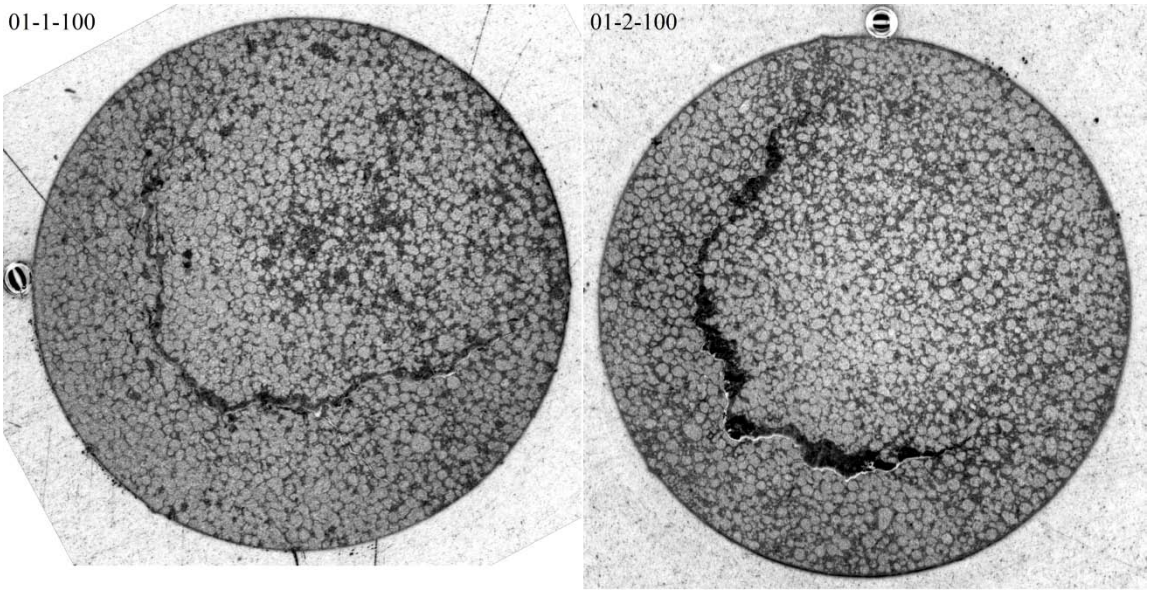

Figure 52. Optical Scan of UO_2-10v% Jet-Milled BeO

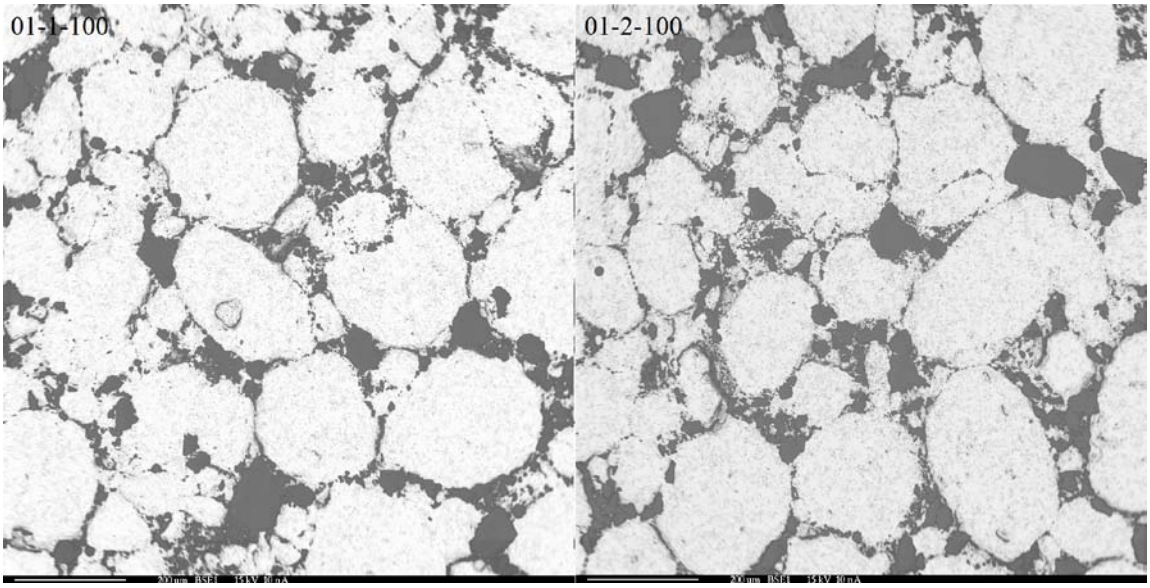

Figure 53. BSE of UO_2-10v% Jet-Milled BeO

The last BeO powder tested was raw powder that was sieved through a 325 mesh. This powder appeared to create the best continuous matrix out of all the other BeO powder sizes. This can be seen in the optical images, Figure 54, as well as the BSE images, Figure 55. Figure 55 even shows the size most of large UO_2 spheres to be roughly 50 to 200µm and even a few larger than 300µm.

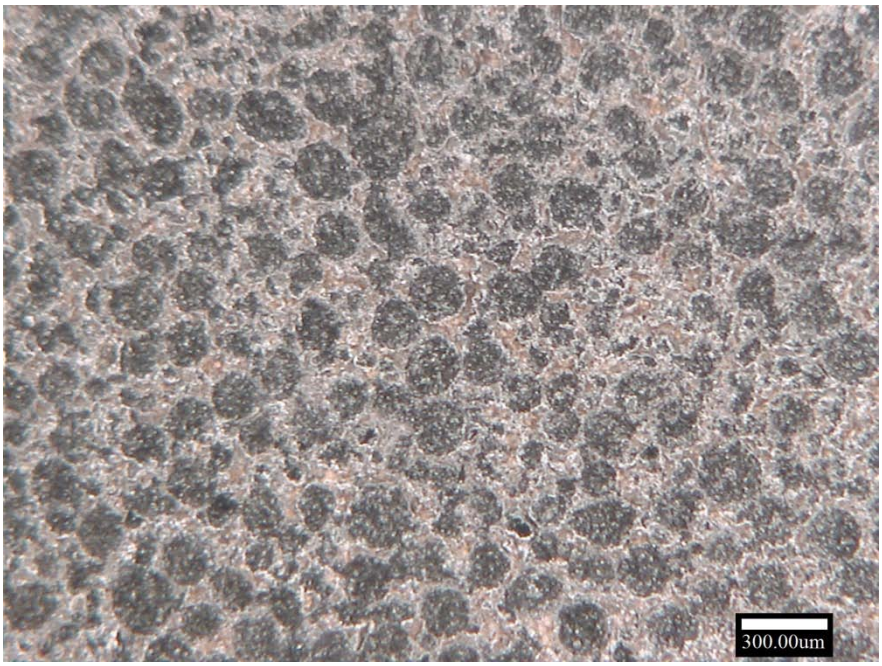

Figure 54. Optical Image of UO_2-10v% Sieved BeO

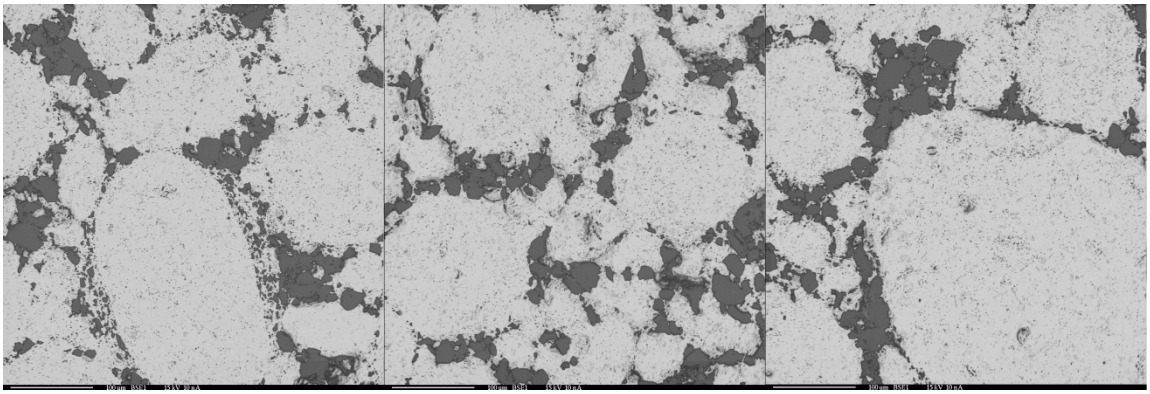

Figure 55. BSE of UO_2-10v% Sieved BeO

4.6.4 Pellets with Various BeO Volume Fractions

Once the parametric studies (Sections 4.4) established the optimal processing parameter (Section 3.5), a sequence of pellets was prepared with varying BeO compositions. The pellet volume fractions were measured using CATH images to compare to the target values. This was done for BeO volume fractions 10v%, 7.5v%, 5v%, and 2.5v%, and these samples used the jet-milled BeO powder. A total of 64 CATH images at 500X were collected for each pellet. Figure 56 shows a representative CATH images of each composition. It is evident that the BeO matrix becomes less visibly coherent below 5v%BeO. Several large BeO features are present in all images indicating that further process improvements can be made.

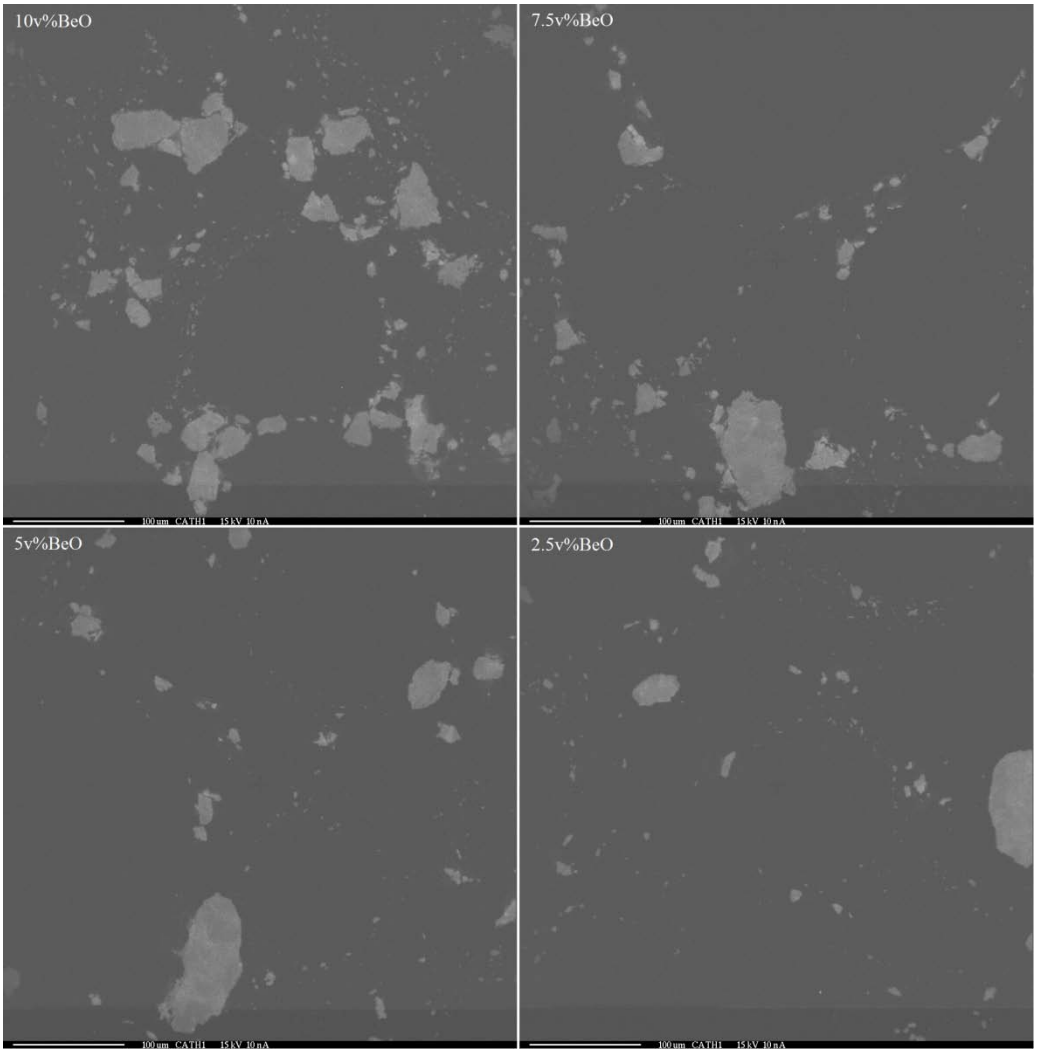

Figure 56. CATH of 10, 7.5, 5, and 2.5v%BeO

The overall BeO particle size ditributions are provided in Figure 57. It is evident that there is much variation throughout the surface of one sample. The distribution also appears narrower with smaller BeO volume fractions. It is noteworthy that while the large partiles dominate the image area, their relative population is small.

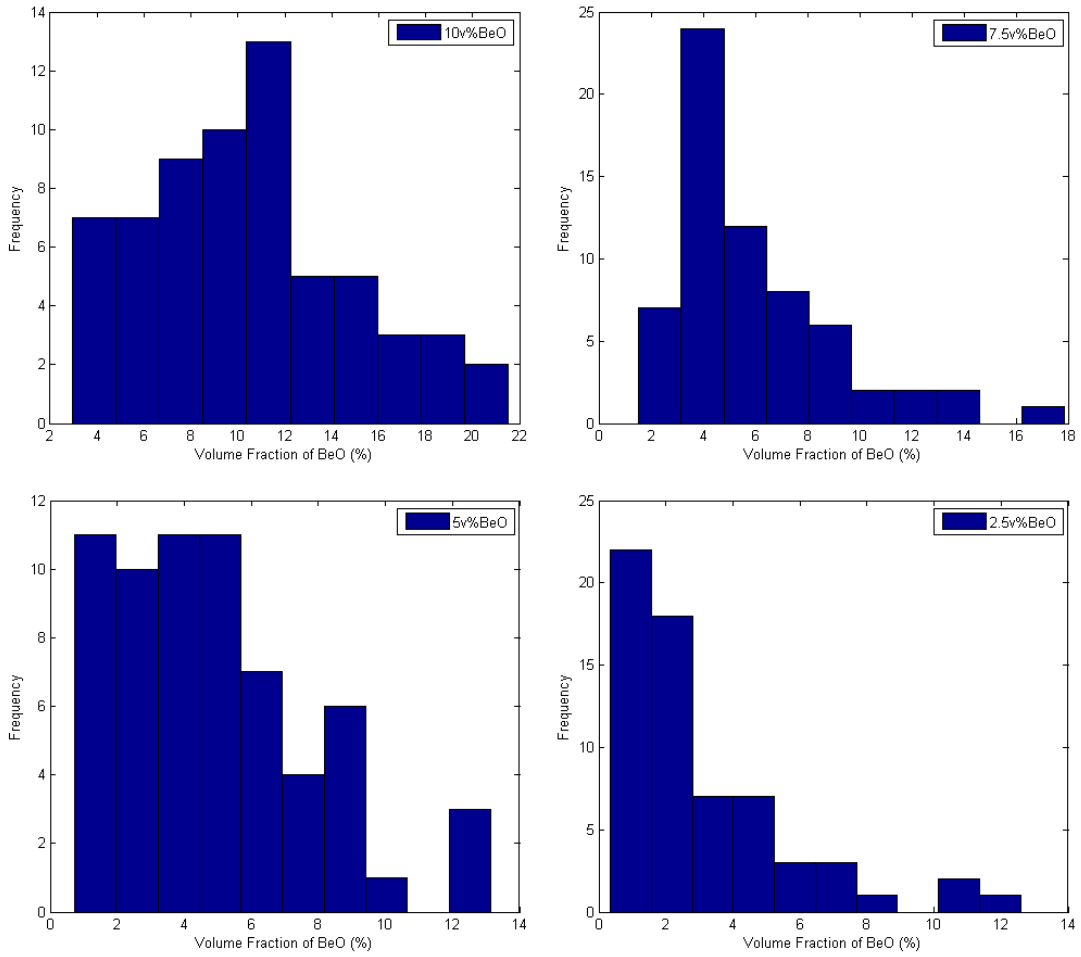

Figure 57. Distribution of Volume Fraction in a Sample

The final result of this exercise is presented in Table 8 where the resulting mean values for the pellet BeO volume fractions as well as their two tail p values from their respective one sample t-test. The mean volume fractions are not significantly different from the expected values for the pellets prepared to be 2.5, 5.0, and 10.0 vol.% BeO. However, the mean volume fraction for the 7.5v%BeO pellet was measured to be far lower than planned at 6.0 vol.% BeO.

Table 8. Measured Volume Fraction of BeO

Expected Volume Fraction	*Mean Volume Fraction*	*Standard Error*	*P value*
10	10.3	0.55	0.5453
7.5	6.0	0.40	0.0175
5.0	4.9	0.37	0.7569
2.5	3.0	0.33	0.109

4.6.5 Pellets with Alumina Contamination

For the pellets prepared with a minor quantity of alumina image analysis was attempted for two volume fractions of alumina, 0.77v% and 1.41v%. Figure 58 shows the BSE and CATH of the 0.77v%Al_2O_3. With the BSE image, it is difficult to determine the difference between BeO and Al_2O_3, but the difference is much clearer using CATH. The Al_2O_3 however does generate streaks in the CATH since alumina is much more luminescent and distort the image. There was not a noticeable difference in the structure with and without alumina, and the Al_2O_3 remained with the BeO. Quantitative image analysis was therefore not possible.

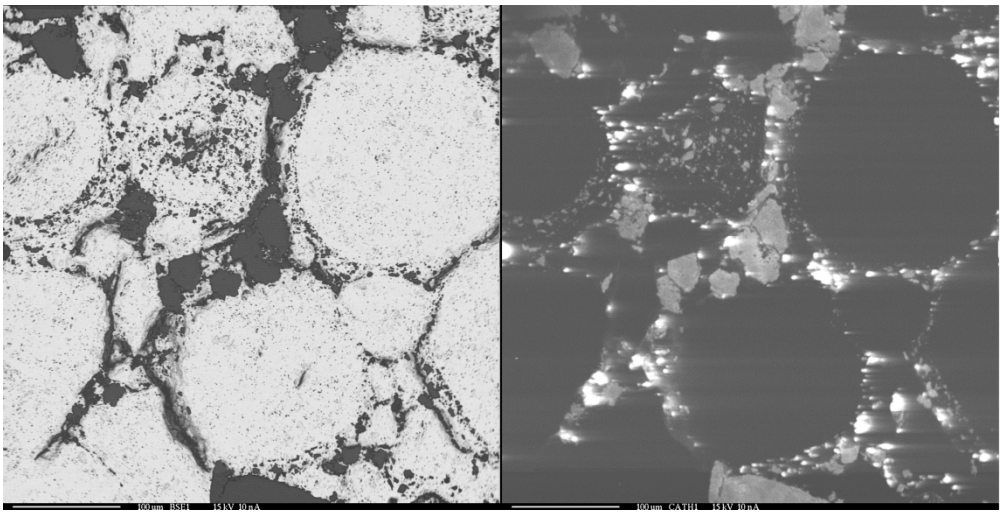

Figure 58. BSE and CATH of UO_2-BeO with 0.77v%Al_2O_3

Figure 59 shows a closer view of the Al_2O_3 in the 0.77v%, and the alumina does not appear to have interacted with the BeO or UO_2. At this magnification the difference between BeO and Al_2O_3 is a little clearer with BeO being slightly darker then Al_2O_3.

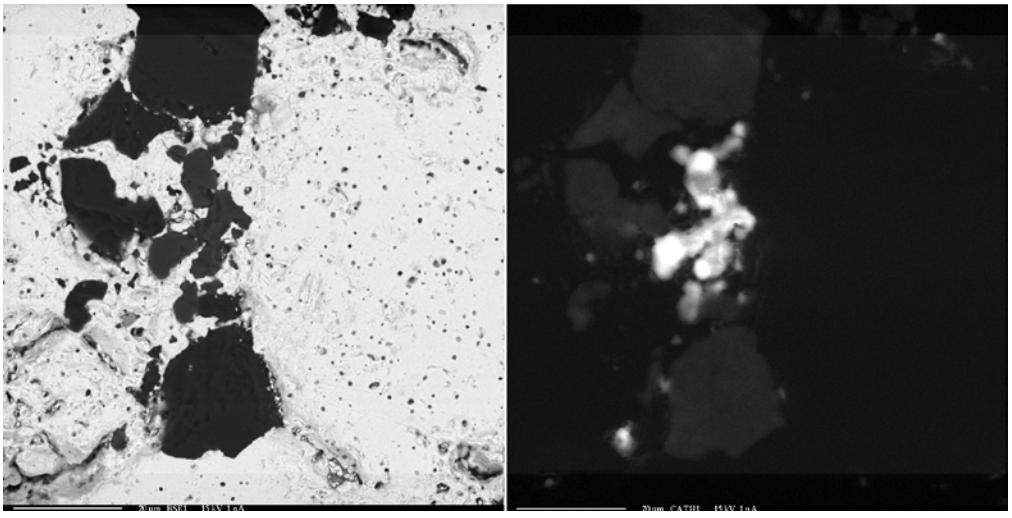

Figure 59. High Magnification of UO_2-BeO with 0.77v%Al_2O_3

The two different alumina contamination fractions were then compared in Figure 60. The structure did not seem to change with the two Al_2O_3 fractions. The major difference found from the two different contamination fractions were that the Al_2O_3 would sometimes for larger groups at larger volume fractions.

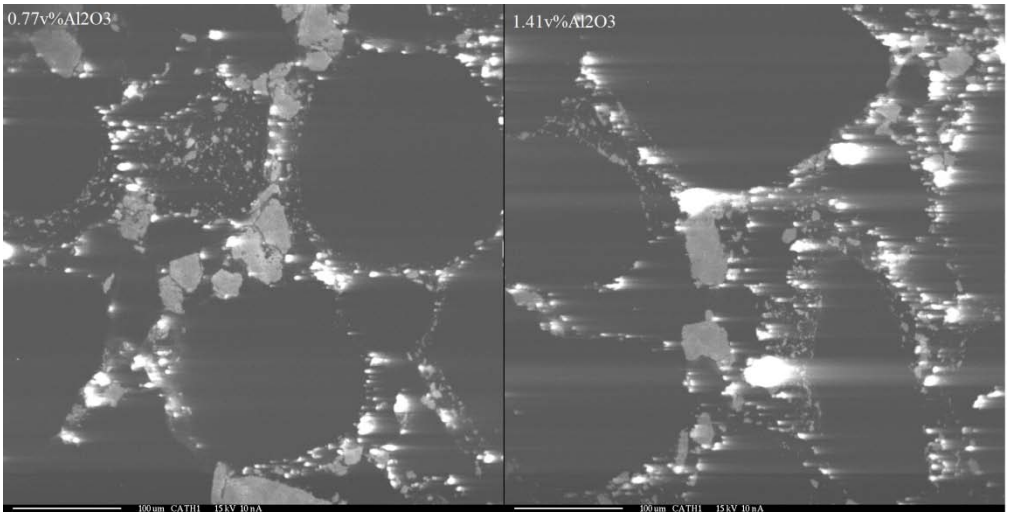

Figure 60. Different Contamination Fraction in UO_2-10v%BeO

4.7 Thermal Analysis of UO_2-BeO Pellets

The thermal diffusivities and densities of pellets were measured using the procedures outlined in Sections 3.6 and 3.7 and the raw data are compiled and presented in Appendix E. The series of pellets with 10 vol% BeO were evaluated to determine the impact of the LFA sample thickness (02-2-100A, 02-2-100C, 03-2-100, 03-2-100A, 03-2-100B, 03-2-100C, 06-1-100, and 07-1-100). The densities and diffusivities can be found in Appendix D and E respectively. In Figure 61, it is evident that thicker samples give higher values of thermal diffusivity than thinner samples. Pellets that are sectioned

to be 2mm thick and smaller seem to cluster together with large variation between samples.

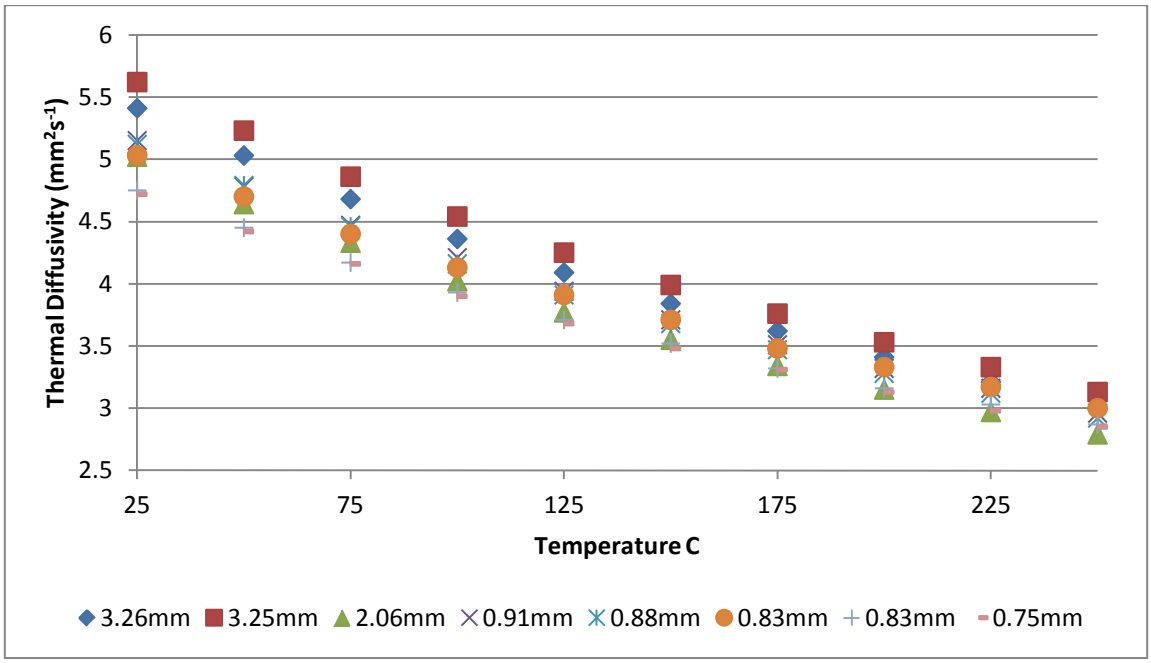

Figure 61. Effects of Sample Thickness on Thermal Diffusivity Measurements

The thermal diffusivities where then measured for samples of various BeO concentrations, as shown if Figure 62. As expected, the addition of BeO is shown to improve the diffusivity of the samples compared to UO_2 (02-1-00B), with the diffusivity almost doubled for 10vol% BeO samples (03-2-100 and 06-1-100).

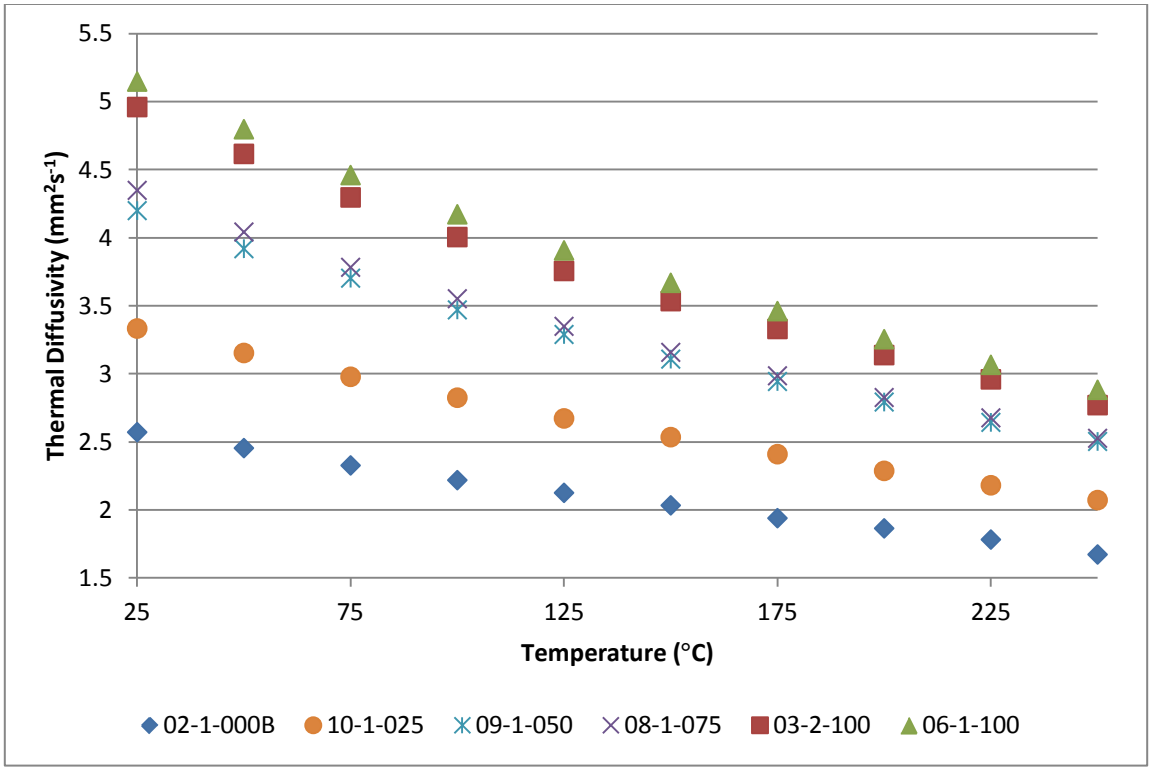

Figure 62. Thermal Diffusivity of UO_2-BeO Pellets of Different BeO Concentrations

The alumina bearing samples were measured to determine the effects of Al_2O_3 contamination. Fig shows that up to 1.41v%Al_2O_3 there are negligible effects from the contamination, after which the conductivity begins to drop. It also appears that the conductivity may slightly improve with less than 1.00v%Al_2O_3 contamination.

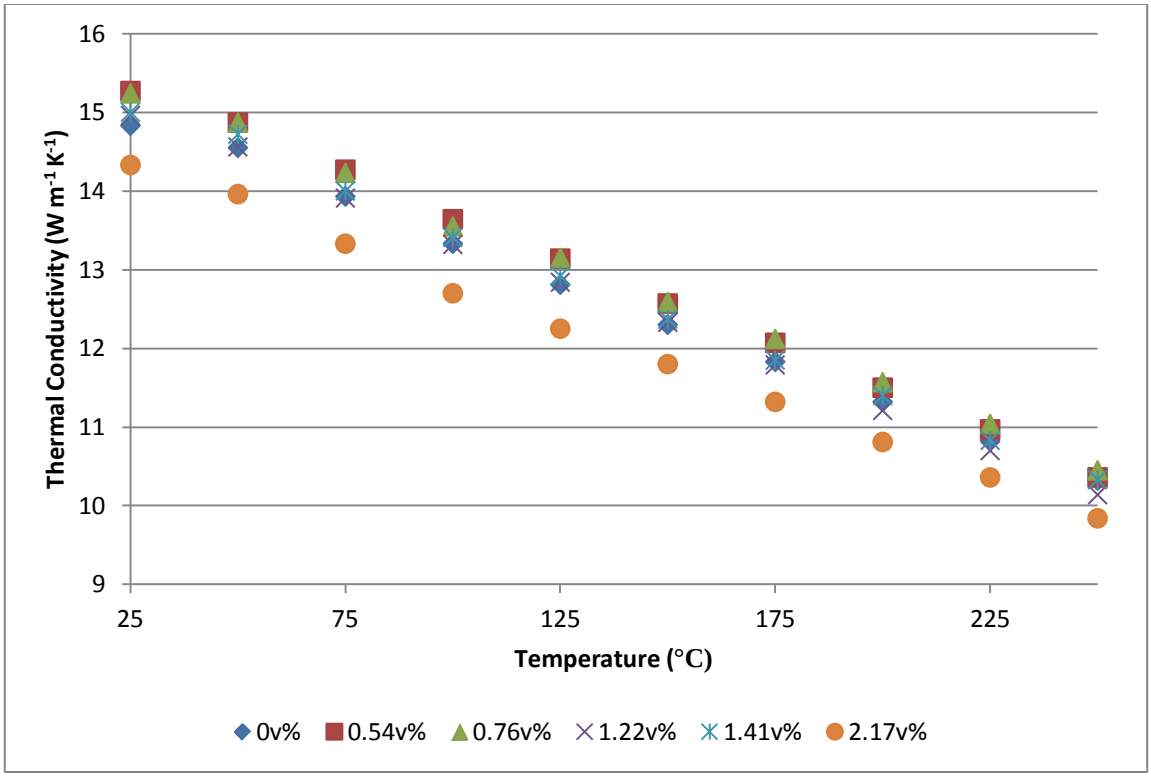

Figure 63. Effect of Contamination on Conductivity Measurements

This was repeated except with the addition of 0.5v%Al_2O_3 contamination. The results again showed negligible variation from samples without contamination, with the exception of 7.5v%BeO. The sample with contamination was significantly higher for that sample as seen in Figure 64.

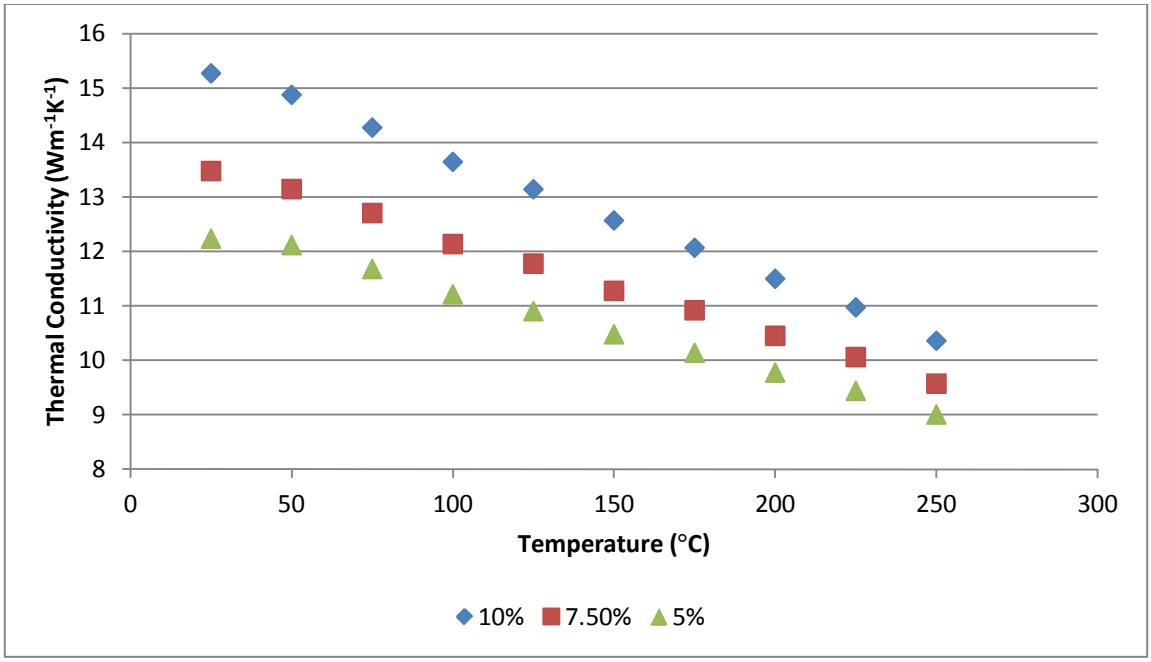

Figure 64. Thermal Conductivity for Various BeO Volume Fractions with Al_2O_3 Contamination

5. DISCUSSION

As reported in Chapter 4, processing methods were established for UO_2-BeO pellet fabrication based on the prior work of Solomon, et al. [12, 13] Parametric studies on compaction pressure (Section 4.3) and sintering temperature (Section 4.4) were performed and the results were used to refine the pellet preparation methodology. Once the methods were established, pellets were prepared with 2.5, 5.0, 7.5, and 10.0 vol. % BeO to measure the variation in thermal diffusivity. The following discussion considers the outcomes reported in Chapter 4 to develop understanding that contributes to the continued fuel development for UO_2-BeO. Section 5.1 presents the conversion of the reported thermal diffusivity data into a thermal conductivity estimate that demonstrates notable increases over raw UO_2. Section 5.2 presents a discussion regarding the improved processing methodology.

5.1 Thermal Conductivity Analysis of UO_2-BeO

The thermal diffusivities and densities of pellets were measured using the procedures outlined in Sections 3.6 and 3.7 and the raw data are compiled and presented in Appendix E. These basic measurements were made to enable the estimation of the pellet thermal conductivities. In order to make that estimation, the specific heat for each composition was estimated using the rule of mixing and the estimate temperature dependent values of cp are presented in Figure 65. With the measured diffusivities and densities and the estimated cp, the thermal conductivities were calculated according to

eq.(26) (Section 3.7). The thermal conductivity was then normalized to a relative density of 95% according to the method outlined in Section 2.3. This normalization was necessary to make direct comparison to the literature correlations in Section 2.3.

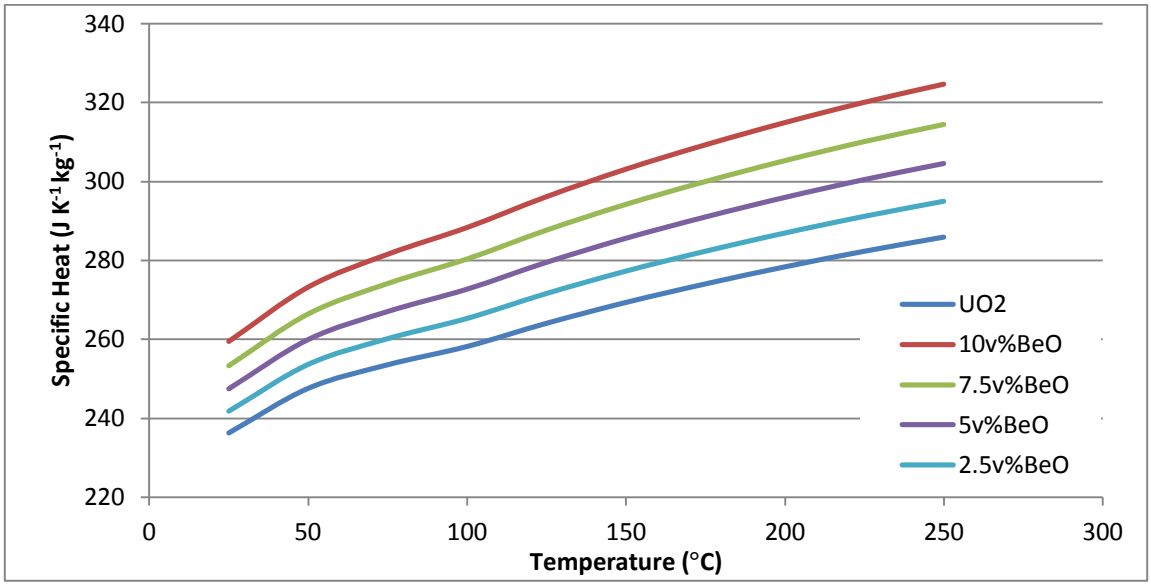

Figure 65. Calculated Specific Heat Vs Temperature for Different BeO Volume Fractions using the Rule of Mixing.

The next step was to evaluate how well the thermal conductivity is improved compared to UO_2. It was also compared to the bounds of the rule of mixing, FEM fitted curve to this fuel form, as well as value from Solomon et al [12, 13]. Figure 66 shows these comparisons as they are divided by the thermal conductivity of UO_2. This showed the conductivity is slightly more than twice that of UO_2 and at higher temperatures begins to follow the FEM fitting.

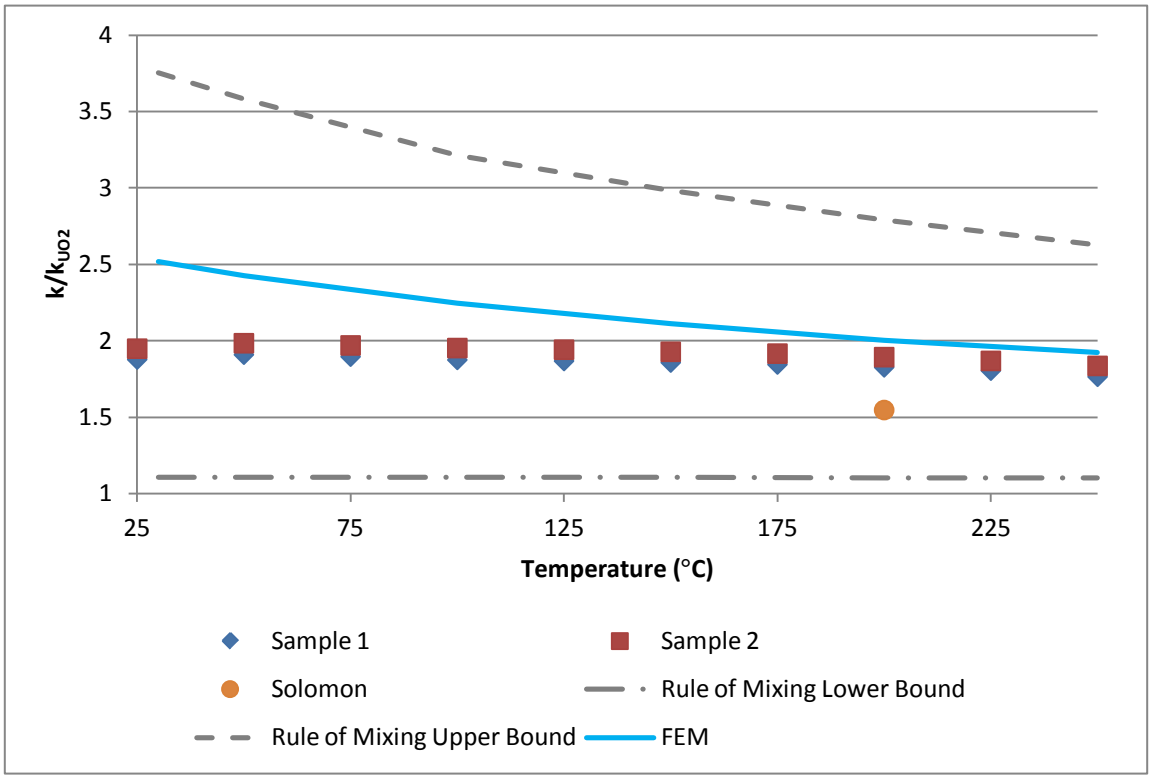

Figure 66. Comparison of Thermal Conductivity Improvement over UO_2

The thermal conductivity was then calculated for UO_2-xBeO of various compositions (x = 2.5, 5, 7.5 and 10v%), Figure 67. With each 2.5v%BeO added there was an approximate 24±2% (or 9.6±0.9% per volume fraction of BeO) improvement in the thermal conductivity compared to UO_2 over this temperature range, Figure 68. The low data at 7.5v%BeO can be attributed to the low volume fraction measured from the structure analysis of being closer to 6v%. This outlier is then understandable to have an average conductivity improvement of 60% if for every 1v%BeO corresponds to approximately 10% increase in thermal conductivity.

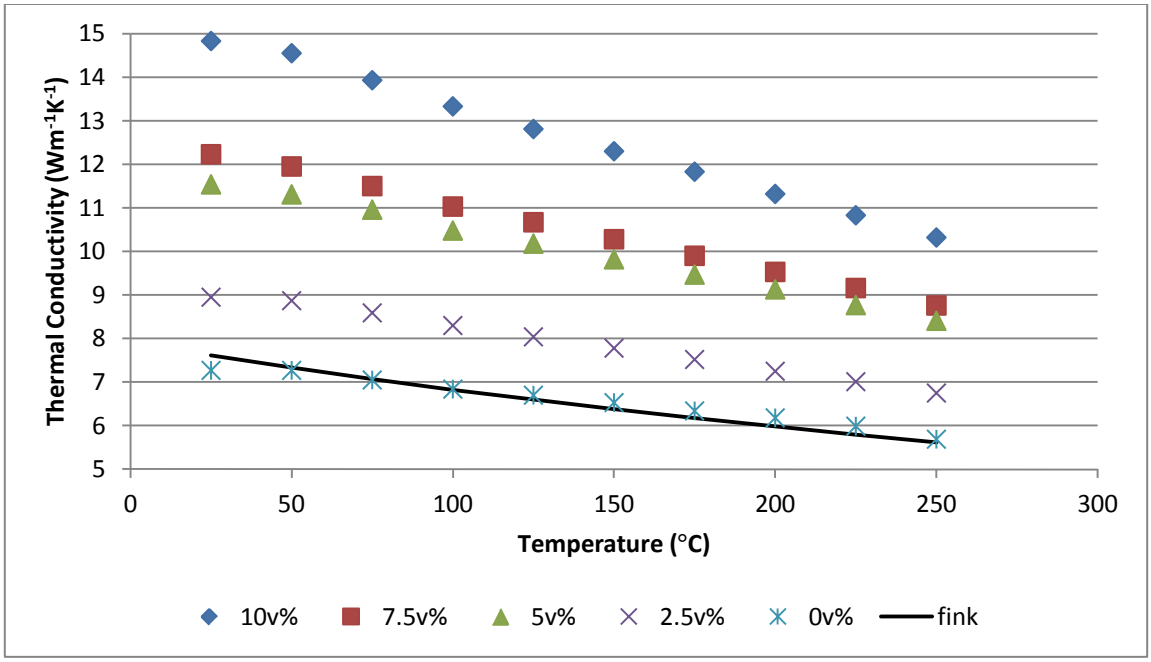

Figure 67. Thermal Conductivity for Various BeO Volume Fractions

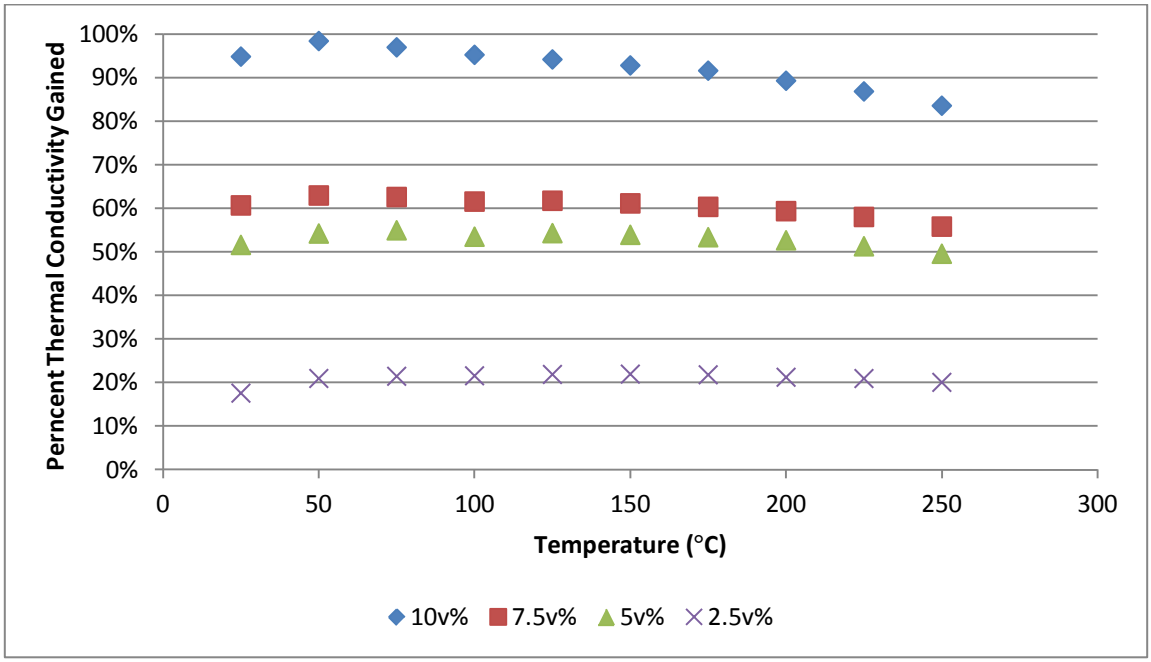

Figure 68. Percent Thermal conductivity Improvement with Various BeO Fractions

5.2 Improvements to Pellet Processing Methodology

5.2.1 Powder Characteristics

The uranium and beryllium oxide powders were characterized to understand how the composite pellets would sinter. The characteristics of interest were the oxygen to metal ratio, particle size, and specific surface area. As noted in Section 4.2 the uranium oxide was initially observed to be hyperstoichiometric ($UO_{2.29}$). The uranium oxide was ball milled from an initial size of less than 300µm to less than 10µm. The ball milling was successfully and reduced the powder size, but it was found that the time of milling should be limited to less than four hour. Longer milling durations resulted in the powder compacting on the walls of the jar in a thick layer. The BeO was then jet-milled to a smaller size from 150µm to less than 10µm The jet mill darkened the BeO, and when looked at under a microscope it was clear there was a small amount of an unknown contamination in the BeO powder after jet-milling, most likely from abrasion of the steel. A different BeO milling method, such high impact ball milling, should be considered.

5.2.2 Sintering and Processing Studies of UO_2-BeO

The sintering data in Chapter 4 revealed notable trends that were seen in the bulk measurements. The first was that all samples underwent moderately anisotropic shrinkage with average diameter to height shrinkage ratio of 1.15±0.07. This may be an

artifact of the high pre-compaction pressure, since it is known that pre-compaction pressures could induce anisotropic sintering for some systems [86].

The final compaction pressure had a strong influence on the final density of the sintered pellets. The pellets pressed with compaction pressures on the order of standard pressures used for UO_2 exhibited low densities and low shrinkage. It was also noted that pellets prepared using high final compaction pressures had circumferential cracks, which is a common indicator that the compaction pressure is too high.

It was also observer that with increasing BeO volume fractions, the densification and shrinkage was reduced. This could be due to the UO_2-BeO interface separating during sintering, and with increasing BeO fractions there are fewer UO_2-UO_2 interfaces resulting from the pre-compacted agglomerates touching prior to sintering.

5.2.3 UO_2-BeO Microstructure Analysis

The microstructure analysis showed that the structure of a continuous BeO matrix was not the same as that found in Solomon et al. [12, 13]. This could be due to mixing methods or coarsening effects during sinter from the long sintering times. Possible methods to achieve the correct structure could involve sieving out the fine powder from the large granules, which could be left out from the mixing or mix the fine UO_2 granules with the fine BeO powder. Another possible method is to have a tighter size distribution of the large UO_2 granules. This structure did have a large improvement to the thermal conductivity of UO_2, though the BeO phase does not appear completely continuous. This suggests some continuity of the BeO phase. The improvement over

Solomon et al. [12, 13] finding could be due to the large sizes of the BeO between the UO_2, since BeO's phonons have a large mean free path and there are less UO_2-BeO interfaces within the BeO phase. Ishimoto et al. [79] also had higher conductivity with the lamellate structure than Solomon et al. [12, 13] and had no UO_2 within the BeO phase.

6. CONCLUSION

It was the objective of this research to reproduce and improve on the prior work of Solomon et al. [12, 13] for UO_2-BeO composite was successfully met. The pelletization and sintering procedures were modified from this previous work with using a lower sintering temperature of 1600°C in place of 1700°C in order to conduct the dilatometer study (the alumina rod softens after 1600°C). An optimum final compaction pressure was found to be between 225 and 200MPa from a parametric study focusing on this pressure, Figure 28 pg.61. These procedures were able to achieve pellets with densities ranging from 9.17 to 9.38g/cm^3 (90.4% to 92.2%TD) for 10vol%BeO. With lower BeO volume fractions the densities did improve (Figure 32, pg.65).

The thermal conductivity of the UO_2-BeO composite was the primary focus of this study which was calculated and normalized to 95%TD for the temperature range of 25°C to 250°C. The thermal conductivity was found to be 14.5±1.0 $Wm^{-1}K^{-1}$ at room temperature for 10vol%BeO, which is a 90% improvement from UO_2. A Parametric study of different volume fractions (2.5, 5.0 7.5, and 10.0vol%BeO) were then used to determine their respective conductivity improvement. It was found that the average thermal conductivity improvement to UO_2 over the temperature range was found to be approximately 10% per additional volume fraction of BeO to the composite. These improvements did decrease with increasing temperatures and is expected to be much lower at higher temperatures.

From this work the following recommendations are made for the production and thermal testing of this composite:

- Lower final compaction pressure (200-225MPa)
- Further testing of pre-compaction pressure
- Tests different sintering temperatures and times effect on grain microstructure
- Thermal diffusivity measurement samples have a thickness of at least 3.25mm
- More thermal diffusivity measurement are needed

REFERENCES

[1] R.B. Holden, Ceramic Fuel Elements, Gordon and Breach, 1966.

[2] G.A. Slack, S. Austerman, Thermal Conductivity of BeO Single Crystals, Journal of Applied Physics, 42 (2003) 4713-4717.

[3] K.D. Reeve, K. Jones, Sintering Studies on Ceramic Fuel Materials, in: A.A.E. Commission (Ed.), Australian Nuclear Science and Technology Organisation, 1964.

[4] J. Fourcade, K. Sarma, S. Lee, A. Solomon, Enhanced Thermal Conductivity Oxide or ECO Fuels, Transactions of the American Nuclear Society, 92 (2005) 179-180.

[5] W. Manly, Utilization of BeO in Reactors, Journal of Nuclear Materials, 14 (1964) 3-18.

[6] E. Parma, R. Coats, J. Dahl, Sandia National Laboratories Medical Isotope Reactor Concept, Sandia Report 2010-1816, (2010).

[7] W.M. Stacey, Nuclear Reactor Physics, John Wiley & Sons, 2007.

[8] J.E. Turner, Atoms, Radiation, and Radiation Protection, John Wiley & Sons, 2008.

[9] D.E. Johnson, R. Mills, Irradiation Behavior of BeO-UO_2 Fuel as a Function of Fuel-Partical Size, General Atomic Division, General Dynamics Corporation, John Jay Hopkins Laboratory for Pure and Applied Science, 1963.

[10] R. Mills, J. Barner, D. Johnson, M. Simnad, Irradiation Effects on Dispersion Type BeO-UO_2 Fuels for EBOR, Journal of Nuclear Materials, 14 (1964) 482-486.

[11] G. Titus, J. Saling, High-Temperature Irradiation of UO_2-BeO Bodies, in, Aerojet-General Nucleonics, San Ramon, Calif.; Battelle Memorial Inst., Columbus, Ohio, 1963.

[12] A. Solomon, S. Revankar, J.K. McCoy, Enhanced Thermal Conductivity Oxide Fuels, in, Purdue University School of Nuclear Engineering, 2006.

[13] K. Sarma, J. Fourcade, S. Lee, A. Solomon, New Processing Methods to Produce silicon Carbide and Beryllium Oxide Inert Matrix and Enhanced Thermal Conductivity Oxide Fuels, Journal of nuclear materials, 352 (2006) 324-333.

[14] M. Lyons, R. Boyle, J. Davies, V. Hazel, T. Rowland, UO_2 Properties Affecting Performance, Nuclear engineering and design, 21 (1972) 167-199.

[15] D.R. Olander, Fundamental Aspects of Nuclear Reactor Fuel Elements: Solutions to Problems, in, California Univ., Berkeley (USA). Dept. of Nuclear Engineering, 1976.

[16] V. Tikare, E.A. Holm, Simulation of Grain Growth and Pore Migration in a Thermal Gradient, Journal of the American Ceramic Society, 81 (1998) 480-484.

[17] C. Walker, D. Staicu, M. Sheindlin, D. Papaioannou, W. Goll, F. Sontheimer, On the Thermal Conductivity of UO_2 Nuclear Fuel at a High Burn-Up of Around 100MWd/kgHM, Journal of nuclear materials, 350 (2006) 19-39.

[18] C. Baker, The Fission Gas Bubble Distribution in Uranium Dioxide from High Temperature Irradiated SGHWR Fuel Pins, Journal of Nuclear Materials, 66 (1977) 283-291.

[19] H. Stehle, Performance of Oxide Nuclear Fuel in Water-Cooled Power Reactors, Journal of Nuclear Materials, 153 (1988) 3-15.

[20] J.D. Lambert, R. Strain, Oxide Fuels, Materials Science and Technology.

[21] S. Kim, W. Ko, H. Kim, Y. Chung, S. Bang, S.T. Revankar, Economic Viability to BeO-UO_2 Fuel Burnup Extension, Nucl. Eng. Tech, 43 (2010) 141-148.

[22] Y.A. Kocherzhinskii, E. Shishkin, L. Yupko, Determination of the Phase-Transformation Temperature of Beryllium Oxide, Refractories and Industrial Ceramics, 10 (1969) 314-315.

[23] C. McNeilly, The Pseudo Ternary System BeO--UO_2--PuO_2, in, Battelle-Northwest, Richland, Wash. Pacific Northwest Lab., 1967.

[24] J.A. Khan, T.W. Knight, S.B. Pakala, W. Jiang, F. RUIXIAN, J.S. Tulenko, Enhanced Thermal Conductivity for LWR Fuel, Nuclear technology, 169 (2010) 61-72.

[25] J.A. Khan, S.B. Pakala, T.W. Knight, J.S. Tulenko, Enhanced Thermal Conductivity for LWR Fuel, TRANSACTIONS-AMERICAN NUCLEAR SOCIETY, 93 (2005) 469.

[26] R. Latta, S.T. Revankar, A.A. Solomon, Modeling and Measurement of Thermal Properties of Ceramic Composite Fuel for Light Water Reactors, Heat Transfer Engineering, 29 (2008) 357-365.

[27] W. Lippmann, J. Knorr, R. Nöring, M. Umbreit, Investigation of the Use of Ceramic Materials in Innovative Light Water Reactor–Fuel Rod Concepts, Nuclear engineering and design, 205 (2001) 13-22.

[28] G.A. Slack, Thermal Conductivity of Pure and Impure Silicon, Silicon Carbide, and Diamond, Journal of Applied Physics, 35 (2004) 3460-3466.

[29] A.A. Solomon, J. Fourcade, S.-G. Lee, K. Sarma, S. Revankar, R. Latta, The Polymer Impregnation and Pyrolysis Method for Producing Enhanced Conductivity LWR Fuels, in: Proceedings of the 2004 International Meeting on LWR Fuel Performance, Orlando, Florida, 2004, pp. 146-155.

[30] R. Verrall, M. Vlajic, V. Krstic, Silicon Carbide as an Inert-Matrix for a Thermal Reactor Fuel, Journal of Nuclear Materials, 274 (1999) 54-60.

[31] S. Yeo, E. Mckenna, R. Baney, G. Subhash, J. Tulenko, Enhanced Thermal Conductivity of Uranium Dioxide–Silicon Carbide Composite Fuel Pellets Prepared by Spark Plasma Sintering (SPS), Journal of Nuclear Materials, 433 (2013) 66-73.

[32] I. Kurina, V. Popov, V. Rumyantsev, Investigation of the Properties of Modified Uranium Dioxide, Atomic energy, 101 (2006) 802-808.

[33] A. Goodjohn, H. Stewart, The Use of BeO in Advanced Reactor Concepts, Journal of Nuclear Materials, 14 (1964) 19-28.

[34] K. McCoy, C. Mays, Enhanced Thermal Conductivity Oxide Nuclear Fuels by Co-Sintering with BeO: II. Fuel Performance and Neutronics, Journal of Nuclear Materials, 375 (2008) 157-167.

[35] D.A. Ditmars, D.C. Ginnings, Thermal Conductivity of Beryllium Oxide from 40 to 750 C, J. Res. Natl. Bur. Stand.–1957.–59.–P, 93 (1957).

[36] C.R. McCullough, Summary Report on Design and Development of High Temperature Gas-Cooled Power Pile, in, Clinton Labs., Oak Ridge, Tenn., 1947.

[37] K.A. Trickett, Maritime Gas-Cooled Reactor Program. A Review of the Maritime Gas-Cooled Reactor Program, in, General Atomic Div. General Dynamics Corp., San Diego, Calif., 1961.

[38] W. Manly, G. Adamson Jr, J. Coobs, J. DeVan, D. Douglas, E. Hoffman, P. Patriarca, Aircraft Reactor Expermiment--Metallurgical Aspects, in, Oak Ridge National Lab., Tenn., 1958.

[39] E. Bettis, R. Schroeder, G. Cristy, H. Savage, R. Affel, L. Hemphill, The Aircraft Reactor Experiment—Design and Construction, Nucl. Sci. Eng, 2 (1957) 804-825.

[40] R.C. Briant, A.M. Weinberg, Molten Fluorides as Power Reactor Fuels, Nuclear science and engineering, 2 (1957) 797-803.

[41] W. Ergen, A. Callihan, C. Mills, D. Scott, The Aircraft Reactor Experiment-Physics1, Nuclear Science and Engineering, 2 (1957) 826-840.

[42] W. Moore, The Experimental Beryllium Oxide Reactor. Maritime Gas-Cooled Reactor Program, in, General Atomic Div. General Dynamics Corp., San Diego, Calif., 1961.

[43] W. Hallstead, Aptly Named After the God of the Underworld, the Pluto Project Created a Cruise Missile from Hell, Aviation History, 13 (2003) 4.

[44] W. Sandholtz, Pluto Fuel Element Fabrication at Lawrence Radiation Laboratory, in, California Univ., Livermore (USA). Lawrence Livermore Lab., 1965.

[45] J. Matos, LEU Conversion Status of US Research Reactors September 1996, in, Argonne National Lab., IL (United States), 1996.

[46] J. Fink, Thermophysical Properties of Uranium Dioxide, Journal of Nuclear Materials, 279 (2000) 1-18.

[47] Y. Kim, J. Park, J. Cleveland, Thermophysical Properties Database of Materials for Light Water Reactors and Heavy Water Reactors, IAEA, Vienna, (2006).

[48] S.G.T. Europe, Thermodynamic Properties of Inorganic Materials: Pure Substances. Part 4: Compounds from HgH to ZnTe, in: R.-W.T.H.A. Lehrstuhl für Theoretische Hüttenkunde (Ed.), Springer-Verlag, Germany, 2001.

[49] C. Ronchi, M. Sheindlin, M. Musella, G. Hyland, Thermal Conductivity of Uranium Dioxide up to 2900 K from Simultaneous Measurement of the Heat Capacity and Thermal Diffusivity, Journal of Applied Physics, 85 (1999) 776-789.

[50] K. Yamada, K. Kurosaki, M. Uno, S. Yamanaka, Evaluation of Thermal Properties of Uranium Dioxide by Molecular Dynamics, Journal of alloys and compounds, 307 (2000) 10-16.

[51] R.A. Young, Model for the Electronic Contribution to the Thermal and Transport Properties of ThO_2, UO_2, and PuO_2 in the Solid and Liquid Phases, Journal of Nuclear Materials, 87 (1979) 283-296.

[52] J. Harding, D. Martin, A Recommendation for the Thermal Conductivity of UO_2, Journal of nuclear materials, 166 (1989) 223-226.

[53] G. Hyland, Thermal Conductivity of Solid UO_2: Critique and Recommendation, Journal of Nuclear Materials, 113 (1983) 125-132.

[54] C. Hann, C.E. Beyer, L. Parchen, GAPCON-THERMAL-1: A Computer Program for Calculating the Gap Conductance in Oxide Fuel Pins, in, Battelle Pacific Northwest Labs., Richland, Wash.(USA), 1973.

[55] S. Ogawa, E. Lees, M. Lyons, Power Reactor High Performance UO_2 Program. Fuel Design Summary and Program Status, in, General Electric Co., San Jose, Calif. Nuclear Fuels Dept., 1968.

[56] J. MacEwan, R. Stoute, M. Notley, Effect of Porosity on the Thermal Conductivity of UO_2, Journal of Nuclear Materials, 24 (1967) 109-112.

[57] K. Bakker, H. Kwast, E. Cordfunke, Determination of a Porosity Correction Factor for the Thermal Conductivity of Irradiated UO_2 Fuel by Means of the Finite Element Method, Journal of nuclear materials, 226 (1995) 128-143.

[58] K. Bakker, H. Kwast, E. Cordfunke, The Contribution of Thermal Radiation to the Thermal Conductivity of Porous UO_2, Journal of nuclear materials, 223 (1995) 135-142.

[59] V. Krett, J. Cleveland, Thermophysical Properties of Materials for Water Cooled Reactors, in, IAEA-TECDOC-949, International Atomic Energy Agency, Vienna, Austria, 1997.

[60] K. Chockalingam, P.C. Millett, M. Tonks, Effects of Intergranular Gas Bubbles on Thermal Conductivity, Journal of Nuclear Materials, 430 (2012) 166-170.

[61] S.-i. Higuchi, A Molecular Dynamics Study of Thermal Conductivity of UO_2 with Impurities, Journal of Nuclear Science and Technology, 35 (1998) 833-835.

[62] S. Hu, C.H. Henager Jr, H.L. Heinisch, M. Stan, M.I. Baskes, S.M. Valone, Phase-Field Modeling of Gas Bubbles and Thermal Conductivity Evolution in Nuclear Fuels, Journal of Nuclear Materials, 392 (2009) 292-300.

[63] P. Lucuta, H. Matzke, I. Hastings, A Pragmatic Approach to Modelling Thermal Conductivity of Irradiated UO_2 Fuel: Review and Recommendations, Journal of Nuclear Materials, 232 (1996) 166-180.

[64] J. MacEwan, R. Stoute, Effect of Irradiation on the Thermal Conductivity of $UO_{2-\chi}$, UO_2 and $UO_{2+\chi}$ at 60° C, Journal of Nuclear Materials, 21 (1967) 70-76.

[65] R. Taylor, Thermal Conductivity and Expansion of Beryllia at High Temperatures, Journal of the American Ceramic Society, 45 (1962) 74-78.

[66] K. Kelley, The Specific Heats at Low Temperatures of Beryllium Oxide and Beryllium Orthosilicate (Phenacite), Journal of the American Chemical Society, 61 (1939) 1217-1218.

[67] R. Swindeman, Thermal Shock Tests on Beryllia, Journal of Nuclear Materials, 14 (1964) 404-415.

[68] A.C. Victor, T.B. Douglas, Thermodynamic Properties of Magnesium Oxide and Beryllium Oxide from 298 to 1200 K, Journal of Research of the National Bureau of Standards A, 67 (1963) 325-329.

[69] M. Cooper, A. Palmer, G. Stolarski, The Effect of Neutron Irradiation on the Thermal Conductivity of Beryllium Oxide, Journal of Nuclear Materials, 9 (1963) 320-326.

[70] J.C. Maxwell, A Treatise on Electricity and Magnetism, 3rd ed., Dover Publishing Company, 1954.

[71] H. Fricke, A Mathematical Treatment of the Electric Conductivity and Capacity of Disperse Systems I. The Electric Conductivity of a Suspension of Homogeneous Spheroids, Physical Review, 24 (1924) 575.

[72] R. Hamilton, O. Crosser, Thermal Conductivity of Heterogeneous Two-Component Systems, Industrial & Engineering chemistry fundamentals, 1 (1962) 187-191.

[73] J.F. Kerrisk, Thermal Diffusivity of Heterogeneous Materials. II. Limits of the Steady-State Approximation, Journal of Applied Physics, 43 (2003) 112-117.

[74] W. Kingery, Thermal Conductivity: XIV, Conductivity of Multicomponent Systems, Journal of the American Ceramic Society, 42 (1959) 617-627.

[75] L. Verma, A. Shrotriya, R. Singh, D. Chaudhary, Thermal Conduction in Two-Phase Materials with Spherical and Non-Spherical Inclusions, Journal of Physics D: Applied Physics, 24 (1991) 1729.

[76] K. Singh, R. Singh, D. Chaudhary, Heat Conduction and a Porosity Correction Term for Spherical and Cubic Particles in a Simple Cubic Packing, Journal of Physics D: Applied Physics, 31 (1998) 1681.

[77] C. Richter, H.J. Viljoen, N. Van Rensburg, Effective Thermal Conductivity Estimates of Particulate Mixtures, Journal of applied physics, 93 (2003) 2663-2670.

[78] D.M. Staicu, D. Jeulin, M. Beauvy, M. Laurent, C. Berlanga, N. Negrello, D. Gosset, Effective Thermal Conductivity of Heterogeneous Materials: Calculation Methods and Application to Different Microstructures, HIGH TEMPERATURES HIGH PRESSURES, 33 (2001) 293-302.

[79] S. Ishimoto, M. Hirai, K. Ito, Y. Korei, Thermal Conductivity of UO_2-BeO Pellet, Journal of Nuclear Science and Technology, 33 (1996) 134-140.

[80] S.M. McDeavitt, M. Naramore, R. Miller, J.C. Ragusa, S.T. Revankar, A.A. Solomon, J. Malone, Introducing a High Thermal Conductivity UO_2-BeO Nuclear Fuel Concept, Transactions of the American Nuclear Society, 103 (2010) 273-274.

[81] D. Li, H. Garmestani, J. Schwartz, Modeling Thermal Conductivity in UO_2 with BeO Additions as a Function of Microstructure, Journal of Nuclear Materials, 392 (2009) 22-27.

[82] N.B. Vatsaraj, D. Gao, D.L. Kowalski, Optimization of the Operating Conditions of a Lab Scale Aljet Mill Using Lactose and Sucrose: A Technical Note, AAPS PharmSciTech, 4 (2003) 141-146.

[83] S.H. Na, Effect of Ball-mill Treatment on Powder Characteristics, Compaction, and Sintering Behaviors of ex-AUC and ex-ADU UO, Powder, Journal of the Korean Nuclear Society, 34 (2002) 60-67.

[84] P. Balakrishna, C.K. Asnani, R. Kartha, K. Ramachandran, K. Sarat Babu, V. Ravichandran, B.N. Murty, C. Ganguly, Uranium dioxide powder preparation, pressing, and sintering for optimum yield, Nuclear technology, 127 (1999) 375-381.

[85] M. Bannister, The Kinetics of Sintering and Grain Growth of Beryllia, Journal of Nuclear Materials, 14 (1964) 315-321.

[86] A. Zavaliangos, J. Missiaen, D. Bouvard, Anisotropy in Shrinkage During Sintering, Science of Sintering, 38 (2006) 13-25.

APPENDIX A

RAW WDS DATA TABLES

Table 9. WDS of First Raw Uranium Oxide Powder

	wt%		*at%*		
	O	*U*	*O*	*U*	*O/U*
UO_2 Standard	11.822	87.263	66.777	33.134	2.02
UO_X 1	15.401	83.298	73.241	26.627	2.75
UO_X 2	15.506	83.019	73.451	26.435	2.78

Table 10. WDS of Second Raw Uranium Oxide Powder

	wt%		*at%*		*Sigma (wt%)*		*Sigma (at%)*		
	U	*O*	*U*	*O*	*U*	*O*	*U*	*O*	*O/U*
3_A	85.56	13.154	30.42	69.578	0.896	0.090	0.319	0.476	2.287
3_A	85.375	12.328	31.754	68.216	0.894	0.086	0.333	0.475	2.148
3_A	84.109	13.255	29.893	70.086	0.882	0.090	0.313	0.478	2.345
3_A	84.122	14.086	28.64	71.342	0.882	0.094	0.300	0.478	2.491
3_B	85.789	11.953	32.541	67.453	0.898	0.084	0.341	0.475	2.073
3_B	85.315	13.718	29.476	70.509	0.894	0.092	0.309	0.474	2.392
3_B	85.162	13.573	29.655	70.314	0.892	0.092	0.311	0.475	2.371
3_B	84.967	13.129	30.309	69.673	0.890	0.090	0.318	0.475	2.299
4_A	84.954	13.913	29.098	70.893	0.890	0.093	0.305	0.476	2.436
4_A	85.461	13.453	29.919	70.065	0.895	0.091	0.313	0.475	2.342
4_A	85.677	13.663	29.652	70.344	0.897	0.092	0.311	0.475	2.372
4_A	85.195	13.85	29.248	70.737	0.893	0.093	0.306	0.476	2.419
4_B	84.046	14.362	28.231	71.769	0.881	0.095	0.296	0.476	2.542
4_B	85.55	13.378	30.063	69.937	0.896	0.091	0.315	0.474	2.326
4_B	85.905	13.347	30.198	69.802	0.899	0.091	0.316	0.475	2.311
4_B	85.589	13.28	30.224	69.765	0.896	0.090	0.317	0.474	2.308
4_C	85.303	12.98	30.629	69.337	0.893	0.089	0.321	0.476	2.264
4_C	83.431	13.541	29.286	70.712	0.875	0.092	0.307	0.478	2.415
4_C	82.534	11.697	32.171	67.829	0.866	0.083	0.338	0.481	2.108
4_C	83.992	11.134	33.636	66.333	0.880	0.080	0.353	0.479	1.972
5_A	85.883	14.16	28.96	71.032	0.899	0.094	0.303	0.473	2.453
5_A	84.402	14.467	28.164	71.819	0.885	0.096	0.295	0.476	2.550
5_B	83.901	15.845	26.249	73.747	0.880	0.102	0.275	0.475	2.810
5_B	86.625	13.395	30.296	69.693	0.907	0.091	0.317	0.473	2.300
5_B	85.166	11.715	32.825	67.17	0.892	0.083	0.344	0.476	2.046

5_B	84.529	12.431	31.358	68.607	0.886	0.087	0.329	0.478	2.188
5_C	87.306	11.413	33.959	66.041	0.913	0.081	0.355	0.471	1.945
5_C	84.69	11.877	32.388	67.573	0.887	0.084	0.339	0.476	2.086
5_C	85.707	11.552	33.263	66.696	0.897	0.082	0.348	0.475	2.005
5_C	85.734	11.976	32.486	67.509	0.898	0.084	0.340	0.476	2.078

Table 11. First U_3O_8 Reduction

	wt%		*at%*		
	O	*U*	*O*	*U*	*O/U*
UO_2 Standard	11.859	87.747	99.606	66.784	33.216
Sample Point 1	12.221	87.031	99.252	67.627	32.373
Sample Point 2	12.100	87.230	99.330	67.360	32.640
Sample Point 3	12.484	86.969	99.453	68.108	31.892

Table 12. Second U_3O_8 Reduction

	wt%				*at%*			
	U	*W*	*Al*	*O*	*U*	*W*	*Al*	*O*
B1_A	87	0.036	0	12.64	31.626	0.017	0	68.357
B1_B	84.258	0.026	0.001	13.208	30.007	0.012	0.003	69.978
B1_C	84.182	0.047	0	12.325	31.457	0.023	0	68.52
B2_A	83.772	0.022	0	12.838	30.487	0.01	0	69.503
B2_B	83.065	0	0.005	12.868	30.256	0	0.016	69.728
B3_A	83.954	0	0	12.339	31.383	0	0	68.617
B3_B	83.93	0.013	0.001	12.365	31.328	0.006	0.003	68.663
B4_A	84.373	0.013	0	11.704	32.638	0.007	0	67.356
B4_B	84.108	0.027	0.008	11.419	33.101	0.014	0.029	66.856
M1_A	90.032	0.05	0	12.124	33.287	0.024	0	66.689
M1_B	85.35	0.057	0	12.861	30.84	0.027	0	69.133
M2_A	85.229	0	0	12.323	31.735	0	0	68.265
M2_B	84.267	0.03	0	12.744	30.766	0.014	0	69.22
M3_A	82.96	0	0	12.56	30.748	0	0	69.252
M3_B	82.303	0	0	13.145	29.621	0	0	70.379
M4_A	82.808	0.043	0	12.591	30.65	0.021	0	69.33
M4_B	81.939	0.006	0	13.53	28.931	0.003	0	71.066
M4_C	82.253	0.039	0.009	12.721	30.281	0.018	0.028	69.672
T1_A	88.683	0.097	0.001	12.809	31.743	0.045	0.004	68.208

T1_B	83.812	0.066	0	12.452	31.14	0.032	0	68.828
T1_C	82.834	0.045	0	11.105	33.387	0.024	0	66.59
T2_A	80.702	0.028	0	13.824	28.178	0.012	0	71.81
T2_B	78.036	0.074	0	13.62	27.796	0.034	0	72.17
T3_A	82.761	0.047	0.001	12.859	30.189	0.022	0.004	69.785
T3_B	82.069	0	0.002	12.665	30.339	0	0.007	69.654
T3_C	82.347	0	0	12.188	31.232	0	0	68.768
T4_A	81.945	0.084	0	11.817	31.78	0.042	0	68.178
T4_B	82.973	0.024	0	12.373	31.068	0.012	0	68.92
MX1_A	87.061	0	0	12.783	31.404	0	0	68.596
MX1_B	84.588	0.018	0	12.219	31.754	0.009	0	68.238
MX1_C	83.853	0.018	0	11.974	32.004	0.009	0	67.988
MX2_A	82.846	0.043	0	11.953	31.775	0.021	0	68.203
MX2_B	82.467	0	0.006	12.444	30.812	0	0.02	69.168
MX3_A	82.859	0	0	12.197	31.348	0	0	68.652
MX3_B	81.774	0.066	0	12.383	30.732	0.032	0	69.235
MX4_A	82.341	0.028	0	12.476	30.727	0.014	0	69.259
MX4_B	81.348	0.026	0	13.137	29.387	0.012	0	70.601
MX4_C	81.734	0.057	0	12.795	30.031	0.027	0	69.942
MX5_A	89.31	0.037	0	12.373	32.663	0.018	0	67.319
MX5_B	84.995	0.019	0.004	12.481	31.394	0.009	0.014	68.583
MX5_C	83.487	0.027	0.002	12.433	31.093	0.013	0.006	68.888
MX6_A	84.669	0	0	12.066	32.05	0	0	67.95
MX6_B	84.049	0.069	0	12.218	31.608	0.034	0	68.358
MX6_C	84.247	0.05	0.007	11.747	32.512	0.025	0.024	67.439
MX7_A	79.049	0.031	0	13.982	27.535	0.014	0	72.452
MX7_B	72.36	0.016	0	14.852	24.668	0.007	0	75.325
MX8_A	83.676	0.039	0	12.487	31.048	0.019	0	68.933
MX8_B	83.31	0.002	0	12.704	30.594	0.001	0	69.405

APPENDIX B

RAW GEOMETRIC MEASURMENT DATA

Table 13. Geometric Measurements of Sintered Sample Pellets

	Green Measurements			***Post Sintering Measurements***		
Sample	**Height (mm)**	**Diameter (mm)**	**Mass (g)**	**Height (mm)**	**Diameter (mm)**	**Mass (g)**
01-1-100	4.02	13.20	3.3531	3.60	11.44	3.2898
	4.03	13.20		3.62	11.44	
	4.02	13.24		3.62	11.49	
	4.02	13.15		3.60	11.50	
	4.02	13.24		3.61	11.48	
					11.46	
01-2-100	4.01	13.24	3.3523	3.56	11.43	3.2916
	4.01	13.24		3.62	11.48	
	4.01	13.15		3.57	11.45	
	4.01	13.17		3.62	11.46	
	4.01	13.25		3.62	11.47	
					11.52	
01-3-100	3.96	13.19	3.3438	3.80	11.63	3.2797
	3.97	13.19		3.84	11.57	
	3.97	13.17		3.82	11.55	
	3.98	13.25		3.77	11.58	
	3.99	13.18		3.81	11.50	
				3.66	11.60	
				3.82		
				3.83		
02-1-000	4.31	13.15	3.7743	3.71	11.21	3.7045
	4.30	13.16		3.73	11.22	
	4.30	13.16		3.73	11.23	
	4.30	13.16		3.73	11.29	
	4.29	13.19		3.74	11.28	
		13.19		3.75	11.22	
		13.23		3.72	11.23	
				3.73	11.22	
02-2-100	4.18	13.16	3.4976	3.69	11.41	3.4309
	4.18	13.15		3.70	11.43	
	4.18	13.15		3.70	11.45	

	4.19	13.25		3.71	11.51	
	4.19	13.15		3.71	11.38	
		13.15		3.71	11.40	
		13.16		3.70	11.39	
		13.17			11.40	
					11.46	
03-2-100	3.71	15.07	4.0093	3.24	12.97	3.9363
	3.72	15.07		3.26	12.98	
	3.72	15.09		3.29	12.98	
	3.72	15.10		3.26	12.99	
	3.73	15.07		3.22	13.00	
				3.25	12.97	
				3.23	12.97	
				3.30	12.99	
04-1-100	3.67	15.10	4.0298	3.32	13.14	3.9534
	3.70	15.11		3.32	13.10	
	3.70	15.14		3.34	13.10	
	3.69	15.10		3.26	13.12	
	3.64	15.10		3.30	13.13	
	3.72	15.10		3.30	13.11	
		15.10		3.28	13.11	
				3.31	13.11	
				3.33		
04-2-100	3.69	15.08	4.0214	3.33	13.10	3.9193
	3.70	15.09		3.33	13.15	
	3.69	15.10		3.34	13.14	
	3.70	15.13		3.35	13.10	
	3.69	15.15		3.29	13.11	
	3.73	15.15		3.27	13.11	
	3.69	15.08		3.33	13.12	
		15.08		3.36	13.14	
				3.27	13.11	
04-3-100	1.61	15.03	1.5429	1.49	13.05	1.4876
	1.61			1.42	13.07	
	1.62			1.42		
	1.62			1.50		
	1.64					
	1.61					
	1.62					

05-1-100	3.69	15.11	4.0325	3.24	13.02	3.9553
	3.70	15.11		3.25	13.04	
	3.71	15.12		3.25	13.06	
	3.72	15.13		3.28	13.07	
	3.72	15.17		3.29	13.08	
	3.72	15.17		3.30	13.08	
		15.18		3.31	13.05	
				3.31	13.03	
					13.08	
05-2-100	3.68	15.07	4.0270	3.23	13.00	3.9538
	3.70	15.07		3.23	13.00	
	3.70	15.07		3.26	13.00	
	3.72	15.08		3.27	13.01	
	3.72	15.08		3.28	13.01	
	3.72	15.08		3.28	13.01	
	3.72			3.29	13.01	
					13.02	
05-3-100	3.73	15.08	4.0327	3.27	12.99	3.9562
	3.74	15.09		3.28	13.00	
	3.74	15.09		3.28	13.01	
	3.74	15.09		3.28	13.01	
	3.74	15.09		3.28	13.02	
	3.75	15.12		3.28	13.05	
	3.75	15.12		3.30	13.05	
				3.32	13.09	
06-1-100	3.71	15.11	3.937	3.28	12.99	3.8482
	3.72	15.11		3.27	13.02	
	3.73	15.11		3.22	12.98	
	3.74	15.11		3.25	12.99	
	3.74	15.12		3.25	13.03	
	3.76	15.12		3.28	13.01	
		15.12		3.23	12.99	
					12.99	
					13.00	
06-2-100	3.72	15.08	4.0729	3.32	13.01	3.9978
	3.73	15.08		3.32	12.97	
	3.73	15.08		3.30	13.01	
	3.74	15.08		3.31	12.98	
	3.74	15.08		3.31	12.99	

	3.75	15.09		3.32	12.98	
				3.28	12.98	
				3.30	12.97	
					13.00	
06-3-100	3.74	15.07	4.0526	3.28	13.01	3.9782
	3.74	15.07		3.28	13.01	
	3.75	15.07		3.33	12.99	
	3.75	15.07		3.27	13.02	
	3.76	15.08		3.28	13.02	
	3.78	15.08		3.31	13.00	
				3.27	13.04	
				3.28	13.01	
					13.01	
06-4-025	3.77	15.07	4.2823	3.27	12.78	4.202
	3.77	15.08		3.26	12.78	
	3.78	15.08		3.25	12.79	
	3.79	15.08		3.25	12.79	
	3.8	15.09		3.25	12.78	
	3.81	15.09		3.25	12.78	
				3.25		
06-5-050	3.73	15.07	4.1662	3.24	12.88	4.0792
	3.74	15.07		3.25	12.88	
	3.75	15.08		3.26	12.89	
	3.75	15.08		3.26	12.87	
	3.76	15.08		3.25	12.86	
	3.76	15.08		3.26	12.87	
	3.77			3.25	12.89	
				3.24	12.86	
				3.25	12.88	
06-6-075	3.71	15.07	4.1016	3.24	12.95	4.0252
	3.72	15.07		3.25	12.91	
	3.72	15.08		3.26	12.90	
	3.73	15.08		3.25	12.96	
	3.73	15.08		3.21	12.95	
	3.74	15.08		3.24	12.91	
	3.76	15.09		3.25	12.95	
				3.22	12.93	
07-1-100	3.7	15.09	3.9215	3.23	12.95	3.8357
	3.69	15.09		3.25	12.96	

	3.75	15.11		3.30	12.96	
	3.74	15.08		3.21	12.96	
	3.68	15.11		3.25	12.96	
	3.66	15.08		3.04	12.95	
	3.7			3.23	12.95	
	3.75			3.23	12.95	
	3.7			3.29	12.95	
	3.66			3.27	12.96	
08-1-075	3.74	15.08	4.1049	3.22	12.88	4.0156
	3.75	15.08		3.24	12.85	
	3.72	15.08		3.26	12.87	
	3.76	15.08		3.28	12.89	
	3.8	15.09		3.28	12.90	
	3.74	15.09		3.21	12.92	
	3.74			3.23	12.88	
	3.74			3.27	12.89	
	3.72			3.24	12.90	
				3.28	12.91	
09-1-050	3.83	15.09	4.1662	3.21	12.80	4.0728
	3.81	15.09		3.26	12.80	
	3.75	15.09		3.27	12.81	
	3.74	15.09		3.27	12.81	
	3.76	15.09		3.27	12.81	
	3.75	15.08		3.24	12.82	
	3.78	15.08		3.25	12.82	
	3.8			3.26	12.83	
	3.8			3.26	12.79	
	3.8			3.25	12.79	
10-1-025	3.79	15.08	4.2077	3.30	12.78	4.1125
	3.78	15.07		3.30	12.77	
	3.82	15.08		3.26	12.76	
	3.82	15.08		3.25	12.77	
	3.78	15.08		3.27	12.77	
	3.78	15.08		3.31	12.80	
				3.24	12.78	
				3.31		

Table 14. LFA Sectioned Samples

Sample	*h (mm)*	*D (mm)*	*m (g)*	*Sample*	*h (mm)*	*D (mm)*	*m (g)*
02-1-000A	0.87	11.20	0.7986	05-1-100A	0.64	13.10	0.7332
	0.84	11.21			0.65	13.06	
	0.82	11.27			0.66	13.07	
	0.88	11.20			0.67	13.09	
	0.86	11.26			0.67	13.09	
	0.85				0.68	13.07	
					0.63	13.08	
					0.66	13.09	
					0.65		
02-1-000B	1.17	11.24	1.1854	05-1-100B	0.98	13.04	1.1970
	1.21	11.29			0.96	13.05	
	1.17	11.22			0.97	13.05	
	1.16	11.22			1.00	13.06	
	1.18	11.29			1.02	13.06	
	1.19	11.24			1.01	13.07	
					0.96	13.08	
					0.96	13.07	
					0.96	13.06	
						13.04	
02-1-000C	1.05	11.26	0.9506	05-1-100C	0.85	13.01	1.0644
	0.99	11.27			0.86	13.01	
	0.95	11.22			0.86	13.02	
	1.04	11.25			0.87	13.03	
	0.95	11.24			0.87	13.04	
	1.01				0.87	13.02	
	0.97				0.95	13.02	
					0.98	13.02	
					0.92	13.03	
					0.80		
02-2-100A	0.98	11.37	0.7350	05-2-100A	0.66	12.96	0.7722
	0.85	11.39			0.67	12.97	
	0.76	11.41			0.70	12.97	
	0.75	11.36			0.71	12.97	
	0.77	11.37			0.69	13.00	
	0.88	11.39			0.63	12.97	
	0.85	11.37			0.63	12.97	
	0.81				0.64	12.99	

					0.69		
02-2-100B	0.75	11.34	0.6810	05-2-100B	0.92	13.00	1.1439
	0.77	11.34			0.93	13.01	
	0.71	11.38			0.93	13.02	
	0.76	11.34			0.93	13.02	
	0.72	11.32			0.93	13.02	
	0.71				0.94	13.02	
					0.96	13.01	
					1.00	13.02	
					1.00	13.02	
						12.99	
02-2-100C	0.83	11.34	0.7053	05-2-100C	0.92	13.00	1.0843
	0.84	11.28			0.93	13.00	
	0.83	11.33			0.89	13.00	
	0.84	11.29			0.87	13.00	
	0.85	11.29			0.90	13.01	
	0.77	11.32			0.89	13.01	
	0.81				0.89	13.01	
	0.84				0.94	13.01	
					0.93		
					0.89		
03-2-100A	0.74	12.93	0.8631	05-3-100A	0.56	12.93	0.7115
	0.76	12.93			0.56	12.94	
	0.74	12.92			0.57	12.95	
	0.73	12.93			0.63	12.96	
	0.76	12.94			0.63	12.96	
	0.78	12.93			0.61	12.97	
	0.75				0.64	12.94	
	0.73				0.57	12.94	
					0.58	12.93	
03-2-100B	0.85	12.94	1.0523	05-3-100B	0.88	12.96	1.0872
	0.89	12.95			0.89	12.98	
	0.89	12.97			0.93	12.98	
	0.89	12.96			1.00	12.98	
	0.85	12.95			0.89	12.99	
	0.89	12.95			0.89	12.99	
	0.95	12.96			0.89	12.96	
	0.85				0.89	12.97	

	0.85				0.91	12.98	
	0.90				0.94	13.00	
03-2-100C	0.90	12.96	1.0578	05-3-100C	0.98	13.01	1.1952
	0.91	12.97			1.00	13.01	
	0.92	12.96			1.02	13.03	
	0.91	12.95			1.06	13.03	
	0.89	12.95			1.06	13.04	
	0.90	13.00			1.06	13.04	
	0.92	12.97			1.03	13.05	
	0.92	12.97			1.01	13.02	
	0.90	12.96			1.03	13.02	
					1.03	13.05	

APPENDIX C

RAW ARCHEMEDIS MEASURMENT DATA

Sample	BeO vol%	Dry mass (g)	Immersed mass (g)	Wet Mass (g)	Temp. (°C)	Density of ethanol
01-1-100	10.0	3.2898	3.0202	3.3037	20.0	0.78945
01-2-100	10.0	3.2916	3.0258	3.3102	20.0	0.78945
01-3-100	10.0	3.2797	3.0057	3.3032	20.0	0.78945
02-1-000	0.0	3.7045	3.4092	3.6892		0.78945
02-2-100	10.0	3.4309	3.1508	3.4382		0.78945
03-2-100	10.0	3.9363	3.6180	3.9461	25	0.78522
03-3-100	10.0	2.0918	1.9267	2.1216	25	0.78522
04-1-100	10.0	3.9532	3.599	3.9659	23.5	0.786452
04-2-100	10.0	3.9192	3.6316	3.9339	23.5	0.786452
04-3-100	10.0	1.4872	1.3678	1.4992	23.5	0.786452
05-1-100	10.0	*3.9553*	3.6291	3.9687	23.3	0.78661
05-2-100	10.0	*3.9538*	3.6292	3.9643	23.3	0.78661
05-3-100	10.0	*3.9562*	3.6315	3.971	23.3	0.78661
06-1-100	10.0	3.8484	3.5364	3.8617	22.7	0.787082
06-2-100	10.0	3.9978	3.6711	4.0092	22.7	0.787082
06-3-100	10.0	3.9782	3.6526	3.9919	22.7	0.787082
06-4-025	2.5	4.202	3.8805	4.2088	22.7	0.787082
06-5-	5.0	4.0792	3.7587	4.0841	22.7	0.787082

050						
06-6-075	7.5	4.0252	3.7033	4.0318	22.7	0.787082
07-1-100	10.0	3.8359	3.5244	3.8462	23	0.786846
08-1-075	7.5	4.0158	3.6961	4.0248	23	0.786846
09-1-050	5.0	4.0728	3.7541	4.0791	23	0.786846
10-1-025	2.5	4.1125	3.7956	4.1191	32.2	0.779596

APPENDIX D

LABVIEW LVDT DATA COLLECTION VI

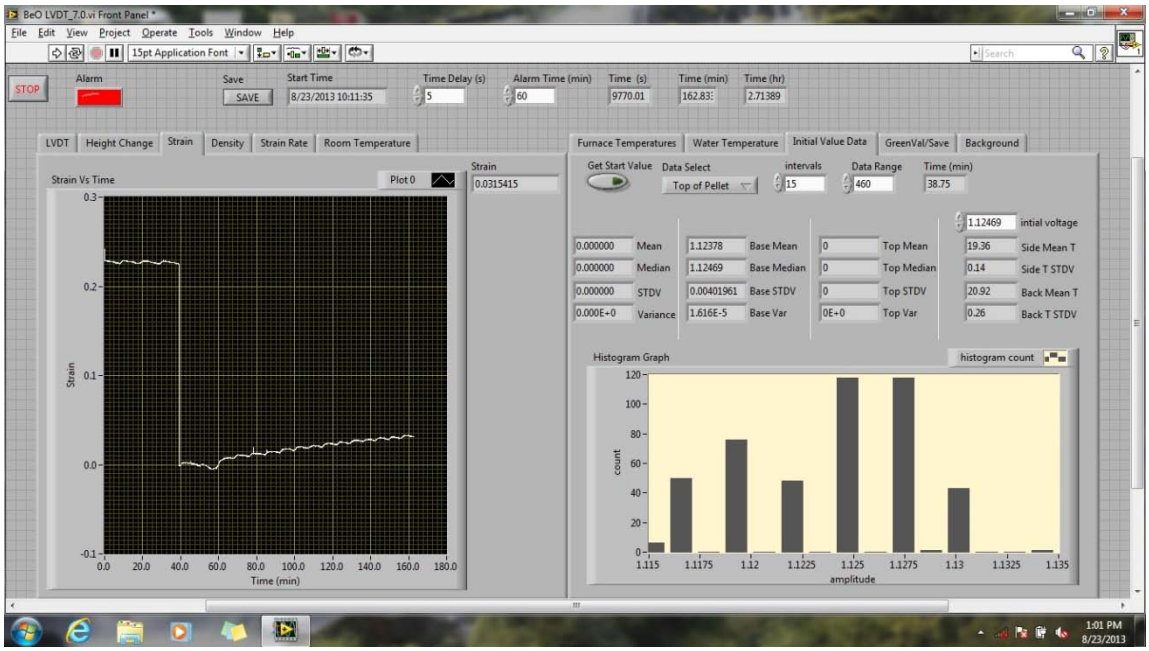

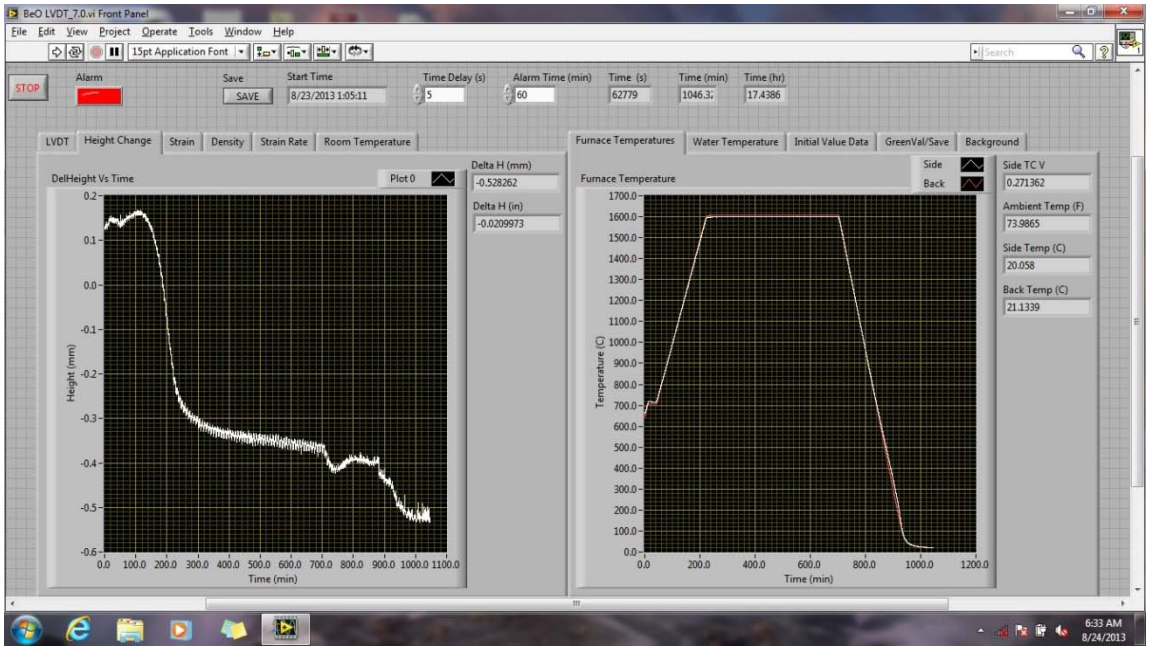

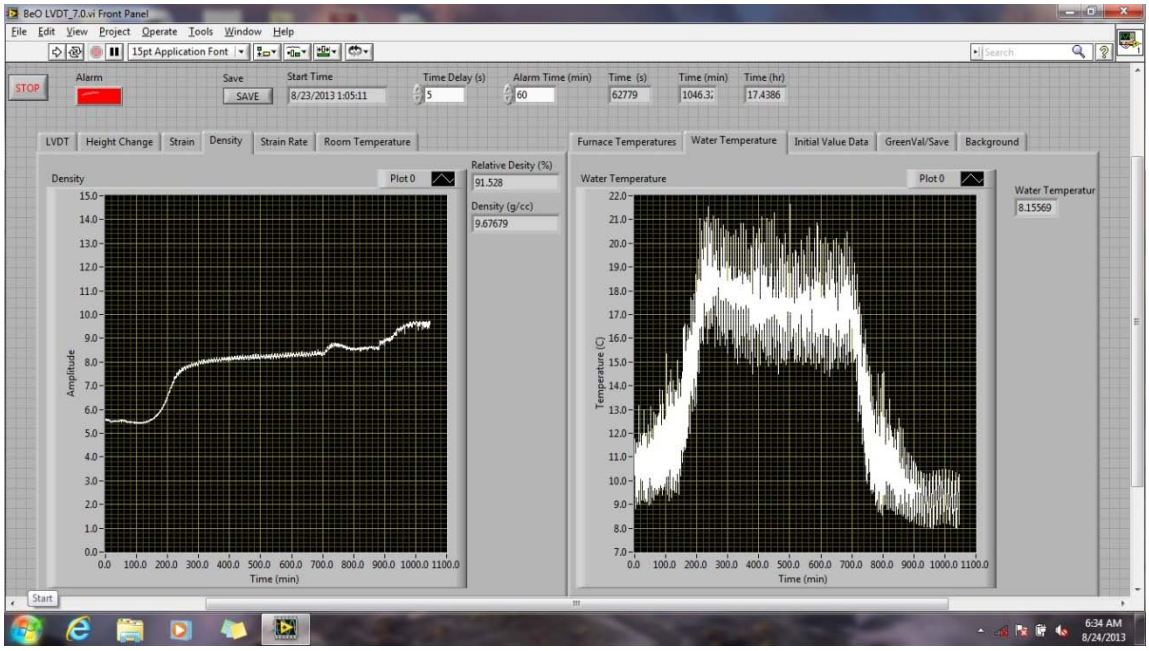
BeO LVDT_7.0.vi Front Panel
File Edit View Project Operate Tools Window Help
15pt Application Font
STOP
Alarm
Save
SAVE
Start Time
8/23/2013 1:05:11
Time Delay (s)
5
Alarm Time (min)
60
Time (s)
62779
Time (min)
1046.3
Time (hr)
17.4386
LVDT
Height Change
Strain
Density
Strain Rate
Room Temperature
Furnace Temperatures
Water Temperature
Initial Value Data
GreenVal/Save
Background
Density
Plot 0
Relative Desity (%)
91.528
Density (g/cc)
9.67679
Amplitude
Time (min)
Water Temperature
Plot 0
Water Temperatur
8.15569
Temperature (C)
Time (min)
Start
6:34 AM
8/24/2013

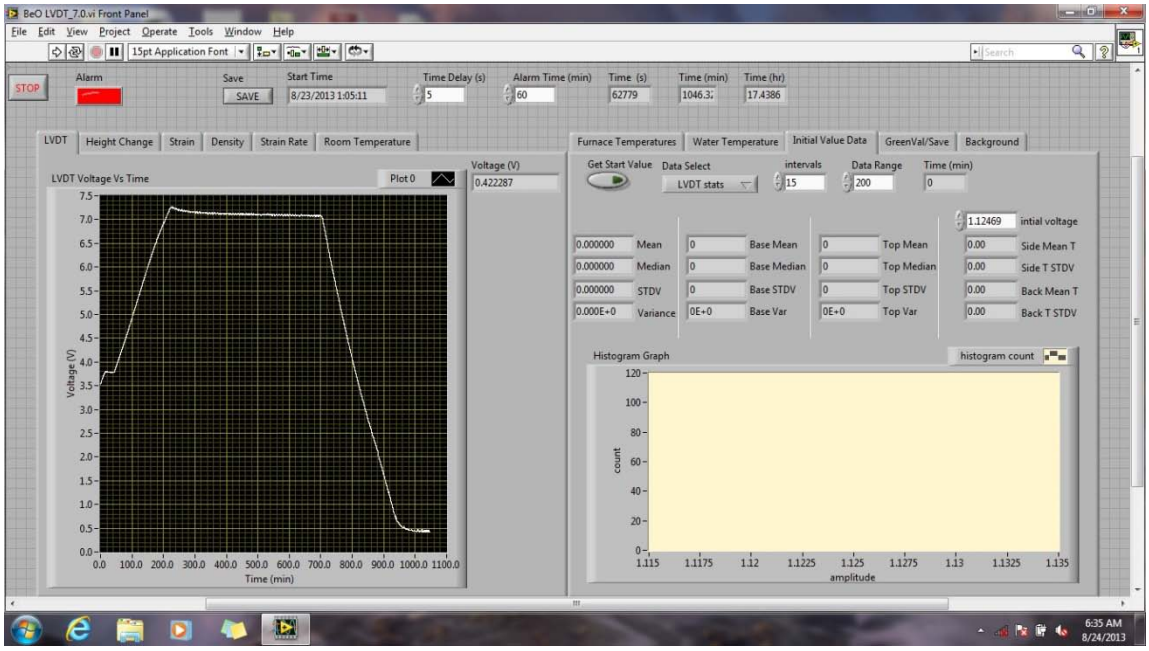
BeO LVDT_7.0.vi Front Panel
File Edit View Project Operate Tools Window Help
15pt Application Font
STOP
Alarm
Save
SAVE
Start Time
8/23/2013 1:05:11
Time Delay (s)
5
Alarm Time (min)
60
Time (s)
62779
Time (min)
1046.3
Time (hr)
17.4386
LVDT
Height Change
Strain
Density
Strain Rate
Room Temperature
Furnace Temperatures
Water Temperature
Initial Value Data
GreenVal/Save
Background
LVDT Voltage Vs Time
Plot 0
Voltage (V)
0.422287
Voltage (V)
Time (min)
Get Start Value
Data Select
LVDT stats
intervals
15
Data Range
200
Time (min)
0
1.12469
intial voltage
0.000000 Mean
0 Base Mean
0 Top Mean
0.00 Side Mean T
0.000000 Median
0 Base Median
0 Top Median
0.00 Side T STDV
0.000000 STDV
0 Base STDV
0 Top STDV
0.00 Back Mean T
0.000E+0 Variance
0E+0 Base Var
0E+0 Top Var
0.00 Back T STDV
Histogram Graph
histogram count
count
amplitude
6:35 AM
8/24/2013

APPENDIX E

MATLAB PROGRAM FOR LVDT DATA ANALYSIS

```
clear
clc

%Get the Background Curves From Sapphire Data
[TvD,TmpTvD]=BckGrnd;

%clear screan
clc

%Ask user which Data to be analyled
fprintf('Avaliable Heat Runs: 7, 8, 9, 10 \nWhich Heat runs do you want
to analyze\n')
HR=input('Enter HR value:  ');

%Intial values
lnHR=length(HR);
HRTb=zeros(1,lnHR);
HRt=zeros(1,lnHR);
HRLVDT=zeros(1,lnHR);
HRdH=zeros(1,lnHR);
HRstrn=zeros(1,lnHR);
HRstrnrt=zeros(1,lnHR);
lnt=zeros(1,lnHR);
indi=lnt;
indi2=indi;


%Get LVDT Data from the spreadsheet
for i=1:lnHR

    [tmpTb,tmpt,tmpdH,tmpstrn,tmpstrnrt,tmprho,tmpthrho] =
GetHRdata2(HR(i),TvD,TmpTvD);

    lnt(i)=length(tmpTb);
    HRt(1:lnt(i),i)=tmpt;
    HRTb(1:lnt(i),i)=tmpTb;
    HRdH(1:lnt(i),i)=tmpdH;
    HRstrn(1:lnt(i),i)=tmpstrn;
    HRstrnrt(1:lnt(i),i)=tmpstrnrt;
    rho(1:lnt(i),i)=tmprho;
    thryrho(1:lnt(i),i)=tmpthrho;

    fprintf('\nHR%2.0f COMPLETE\n',HR(i))

end
```

```
%alline all data sets
for j=1:lnHR
    [indi(j),indi2(j)]=timecrct(HRt(:,j),HRTb(:,j));
    tims(j)=HRt(indi(j),j);
end

tfix=tims-min(tims);
%tfix=max(tims);
HRt2=zeros(size(HRt));

for k=1:lnHR
    HRt2(:,k)=HRt(:,k)-tfix(k)-min(tims);
    %HRt2(:,k)=HRt(:,k)-tfix;
end
HRt2=HRt2/60;
tst= input('\n\nDo you want to plot data?\nEnter "0" for no "1" for
yes:  ');


while tst==1
    %clc
    fprintf('\nHeight Change VS Time:             1\n')
    fprintf('Height Change VS Temperature:      2\n')
    fprintf('Temperature VS Time:               3\n')
    fprintf('Strain VS Time:                    4\n')
    fprintf('Strain Rate VS Time:               5\n')
    fprintf('Strain VS Temperature:             6\n')
    fprintf('Strain Rate VS Temperature:        7\n')
    fprintf('Density VS Time:                   8\n')
    fprintf('Relative Density VS Time:          9\n')
    fprintf('Density VS Temperature:            10\n')
    fprintf('Relative Density VS Temperature:   11\n')
    HRplt=input('\nWhich data do you want to plot: ');
    fprintf('\nAvailiable Heat runs: ')
    fprintf('%2.0f  ',HR)
    HRnspt=input('\nWhich HRs do you want to plot : ');

    if HRplt==1
        HRpltin(HRplt,HRnspt,HR,lnt,HRt2,HRdH,indi,indi2);
    elseif HRplt==2
        HRpltin(HRplt,HRnspt,HR,lnt,HRTb,HRdH,indi,indi2);
    elseif HRplt==3
        HRpltin(HRplt,HRnspt,HR,lnt,HRt2,HRTb,indi,indi2);
    elseif HRplt==4
        HRpltin(HRplt,HRnspt,HR,lnt,HRt2,HRstrn,indi,indi2);
    elseif HRplt==5
        HRpltin(HRplt,HRnspt,HR,lnt,HRt2,HRstrnrt,indi,indi2);
    elseif HRplt==6
        HRpltin(HRplt,HRnspt,HR,lnt,HRTb,HRstrn,indi,indi2);
    elseif HRplt==7
        HRpltin(HRplt,HRnspt,HR,lnt,HRTb,HRstrnrt,indi,indi2);
```

```
    elseif HRplt==8
        HRpltin(HRplt,HRnspt,HR,lnt,HRt2,rho,indi,indi2);
    elseif HRplt==9
        HRpltin(HRplt,HRnspt,HR,lnt,HRt2,thryrho,indi,indi2);
    elseif HRplt==10
        HRpltin(HRplt,HRnspt,HR,lnt,HRTb,rho,indi,indi2);
    elseif HRplt==11
        HRpltin(HRplt,HRnspt,HR,lnt,HRTb,thryrho,indi,indi2);
    end

    tst= input('\n\nDo you want to plot angain?\nEnter "0" for no "1"
for yes:  ');

end
% [AX,H1,H2]=plotyy(HRt,HRLVDT,HRt,HRTwtr)


%
%EVALUATE FURNACE BACKGROUND
%
function [TvD,TmpTvD]=BckGrnd



Tback=xlsread('SapBckGrnd.xlsx','B2:B16649');%MRF Back T/C (C)
t=xlsread('SapBckGrnd.xlsx','D2:D16649');%Time (min)
DelH=xlsread('SapBckGrnd.xlsx','F2:F16649');%Change in height (mm)


%smooth temperatures
Tback=smooth(t,Tback,300,'loess');
Del=DelH;
DelH=smooth(t,DelH,300,'loess');


%Standard
    Dst=5; %mm
    Hst=10.03; %mm
    dLL=xlsread('SapphireStandard.xlsx','B2:B41');
    T_dLL=xlsread('SapphireStandard.xlsx','A2:A41');

    sapDelH=interp1(T_dLL,dLL,Tback,'linear','extrap')*Hst*10^(-6);

    DelHp=DelH-sapDelH;


%subtract furnace Temp
N=9;

    [TvDH1,S1]=polyfit(Tback(1:792),DelHp(1:792),N);
```

```
    [TvDH2,S2]=polyfit(Tback(792:1758),DelHp(792:1758),N);
    [TvDH3,S3]=polyfit(Tback(2140:4300),DelHp(2140:4300),N);%2123

    TvD=[TvDH1;TvDH2;TvDH3];
    TmpTvD=[300;700;1600];

    tempY1=polyval(TvDH1,Tback(10:792));
    tempY2=polyval(TvDH2,Tback(792:1758));
    tempY3=polyval(TvDH3,Tback(2150:4300));

end


%This function gets the respective data from a sintering heat run from
the
%appropreate excel file


function [HRTb,HRt,HRdH,HRstrn,HRstrnrt,rho,thryrho] =
GetHRdata2(HR,TvD,TmpTvD)

fprintf('\n  [XXXXXXXX]\n  [')
    if HR==7
        HRTb=xlsread('HRs.xlsx','HR07','C370:C15288');%MRF Back T/C (C)
        fprintf('X')
        HRt=xlsread('HRs.xlsx','HR07','B370:B15288');%Time (min)
        fprintf('X')
        HRLVDT=xlsread('HRs.xlsx','HR07','G370:G15288');%LVDT signal
(V)
        fprintf('X')
        HRH=xlsread('HRs.xlsx','HR07','S2:S11');%Heigh measurements
        fprintf('X')
        rhof=xlsread('HRs.xlsx','HR07','W2');%final density
        thry=xlsread('HRs.xlsx','HR07','P2');%Theoretical density
        M=0.0298935;%Slope
        Vi=1.14505;%intial voltage

    elseif HR==8
        HRTb=xlsread('HRs.xlsx','HR08','C562:C14035');%MRF Back T/C (C)
        fprintf('X')
        HRt=xlsread('HRs.xlsx','HR08','B562:B14035');%Time (min)
        fprintf('X')
        HRLVDT=xlsread('HRs.xlsx','HR08','G562:G14035');%LVDT signal
(V)
        fprintf('X')
        HRH=xlsread('HRs.xlsx','HR08','S2:S11');%Heigh measurements
        fprintf('X')
        rhof=xlsread('HRs.xlsx','HR08','W2');%final density
        thry=xlsread('HRs.xlsx','HR08','P2');%Theoretical density
        M=0.0298935;
        Vi=1.12469;
```

```
    elseif HR==9
        HRTb=xlsread('HRs.xlsx','HR09','C480:C14462');%MRF Back T/C (C)
        fprintf('X')
        HRt=xlsread('HRs.xlsx','HR09','B480:B14462');%Time (min)
        fprintf('X')
        HRLVDT=xlsread('HRs.xlsx','HR09','G480:G14462');%LVDT signal
(V)
        fprintf('X')
        HRH=xlsread('HRs.xlsx','HR09','S2:S11');%Heigh measurements
        fprintf('X')
        rhof=xlsread('HRs.xlsx','HR09','W2');%final density
        thry=xlsread('HRs.xlsx','HR09','P2');%Theoretical density
        M=0.0298935;
        Vi=1.12469;

    elseif HR==10
        HRTb=xlsread('HRs.xlsx','HR10','C454:C16720');%MRF Back T/C (C)
        fprintf('X')
        HRt=xlsread('HRs.xlsx','HR10','B454:B16720');%Time (min)
        fprintf('X')
        HRLVDT=xlsread('HRs.xlsx','HR10','G454:G16720');%LVDT signal
(V)
        fprintf('X')
        HRH=xlsread('HRs.xlsx','HR10','S2:S11');%Heigh measurements
        fprintf('X')
        rhof=xlsread('HRs.xlsx','HR10','W2');%final density
        thry=xlsread('HRs.xlsx','HR10','P2');%Theoretical density
        M=0.0298935;
        Vi=1.26720;

    else
        fprintf('Not Valid Heat Run\n\n')
    end
    fprintf(']\n')

%Smooth Data
    fprintf('  [')
    fprintf('X')
    HRTb=smooth(HRt,HRTb,150,'loess');
    fprintf('X')
    HRLVDT=smooth(HRt,HRLVDT,300,'loess');
    fprintf('X')

%Solve for HRdH
    HRdH=(HRLVDT-Vi)*M*25.4;%25.4 converts from in to mm
    %find the indaceas for each temperature
    [j2,j3]=timecrct(HRt,HRTb);
    j1=dsearchn(HRTb(1:j2),TmpTvD(1));
    j4=dsearchn(HRTb((j3):end),TmpTvD(2))+j3;
    j5=dsearchn(HRTb((j3):end),TmpTvD(1))+j3;
    %correcting DH by subtracting out background
    HRdH(1:j1)=HRdH(1:j1)-polyval(TvD(1,:),HRTb(1:j1));
    HRdH(j1+1:j2)=HRdH(j1+1:j2)-polyval(TvD(2,:),HRTb(j1+1:j2));
```

```
    HRdH(j2+1:j4)=HRdH(j2+1:j4)-polyval(TvD(3,:),HRTb(j2+1:j4));
    HRdH(j4+1:j5)=HRdH(j4+1:j5)-polyval(TvD(2,:),HRTb(j4+1:j5));
    HRdH(j5+1:end)=HRdH(j5+1:end)-polyval(TvD(1,:),HRTb(j5+1:end));

%Solve fro strain and strain rate
    Hi=mean(HRH(find(HRH)));
    HRstrn=HRdH/Hi;

HRstrnrt=gradient(smooth(HRt,HRstrn,300,'loess'))./gradient(HRt*60);
    HRstrn=smooth(HRt,HRstrn,300,'loess');
    fprintf('X')
    HRstrnrt=smooth(HRt,HRstrnrt,500,'loess');
    fprintf('X]\n')

%Density measurements
    rho=rhof*((HRstrn(j3)+1).^3).*((HRstrn+1).^(-3));
    thryrho=rho*100/thry;
end



%
%Aligns LVDT signal

function [j,j2]=timecrct(t,Tmp)

indi=find(Tmp>600&Tmp<800&t<400&t>10);
dTdt=gradient(Tmp)./gradient(t);
ddTddt=gradient(dTdt)./gradient(t);

[M,Mi]=max(ddTddt(indi));

j=indi(1)+Mi;

indi2=find(Tmp>1550&Tmp<1650&t>(200+t(j)));

[M2,Mi2]=min(ddTddt(indi2));

j2=indi2(1)+Mi2;

plotyy(t(indi2),ddTddt(indi2),t(indi2),Tmp(indi2))

Tmp(j2)
end



function HRpltin(HRplt,HRnspt,HR,lnt,X,Y,in,in2)


HRlnt=length(HRnspt);
HRndx=zeros(1,HRlnt);
```

```
HRnspt=sort(HRnspt);
for k=1:HRlnt
    HRndx(k)=find((HR-HRnspt(k))./(HR-HRnspt(k))-1);
    %Set legend
    if HRnspt(k)<10
        HRLeg(k,1:4)=sprintf('HR0%1i',HRnspt(k));
    else
        HRLeg(k,1:4)=sprintf('HR%2i',HRnspt(k));
    end

end

HRndx

%set Axis
if HRplt==1
    axX='Time (hr)';
    axY='Height Change (mm)';
elseif HRplt==2
    axX=sprintf('Temperature (%cC)', char(176));
    axY='Height Change (mm)';
elseif HRplt==3
    axX='Time (hr)';
    axY=sprintf('Temperature (%cC)', char(176));
elseif HRplt==4
    axX='Time (hr)';
    axY='Strain';
elseif HRplt==5
    axX='Time (hr)';
    axY='StrainRate (s^(-1))';
elseif HRplt==6
    axX=sprintf('Temperature (%cC)', char(176));
    axY='Strain';
elseif HRplt==7
    axX=sprintf('Temperature (%cC)', char(176));
    axY='Strain Rate (s^(-1))';
elseif HRplt==8
    axX='Time (hr)';
    axY='Density (g/cc)';
elseif HRplt==9
    axX='Time (hr)';
    axY='Relative Density (%)';
elseif HRplt==10
    axX=sprintf('Temperature (%cC)', char(176));
    axY='Density (g/cc)';
elseif HRplt==11
    axX=sprintf('Temperature (%cC)', char(176));
    axY='Relative Density (%)';
end

if HRlnt==1
    %plot(X(1:lnt(HRndx(1)),HRndx(1)),Y(1:lnt(HRndx(1)),HRndx(1)),'k-')
    %plot(X(1:lnt(HRndx(1)),HRndx(1)),Y(1:lnt(HRndx(1)),HRndx(1)))
```

```
    plot(X(in:in2,HRndx(1)),Y(in:in2,HRndx(1)))
    legend(HRLeg)
    xlabel(axX)
    ylabel(axY)
elseif HRlnt==2
    %plot(X(1:lnt(HRndx(1)),HRndx(1)),Y(1:lnt(HRndx(1)),HRndx(1)),'k-
',X(1:lnt(HRndx(2)),HRndx(2)),Y(1:lnt(HRndx(2)),HRndx(2)),'k--')

%plot(X(1:lnt(HRndx(1)),HRndx(1)),Y(1:lnt(HRndx(1)),HRndx(1)),X(1:lnt(H
Rndx(2)),HRndx(2)),Y(1:lnt(HRndx(2)),HRndx(2)))

plot(X(in(HRndx(1)):in2(HRndx(1)),HRndx(1)),Y(in(HRndx(1)):in2(HRndx(1)
),HRndx(1)),X(in(HRndx(2)):in2(HRndx(2)),HRndx(2)),Y(in(HRndx(2)):in2(H
Rndx(2)),HRndx(2)))
    legend(HRLeg)
    xlabel(axX)
    ylabel(axY)
elseif HRlnt==3
    %plot(X(1:lnt(HRndx(1)),HRndx(1)),Y(1:lnt(HRndx(1)),HRndx(1)),'k-
',X(1:lnt(HRndx(2)),HRndx(2)),Y(1:lnt(HRndx(2)),HRndx(2)),'k--
',X(1:lnt(HRndx(3)),HRndx(3)),Y(1:lnt(HRndx(3)),HRndx(3)),'k-.')

%plot(X(1:lnt(HRndx(1)),HRndx(1)),Y(1:lnt(HRndx(1)),HRndx(1)),X(1:lnt(H
Rndx(2)),HRndx(2)),Y(1:lnt(HRndx(2)),HRndx(2)),X(1:lnt(HRndx(3)),HRndx(
3)),Y(1:lnt(HRndx(3)),HRndx(3)))

plot(X(in(HRndx(1)):in2(HRndx(1)),HRndx(1)),Y(in(HRndx(1)):in2(HRndx(1)
),HRndx(1)),X(in(HRndx(2)):in2(HRndx(2)),HRndx(2)),Y(in(HRndx(2)):in2(H
Rndx(2)),HRndx(2)),X(in(HRndx(3)):in2(HRndx(3)),HRndx(3)),Y(in(HRndx(3)
):in2(HRndx(3)),HRndx(3)))
    legend(HRLeg)
    xlabel(axX)
    ylabel(axY)
else
    %plot(X(1:lnt(HRndx(1)),HRndx(1)),Y(1:lnt(HRndx(1)),HRndx(1)),'k-
',X(1:lnt(HRndx(2)),HRndx(2)),Y(1:lnt(HRndx(2)),HRndx(2)),'k--
',X(1:lnt(HRndx(3)),HRndx(3)),Y(1:lnt(HRndx(3)),HRndx(3)),'k-
.',X(1:lnt(HRndx(4)),HRndx(4)),Y(1:lnt(HRndx(4)),HRndx(4)),'k:')

%plot(X(1:lnt(HRndx(1)),HRndx(1)),Y(1:lnt(HRndx(1)),HRndx(1)),X(1:lnt(H
Rndx(2)),HRndx(2)),Y(1:lnt(HRndx(2)),HRndx(2)),X(1:lnt(HRndx(3)),HRndx(
3)),Y(1:lnt(HRndx(3)),HRndx(3)),X(1:lnt(HRndx(4)),HRndx(4)),Y(1:lnt(HRn
dx(4)),HRndx(4)))

plot(X(in(HRndx(1)):in2(HRndx(1)),HRndx(1)),Y(in(HRndx(1)):in2(HRndx(1)
),HRndx(1)),X(in(HRndx(2)):in2(HRndx(2)),HRndx(2)),Y(in(HRndx(2)):in2(H
Rndx(2)),HRndx(2)),X(in(HRndx(3)):in2(HRndx(3)),HRndx(3)),Y(in(HRndx(3)
):in2(HRndx(3)),HRndx(3)),X(in(HRndx(4)):in2(HRndx(4)),HRndx(4)),Y(in(H
Rndx(4)):in2(HRndx(4)),HRndx(4)))
    %legend(HRLeg)
    legend('10 vol%','7.5 vol%','5 vol%','2.5
vol%','Location','SouthEast')
    xlabel(axX)
```

```
    ylabel(axY)
end

h=gcf;
%set(findall(h,'type','text'),'fontSize',16,'fontWeight','bold')

% if HRplt==7||HRplt==5
%     ylim([-0.00005,0.00005])
% end
%


end
```

APPENIDIX F

UO_2 POWDER IMPURITY TESTS

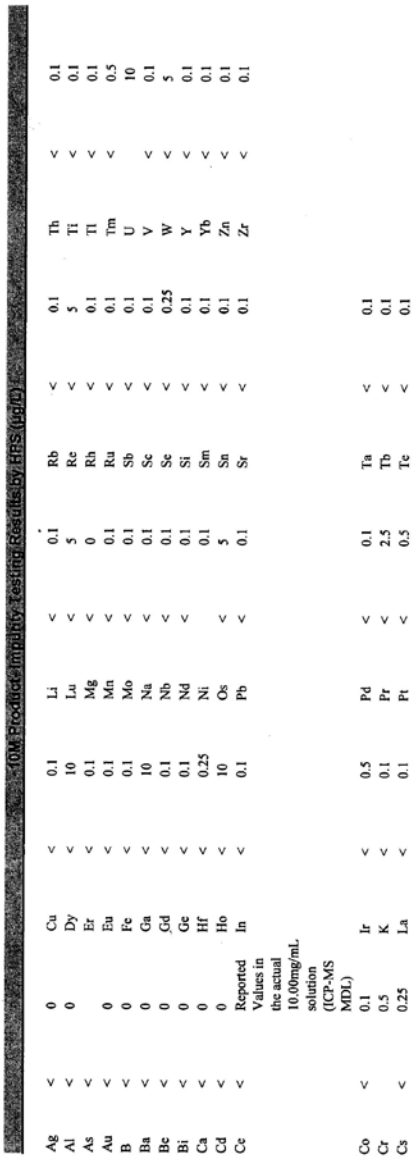

ICM Product Impurity Testing Results by HRS (ppm)

Ag	<	0	Cu	<	0.1	Li	<	0.1	Rb	<	0.1	Th	<	0.1
Al	<	0	Dy	<	10	Lu	<	5	Re	<	5	Ti	<	0.1
As	<		Er	<	0.1	Mg	<	0	Rh	<	0.1	Tl	<	0.1
Au	<	0	Eu	<	0.1	Mn	<	0.1	Ru	<	0.1	Tm	<	0.5
B	<	0	Fe	<	0.1	Mo	<	0.1	Sb	<	0.1	U		10
Ba	<	0	Ga	<	10	Na	<	0.1	Sc	<	0.1	V	<	0.1
Be	<	0	Gd	<	0.1	Nb	<	0.1	Se	<	0.25	W	<	5
Bi	<	0	Ge	<	0.1	Nd	<	0.1	Si	<	0.1	Y	<	0.1
Ca	<	0	Hf	<	0.25	Ni		0.1	Sm	<	0.1	Yb	<	0.1
Cd	<	0	Ho	<	10	Os	<	5	Sn	<	0.1	Zn	<	0.1
Ce	<	Reported Values in the actual 10.00mg/mL solution (ICP-MS MDL)	In	<	0.1	Pb	<	0.1	Sr	<	0.1	Zr	<	0.1
Co	<	0.1	Ir	<	0.5	Pd	<	0.1	Ta	<	0.1			
Cr		0.5	K	<	0.1	Pr	<	2.5	Tb	<	0.1			
Cs	<	0.25	La	<	0.1	Pt	<	0.5	Te	<	0.1			

Ours UO_2 Pure for Rack

10M Product Impurity Testing Results by HPS (ug/L)													
Ag	<	0	Cu	<	0.1	Li	<	0.1	Rb	<	0.1	Th	<	0.1
Al	<	0	Dy	<	10	Lu	<	5	Re	<	5	Ti	<	0.1
As	<		Er	<	0.1	Mg	<	0	Rh	<	0.1	Tl	<	0.1
Au	<	0	Eu	<	0.1	Mn	<	0.1	Ru	<	0.1	Tm	<	0.5
B	<	0	Fe	<	0.1	Mo	<	0.1	Sb	<	0.1	U		10
Ba	<	0	Ga	<	10	Na	<	0.1	Sc	<	0.1	V	<	0.1
Be	<	0	Gd	<	0.1	Nb	<	0.1	Se	<	0.25	W	<	5
Bi	<	0	Ge	<	0.1	Nd	<	0.1	Si	<	0.1	Y	<	0.1
Ca	<	0	Hf	<	0.25	Ni		0.1	Sm	<	0.1	Yb	<	0.1
Cd	<	0	Ho	<	10	Os	<	5	Sn	<	0.1	Zn	<	0.1
Ce	<	Reported Values in the actual 10.00mg/mL solution (ICP-MS MDL)	In	<	0.1	Pb	<	0.1	Sr	<	0.1	Zr	<	0.1
Co	<	0.1	Ir	<	0.5	Pd	<	0.1	Ta	<	0.1			
Cr		0.5	K	<	0.1	Pr	<	2.5	Tb	<	0.1			
Cs	<	0.25	La	<	0.1	Pt	<	0.5	Te	<	0.1			

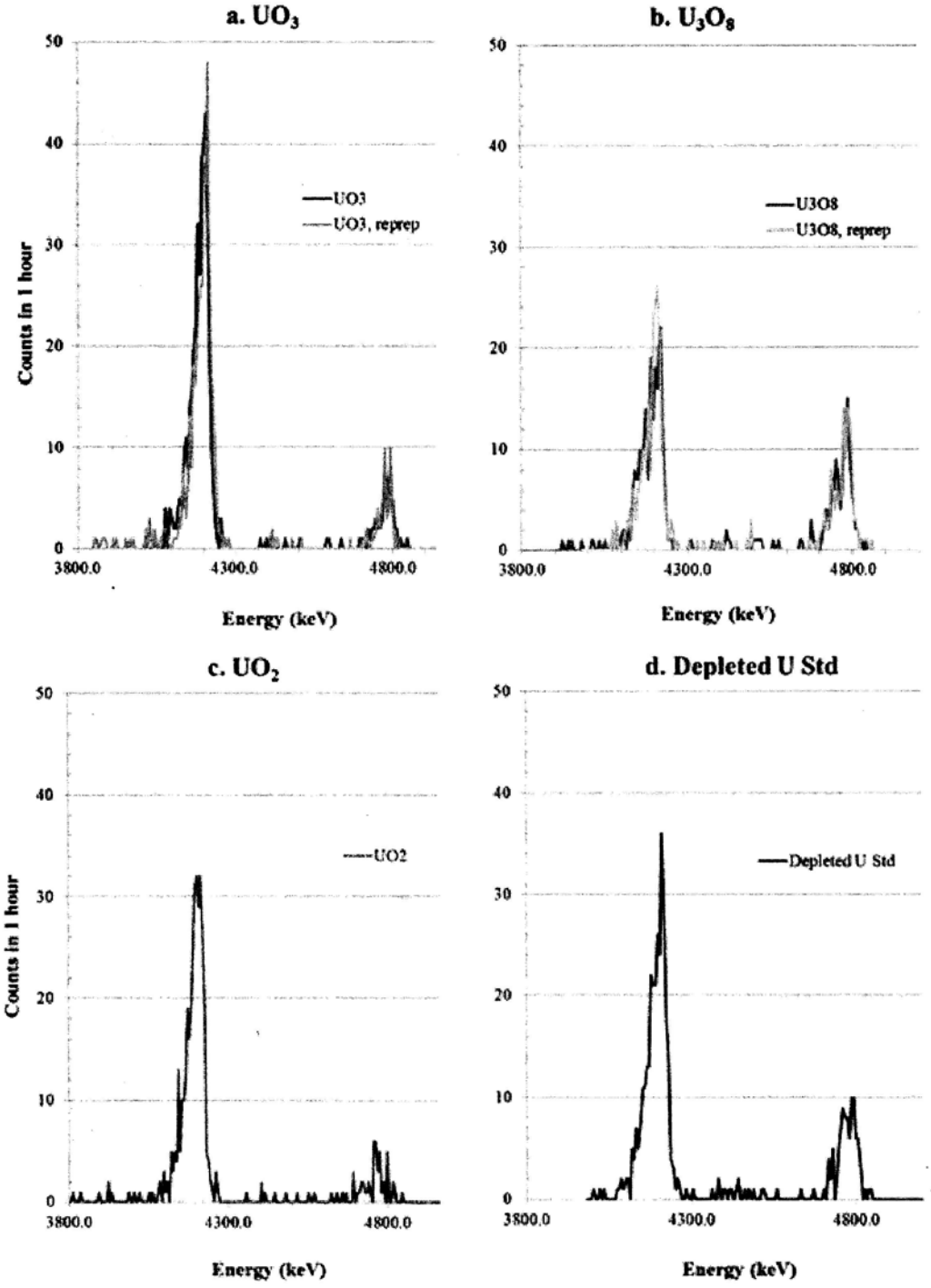
a. UO3
b. U3O8
c. UO2
d. Depleted U Std
Counts in 1 hour
Energy (keV)
UO3
UO3, reprep
U3O8
U3O8, reprep
UO2
Depleted U Std
3800.0
4300.0
4800.0
0
10
20
30
40
50

APPENDIX G

BSE IMAGES ANALIZED

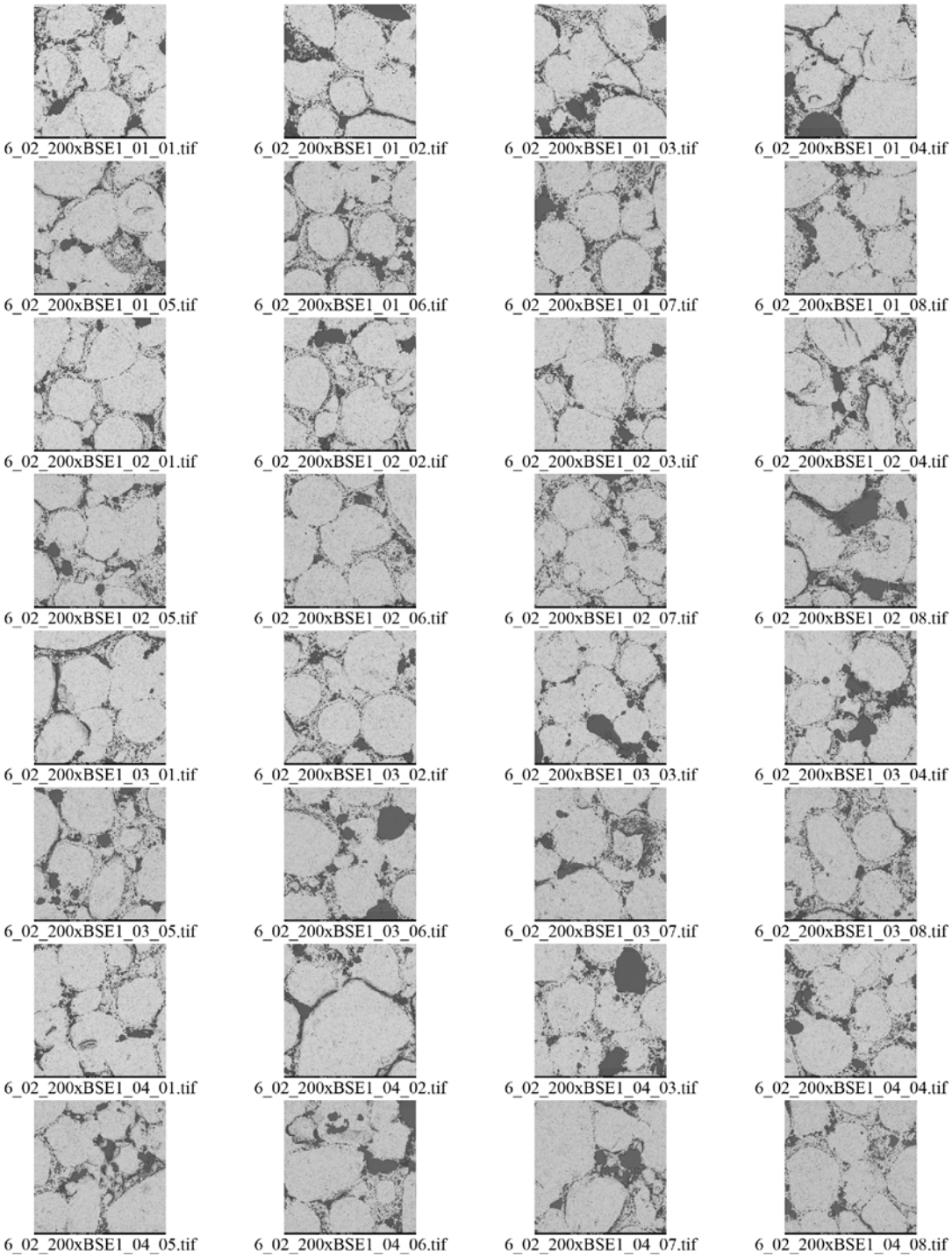

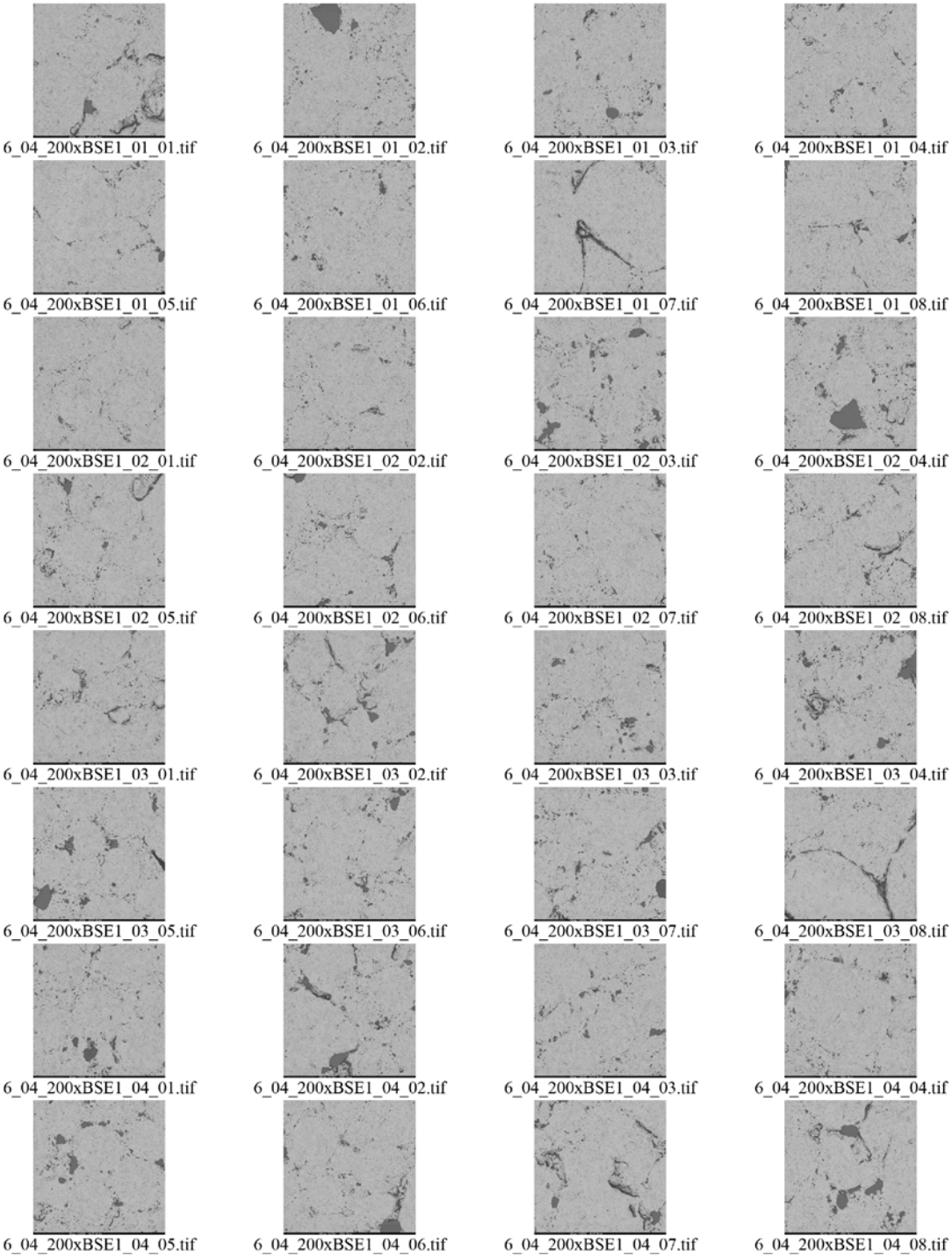
6_04_200xBSE1_01_01.tif
6_04_200xBSE1_01_02.tif
6_04_200xBSE1_01_03.tif
6_04_200xBSE1_01_04.tif
6_04_200xBSE1_01_05.tif
6_04_200xBSE1_01_06.tif
6_04_200xBSE1_01_07.tif
6_04_200xBSE1_01_08.tif
6_04_200xBSE1_02_01.tif
6_04_200xBSE1_02_02.tif
6_04_200xBSE1_02_03.tif
6_04_200xBSE1_02_04.tif
6_04_200xBSE1_02_05.tif
6_04_200xBSE1_02_06.tif
6_04_200xBSE1_02_07.tif
6_04_200xBSE1_02_08.tif
6_04_200xBSE1_03_01.tif
6_04_200xBSE1_03_02.tif
6_04_200xBSE1_03_03.tif
6_04_200xBSE1_03_04.tif
6_04_200xBSE1_03_05.tif
6_04_200xBSE1_03_06.tif
6_04_200xBSE1_03_07.tif
6_04_200xBSE1_03_08.tif
6_04_200xBSE1_04_01.tif
6_04_200xBSE1_04_02.tif
6_04_200xBSE1_04_03.tif
6_04_200xBSE1_04_04.tif
6_04_200xBSE1_04_05.tif
6_04_200xBSE1_04_06.tif
6_04_200xBSE1_04_07.tif
6_04_200xBSE1_04_08.tif

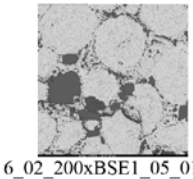
6_02_200xBSE1_05_01.tif

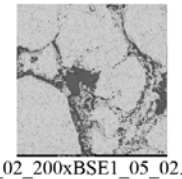
6_02_200xBSE1_05_02.tif

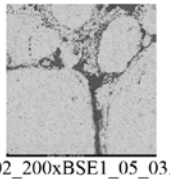
6_02_200xBSE1_05_03.tif

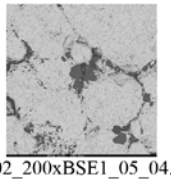
6_02_200xBSE1_05_04.tif

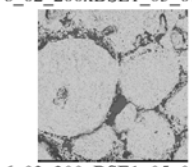
6_02_200xBSE1_05_05.tif

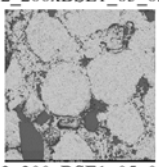
6_02_200xBSE1_05_06.tif

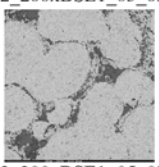
6_02_200xBSE1_05_07.tif

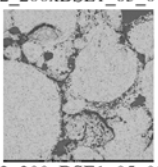
6_02_200xBSE1_05_08.tif

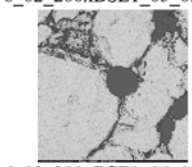
6_02_200xBSE1_06_01.tif

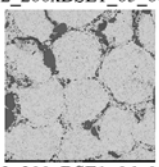
6_02_200xBSE1_06_02.tif

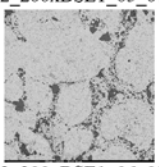
6_02_200xBSE1_06_03.tif

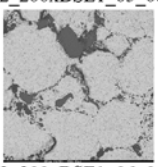
6_02_200xBSE1_06_04.tif

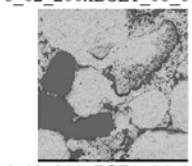
6_02_200xBSE1_06_05.tif

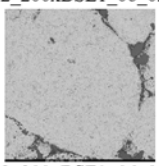
6_02_200xBSE1_06_06.tif

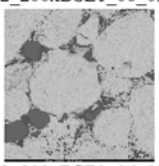
6_02_200xBSE1_06_07.tif

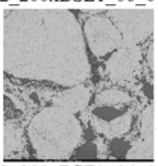
6_02_200xBSE1_06_08.tif

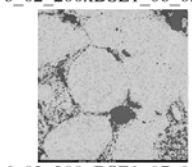
6_02_200xBSE1_07_01.tif

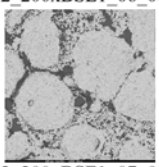
6_02_200xBSE1_07_02.tif

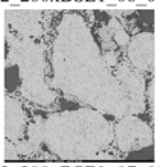
6_02_200xBSE1_07_03.tif

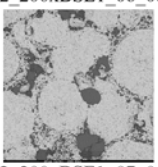
6_02_200xBSE1_07_04.tif

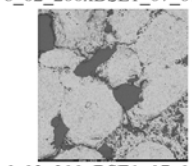
6_02_200xBSE1_07_05.tif

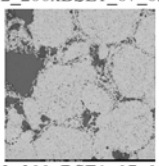
6_02_200xBSE1_07_06.tif

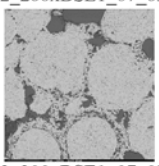
6_02_200xBSE1_07_07.tif

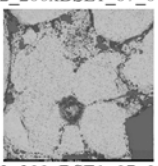
6_02_200xBSE1_07_08.tif

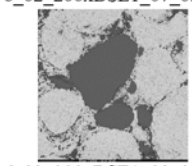
6_02_200xBSE1_08_01.tif

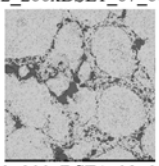
6_02_200xBSE1_08_02.tif

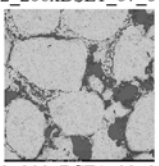
6_02_200xBSE1_08_03.tif

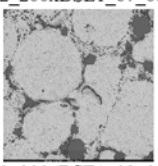
6_02_200xBSE1_08_04.tif

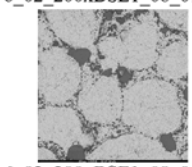
6_02_200xBSE1_08_05.tif

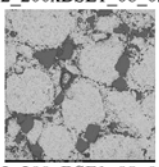
6_02_200xBSE1_08_06.tif

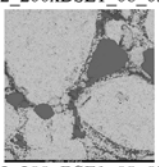
6_02_200xBSE1_08_07.tif

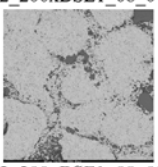
6_02_200xBSE1_08_08.tif

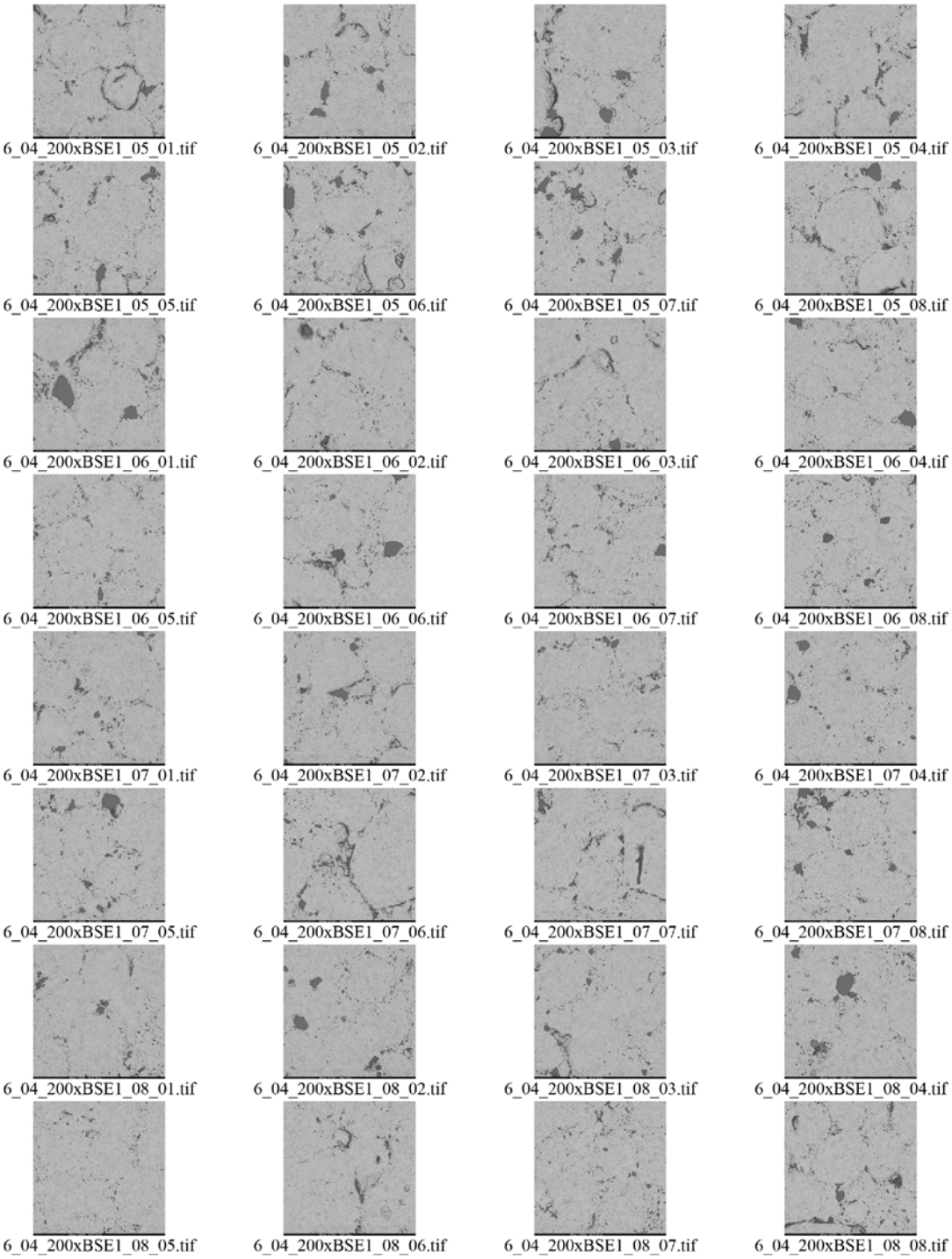
6_04_200xBSE1_05_01.tif
6_04_200xBSE1_05_02.tif
6_04_200xBSE1_05_03.tif
6_04_200xBSE1_05_04.tif
6_04_200xBSE1_05_05.tif
6_04_200xBSE1_05_06.tif
6_04_200xBSE1_05_07.tif
6_04_200xBSE1_05_08.tif
6_04_200xBSE1_06_01.tif
6_04_200xBSE1_06_02.tif
6_04_200xBSE1_06_03.tif
6_04_200xBSE1_06_04.tif
6_04_200xBSE1_06_05.tif
6_04_200xBSE1_06_06.tif
6_04_200xBSE1_06_07.tif
6_04_200xBSE1_06_08.tif
6_04_200xBSE1_07_01.tif
6_04_200xBSE1_07_02.tif
6_04_200xBSE1_07_03.tif
6_04_200xBSE1_07_04.tif
6_04_200xBSE1_07_05.tif
6_04_200xBSE1_07_06.tif
6_04_200xBSE1_07_07.tif
6_04_200xBSE1_07_08.tif
6_04_200xBSE1_08_01.tif
6_04_200xBSE1_08_02.tif
6_04_200xBSE1_08_03.tif
6_04_200xBSE1_08_04.tif
6_04_200xBSE1_08_05.tif
6_04_200xBSE1_08_06.tif
6_04_200xBSE1_08_07.tif
6_04_200xBSE1_08_08.tif

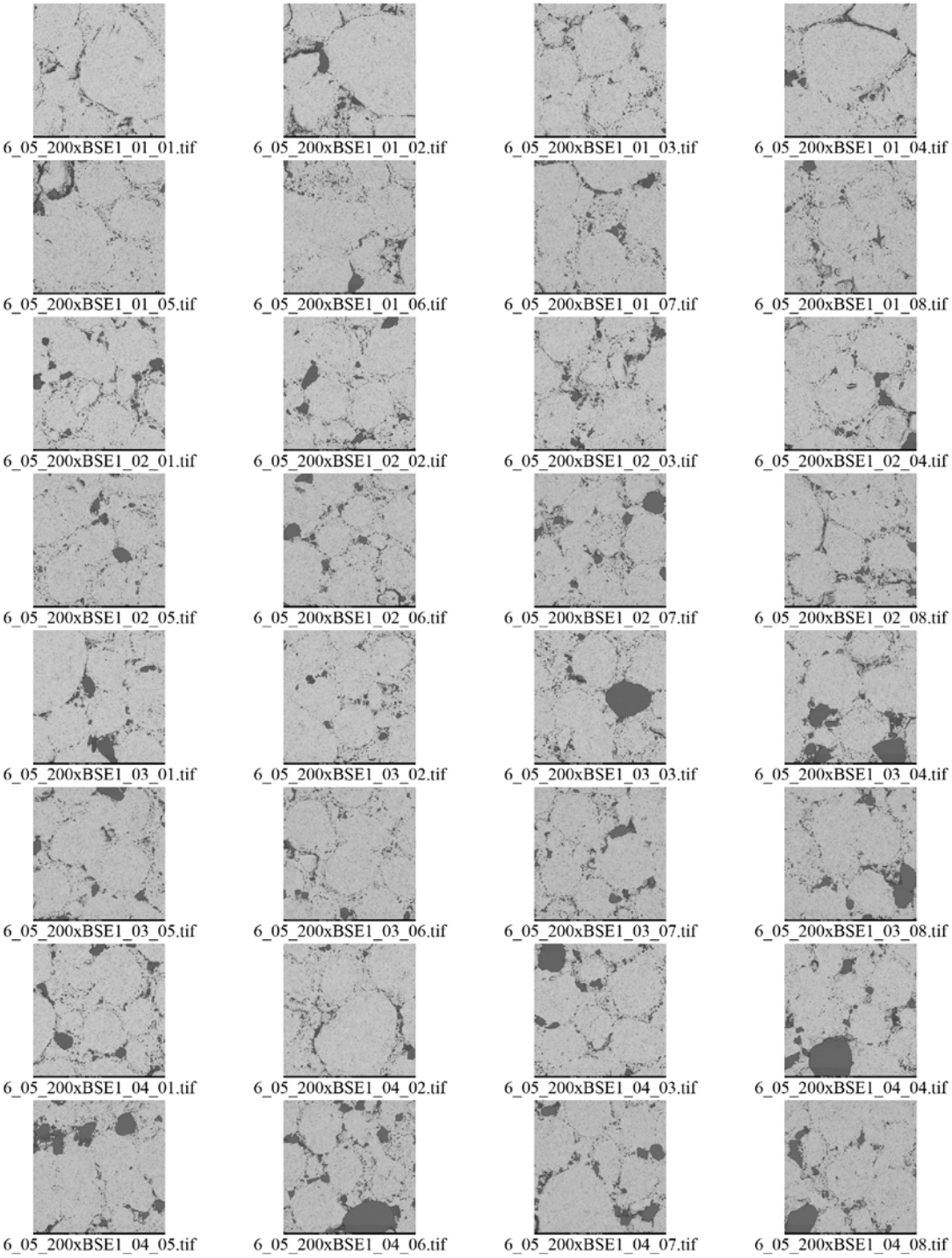
6_05_200xBSE1_01_01.tif
6_05_200xBSE1_01_02.tif
6_05_200xBSE1_01_03.tif
6_05_200xBSE1_01_04.tif
6_05_200xBSE1_01_05.tif
6_05_200xBSE1_01_06.tif
6_05_200xBSE1_01_07.tif
6_05_200xBSE1_01_08.tif
6_05_200xBSE1_02_01.tif
6_05_200xBSE1_02_02.tif
6_05_200xBSE1_02_03.tif
6_05_200xBSE1_02_04.tif
6_05_200xBSE1_02_05.tif
6_05_200xBSE1_02_06.tif
6_05_200xBSE1_02_07.tif
6_05_200xBSE1_02_08.tif
6_05_200xBSE1_03_01.tif
6_05_200xBSE1_03_02.tif
6_05_200xBSE1_03_03.tif
6_05_200xBSE1_03_04.tif
6_05_200xBSE1_03_05.tif
6_05_200xBSE1_03_06.tif
6_05_200xBSE1_03_07.tif
6_05_200xBSE1_03_08.tif
6_05_200xBSE1_04_01.tif
6_05_200xBSE1_04_02.tif
6_05_200xBSE1_04_03.tif
6_05_200xBSE1_04_04.tif
6_05_200xBSE1_04_05.tif
6_05_200xBSE1_04_06.tif
6_05_200xBSE1_04_07.tif
6_05_200xBSE1_04_08.tif

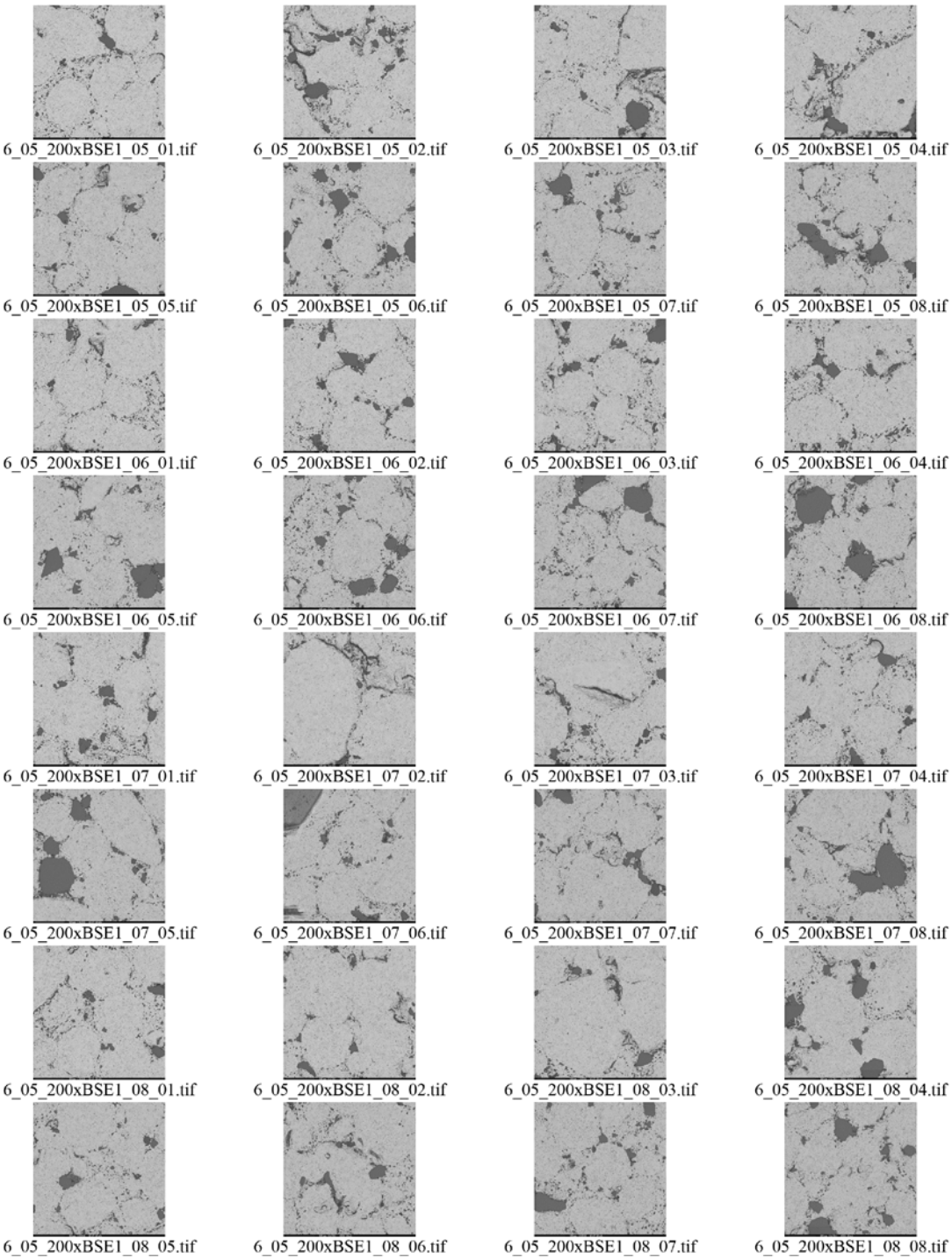
6_05_200xBSE1_05_01.tif
6_05_200xBSE1_05_02.tif
6_05_200xBSE1_05_03.tif
6_05_200xBSE1_05_04.tif
6_05_200xBSE1_05_05.tif
6_05_200xBSE1_05_06.tif
6_05_200xBSE1_05_07.tif
6_05_200xBSE1_05_08.tif
6_05_200xBSE1_06_01.tif
6_05_200xBSE1_06_02.tif
6_05_200xBSE1_06_03.tif
6_05_200xBSE1_06_04.tif
6_05_200xBSE1_06_05.tif
6_05_200xBSE1_06_06.tif
6_05_200xBSE1_06_07.tif
6_05_200xBSE1_06_08.tif
6_05_200xBSE1_07_01.tif
6_05_200xBSE1_07_02.tif
6_05_200xBSE1_07_03.tif
6_05_200xBSE1_07_04.tif
6_05_200xBSE1_07_05.tif
6_05_200xBSE1_07_06.tif
6_05_200xBSE1_07_07.tif
6_05_200xBSE1_07_08.tif
6_05_200xBSE1_08_01.tif
6_05_200xBSE1_08_02.tif
6_05_200xBSE1_08_03.tif
6_05_200xBSE1_08_04.tif
6_05_200xBSE1_08_05.tif
6_05_200xBSE1_08_06.tif
6_05_200xBSE1_08_07.tif
6_05_200xBSE1_08_08.tif

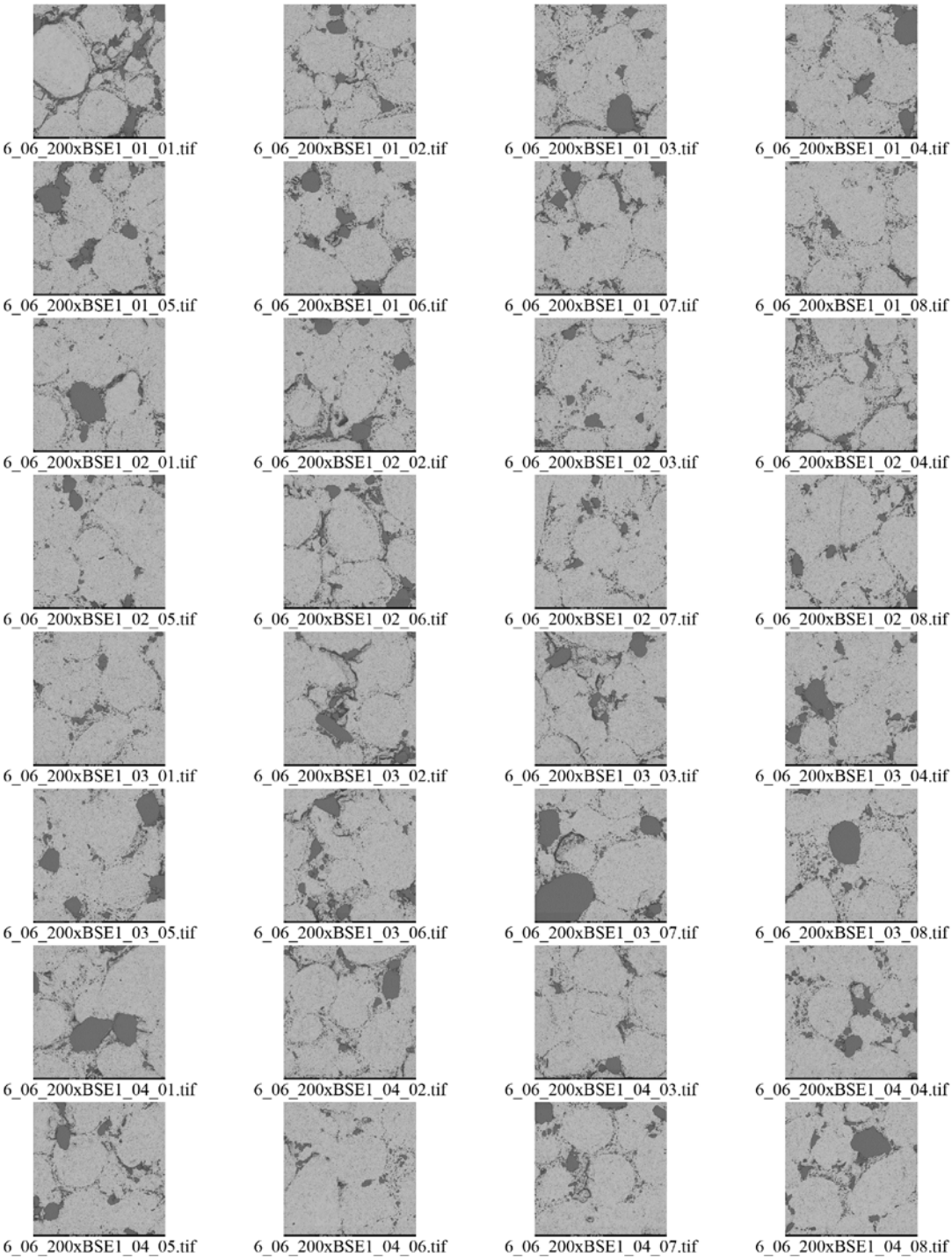
6_06_200xBSE1_01_01.tif
6_06_200xBSE1_01_02.tif
6_06_200xBSE1_01_03.tif
6_06_200xBSE1_01_04.tif
6_06_200xBSE1_01_05.tif
6_06_200xBSE1_01_06.tif
6_06_200xBSE1_01_07.tif
6_06_200xBSE1_01_08.tif
6_06_200xBSE1_02_01.tif
6_06_200xBSE1_02_02.tif
6_06_200xBSE1_02_03.tif
6_06_200xBSE1_02_04.tif
6_06_200xBSE1_02_05.tif
6_06_200xBSE1_02_06.tif
6_06_200xBSE1_02_07.tif
6_06_200xBSE1_02_08.tif
6_06_200xBSE1_03_01.tif
6_06_200xBSE1_03_02.tif
6_06_200xBSE1_03_03.tif
6_06_200xBSE1_03_04.tif
6_06_200xBSE1_03_05.tif
6_06_200xBSE1_03_06.tif
6_06_200xBSE1_03_07.tif
6_06_200xBSE1_03_08.tif
6_06_200xBSE1_04_01.tif
6_06_200xBSE1_04_02.tif
6_06_200xBSE1_04_03.tif
6_06_200xBSE1_04_04.tif
6_06_200xBSE1_04_05.tif
6_06_200xBSE1_04_06.tif
6_06_200xBSE1_04_07.tif
6_06_200xBSE1_04_08.tif

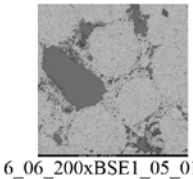
6_06_200xBSE1_05_01.tif

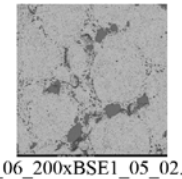
6_06_200xBSE1_05_02.tif

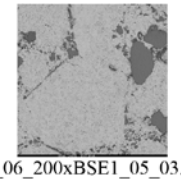
6_06_200xBSE1_05_03.tif

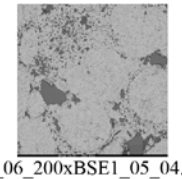
6_06_200xBSE1_05_04.tif

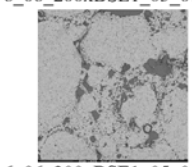
6_06_200xBSE1_05_05.tif

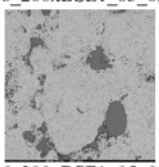
6_06_200xBSE1_05_06.tif

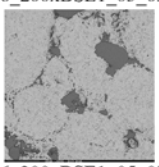
6_06_200xBSE1_05_07.tif

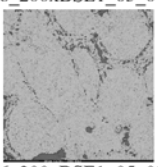
6_06_200xBSE1_05_08.tif

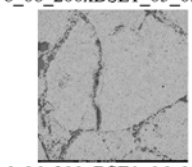
6_06_200xBSE1_06_01.tif

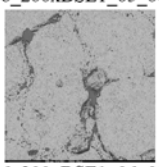
6_06_200xBSE1_06_02.tif

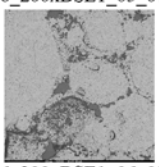
6_06_200xBSE1_06_03.tif

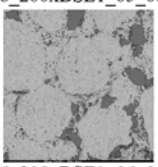
6_06_200xBSE1_06_04.tif

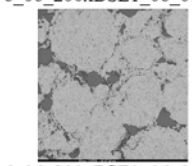
6_06_200xBSE1_06_05.tif

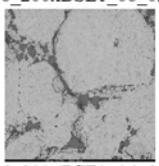
6_06_200xBSE1_06_06.tif

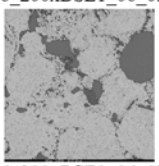
6_06_200xBSE1_06_07.tif

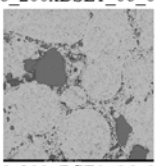
6_06_200xBSE1_06_08.tif

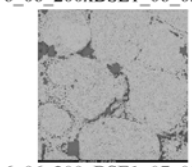
6_06_200xBSE1_07_01.tif

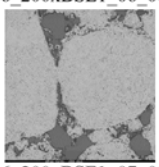
6_06_200xBSE1_07_02.tif

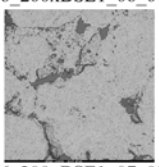
6_06_200xBSE1_07_03.tif

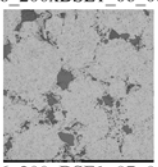
6_06_200xBSE1_07_04.tif

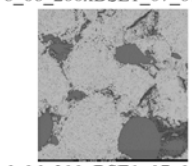
6_06_200xBSE1_07_05.tif

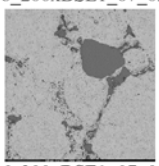
6_06_200xBSE1_07_06.tif

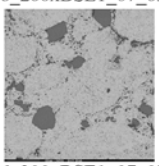
6_06_200xBSE1_07_07.tif

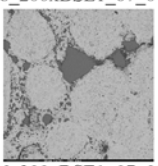
6_06_200xBSE1_07_08.tif

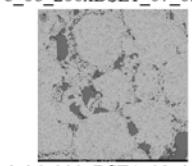
6_06_200xBSE1_08_01.tif

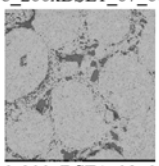
6_06_200xBSE1_08_02.tif

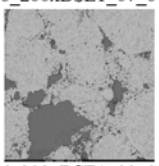
6_06_200xBSE1_08_03.tif

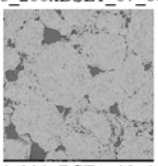
6_06_200xBSE1_08_04.tif

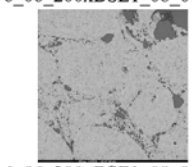
6_06_200xBSE1_08_05.tif

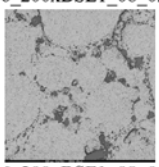
6_06_200xBSE1_08_06.tif

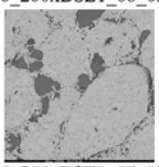
6_06_200xBSE1_08_07.tif

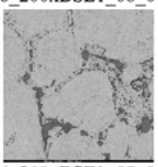
6_06_200xBSE1_08_08.tif

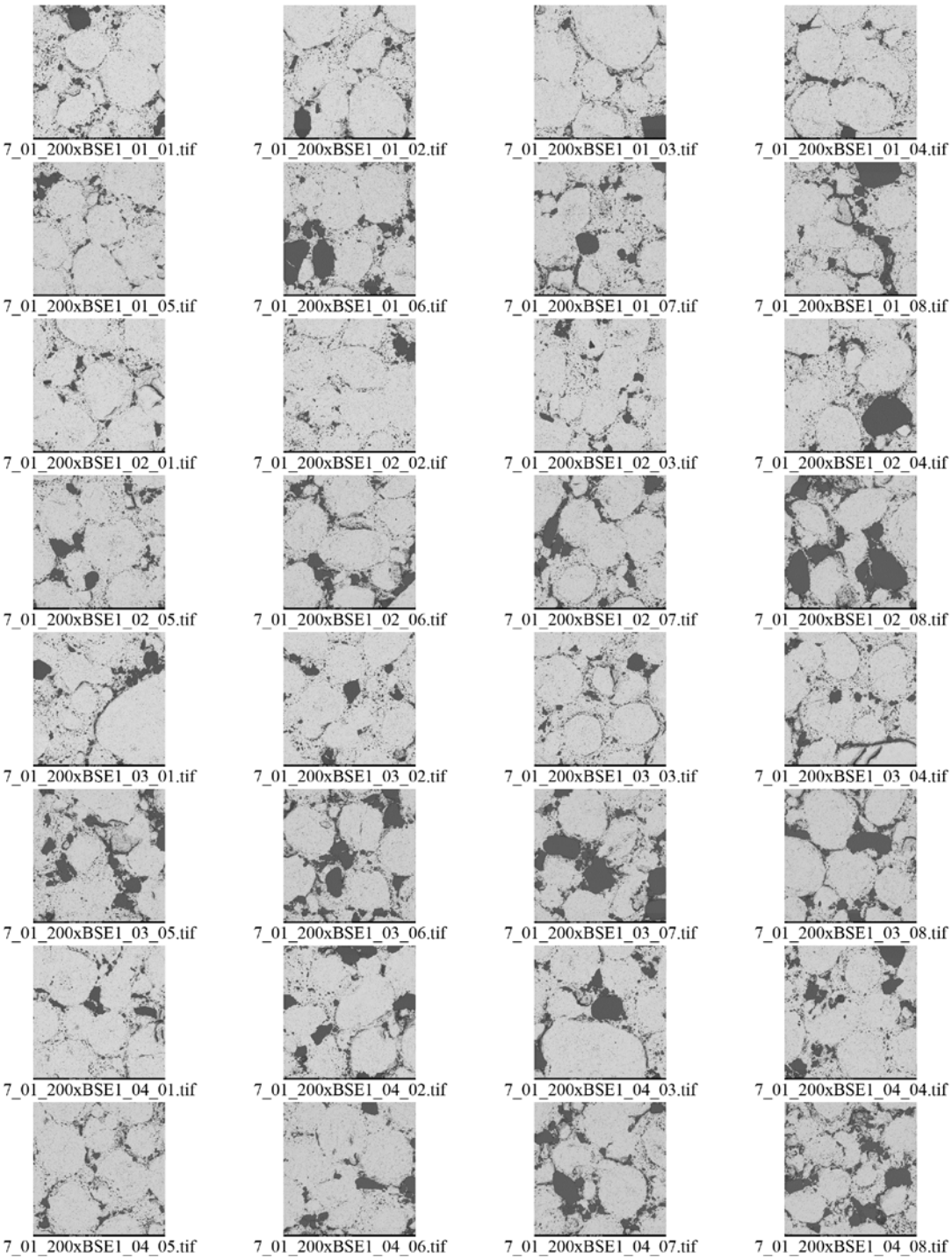
7_01_200xBSE1_01_01.tif
7_01_200xBSE1_01_02.tif
7_01_200xBSE1_01_03.tif
7_01_200xBSE1_01_04.tif
7_01_200xBSE1_01_05.tif
7_01_200xBSE1_01_06.tif
7_01_200xBSE1_01_07.tif
7_01_200xBSE1_01_08.tif
7_01_200xBSE1_02_01.tif
7_01_200xBSE1_02_02.tif
7_01_200xBSE1_02_03.tif
7_01_200xBSE1_02_04.tif
7_01_200xBSE1_02_05.tif
7_01_200xBSE1_02_06.tif
7_01_200xBSE1_02_07.tif
7_01_200xBSE1_02_08.tif
7_01_200xBSE1_03_01.tif
7_01_200xBSE1_03_02.tif
7_01_200xBSE1_03_03.tif
7_01_200xBSE1_03_04.tif
7_01_200xBSE1_03_05.tif
7_01_200xBSE1_03_06.tif
7_01_200xBSE1_03_07.tif
7_01_200xBSE1_03_08.tif
7_01_200xBSE1_04_01.tif
7_01_200xBSE1_04_02.tif
7_01_200xBSE1_04_03.tif
7_01_200xBSE1_04_04.tif
7_01_200xBSE1_04_05.tif
7_01_200xBSE1_04_06.tif
7_01_200xBSE1_04_07.tif
7_01_200xBSE1_04_08.tif

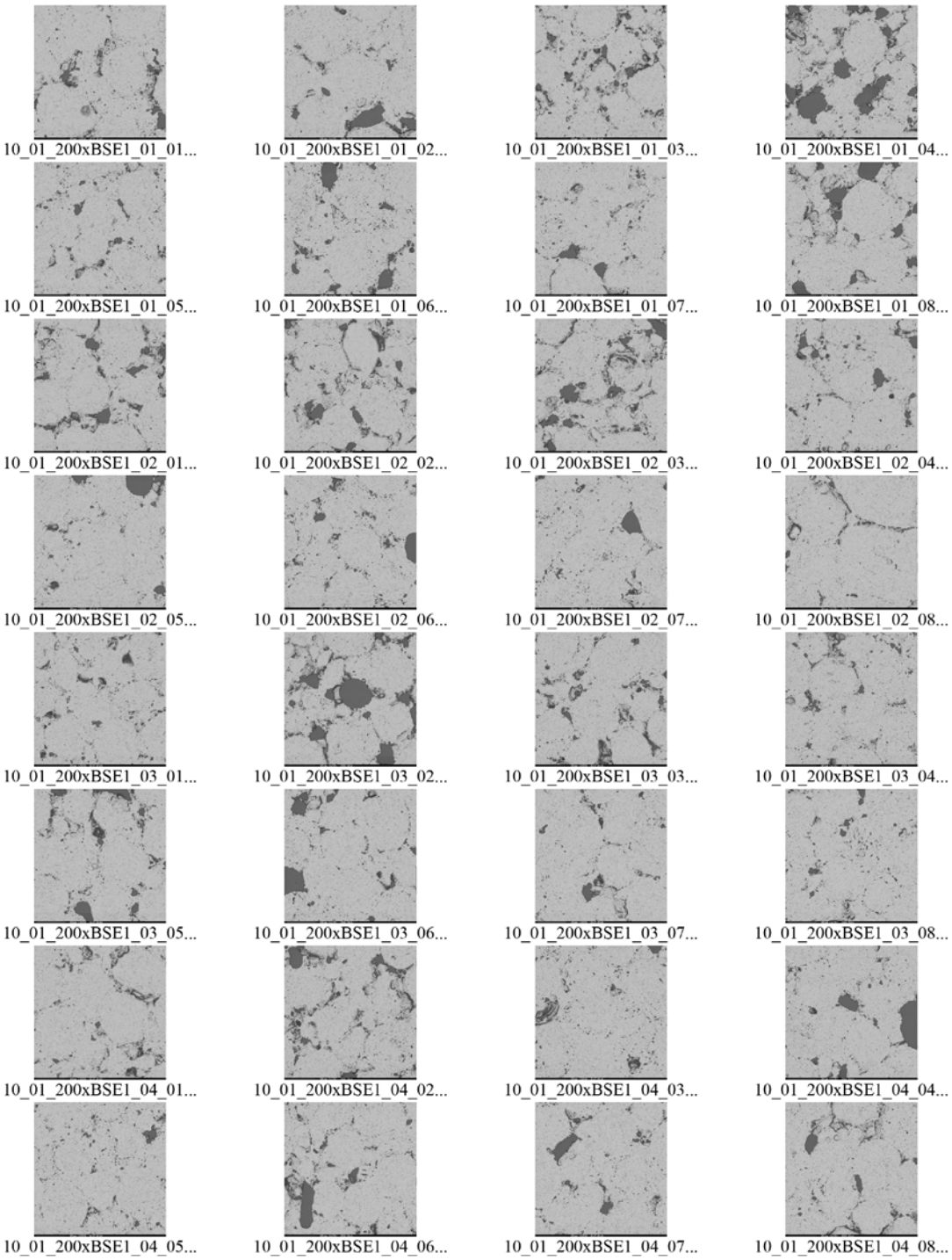
10_01_200xBSE1_01_01...
10_01_200xBSE1_01_02...
10_01_200xBSE1_01_03...
10_01_200xBSE1_01_04...
10_01_200xBSE1_01_05...
10_01_200xBSE1_01_06...
10_01_200xBSE1_01_07...
10_01_200xBSE1_01_08...
10_01_200xBSE1_02_01...
10_01_200xBSE1_02_02...
10_01_200xBSE1_02_03...
10_01_200xBSE1_02_04...
10_01_200xBSE1_02_05...
10_01_200xBSE1_02_06...
10_01_200xBSE1_02_07...
10_01_200xBSE1_02_08...
10_01_200xBSE1_03_01...
10_01_200xBSE1_03_02...
10_01_200xBSE1_03_03...
10_01_200xBSE1_03_04...
10_01_200xBSE1_03_05...
10_01_200xBSE1_03_06...
10_01_200xBSE1_03_07...
10_01_200xBSE1_03_08...
10_01_200xBSE1_04_01...
10_01_200xBSE1_04_02...
10_01_200xBSE1_04_03...
10_01_200xBSE1_04_04...
10_01_200xBSE1_04_05...
10_01_200xBSE1_04_06...
10_01_200xBSE1_04_07...
10_01_200xBSE1_04_08...

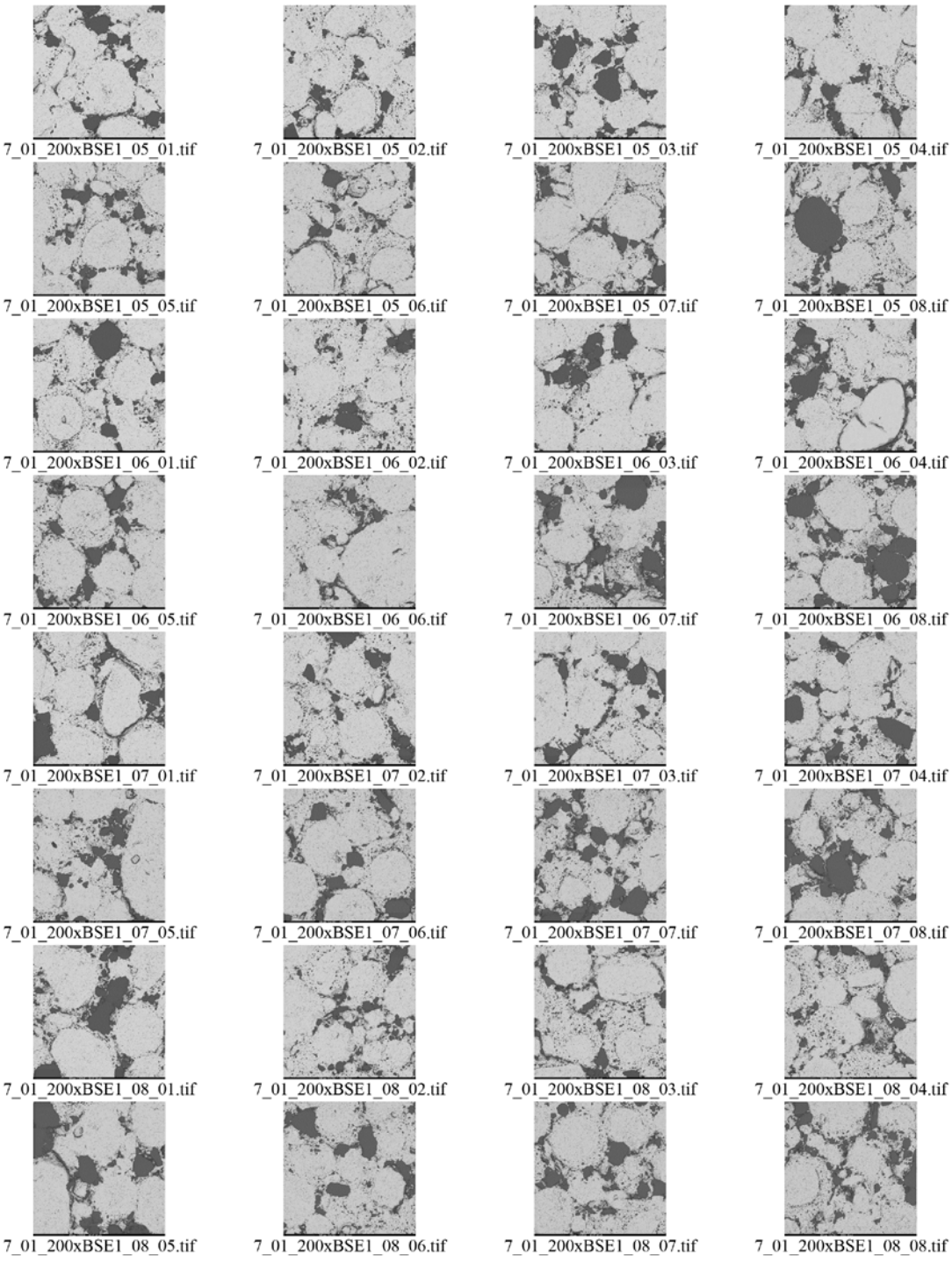
7_01_200xBSE1_05_01.tif
7_01_200xBSE1_05_02.tif
7_01_200xBSE1_05_03.tif
7_01_200xBSE1_05_04.tif
7_01_200xBSE1_05_05.tif
7_01_200xBSE1_05_06.tif
7_01_200xBSE1_05_07.tif
7_01_200xBSE1_05_08.tif
7_01_200xBSE1_06_01.tif
7_01_200xBSE1_06_02.tif
7_01_200xBSE1_06_03.tif
7_01_200xBSE1_06_04.tif
7_01_200xBSE1_06_05.tif
7_01_200xBSE1_06_06.tif
7_01_200xBSE1_06_07.tif
7_01_200xBSE1_06_08.tif
7_01_200xBSE1_07_01.tif
7_01_200xBSE1_07_02.tif
7_01_200xBSE1_07_03.tif
7_01_200xBSE1_07_04.tif
7_01_200xBSE1_07_05.tif
7_01_200xBSE1_07_06.tif
7_01_200xBSE1_07_07.tif
7_01_200xBSE1_07_08.tif
7_01_200xBSE1_08_01.tif
7_01_200xBSE1_08_02.tif
7_01_200xBSE1_08_03.tif
7_01_200xBSE1_08_04.tif
7_01_200xBSE1_08_05.tif
7_01_200xBSE1_08_06.tif
7_01_200xBSE1_08_07.tif
7_01_200xBSE1_08_08.tif

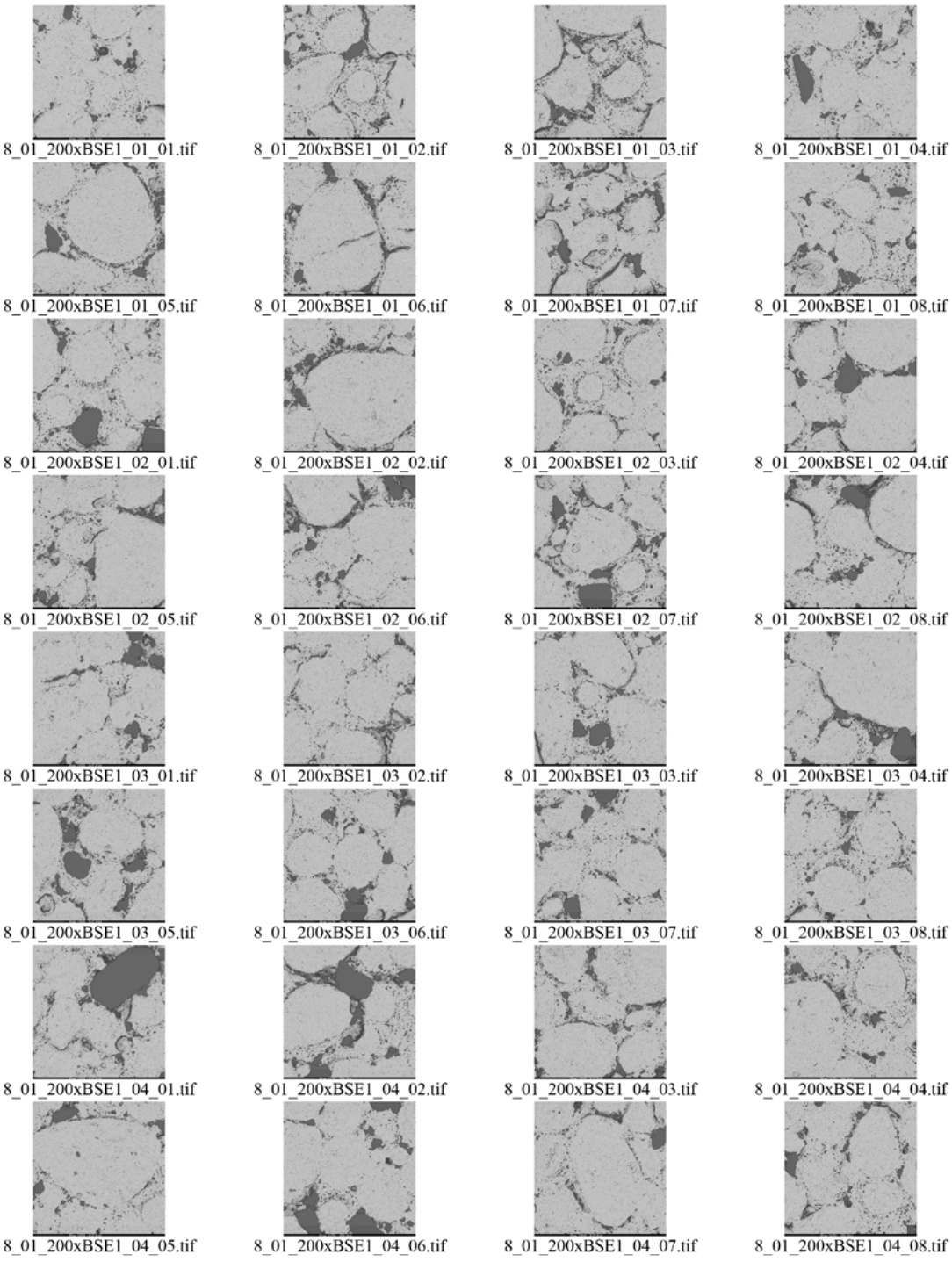
8_01_200xBSE1_01_01.tif
8_01_200xBSE1_01_02.tif
8_01_200xBSE1_01_03.tif
8_01_200xBSE1_01_04.tif
8_01_200xBSE1_01_05.tif
8_01_200xBSE1_01_06.tif
8_01_200xBSE1_01_07.tif
8_01_200xBSE1_01_08.tif
8_01_200xBSE1_02_01.tif
8_01_200xBSE1_02_02.tif
8_01_200xBSE1_02_03.tif
8_01_200xBSE1_02_04.tif
8_01_200xBSE1_02_05.tif
8_01_200xBSE1_02_06.tif
8_01_200xBSE1_02_07.tif
8_01_200xBSE1_02_08.tif
8_01_200xBSE1_03_01.tif
8_01_200xBSE1_03_02.tif
8_01_200xBSE1_03_03.tif
8_01_200xBSE1_03_04.tif
8_01_200xBSE1_03_05.tif
8_01_200xBSE1_03_06.tif
8_01_200xBSE1_03_07.tif
8_01_200xBSE1_03_08.tif
8_01_200xBSE1_04_01.tif
8_01_200xBSE1_04_02.tif
8_01_200xBSE1_04_03.tif
8_01_200xBSE1_04_04.tif
8_01_200xBSE1_04_05.tif
8_01_200xBSE1_04_06.tif
8_01_200xBSE1_04_07.tif
8_01_200xBSE1_04_08.tif

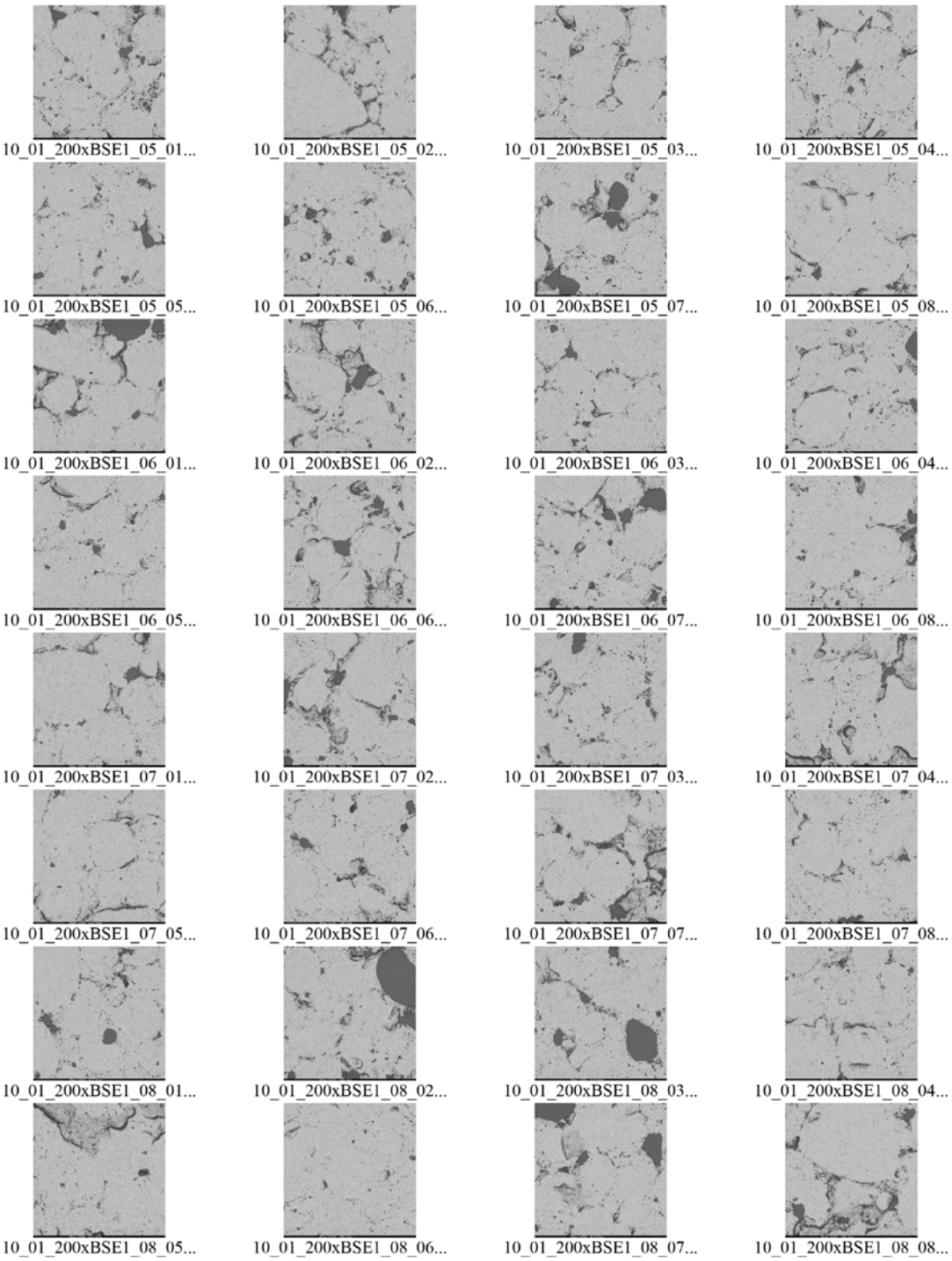
10_01_200xBSE1_05_01...
10_01_200xBSE1_05_02...
10_01_200xBSE1_05_03...
10_01_200xBSE1_05_04...
10_01_200xBSE1_05_05...
10_01_200xBSE1_05_06...
10_01_200xBSE1_05_07...
10_01_200xBSE1_05_08...
10_01_200xBSE1_06_01...
10_01_200xBSE1_06_02...
10_01_200xBSE1_06_03...
10_01_200xBSE1_06_04...
10_01_200xBSE1_06_05...
10_01_200xBSE1_06_06...
10_01_200xBSE1_06_07...
10_01_200xBSE1_06_08...
10_01_200xBSE1_07_01...
10_01_200xBSE1_07_02...
10_01_200xBSE1_07_03...
10_01_200xBSE1_07_04...
10_01_200xBSE1_07_05...
10_01_200xBSE1_07_06...
10_01_200xBSE1_07_07...
10_01_200xBSE1_07_08...
10_01_200xBSE1_08_01...
10_01_200xBSE1_08_02...
10_01_200xBSE1_08_03...
10_01_200xBSE1_08_04...
10_01_200xBSE1_08_05...
10_01_200xBSE1_08_06...
10_01_200xBSE1_08_07...
10_01_200xBSE1_08_08...

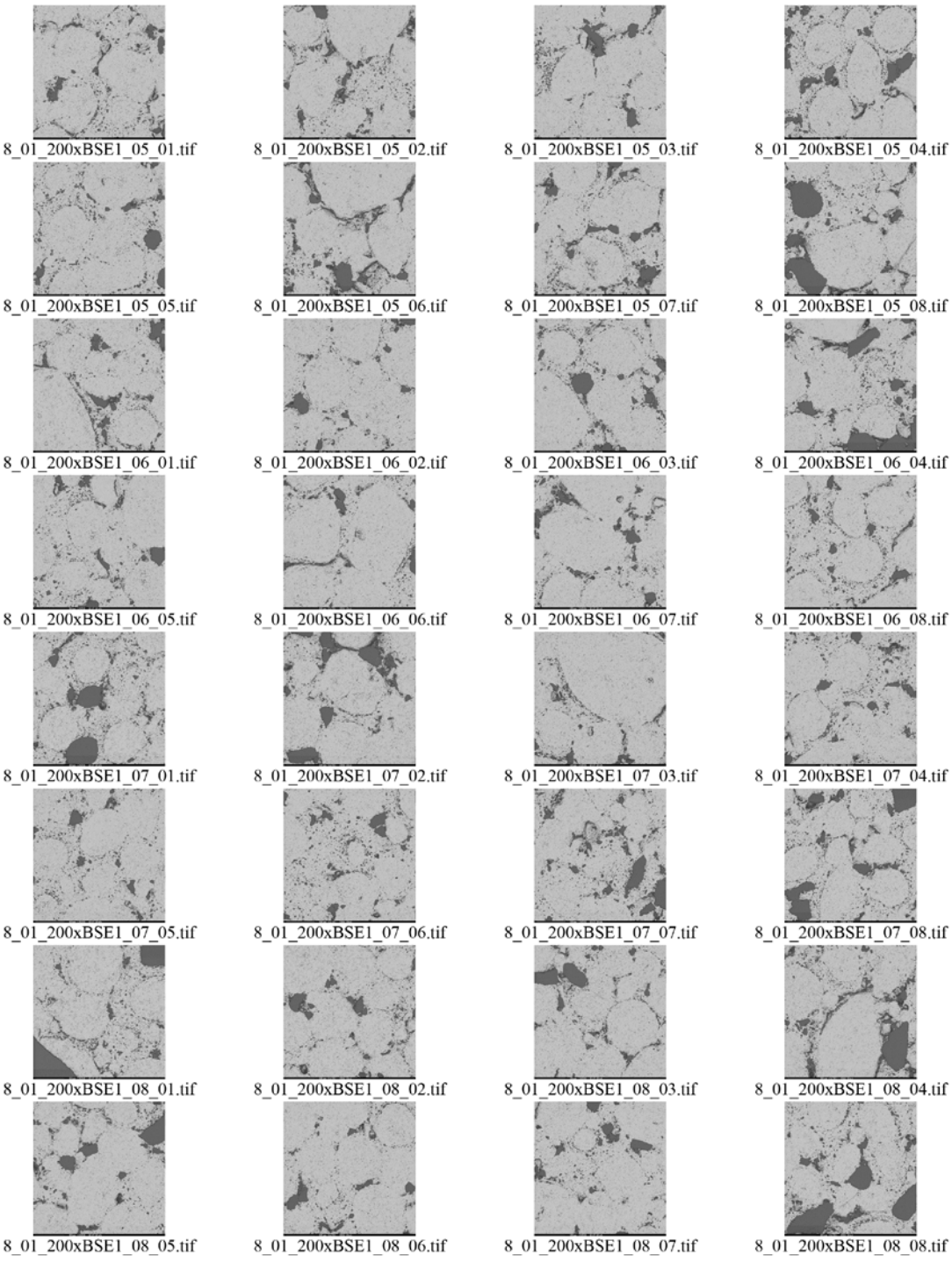
8_01_200xBSE1_05_01.tif
8_01_200xBSE1_05_02.tif
8_01_200xBSE1_05_03.tif
8_01_200xBSE1_05_04.tif
8_01_200xBSE1_05_05.tif
8_01_200xBSE1_05_06.tif
8_01_200xBSE1_05_07.tif
8_01_200xBSE1_05_08.tif
8_01_200xBSE1_06_01.tif
8_01_200xBSE1_06_02.tif
8_01_200xBSE1_06_03.tif
8_01_200xBSE1_06_04.tif
8_01_200xBSE1_06_05.tif
8_01_200xBSE1_06_06.tif
8_01_200xBSE1_06_07.tif
8_01_200xBSE1_06_08.tif
8_01_200xBSE1_07_01.tif
8_01_200xBSE1_07_02.tif
8_01_200xBSE1_07_03.tif
8_01_200xBSE1_07_04.tif
8_01_200xBSE1_07_05.tif
8_01_200xBSE1_07_06.tif
8_01_200xBSE1_07_07.tif
8_01_200xBSE1_07_08.tif
8_01_200xBSE1_08_01.tif
8_01_200xBSE1_08_02.tif
8_01_200xBSE1_08_03.tif
8_01_200xBSE1_08_04.tif
8_01_200xBSE1_08_05.tif
8_01_200xBSE1_08_06.tif
8_01_200xBSE1_08_07.tif
8_01_200xBSE1_08_08.tif

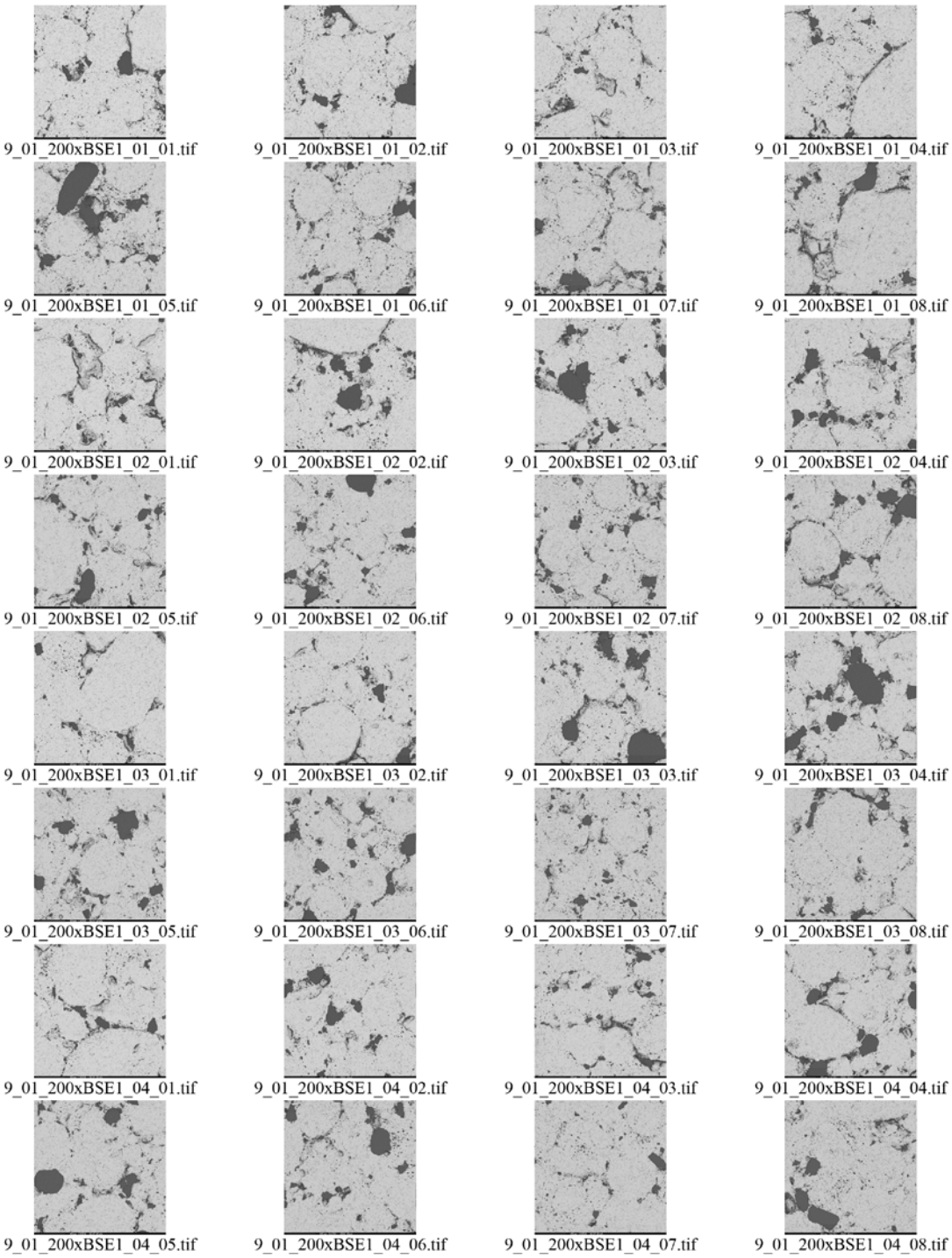
9_01_200xBSE1_01_01.tif
9_01_200xBSE1_01_02.tif
9_01_200xBSE1_01_03.tif
9_01_200xBSE1_01_04.tif
9_01_200xBSE1_01_05.tif
9_01_200xBSE1_01_06.tif
9_01_200xBSE1_01_07.tif
9_01_200xBSE1_01_08.tif
9_01_200xBSE1_02_01.tif
9_01_200xBSE1_02_02.tif
9_01_200xBSE1_02_03.tif
9_01_200xBSE1_02_04.tif
9_01_200xBSE1_02_05.tif
9_01_200xBSE1_02_06.tif
9_01_200xBSE1_02_07.tif
9_01_200xBSE1_02_08.tif
9_01_200xBSE1_03_01.tif
9_01_200xBSE1_03_02.tif
9_01_200xBSE1_03_03.tif
9_01_200xBSE1_03_04.tif
9_01_200xBSE1_03_05.tif
9_01_200xBSE1_03_06.tif
9_01_200xBSE1_03_07.tif
9_01_200xBSE1_03_08.tif
9_01_200xBSE1_04_01.tif
9_01_200xBSE1_04_02.tif
9_01_200xBSE1_04_03.tif
9_01_200xBSE1_04_04.tif
9_01_200xBSE1_04_05.tif
9_01_200xBSE1_04_06.tif
9_01_200xBSE1_04_07.tif
9_01_200xBSE1_04_08.tif

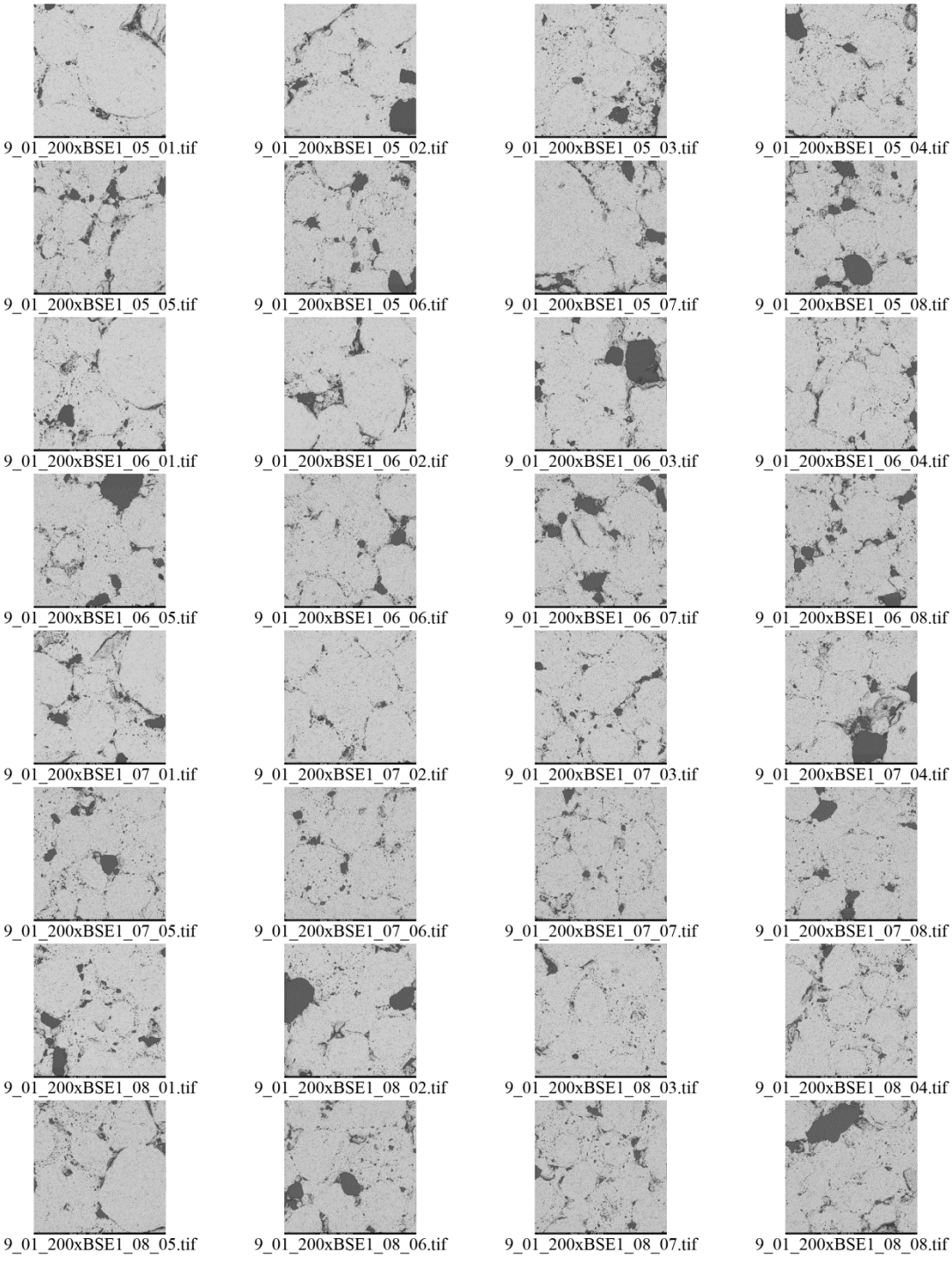
9_01_200xBSE1_05_01.tif
9_01_200xBSE1_05_02.tif
9_01_200xBSE1_05_03.tif
9_01_200xBSE1_05_04.tif
9_01_200xBSE1_05_05.tif
9_01_200xBSE1_05_06.tif
9_01_200xBSE1_05_07.tif
9_01_200xBSE1_05_08.tif
9_01_200xBSE1_06_01.tif
9_01_200xBSE1_06_02.tif
9_01_200xBSE1_06_03.tif
9_01_200xBSE1_06_04.tif
9_01_200xBSE1_06_05.tif
9_01_200xBSE1_06_06.tif
9_01_200xBSE1_06_07.tif
9_01_200xBSE1_06_08.tif
9_01_200xBSE1_07_01.tif
9_01_200xBSE1_07_02.tif
9_01_200xBSE1_07_03.tif
9_01_200xBSE1_07_04.tif
9_01_200xBSE1_07_05.tif
9_01_200xBSE1_07_06.tif
9_01_200xBSE1_07_07.tif
9_01_200xBSE1_07_08.tif
9_01_200xBSE1_08_01.tif
9_01_200xBSE1_08_02.tif
9_01_200xBSE1_08_03.tif
9_01_200xBSE1_08_04.tif
9_01_200xBSE1_08_05.tif
9_01_200xBSE1_08_06.tif
9_01_200xBSE1_08_07.tif
9_01_200xBSE1_08_08.tif

APPENDIX H

CATH IMAGES ANALIZED

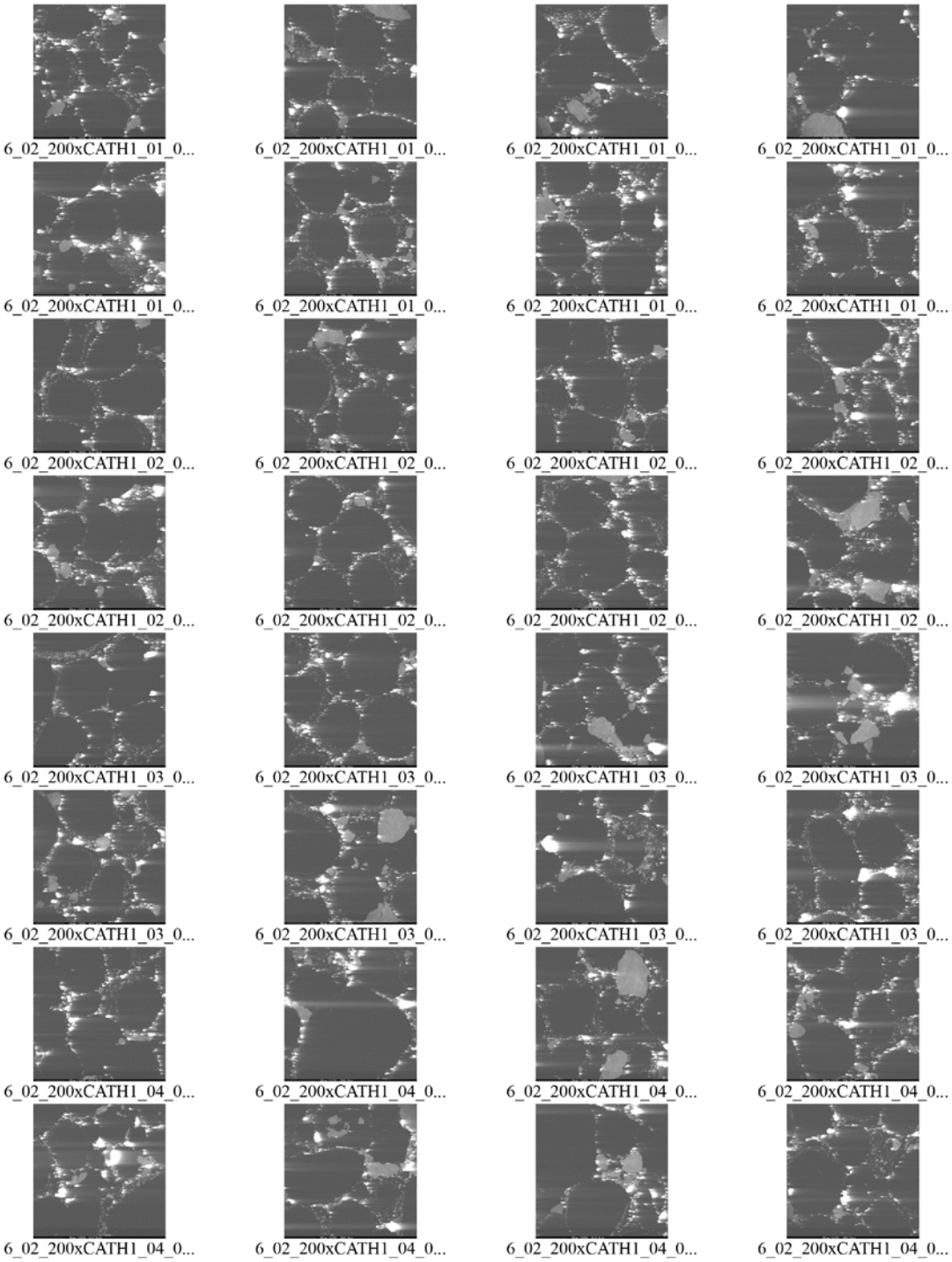

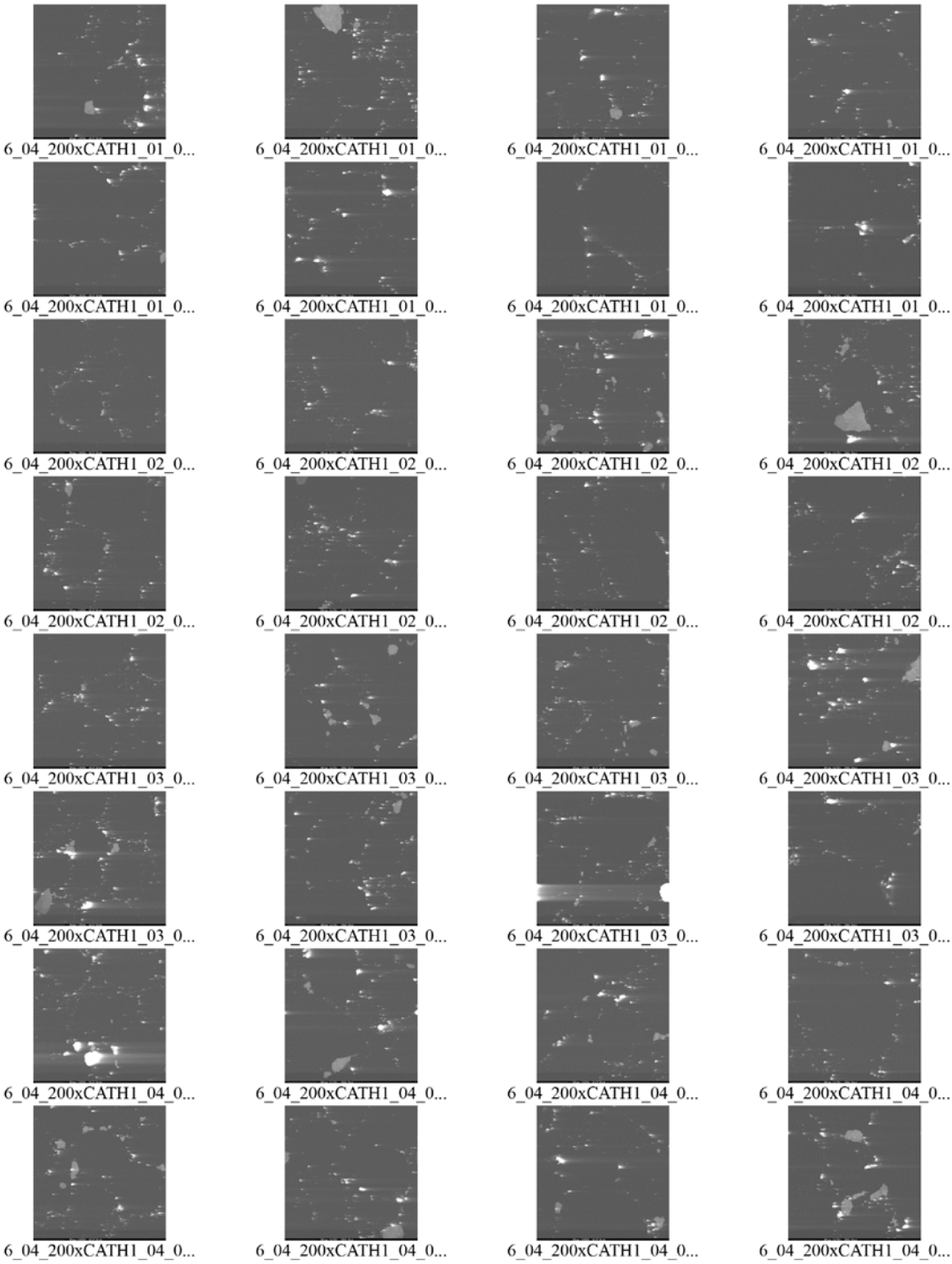
6_04_200xCATH1_01_0...
6_04_200xCATH1_01_0...
6_04_200xCATH1_01_0...
6_04_200xCATH1_01_0...
6_04_200xCATH1_01_0...
6_04_200xCATH1_01_0...
6_04_200xCATH1_01_0...
6_04_200xCATH1_01_0...
6_04_200xCATH1_02_0...
6_04_200xCATH1_02_0...
6_04_200xCATH1_02_0...
6_04_200xCATH1_02_0...
6_04_200xCATH1_02_0...
6_04_200xCATH1_02_0...
6_04_200xCATH1_02_0...
6_04_200xCATH1_02_0...
6_04_200xCATH1_03_0...
6_04_200xCATH1_03_0...
6_04_200xCATH1_03_0...
6_04_200xCATH1_03_0...
6_04_200xCATH1_03_0...
6_04_200xCATH1_03_0...
6_04_200xCATH1_03_0...
6_04_200xCATH1_03_0...
6_04_200xCATH1_04_0...
6_04_200xCATH1_04_0...
6_04_200xCATH1_04_0...
6_04_200xCATH1_04_0...
6_04_200xCATH1_04_0...
6_04_200xCATH1_04_0...
6_04_200xCATH1_04_0...
6_04_200xCATH1_04_0...

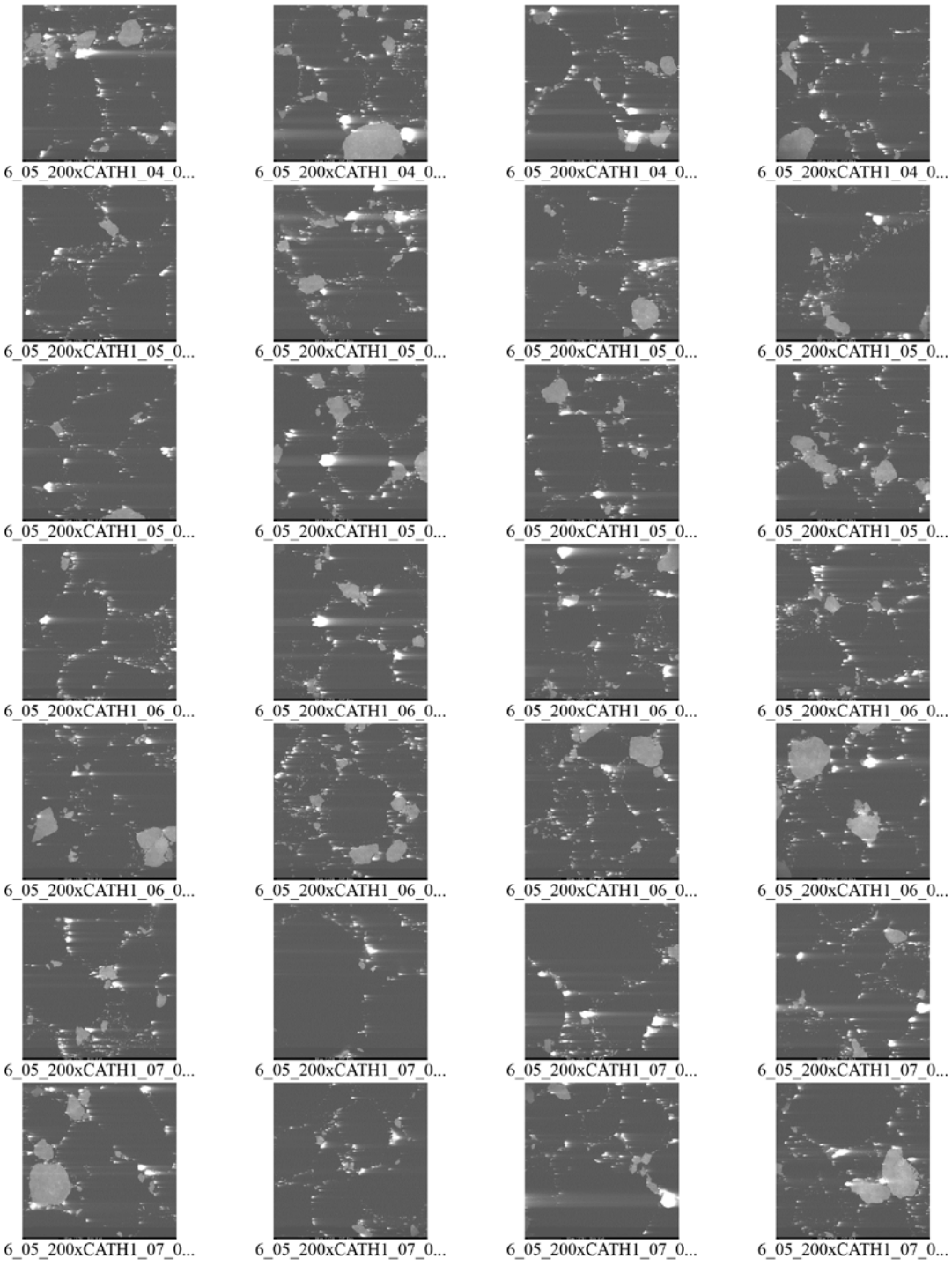
6_05_200xCATH1_04_0...
6_05_200xCATH1_04_0...
6_05_200xCATH1_04_0...
6_05_200xCATH1_04_0...
6_05_200xCATH1_05_0...
6_05_200xCATH1_05_0...
6_05_200xCATH1_05_0...
6_05_200xCATH1_05_0...
6_05_200xCATH1_05_0...
6_05_200xCATH1_05_0...
6_05_200xCATH1_05_0...
6_05_200xCATH1_05_0...
6_05_200xCATH1_06_0...
6_05_200xCATH1_06_0...
6_05_200xCATH1_06_0...
6_05_200xCATH1_06_0...
6_05_200xCATH1_06_0...
6_05_200xCATH1_06_0...
6_05_200xCATH1_06_0...
6_05_200xCATH1_06_0...
6_05_200xCATH1_07_0...
6_05_200xCATH1_07_0...
6_05_200xCATH1_07_0...
6_05_200xCATH1_07_0...
6_05_200xCATH1_07_0...
6_05_200xCATH1_07_0...
6_05_200xCATH1_07_0...
6_05_200xCATH1_07_0...

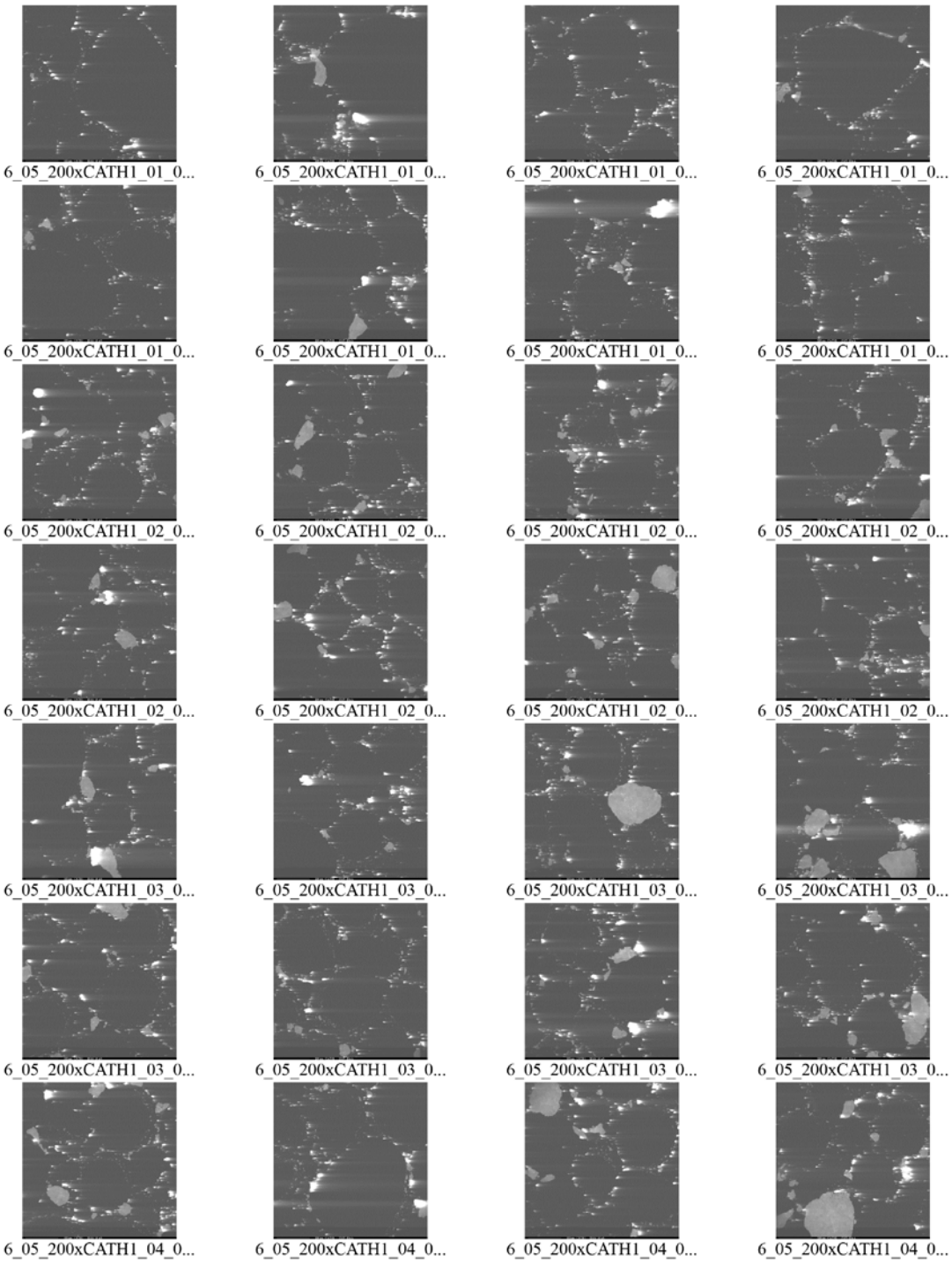
6_05_200xCATH1_01_0...
6_05_200xCATH1_01_0...
6_05_200xCATH1_01_0...
6_05_200xCATH1_01_0...
6_05_200xCATH1_01_0...
6_05_200xCATH1_01_0...
6_05_200xCATH1_01_0...
6_05_200xCATH1_01_0...
6_05_200xCATH1_02_0...
6_05_200xCATH1_02_0...
6_05_200xCATH1_02_0...
6_05_200xCATH1_02_0...
6_05_200xCATH1_02_0...
6_05_200xCATH1_02_0...
6_05_200xCATH1_02_0...
6_05_200xCATH1_02_0...
6_05_200xCATH1_03_0...
6_05_200xCATH1_03_0...
6_05_200xCATH1_03_0...
6_05_200xCATH1_03_0...
6_05_200xCATH1_03_0...
6_05_200xCATH1_03_0...
6_05_200xCATH1_03_0...
6_05_200xCATH1_03_0...
6_05_200xCATH1_04_0...
6_05_200xCATH1_04_0...
6_05_200xCATH1_04_0...
6_05_200xCATH1_04_0...

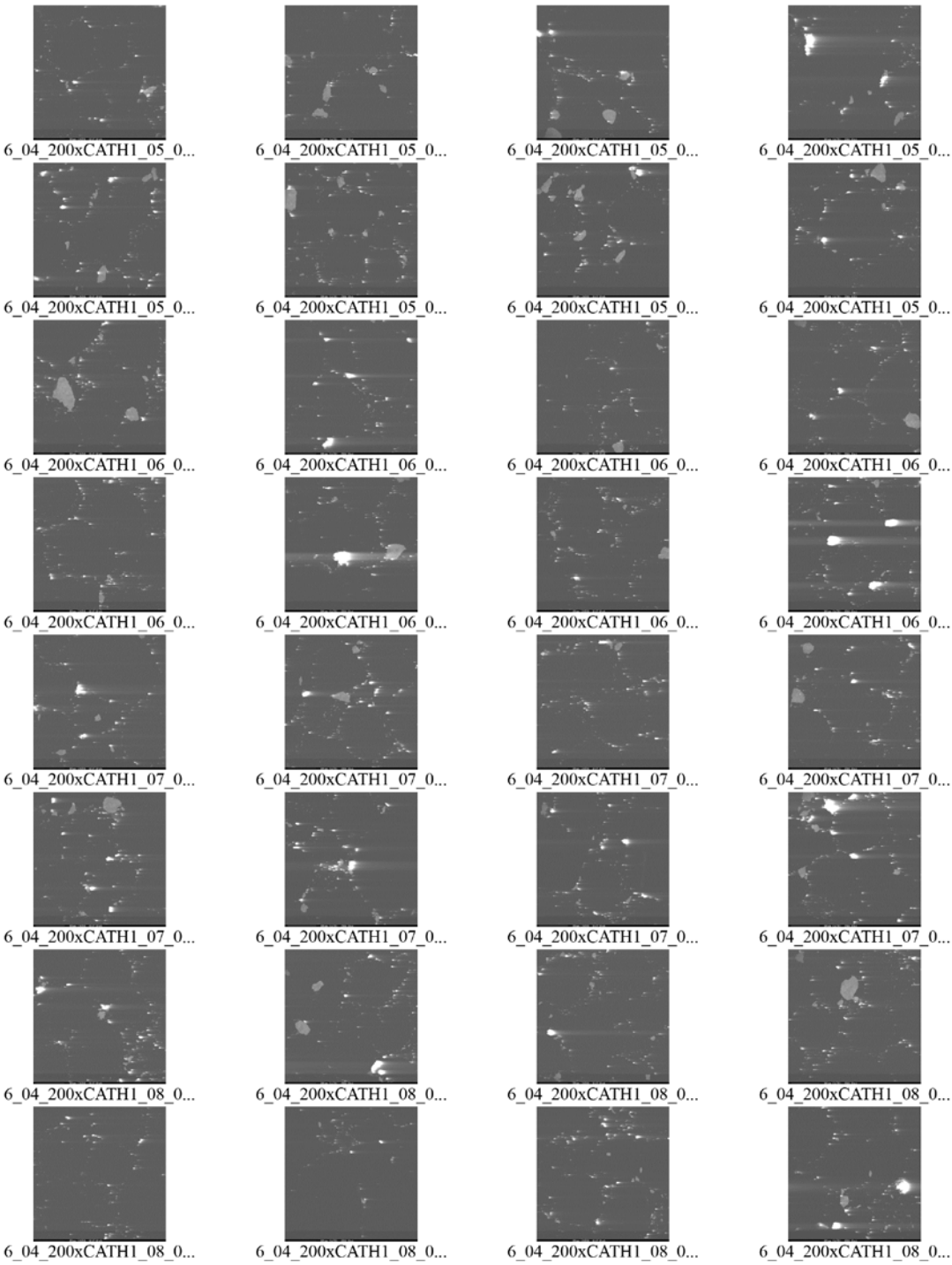
6_04_200xCATH1_05_0...
6_04_200xCATH1_05_0...
6_04_200xCATH1_05_0...
6_04_200xCATH1_05_0...
6_04_200xCATH1_05_0...
6_04_200xCATH1_05_0...
6_04_200xCATH1_05_0...
6_04_200xCATH1_05_0...
6_04_200xCATH1_06_0...
6_04_200xCATH1_06_0...
6_04_200xCATH1_06_0...
6_04_200xCATH1_06_0...
6_04_200xCATH1_06_0...
6_04_200xCATH1_06_0...
6_04_200xCATH1_06_0...
6_04_200xCATH1_06_0...
6_04_200xCATH1_07_0...
6_04_200xCATH1_07_0...
6_04_200xCATH1_07_0...
6_04_200xCATH1_07_0...
6_04_200xCATH1_07_0...
6_04_200xCATH1_07_0...
6_04_200xCATH1_07_0...
6_04_200xCATH1_07_0...
6_04_200xCATH1_08_0...
6_04_200xCATH1_08_0...
6_04_200xCATH1_08_0...
6_04_200xCATH1_08_0...
6_04_200xCATH1_08_0...
6_04_200xCATH1_08_0...
6_04_200xCATH1_08_0...
6_04_200xCATH1_08_0...

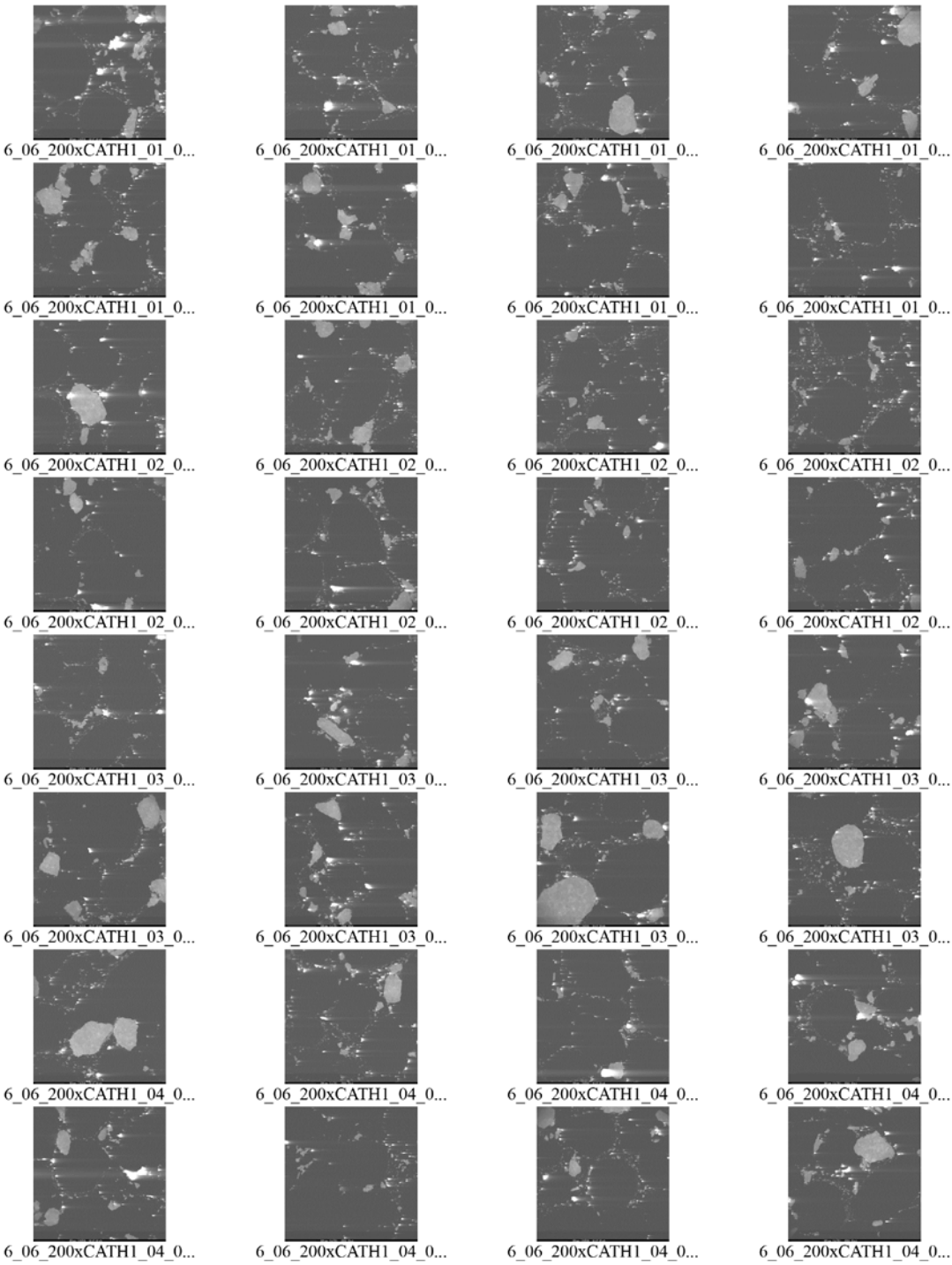
6_06_200xCATH1_01_0...
6_06_200xCATH1_01_0...
6_06_200xCATH1_01_0...
6_06_200xCATH1_01_0...
6_06_200xCATH1_01_0...
6_06_200xCATH1_01_0...
6_06_200xCATH1_01_0...
6_06_200xCATH1_01_0...
6_06_200xCATH1_02_0...
6_06_200xCATH1_02_0...
6_06_200xCATH1_02_0...
6_06_200xCATH1_02_0...
6_06_200xCATH1_02_0...
6_06_200xCATH1_02_0...
6_06_200xCATH1_02_0...
6_06_200xCATH1_02_0...
6_06_200xCATH1_03_0...
6_06_200xCATH1_03_0...
6_06_200xCATH1_03_0...
6_06_200xCATH1_03_0...
6_06_200xCATH1_03_0...
6_06_200xCATH1_03_0...
6_06_200xCATH1_03_0...
6_06_200xCATH1_03_0...
6_06_200xCATH1_04_0...
6_06_200xCATH1_04_0...
6_06_200xCATH1_04_0...
6_06_200xCATH1_04_0...
6_06_200xCATH1_04_0...
6_06_200xCATH1_04_0...
6_06_200xCATH1_04_0...
6_06_200xCATH1_04_0...

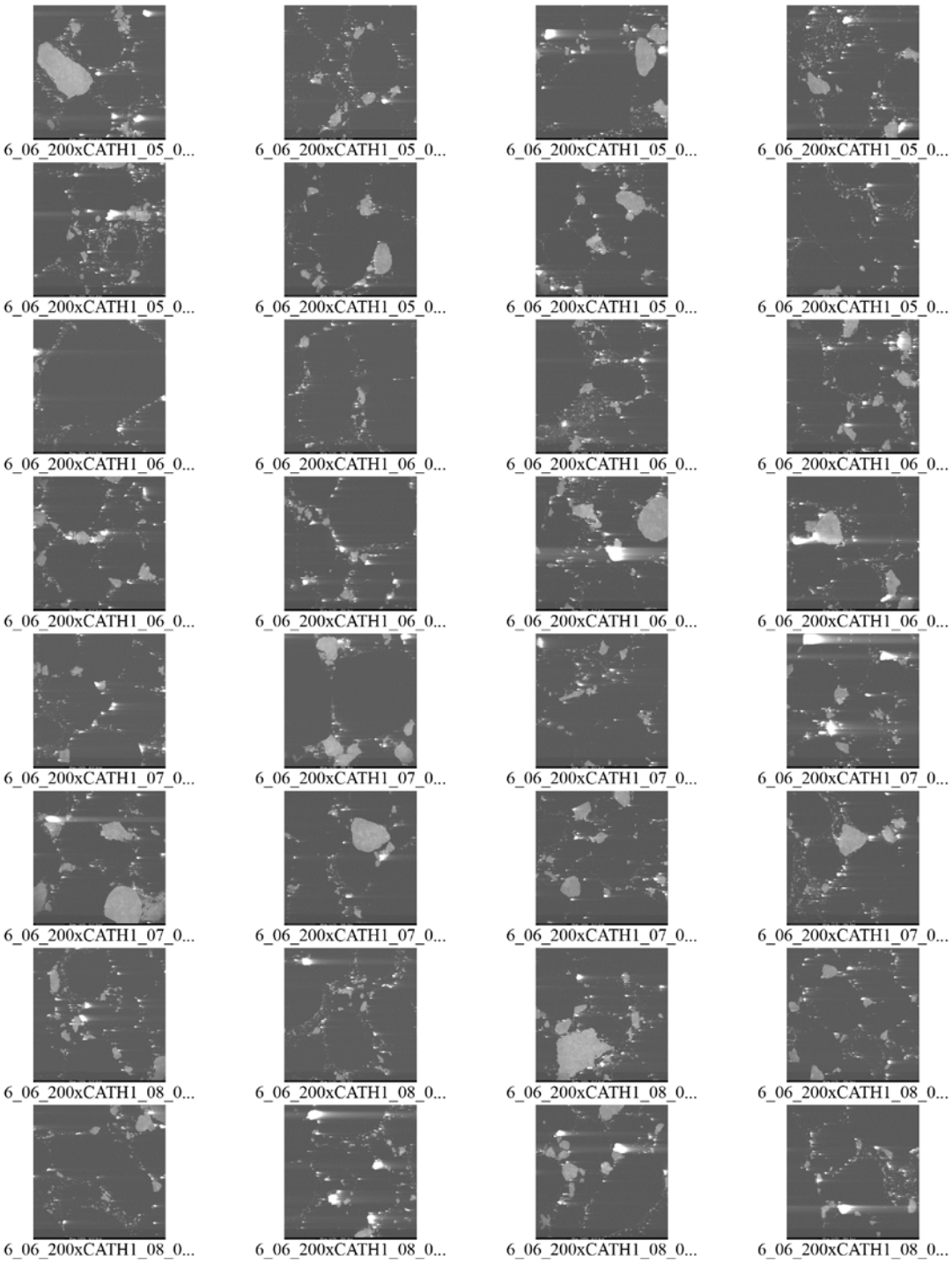
6_06_200xCATH1_05_0...
6_06_200xCATH1_05_0...
6_06_200xCATH1_05_0...
6_06_200xCATH1_05_0...
6_06_200xCATH1_05_0...
6_06_200xCATH1_05_0...
6_06_200xCATH1_05_0...
6_06_200xCATH1_05_0...
6_06_200xCATH1_06_0...
6_06_200xCATH1_06_0...
6_06_200xCATH1_06_0...
6_06_200xCATH1_06_0...
6_06_200xCATH1_06_0...
6_06_200xCATH1_06_0...
6_06_200xCATH1_06_0...
6_06_200xCATH1_06_0...
6_06_200xCATH1_07_0...
6_06_200xCATH1_07_0...
6_06_200xCATH1_07_0...
6_06_200xCATH1_07_0...
6_06_200xCATH1_07_0...
6_06_200xCATH1_07_0...
6_06_200xCATH1_07_0...
6_06_200xCATH1_07_0...
6_06_200xCATH1_08_0...
6_06_200xCATH1_08_0...
6_06_200xCATH1_08_0...
6_06_200xCATH1_08_0...
6_06_200xCATH1_08_0...
6_06_200xCATH1_08_0...
6_06_200xCATH1_08_0...
6_06_200xCATH1_08_0...

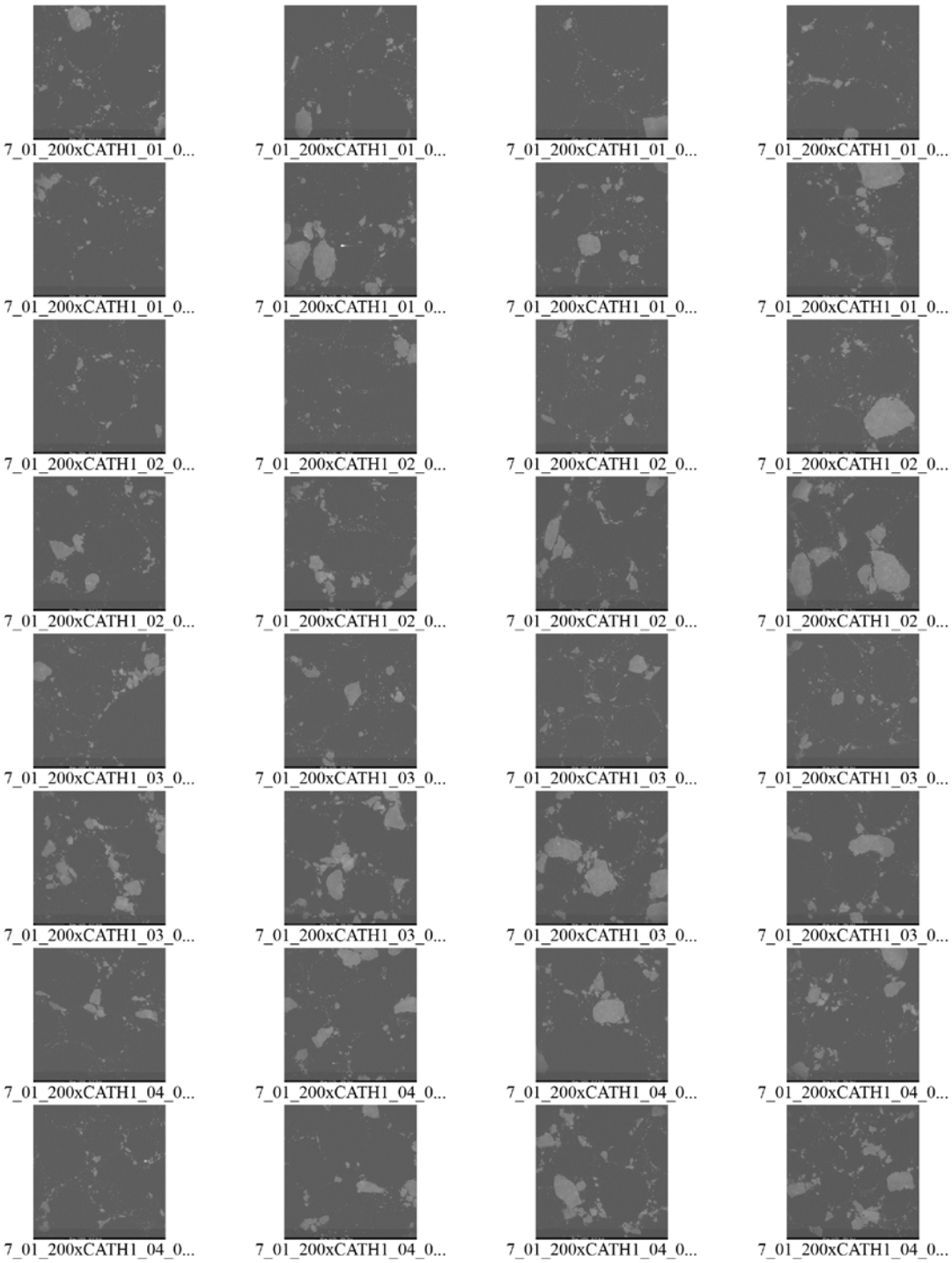
7_01_200xCATH1_01_0...
7_01_200xCATH1_01_0...
7_01_200xCATH1_01_0...
7_01_200xCATH1_01_0...
7_01_200xCATH1_01_0...
7_01_200xCATH1_01_0...
7_01_200xCATH1_01_0...
7_01_200xCATH1_01_0...
7_01_200xCATH1_02_0...
7_01_200xCATH1_02_0...
7_01_200xCATH1_02_0...
7_01_200xCATH1_02_0...
7_01_200xCATH1_02_0...
7_01_200xCATH1_02_0...
7_01_200xCATH1_02_0...
7_01_200xCATH1_02_0...
7_01_200xCATH1_03_0...
7_01_200xCATH1_03_0...
7_01_200xCATH1_03_0...
7_01_200xCATH1_03_0...
7_01_200xCATH1_03_0...
7_01_200xCATH1_03_0...
7_01_200xCATH1_03_0...
7_01_200xCATH1_03_0...
7_01_200xCATH1_04_0...
7_01_200xCATH1_04_0...
7_01_200xCATH1_04_0...
7_01_200xCATH1_04_0...
7_01_200xCATH1_04_0...
7_01_200xCATH1_04_0...
7_01_200xCATH1_04_0...
7_01_200xCATH1_04_0...

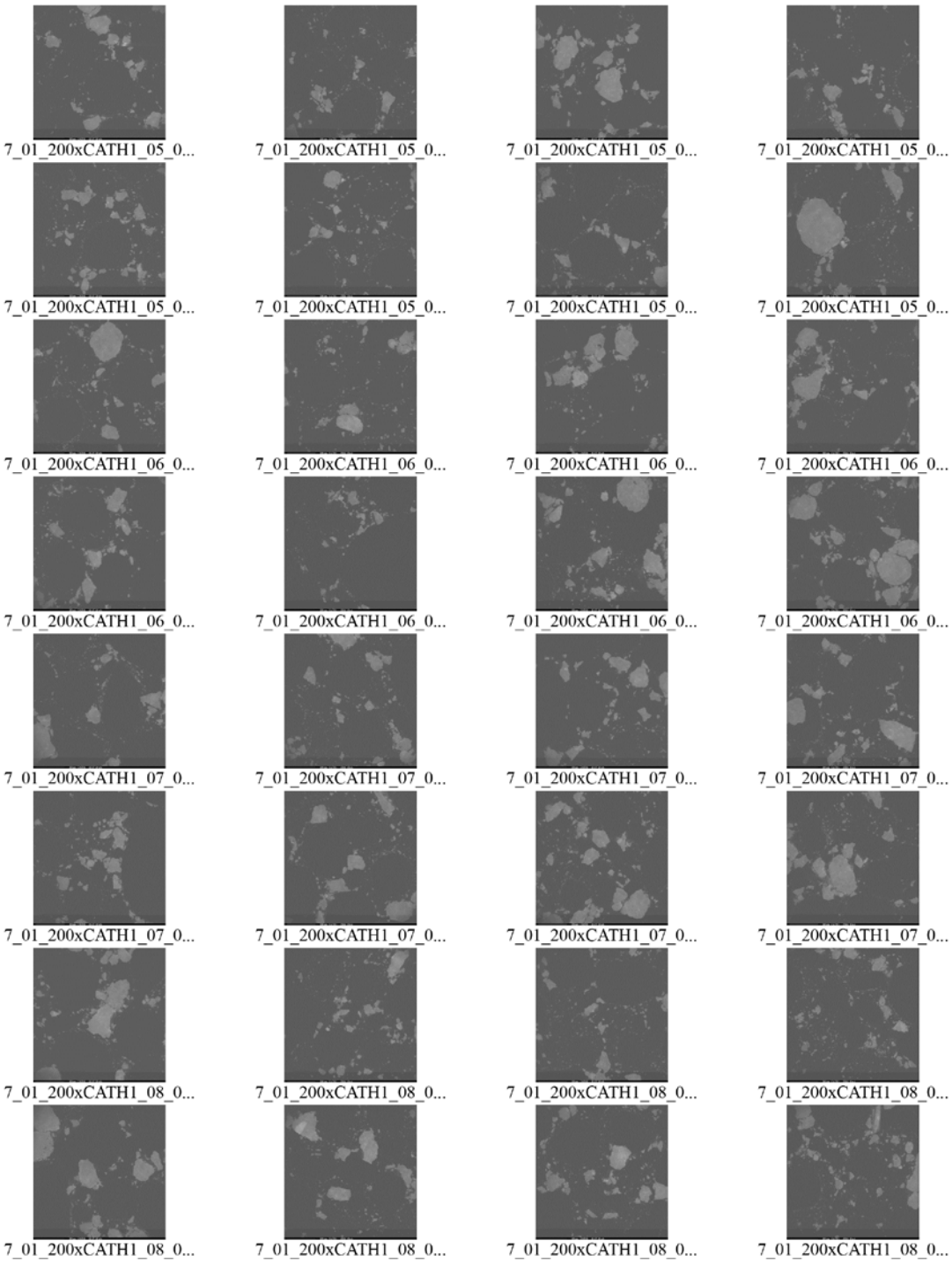
7_01_200xCATH1_05_0...
7_01_200xCATH1_05_0...
7_01_200xCATH1_05_0...
7_01_200xCATH1_05_0...
7_01_200xCATH1_05_0...
7_01_200xCATH1_05_0...
7_01_200xCATH1_05_0...
7_01_200xCATH1_05_0...
7_01_200xCATH1_06_0...
7_01_200xCATH1_06_0...
7_01_200xCATH1_06_0...
7_01_200xCATH1_06_0...
7_01_200xCATH1_06_0...
7_01_200xCATH1_06_0...
7_01_200xCATH1_06_0...
7_01_200xCATH1_06_0...
7_01_200xCATH1_07_0...
7_01_200xCATH1_07_0...
7_01_200xCATH1_07_0...
7_01_200xCATH1_07_0...
7_01_200xCATH1_07_0...
7_01_200xCATH1_07_0...
7_01_200xCATH1_07_0...
7_01_200xCATH1_07_0...
7_01_200xCATH1_08_0...
7_01_200xCATH1_08_0...
7_01_200xCATH1_08_0...
7_01_200xCATH1_08_0...
7_01_200xCATH1_08_0...
7_01_200xCATH1_08_0...
7_01_200xCATH1_08_0...
7_01_200xCATH1_08_0...

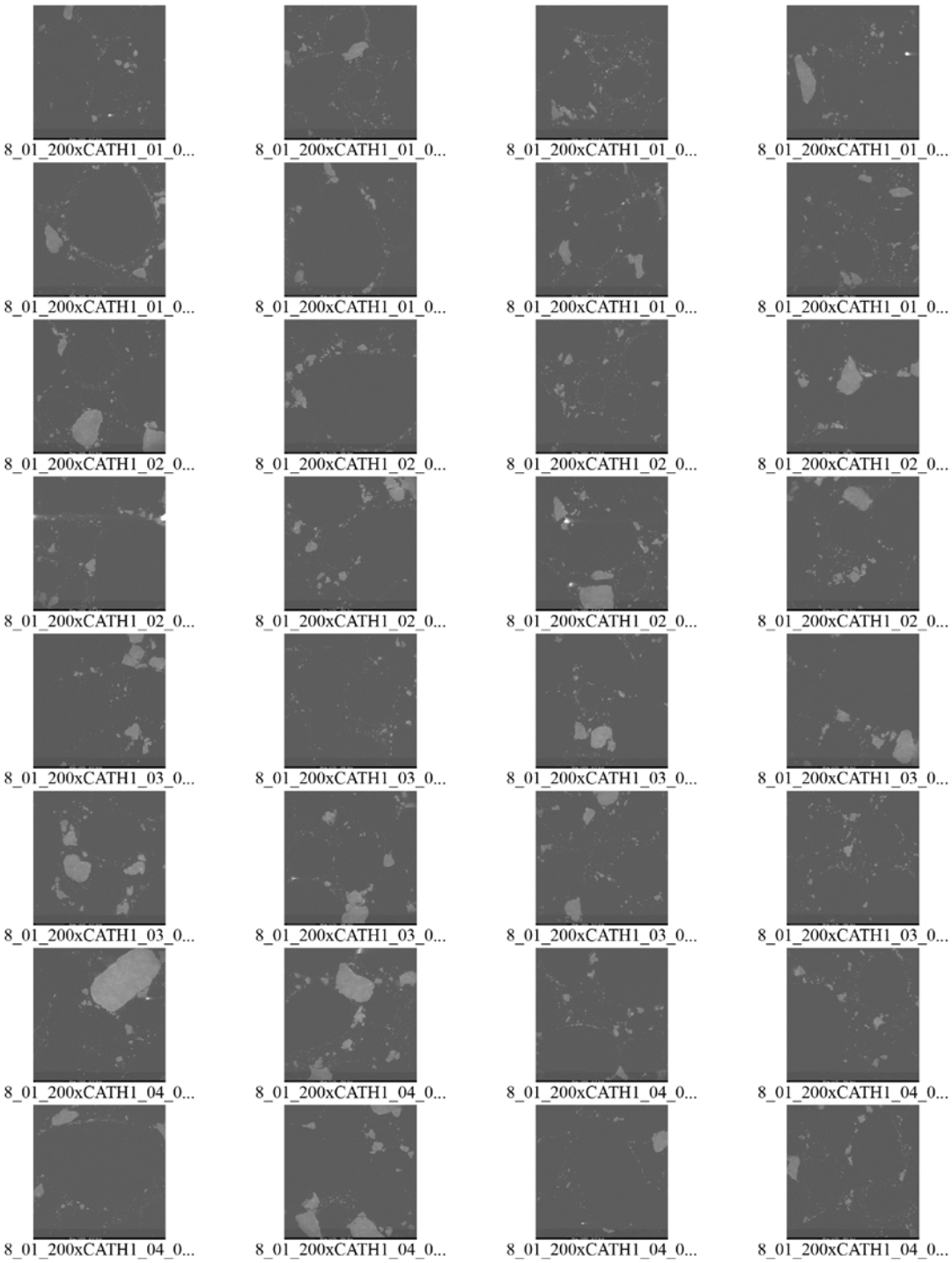
8_01_200xCATH1_01_0...
8_01_200xCATH1_01_0...
8_01_200xCATH1_01_0...
8_01_200xCATH1_01_0...
8_01_200xCATH1_01_0...
8_01_200xCATH1_01_0...
8_01_200xCATH1_01_0...
8_01_200xCATH1_01_0...
8_01_200xCATH1_02_0...
8_01_200xCATH1_02_0...
8_01_200xCATH1_02_0...
8_01_200xCATH1_02_0...
8_01_200xCATH1_02_0...
8_01_200xCATH1_02_0...
8_01_200xCATH1_02_0...
8_01_200xCATH1_02_0...
8_01_200xCATH1_03_0...
8_01_200xCATH1_03_0...
8_01_200xCATH1_03_0...
8_01_200xCATH1_03_0...
8_01_200xCATH1_03_0...
8_01_200xCATH1_03_0...
8_01_200xCATH1_03_0...
8_01_200xCATH1_03_0...
8_01_200xCATH1_04_0...
8_01_200xCATH1_04_0...
8_01_200xCATH1_04_0...
8_01_200xCATH1_04_0...
8_01_200xCATH1_04_0...
8_01_200xCATH1_04_0...
8_01_200xCATH1_04_0...
8_01_200xCATH1_04_0...

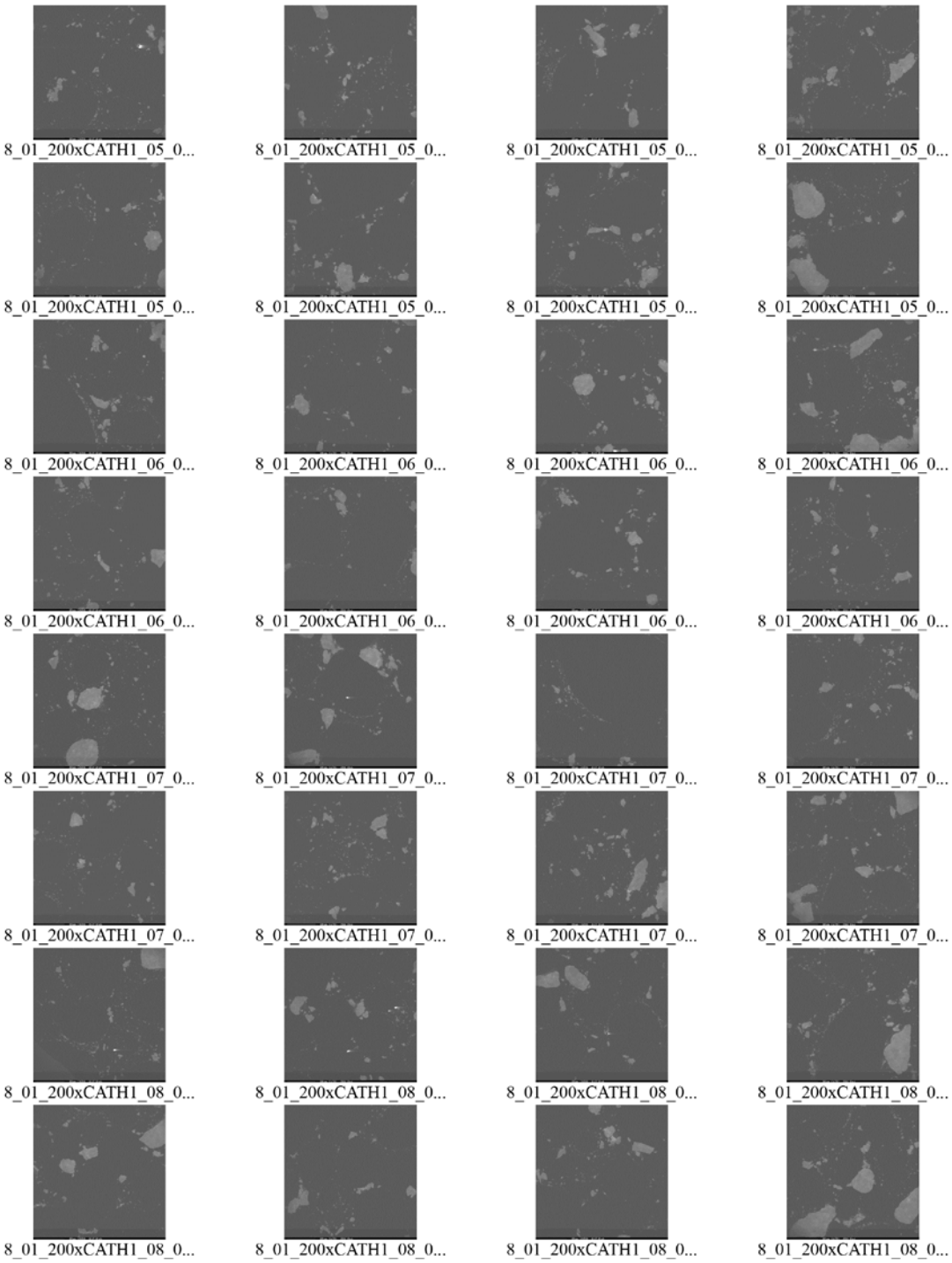
8_01_200xCATH1_05_0...
8_01_200xCATH1_05_0...
8_01_200xCATH1_05_0...
8_01_200xCATH1_05_0...
8_01_200xCATH1_05_0...
8_01_200xCATH1_05_0...
8_01_200xCATH1_05_0...
8_01_200xCATH1_05_0...
8_01_200xCATH1_06_0...
8_01_200xCATH1_06_0...
8_01_200xCATH1_06_0...
8_01_200xCATH1_06_0...
8_01_200xCATH1_06_0...
8_01_200xCATH1_06_0...
8_01_200xCATH1_06_0...
8_01_200xCATH1_06_0...
8_01_200xCATH1_07_0...
8_01_200xCATH1_07_0...
8_01_200xCATH1_07_0...
8_01_200xCATH1_07_0...
8_01_200xCATH1_07_0...
8_01_200xCATH1_07_0...
8_01_200xCATH1_07_0...
8_01_200xCATH1_07_0...
8_01_200xCATH1_08_0...
8_01_200xCATH1_08_0...
8_01_200xCATH1_08_0...
8_01_200xCATH1_08_0...
8_01_200xCATH1_08_0...
8_01_200xCATH1_08_0...
8_01_200xCATH1_08_0...
8_01_200xCATH1_08_0...

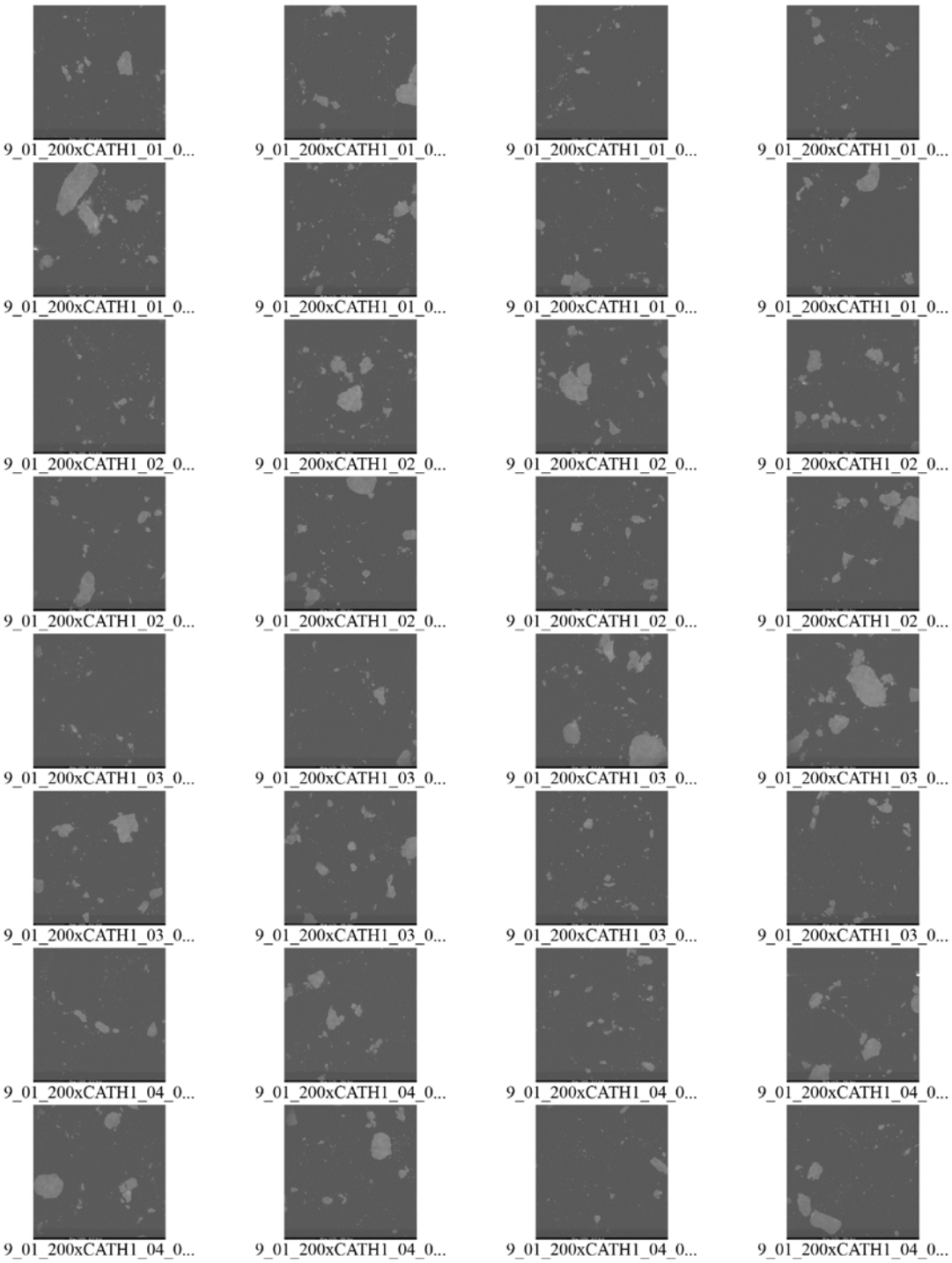
9_01_200xCATH1_01_0...
9_01_200xCATH1_01_0...
9_01_200xCATH1_01_0...
9_01_200xCATH1_01_0...
9_01_200xCATH1_01_0...
9_01_200xCATH1_01_0...
9_01_200xCATH1_01_0...
9_01_200xCATH1_01_0...
9_01_200xCATH1_02_0...
9_01_200xCATH1_02_0...
9_01_200xCATH1_02_0...
9_01_200xCATH1_02_0...
9_01_200xCATH1_02_0...
9_01_200xCATH1_02_0...
9_01_200xCATH1_02_0...
9_01_200xCATH1_02_0...
9_01_200xCATH1_03_0...
9_01_200xCATH1_03_0...
9_01_200xCATH1_03_0...
9_01_200xCATH1_03_0...
9_01_200xCATH1_03_0...
9_01_200xCATH1_03_0...
9_01_200xCATH1_03_0...
9_01_200xCATH1_03_0...
9_01_200xCATH1_04_0...
9_01_200xCATH1_04_0...
9_01_200xCATH1_04_0...
9_01_200xCATH1_04_0...
9_01_200xCATH1_04_0...
9_01_200xCATH1_04_0...
9_01_200xCATH1_04_0...
9_01_200xCATH1_04_0...

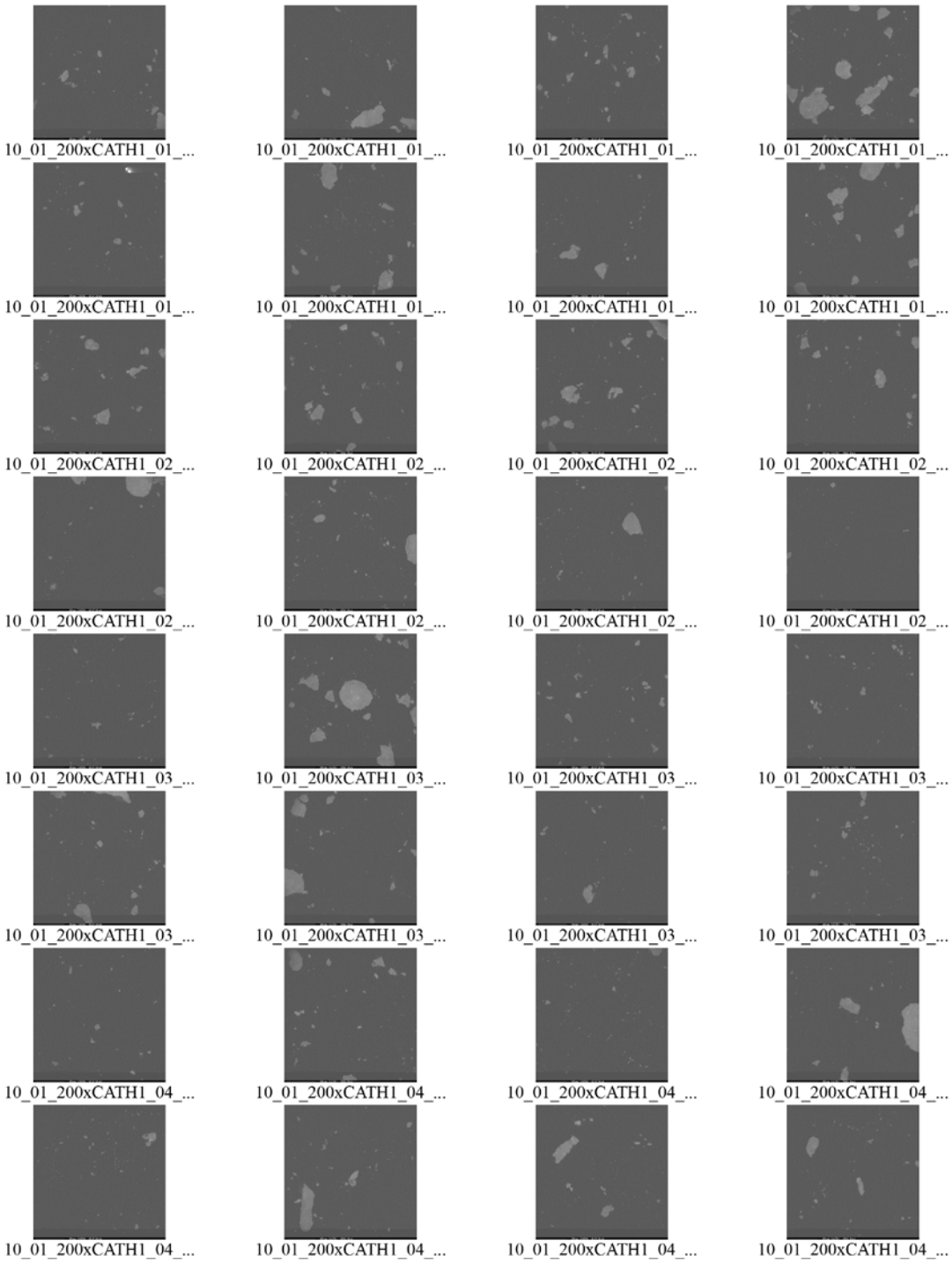
10_01_200xCATH1_01_...
10_01_200xCATH1_01_...
10_01_200xCATH1_01_...
10_01_200xCATH1_01_...
10_01_200xCATH1_01_...
10_01_200xCATH1_01_...
10_01_200xCATH1_01_...
10_01_200xCATH1_01_...
10_01_200xCATH1_02_...
10_01_200xCATH1_02_...
10_01_200xCATH1_02_...
10_01_200xCATH1_02_...
10_01_200xCATH1_02_...
10_01_200xCATH1_02_...
10_01_200xCATH1_02_...
10_01_200xCATH1_02_...
10_01_200xCATH1_03_...
10_01_200xCATH1_03_...
10_01_200xCATH1_03_...
10_01_200xCATH1_03_...
10_01_200xCATH1_03_...
10_01_200xCATH1_03_...
10_01_200xCATH1_03_...
10_01_200xCATH1_03_...
10_01_200xCATH1_04_...
10_01_200xCATH1_04_...
10_01_200xCATH1_04_...
10_01_200xCATH1_04_...
10_01_200xCATH1_04_...
10_01_200xCATH1_04_...
10_01_200xCATH1_04_...
10_01_200xCATH1_04_...

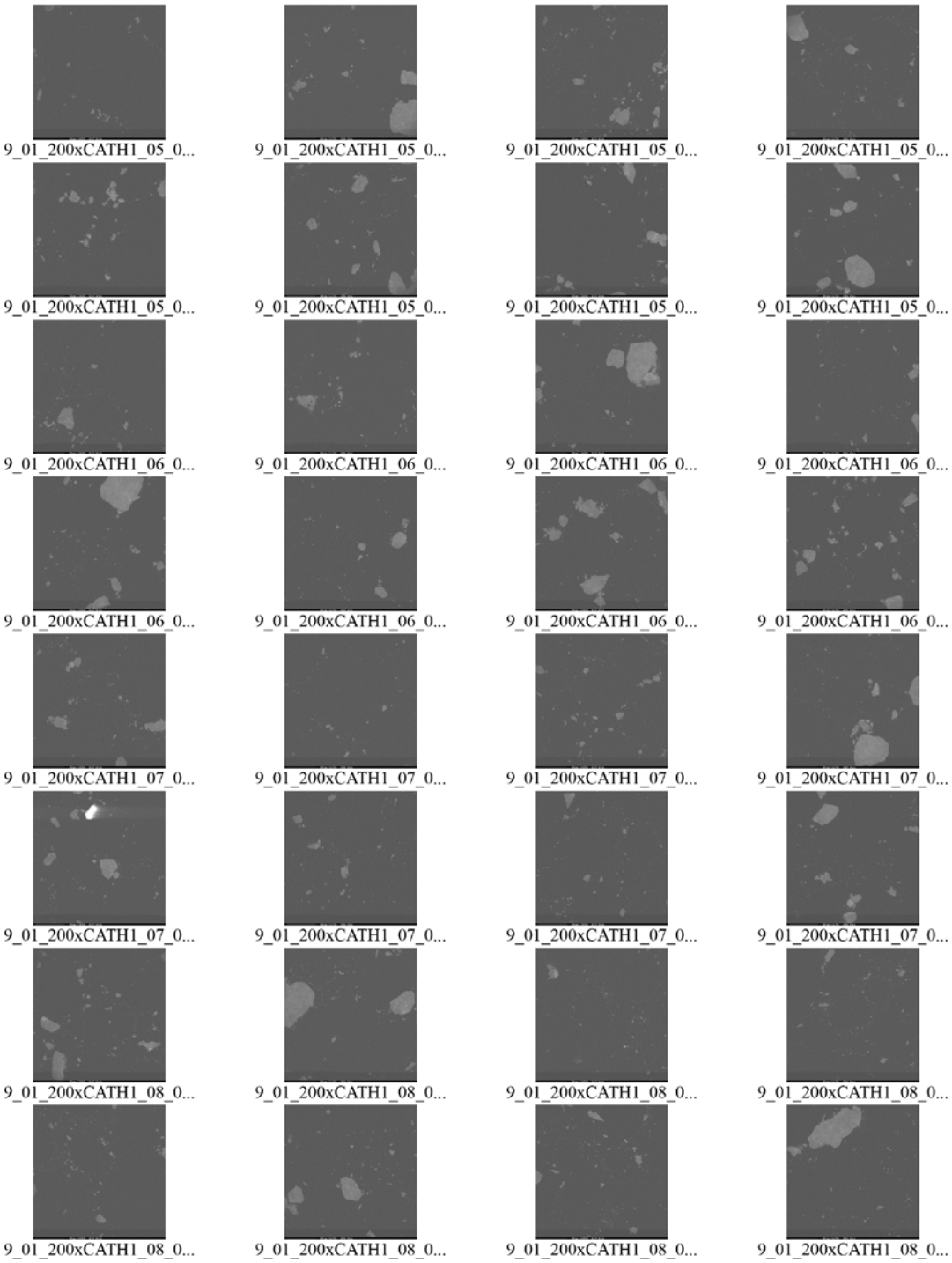
9_01_200xCATH1_05_0...
9_01_200xCATH1_05_0...
9_01_200xCATH1_05_0...
9_01_200xCATH1_05_0...
9_01_200xCATH1_05_0...
9_01_200xCATH1_05_0...
9_01_200xCATH1_05_0...
9_01_200xCATH1_05_0...
9_01_200xCATH1_06_0...
9_01_200xCATH1_06_0...
9_01_200xCATH1_06_0...
9_01_200xCATH1_06_0...
9_01_200xCATH1_06_0...
9_01_200xCATH1_06_0...
9_01_200xCATH1_06_0...
9_01_200xCATH1_06_0...
9_01_200xCATH1_07_0...
9_01_200xCATH1_07_0...
9_01_200xCATH1_07_0...
9_01_200xCATH1_07_0...
9_01_200xCATH1_07_0...
9_01_200xCATH1_07_0...
9_01_200xCATH1_07_0...
9_01_200xCATH1_07_0...
9_01_200xCATH1_08_0...
9_01_200xCATH1_08_0...
9_01_200xCATH1_08_0...
9_01_200xCATH1_08_0...
9_01_200xCATH1_08_0...
9_01_200xCATH1_08_0...
9_01_200xCATH1_08_0...
9_01_200xCATH1_08_0...

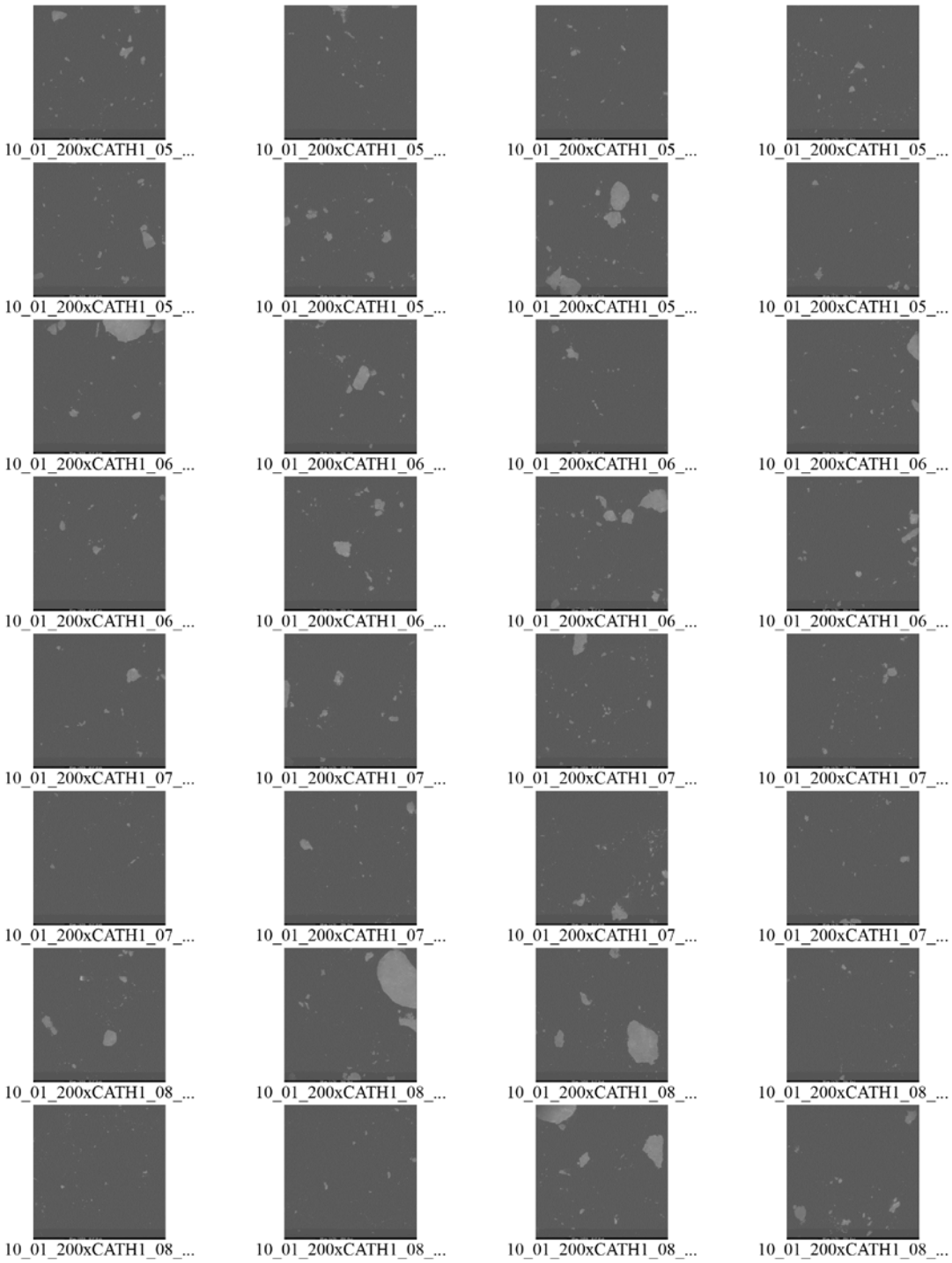
10_01_200xCATH1_05_...
10_01_200xCATH1_05_...
10_01_200xCATH1_05_...
10_01_200xCATH1_05_...
10_01_200xCATH1_05_...
10_01_200xCATH1_05_...
10_01_200xCATH1_05_...
10_01_200xCATH1_05_...
10_01_200xCATH1_06_...
10_01_200xCATH1_06_...
10_01_200xCATH1_06_...
10_01_200xCATH1_06_...
10_01_200xCATH1_06_...
10_01_200xCATH1_06_...
10_01_200xCATH1_06_...
10_01_200xCATH1_06_...
10_01_200xCATH1_07_...
10_01_200xCATH1_07_...
10_01_200xCATH1_07_...
10_01_200xCATH1_07_...
10_01_200xCATH1_07_...
10_01_200xCATH1_07_...
10_01_200xCATH1_07_...
10_01_200xCATH1_07_...
10_01_200xCATH1_08_...
10_01_200xCATH1_08_...
10_01_200xCATH1_08_...
10_01_200xCATH1_08_...
10_01_200xCATH1_08_...
10_01_200xCATH1_08_...
10_01_200xCATH1_08_...
10_01_200xCATH1_08_...

APPENDIX I

MILLED UO_2 IMAGES ANALIZED

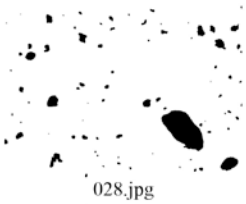

028.jpg

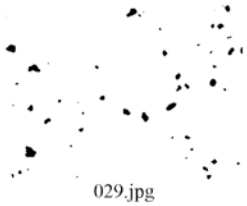

029.jpg

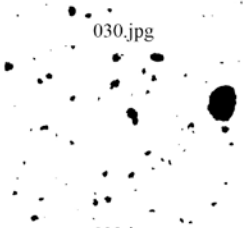

030.jpg

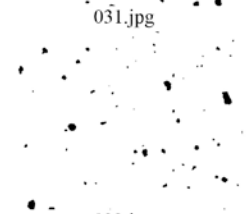

031.jpg

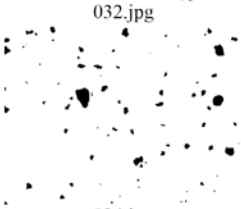

032.jpg

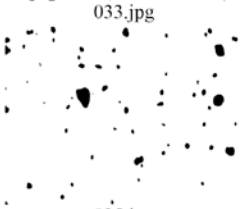

033.jpg

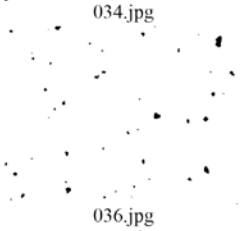

034.jpg

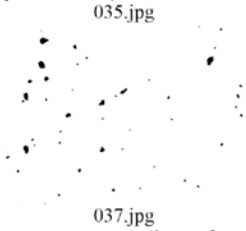

035.jpg

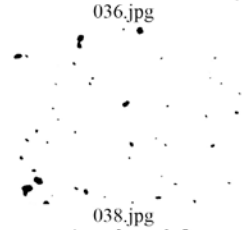

036.jpg

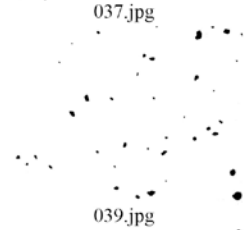

037.jpg

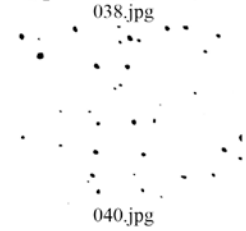

038.jpg

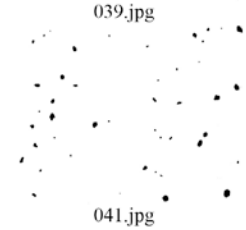

039.jpg

040.jpg

041.jpg

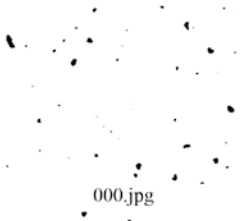

000.jpg

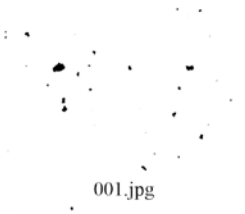

001.jpg

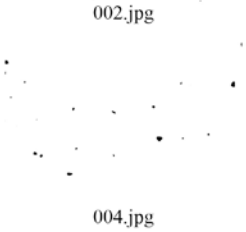

002.jpg

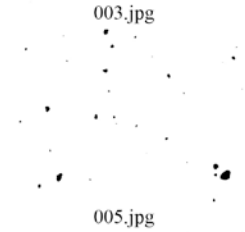

003.jpg

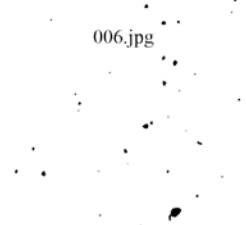

004.jpg

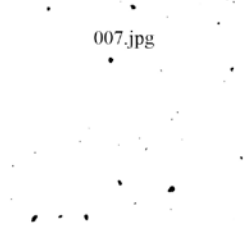

005.jpg

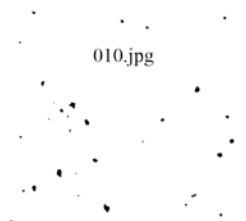

006.jpg

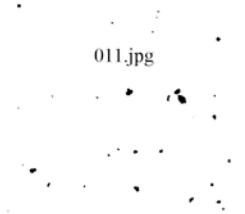

007.jpg

008.jpg

009.jpg

010.jpg

011.jpg

012.jpg

013.jpg

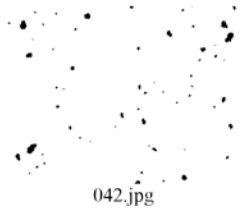

042.jpg

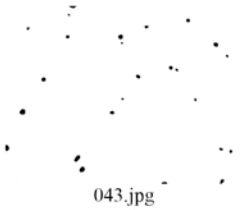

043.jpg

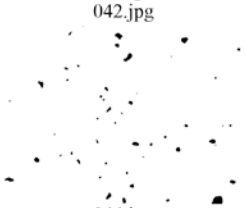

044.jpg

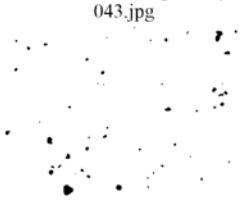

045.jpg

046.jpg

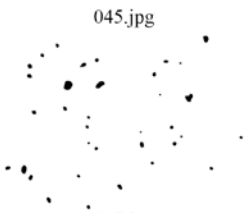

047.jpg

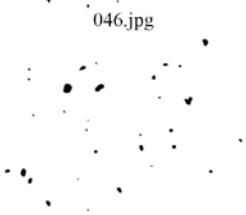

048.jpg

014.jpg

015.jpg

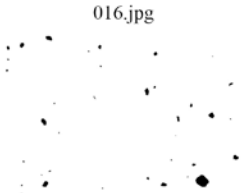

016.jpg

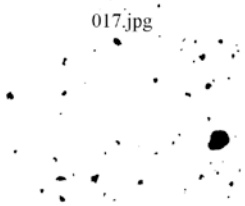

017.jpg

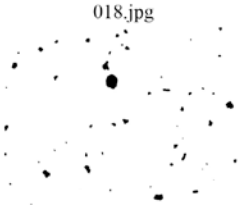

018.jpg

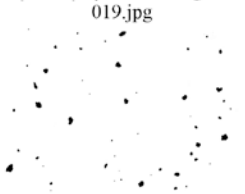

019.jpg

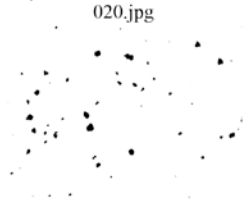

020.jpg

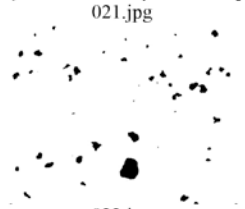

021.jpg

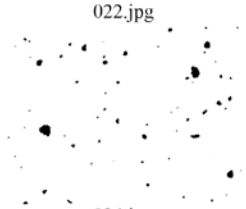

022.jpg

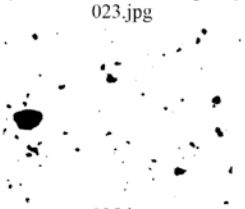

023.jpg

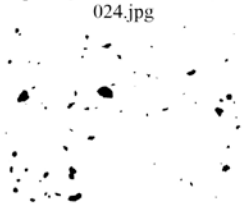

024.jpg

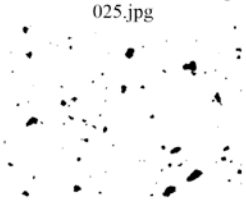

025.jpg

026.jpg

027.jpg

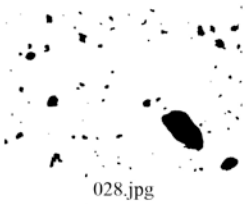

028.jpg

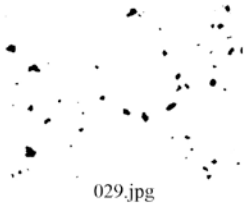

029.jpg

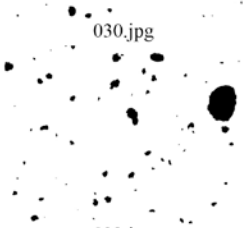

030.jpg

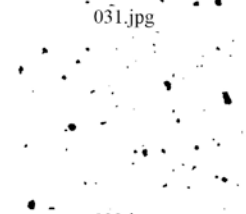

031.jpg

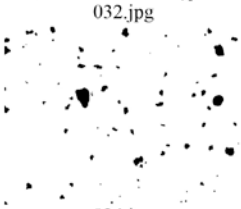

032.jpg

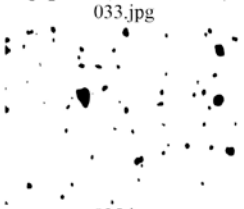

033.jpg

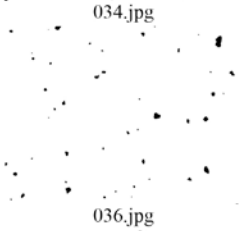

034.jpg

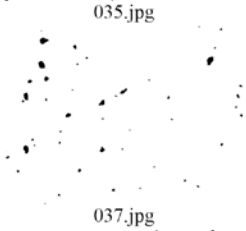

035.jpg

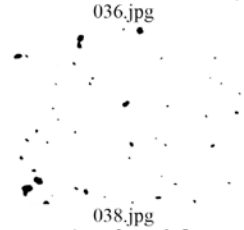

036.jpg

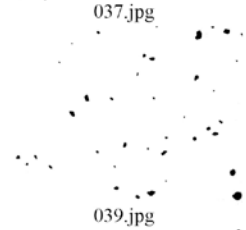

037.jpg

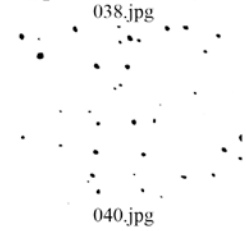

038.jpg

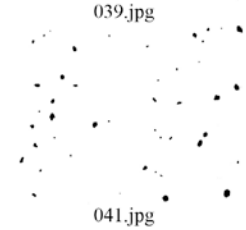

039.jpg

040.jpg

041.jpg

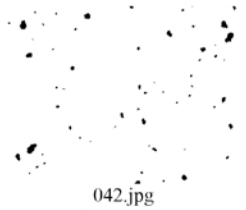

042.jpg

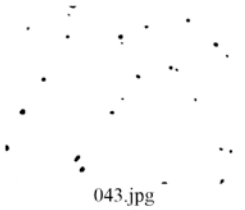

043.jpg

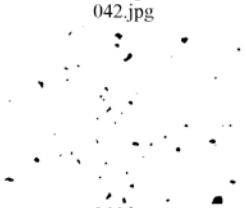

044.jpg

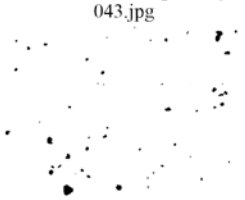

045.jpg

046.jpg

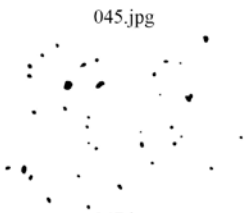

047.jpg

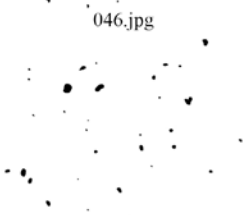

048.jpg

C000.jpg

C001.jpg

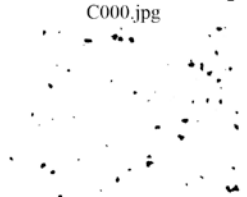

C002.jpg

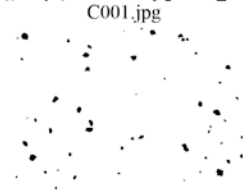

C003.jpg

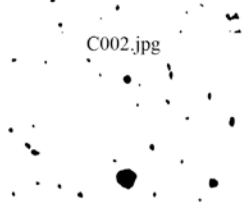

C004.jpg

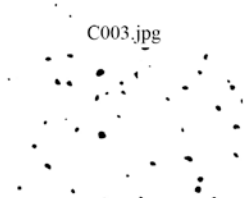

C005.jpg

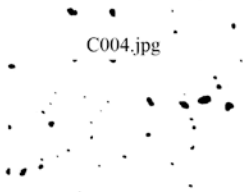

C006.jpg

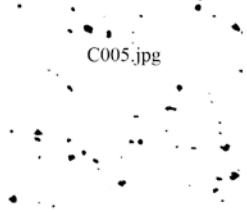

C007.jpg

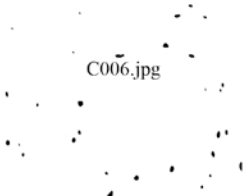

C008.jpg

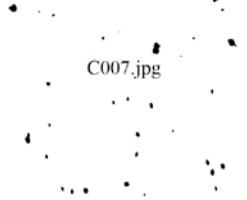

C009.jpg

C010.jpg

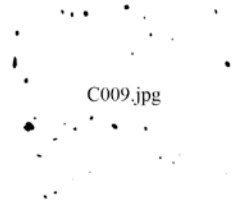

C011.jpg

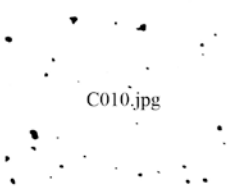

C012.jpg

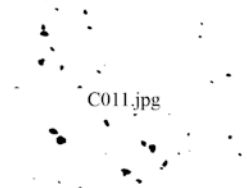

C013.jpg

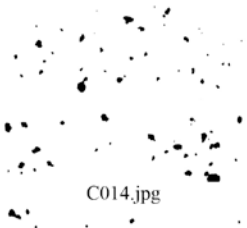

C014.jpg

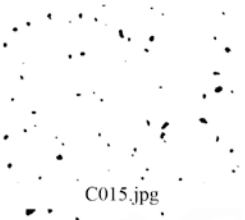

C015.jpg

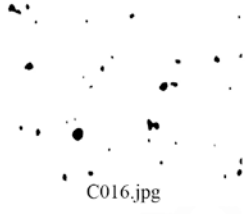

C016.jpg

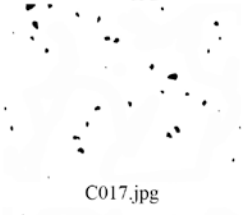

C017.jpg

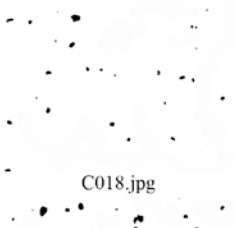

C018.jpg

C019.jpg

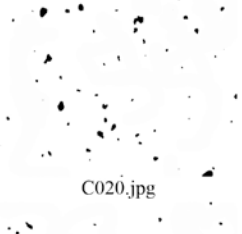

C020.jpg

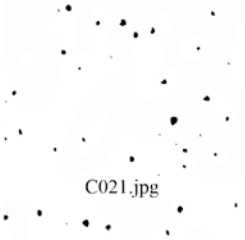

C021.jpg

C022.jpg

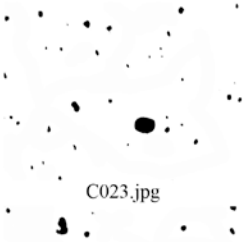

C023.jpg

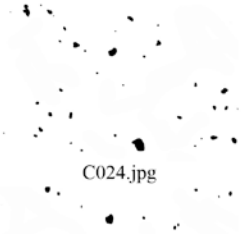

C024.jpg

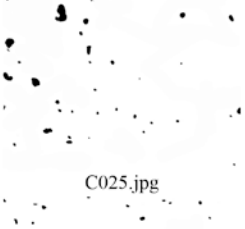

C025.jpg

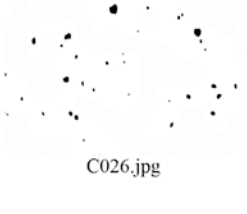

C026.jpg

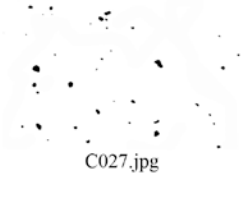

C027.jpg

C028.jpg

C029.jpg

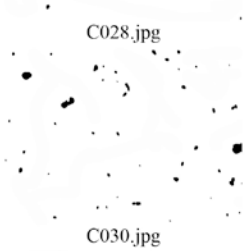

C030.jpg

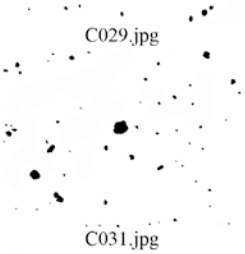

C031.jpg

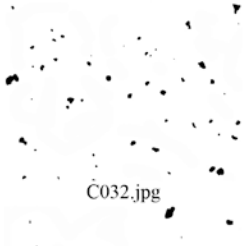

C032.jpg

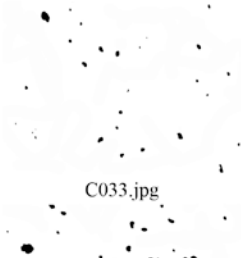

C033.jpg

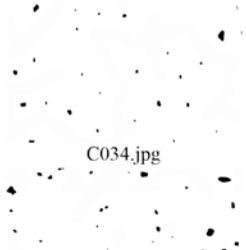

C034.jpg

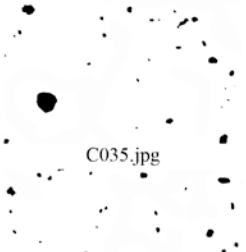

C035.jpg

C036.jpg

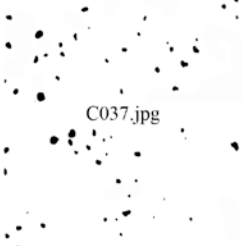

C037.jpg

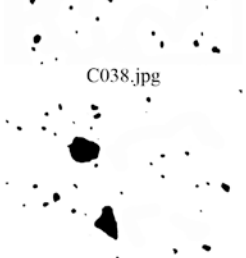

C038.jpg

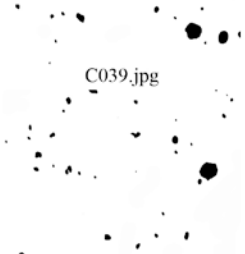

C039.jpg

C040.jpg

C041.jpg

C042.jpg

C043.jpg

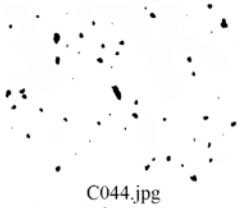

C044.jpg

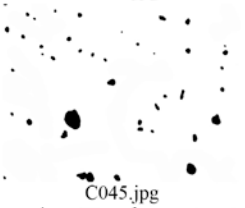

C045.jpg

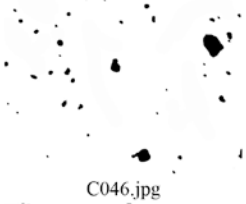

C046.jpg

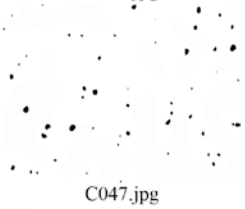

C047.jpg

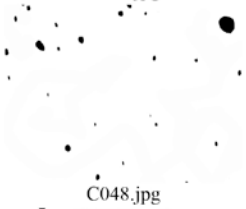

C048.jpg

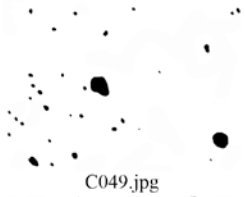

C049.jpg

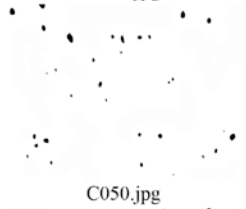

C050.jpg

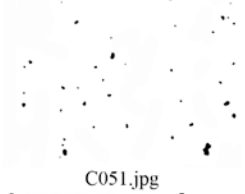

C051.jpg

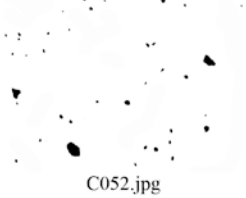

C052.jpg

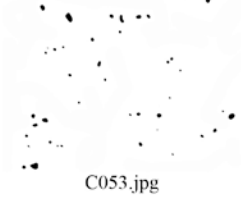

C053.jpg